UNIVERSITY OF LIVERPOOL

Determining the role of laminin polymerisation on cell behaviour using CRISPR-Cas9 genome edited models.

Thesis submitted in accordance with the requirements of the University of Liverpool for the degree of Doctor in Philosophy

By

Liam Shaw

March 2022

Index

Chapter 1: Thesis Introduction

1.1 Abstract

The laminins (LM) are a family of basement membrane glycoproteins with essential roles in supporting epithelia, endothelia, nerve and muscle adhesion, and in regulating a range of processes including cell migration, stem cell maintenance and differentiation. However, important questions regarding the role and mechanisms of LM-LM interactions in regulating cell behaviour, and the dynamics and turnover of LMs at high resolution have not been fully addressed. In this thesis, I harnessed the power of recent advancements in genome-editing technologies to create tools to study these questions in ways that have never before been possible.

LM to LM interaction is dependent on interaction between globular LM N-terminal (LN) domains. The importance of these interactions is illustrated by genetic disorders where point mutations in LN domains result in serious, often fatal, clinical manifestation. However, the mechanisms behind the phenotype of these disorders could be due to multiple overlapping mechanisms which analysis in animal models cannot differentiate. To allow mechanistic investigation, I used CRISPR-Cas9 genome editing to introduce a LN domain disrupting mutation, E234K, into LMα5 in the human lung adenocarcinoma cell line A549, generating a cell-model of these diseases. The mutant cells displayed reduced cell surface expression of LM-binding integrins, reduced attachment rate and strength of adhesion, reduced force exertion, decreased wound healing, migration processivity and proliferation in 2D culture. The mutated cells also showed a reduction in focal adhesion maturation. HEK293 cells cultured on the LMα5 mutant cell-derived matrices also showed a reduced attachment rate and strength of attachment, whereas culturing mutant cells on wildtype cell-derived matrices rescued the strength of attachment phenotype, confirming that these aspects of the phenotype are matrix-driven. Cells cultured on mutant cell-derived matrices also showed a reduced phosphorylation in multiple signalling components of the receptor tyrosine kinase pathways, including AKT phosphorylation. Analyses of the mutant-cell derived matrices identified an increase in LM disorder, as well as an increase in collagen levels in the matrix and other changes to core composition.

One of the big advancements in studying LM deposition was plasmid-mediated expression of fluorescently tagged LMs. However, while extremely useful, these tools had limitations including difficulty in delivery due to large construct size, related to the potential issues with physiological relevance related to overexpression, and being restricted to transient expression. Here, I report two distinct approaches to generate genome-edited cell lines with endogenous expression of tagged LMs for conventional and super-resolution fluorescent microscopy. Using CRISPR-Cas9, I introduced the photoconvertible fluorophore Dendra2 into the C-terminus of LMβ1 in A549 cells. Despite successful

expression of the tagged protein within cells, no detectable LMβ1-Dendra2 protein was deposited to the extracellular matrices or conditioned media of edited cells. However, all was not lost in the quest for a super-resolution, genome-edited LM, with the ground-work here laying the foundations for future a photo-activatable LM tag.

Together, these new tools and data have substantively advanced the field of LM and basement membrane research. The LMα5 mutant cell line has highlighted the complex and diverse role of LM polymerisation, a role once thought to be solely structural.

1.2 List of Abbreviations

Full Name	Abbreviation
(Dulbecco's) Phosphate Buffered Saline	(D)PBS
Adenocarcinomic human alveolar basal epithelial cells	A549
Protein kinase B	AKT
Basement Membrane(s)	BM(s)
Bone morphogenetic protein	BMP
Bullous Pemphigoid 230	BP230
CRISPR-Associated protein 9	Cas9
Cytomegalovirus Promotor	CMV Promoter
Type IV Collagen	ColIV
Type XVII Collagen	ColXVII
Clustered regularly interspaced short palindromic repeats	CRISPR
CRISPR RNA	crRNA
Connective tissue growth factor	CTGF
Dystroglycan	DG

Extracellular Matrix	ECM
Ethylenediaminetetraacetic acid	EDTA
Epidermal growth factor	EGF
Epidermal growth factor-like	EGF-like
Electron microscopy	EM
Filamentous Actin	F-Actin
Focal Adhesion Kinase	FAK
Foetal calf serum	FCS
False discovery rate	FDR
Fibroblast growth factor	FGF
Fibronectin	FN
Glycosaminoglycan	GAG
Green Fluorescent Protein	GFP
Single guide RNA	gRNA
Homology directed repair	HDR
Human embryonic kidney cells	HEK293
Hepatocyte growth factor	HGF
Heparan sulphate	HS

Heparan sulphate proteoglycan	HSPG
Insulin growth factor	IGF
Insertion/deletion mutation	Indels
Knockout	KO
Laminin four	L4/LF
Laminin coiled-coil domain	LCC Domain
Liquid chromatography Mass Spectrometry	LC-MS
Laminin epidermal growth factor like Domain	LE Domain
Laminin globular domain	LG Domain
Laminin(s)	LM(s)
Laminin N-terminal domain	LN Domain
Latent transforming growth factor binding protein	LTBP
Merosin-deficient congenital dystrophy type 1A	MDC1a
Non-homologous end joining	NHEJ
Nuclear localisation signal	NLS
Photo Activated Localisation Microscopy	PALM
Protospacer Adjacent Motif	PAM
Polymerase chain reaction	PCR

Platelet derived growth factor	PDGF
Phosphoinositide 3-kinase	PI3K
Arginine-Glycine-Aspartic acid	RGD
Receptor tyrosine kinase	RTK
Real-time quantitative PCR	RT-qPCR
Sodium dodecyl sulphate	SDS
SDS-polyacrylamide gel electrophoresis	SDS-PAGE
Scanning electron microscopy	SEM
Sulphated glycolipids	SGL
Tris-acetic acid-EDTA buffer	TAE
Transcriptional coactivator with PDZ-binding motif	TAZ
Tris buffered saline	TBS
Transmission electron microscopy	TEM
Transforming growth factor	TGF
Tumour necrosis factor	TNF
Trans-activating RNA	trRNA
Untranslated region	UTR
Yes-associated protein	YAP

1.3 List of Figures

1.4 List of Tables

1.5 Acknowledgements

This thesis is the final step in what has been a life-changing academic adventure of highs and lows. An adventure that I couldn't have done without the help and encouragement of a number of people.

Firstly, a huge thank you to my supervisory team. My primary supervisor Dr Kevin Hamill, the man who responded to my emails and messages stressing about work at silly o'clock, and gave me unwavering guidance and support throughout my PhD. Without him, I wouldn't be the scientist I am today. Additional thanks also to my secondary supervisors Professors Rachel Williams and Roy Quinlan, who's guidance and support have enabled to develop a vast array of valuable skills to further my research.

A big thank you to everyone at the William Henry Duncan Building, with a particular thank you having to go to my hero and mate Lynn Green, who's heart of gold helped me through many a rough day! A big thank you to Sharon, who without her help on last minute orders, I'd still be in 2nd year, and also to Andy for being an all-round top bloke and legend when it came to helping me with lab supplies.

Thank you to my lab group: Lee for being my lab dad and teaching me every method I know, Conor for the constant laughs so we didn't cry, Thanos for the cuddles, and JohnJohnJohn for the questions. Thank you to everyone else who made my PhD the experience it was, my main firm, whether it be lunchtimes

together, nights out or simply rating roast dinners: Alys, Georgia, Sam, Steph, Wasuuuuu, thank you so much for keeping me sane!

And last but certainly not least, to the people I wouldn't have survived without, my mum, my dad and Emily. You have all supported me through thick and thin, through the ups and the down, and I will be forever grateful to you. My absolute rocks, without my family this wouldn't have been possible. I love you all. Obviously I couldn't forget Bobby, Kendal and Jasper…

And Jurgen Norbert Klopp, the only man who can ever make me cry. YNWA. x

1.6 Introduction to thesis

In this thesis, I will describe my investigation into the importance of laminin polymerisation to extracellular matrices and the biology of the cells that interact with these matrices. To put this in context, I will first describe what basement membranes are and why they are so critical to all adherent tissues. I will discuss the core components of a basement membrane and their roles within cell biology. I will then focus specifically on laminins their domain architecture, and how these small molecular building blocks forms the scaffold around which the basement membrane forms. I will discuss what has been learnt about laminin polymerisation through the study of genetic diseases and biochemical protein analyses. Finally, I will discuss how the CRISPR/Cas9 genome-editing technique has allowed development of new methods to study these non-polymerizing mutations in ways that were not previously possible.

Chapter 2: Basement membranes: Laminins and other components

Some of the work in this literature review was published in Frontiers in Genetics (1), available in Chapter 9: Appendix 2.

2.1 Basement membrane overview

Basement membranes (BMs) are flexible, usually 40-120 nm thick sheets that separate cells from underlying connective tissue, and regulate cell behaviours including determining cell polarity and migration, influencing cell metabolism, and contributing to defining cellular differentiation and lineage specification (2, 3) (Figure 2.1.). Most BMs consist of two layers; an electron-lucent layer, lamina lucida, and an electron dense layer, lamina densa (4). The lamina lucida is considered to be predominantly comprised of laminin (LMs) and nidogen, while the lamina densa is predominantly made up of collagen IV and perlecan (2, 3, 5).

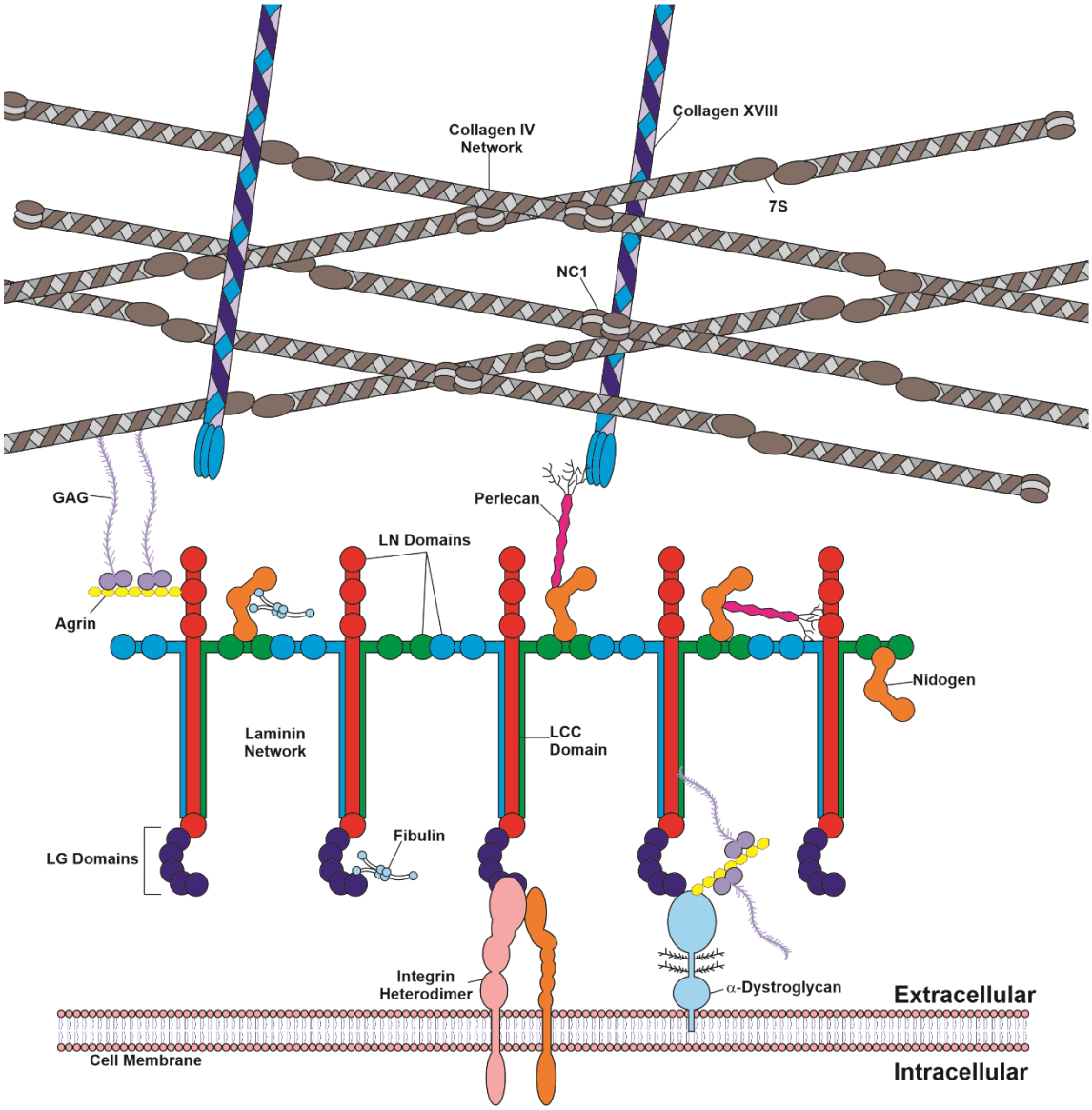

Figure 2.1: The Basement Membrane: Adapted (6) example of an archetypical basement membrane. Laminin and collagen IV networks make up the main structure of the basement membrane, with other major components including the cell attachment molecules integrins and α-dystroglycan, nidogens, perlecans, agrins, fibulins and glycosaminoglycan (GAG). Key domains of the laminin and collagen IV networks are also labelled: laminin globular (LG), laminin coiled-coil (LCC) and laminin N-terminal (LN) domains, as well as the 7S and the non-collagenous (NC1) domains.

BMs assemble through a multistep process, with the current thinking indicating that the LM network assembles first (7). The initial anchoring interaction of cells to a nascent BM occurs primarily through LM carboxy-terminal globular (LG)

domains that are bound by sulphated glycolipids, integrins, dystroglycan, and heparan sulphates. This cell surface anchorage provides a nucleation point that enables the accumulation of nidogen, collagen IV, perlecan, and agrin to the LM scaffold. Non-LM components also have the potential to bind directly to cell surface integrins and/or dystroglycan, but are not able to accumulate on the cell surface to any appreciable degree in the absence of LM (8, 9). Importantly, although the LM network and a collagen IV network can self-assemble in vitro, this self-assembly in vivo is thought to be initiated by binding of LMs to cell surface receptors (8-12), meaning that it is the cells themselves that facilitate the formation of these scaffold matrices, through locally increasing the concentration of BM components (9, 11, 13).

BMs are not a static structure, but rather are dynamic, changing either through protein turnover or reorganisation of its different components at different times (14). These dynamic changes often lead to changes in the mechanical properties of BM, and can play a part in the BMs varied roles to a tissue's biology (15).

2.1.1 Basement membrane roles - Structural

Perhaps the most obvious role of the BM is to act as a structural scaffold, providing support to tissues and allowing cells to organise into higher orders. The importance of the BM structurally can be seen in many diseases were components of the BM are absent, such as Pierson syndrome (16) and epidermolysis bullosa (17, 18) which are described in more detail below. In these BM-associated conditions, the loss of structural support provided by the BM results in loss of tissue function due to loss of integrity of the cell-stromal junctions.

Phenotypic manifestations reflect the distribution of the affected protein, for example leading to loss of glomerular function in Pierson syndrome, or skin fragility and blistering in epidermolysis bullosa. However, to simply put these diseases down to a loss of BM structure could be considered reductionist, and doesn't consider the myriad of other roles a BM plays.

2.1.2 Basement membrane roles - Biophysical sensor

The physical features of BMs play an integral role in regulating how cells perceive biophysical signals (15) via mechanotransduction. Mechanotransduction involves cell surface receptor proteins (predominantly integrins) binding to the proteins of the BM and, via an intracellular complex, providing a physical linkage between the microenvironment and the intracellular actin cytoskeleton. Changes to the BM biochemical features, such as stiffness/compliance, are "sensed" via these linkage which then trigger downstream signalling cascades (19, 20). These mechanical linkage complexes take the form of focal adhesions as linkages to the actin cytoskeleton and hemidesmosomes as linkages to intermediate filaments (21-23). These cytoskeletal connections are critical for the cellular reaction to changes in BMs.

Mechanical effects work bi-directionally. Cells respond to forces on their focal contacts and hemidesmosomes by remodelling the extracellular matrix (ECM) in an almost symbiotic manner; whilst the BM properties influence cells from the outside-in, cells influence the BM through remodelling in an inside-to-outside directional manner. This is highly relevant to laminins and collagens; however, the best studied example of this directional remodelling is through the fibronectin

reassembly in response to stretching (24, 25). When under stretch, cells organise fibronectin and collagen fibrils along the axis of the force, with fibronectin initially binding to the integrin under stress (24). Following this binding, the fibronectin is pulled by cytoskeleton to expose domains that allow for fibril assembly. These fibrils form an insoluble matrix when stretched, which is later lost when contractility is lost (25).

There is also evidence of LM and collagen IV remodelling in response to the extracellular environment by the cells (26). The secretion of ECM-remodelling enzymes such as metalloproteinases and also their inhibitors can by influenced by mechanical stresses through actomyosin contractility, in-turn triggered by upstream integrin signalling (27, 28). Importantly for this thesis, the integrins allow the cells to sense the mechanical properties of its ECM (29). These forces result in cells secreting a matrix that can resist the applied forces (30-32).

The interaction between the integrins and the ECM is of particular importance in this thesis. To understand the importance of laminin polymerisation, it is also important to understand how a cell might react to networks through their integrin signalling pathways. LM to integrin signalling will be discussed in greater detail below.

2.1.2a Cellular Adhesion through Focal Adhesions

Focal adhesions are present in the plasma membranes of cells which lie within 15 nm of an ECM substrate (20, 33). This series of tight interactions between the cells and their ECM enables the cells to respond to their external environment

(34). Focal adhesions are very dynamic, with proteins associating and dissociating continuously as signals are transmitted through the cells. Analyses of the focal adhesion “adhesome” have revealed that these adhesions can contain over 150 different proteins, highlighting considerable diversity in function (35). Within this vast array of proteins, a number of proteins are considered as “core”, being found in most forms of focal adhesions, these include integrins, talin, actinins, paxillin, vinculin and focal adhesion kinase (36).

Integrin receptors are integral to all focal adhesions, acting as complex recruitment centres (34). Each integrin is a heterodimeric protein comprised of an α and a β subunit, of which there are at least 18 α and 8 β subunits combining to form 24 known heterodimeric pairings (37). The resulting heterodimers span the plasma membrane, with different heterodimers displaying differential affinity to the components of the ECM (28, 34). In response to ECM-integrin interactions, talin and α-actinin are recruited to the integrin’s cytosolic domain, where the talin binding to integrin allows the recruitment of vinculin, paxillin and focal adhesion kinase (FAK) to the adhesion site (34, 38). Paxillin acts as a signal transduction adapter protein for focal adhesions, with an N-terminal rich in protein-protein interaction sites (39, 40). FAK is recruited to the paxillin N-terminal, where it tyrosine phosphorylates the paxillin, allowing for the further recruitment of focal adhesion proteins including vinculin (41). Vinculin is typically self-inhibited through the interaction of its head and tail domains, but the interaction of talin with vinculin changes vinculin to its active (open) formation (38). This active formation

then crosslinks the actin cytoskeleton to the focal adhesion (38), triggering signal transduction between the extracellular environment and the cells.

Focal adhesions play an important and complex role in cellular signalling, with over 150 components of adhesion-signalling complex so far described (42). Of these signalling interactions, the interaction between integrin-FAK and protein kinase B (AKT) is the most studied. Integrins binding to the ECM triggers FAK recruitment to the focal adhesion, and upon recruitment to the focal adhesion, FAK phosphorylates phosphoinositide 3-kinase (PI3K), which triggers the activation of AKT and its respective signalling cascade (43-47). Inhibition of FAK confirmed this central importance to the AKT signalling pathway, as following inhibition, AKT signalling was blocked and cell proliferation and migration was reduced (48). Inhibition of FAK has also been shown to induce apoptosis via the AKT pathway (49). Quite interestingly, AKT has also been shown to directly regulate FAK activity through serine phosphorylation, despite FAK typically being considered an upstream mediator of AKT (50)

2.1.2b Cellular Adhesion through Hemidesmosomes

Hemidesmosomes are small, stud-like structures found in keratinocytes of the epidermis and other epithelia, and which anchor the keratin filament cytoskeleton to the extracellular matrices (51). A tightly-ordered complex, hemidesmosomes contain a core of integrin α6β4 and type XVII collagen, these are bound intracellularly by plectin and BP230 which connect to the cytoplasmic keratin intermediate filaments. (22, 23, 52). Type XVII collagen (ColXVII) is a homotrimeric transmembrane protein (53) Comprised of three alpha1(XVII)-

chains, ColXVII interacts directly with integrin β4, plectin and BP230 to form mature hemidesmosomes, (52). Extracellularly, the C-terminus of ColXVII and the extracellular domains of integrin α6β4 bind to LM332 and are required for the correct orientation of the LM (54, 55).

Hemidesmosomes are comparable to focal adhesions in that both are primary forms of attachment of cells to the ECM. However, focal adhesions require an ECM substrate to lie with 15 nm of the cell's plasma membrane and provide relatively weak but dynamic interactions. In comparison, hemidesmosomes span much larger areas and provide a much firmer and more stable adhesion of basal epithelial cells to the underlying basement membrane (56). However, hemidesmosomes have also been shown to regulate actin remodelling (57), as well as interacting in cross-talk mechanisms with the focal adhesion complexes to regulate force transduction (58).

2.1.3 Basement membrane roles - Growth Factor repository and release

A third important role of the BM is regulation of growth factors. The BM sequesters a number of growth factors within its protein components, typically through perlecan and other heparan sulfate proteoglycans. Bound growth factors include fibroblast growth factor family (FGF's) (59, 60), hepatocyte growth factor family (HGFs) (61), platelet derived growth factors A and B (PDGF A and B) (62) and hematopoietic growth factors (63). These growth factors are typically then released through the action of enzymes such as thrombins and plasmins (64). In addition, collagen IV and fibronectin also bind (65) transforming growth factor β

(TGF-β) (66), tumour necrosis factor (TNF-α) (67), PDGF-BB and –AB (62), insulin growth factors (IGFs) (68), and bone morphogenetic protein (BMP) 2 and 7(69). These growth factors are released by metalloproteinases and degradation (65).

Growth factor-ECM interactions have a number of major consequences. These interactions allow for rapid extracellular signalling; with proteolytic release being a much more rapid response option than de novo synthesis (70, 71). There is also evidence that growth factors embedded in the ECM could act as cellular memory. Cells are more susceptible to damage than the matrix structures, and growth factors embedded in the remaining matrix could instruct cells to form the proper structures during wound healing (65).

It is not yet known how, or indeed if, LM polymerisation affects growth factor binding, sequestration and release, but one might predict that formation and dissolution of LM networks could act directly much like collagen IV, or could act indirectly via influencing the assembly of the collagen IV network or perlecan integration to contribute to growth factor regulation.

2.1.4 Basement membrane roles - Barrier

A fourth, and sometimes under-appreciated, role of the BM is the role as a barrier; separating the epithelium or endothelium from connective tissue. Indeed, the remodelling or loss of the BM is absolutely required for tumour metastasis, where cancerous cells must bypass the physical barrier to migrate into the vessels and access distant organs (72). The BM as a barrier, is not purely binary, it can also

serve as a semipermeable selective barrier in some tissues, most notably in the kidneys (73), lungs (74) and brain (75).

2.2 Core components of Basement Membrane (non-laminins)

2.2.1 Collagen IV

Type IV collagen (ColIV) is a non-fibrous heterotrimeric protein that makes up ~50% of the mass of mature BMs (2). Unsurprisingly, ColIV has an essential structural role within the BM, with ColIV knockout (KO) being lethal at the embryonic stages of development. Homozygous or compound heterozygous missense mutations in humans in the genes involved in the formation of the ColIV heterotrimer, COL4A1 and COL4A2, are fatal at the embryonic stage, with heterozygous mutations presenting with severe defects to the brain, eye and kidney function, as well as having defects in vascular stability (76).

In addition to its mechanical role, ColIV also acts as a scaffold for other components of the BM, most notably nidogens and perlecan (77-81). ColIV polymers also act as a reservoir for growth factors such as TGFβ (82, 83), PDGF (84) and EGF(85).

2.2.2 Nidogen/Entactin

Nidogens, known also as entactins, are glycoproteins that make up approximately 2-3% of the BM and are a key component of BM assembly (2). Nidogens have a wide protein-binding repertoire, allowing them to act as a linker protein between the different components of the BM (86). Most notably, nidogens facilitate the binding of LMs to ColIV (78, 79, 87), in addition to binding fibronectin, fibrinogen

and perlecan (88, 89). There are two nidogens in humans, both consist of three globular like domains (G1-3), separated by rods (90). Of these domains, the G3 domain (of nidogen-1*)* has been demonstrated to be capable binding to LM γ1 and γ3 (86, 91). Upon formation of this complex, the nidogen is then able to bind to ColIV via their G2 domain (90).

2.2.3 Perlecan

Perlecan is a macromolecular BM-type heparan sulphate proteoglycan (HSPG) comprised of 5 domains (I –V) (92). Perlecan plays an important role in growth and development, it is also implicated in wound repair, cancer invasion and diabetes (93). Domain I contains three GAG chains, responsible for heparan sulfate (HS) dependent interactions (94); growth factor binding such as FGF2 (95), ECM molecules such as nidogen (96) and collagen (97). Perlecan domain II contains a series of low density lipoprotein repeats that are responsible for the binding of growth factors such as TGF-β (98) and connective tissue growth factor (CTGF) (99). Domain III consists of three Cys-free laminin-like globular domains, that alternate with Cys-rich EGF-like domains (100), similar to the laminin α chain short arm (101), described below. Domain III has been implicated in cellular adhesion through its Arg-Gly-Asp (RGD) sequence (100). Domain IV of perlecan contains 14 immunoglobulin superfamily modules and has been implicated in laminin-nidogen complex binding (102), but also supports cell adhesion and focal adhesion kinase (FAK) activation (implicated in cell spreading) (103). Domain V is involved in the binding of nidogen-laminin complexes and fibulin-2, as well as

promoting integrin β1 mediated cell adhesion (96). Domain V also shares homology with the LG domain of laminin (96).

2.2.4 Agrin

Agrin is a modular proteoglycan, widely expressed in BMs, being of particular note in neuromuscular junctions, glomerular BM and the liver (104-106). Agrin consists of a core protein of ~220 kDa, with two potential glycosaminoglycan side chains, increasing its molecular weight to ~400 kDa (107). Agrin exhibits high-affinity binding to the coiled-coil domain of LM γ1 (107), suggesting an important role in BM reorganisation (108).

2.2.5 Dystroglycans

Dystroglycans are key cell surface receptor for the LG domains of the LM network. Whilst integrins typically bind the LG1-3 domains, dystroglycans bind to the LG4 and 5 domains (79). Dystroglycans are composed of two subunits, a plasma membrane spanning β domain, and extracellular LM binding α domain. LM binds to the highly glycosylated α subunit in a Ca^{2+} and carbohydrate dependent manner (109, 110). It is believed that dystroglycans play an essential role in the assembly of the BM, through the binding of soluble LM and aggregating it to the cell surface where it can form LM networks (111). Indeed, dystroglycan knockouts lack this LM clustering at the cell surface, and are embryonically lethal (111).

2.3 The Laminin Superfamily

LMs are large heterotrimeric proteoglycans that are an obligatory feature of every BM. LM encoding genes are subdivided into α, β, and γ groups, with each LM

being a αβγ heterotrimer (Figure 2.2a). In mammals, five α chains (encoded by the genes *LAMA*1 to 5), four β chains (*LAMB*1-4) and three γ (*LAMC*1-3) chains have been identified (5, 112, 113) (Figure 2.2b). In addition, use of a second promoter in *LAMA*3 gives rise to two major forms, a short α3a form and a longer α3b form (Figure 2.2). These two forms are functionally and structurally distinct and therefore this alternative splicing event effectively increases the number of α chains to six members (114). If all of the possible αβγ-chain combinations were possible, then 72 different heterotrimers could exist, however restrictions in heterotrimerisation potential, as well as differential tissue distribution patterns, means that only 16 LM trimers have been identified as existing to date in vitro (115-119).

LMs are thought to have arisen through a series of gene duplication events, with the netrins also emerging from common LM ancestral genes through evolutionary domain loss and shuffling. This complex evolutionary process has allowed for a diverse repertoire of LMs and netrins to exist in humans and higher order mammals (120).

Briefly, from the common β-LM ancestral gene, LM β1 and netrin-4 emerged after a duplication event, with LM β2 later diverging from the LM β1 gene, and LM β3 from LMβ2. From the common α/ γ/ netrin-1-LM ancestral gene, two further genes emerged through a duplication event, which then duplicated again giving α1 and α2, and α3 and α5. In the α3 gene, a second promoter evolved in exon 38 (presumably) after this initial duplication event which allowed for LM α3a to emerge. From the common γ-LM ancestral gene, LM γ genes and netrin-1

emerged after a duplication event, with LM γ1 and LM γ3 later evolving (120). This common evolutionary divergence is why such a high conservation of critical residues within key domains across α, β, and γ LM chains. This evolutionary conservation is relevant to this thesis as it was an important consideration when designing mutations to introduce.

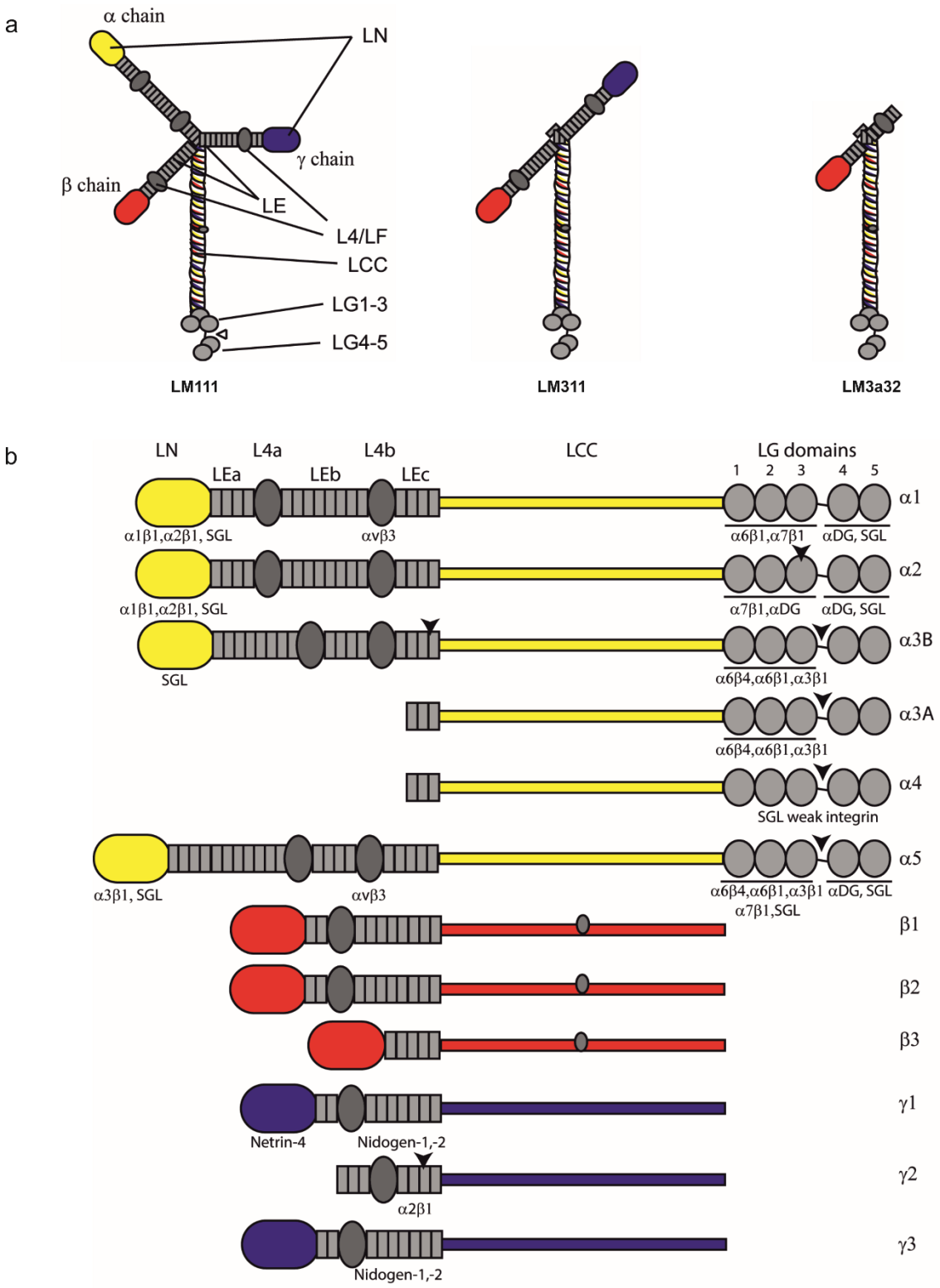

Figure 2.2: The LM Superfamily. a) Examples of a three- (LM111), a two-(LM311) and 1- armed (LM3a32) heterotrimer. b) All LM single chains, their domains (above the chain) and their prospective binding partners (below). DG = Dystroglycan, SGL = sulphated glycolipids.

2.3.1 Laminin structure overview

As a brief overview; beginning from the amino terminus, the archetypal LM chain consists of a large globular N-terminal domain (LN domain, previously known as domain VI), the major role of which is to mediate LM-LM interactions in BMs, allowing the assembly of higher-order LM polymer networks (79, 121, 122). The LN domain is followed by rod-like stretches of LM-type epidermal growth factor-like repeats (LE domains, formerly domain V) which are interspersed with globular domains (L4 or LF domains) (123). The LE repeats are followed by the defining feature of all LMs, a LM coiled coil domain (LCC domain) and it is through this domain that αβγ heterotrimers form (115-117, 119). In α chains, the LCC domain is followed by a C-terminal stretch of five LM globular domains (LG1-5), these LG domain harbour the highest affinity cell-surface receptor sites (124). While this domain architecture holds true for most family members, it should be noted that not all LM chains contain all of the domains described. Specifically, the α3A, α4, β3 and γ2 chains, contain shorter amino terminal arms with the α3A, α4 and γ2 specifically lacking a LN domain, and are sometimes referred to as “headless” or “truncated” (5, 125).

LM chains are typically discussed in relation to two pseudo-domains; the so called “long” and “short” arms (Figure 2.2a) based on the appearance of heterotrimeric proteins in rotary shadowing electron microscopy. LM long-arms are highly conserved, comprised of 561-591 amino acids depending on the chain (112) and contain the LCC domains (112, 117, 119), the α-chains extra LG domains are found at the end of this coiled-coil (124). The shorter arms are more diverse,

varying in length between chains, with the archetypical short arm containing the LN (228-259 residues), stretches of LE (41-70 residues each) interspersed with L4 (169-204 residues) domains (112). The LM short arms, and in particular the LN domains, are essential for the LM-LM interactions that result in polymerisation, and are the main focus of this body of work.

2.3.2 Laminin structure and function - Long arms

2.3.2a LG domains

The LM globular (LG) domains are a module of 5 domains (LG1-5) totalling approximately 200 amino acids that are located at the C-terminus of LM α chains and which contain the highest affinity cell-receptor binding sites (124, 126, 127). Importantly, not all LMs display the same complement of receptor interactions nor do they have the same affinities for different receptors (124). Indeed, it is perceived that the major differences in cellular responses to different LMs is primarily down to differences in their LG domains. LG1-3 have been shown to be essential in LM interaction with integrins at the cell surface, with integrins α3β1, α6β1, α6β4, α7β1 and α9β1 in particular implicated with LG1-3 (128, 129) LG4-5 fragments have been shown to contain a major heparan-binding site (Figure 2.2b) (130). LG4-5 assist in LM-receptor interactions by allowing cell surface sulfate groups to act as co-receptors such as with syndecan family (124).

Interestingly, not only the LM α chains are responsible for the function of LG domains. A fully intact coiled coil domain was shown to be essential to the function of the LG modules (131, 132), suggesting that the other chains of the LM plays a

role in integrin binding. The γ chain had been suggested to either bind integrins directly, or to alter the conformation of LG1-3 into a biologically active conformation (112, 133). In reality it is likely the former, with recent evidence showing that the γ1 chain lies opposed to the metal ion dependent adhesion site in integrin β1, allowing the integrin to bind to the bottom face of the LG1-3 domain (134). Although the role is not as clear, the C-terminal of β chains are also implicated in defining the affinity of integrin binding to LMs (135, 136).

2.3.2b LCC Domains and heterotrimerisation

LM coiled-coil (LCC) domains make up the long arms of LMs and are responsible for heterotrimer formation (137-140). LM heterotrimerisation occurs intracellularly in a multi-step process. The best supported mechanism for this process that a weakly associated heterodimer of the β-chain and γ-chain is formed through disulphide linkages across the LCC domains, before the α-chain is incorporated into a coiled-coil heterotrimer, with further disulphide linkages through the LCC domains (139, 141). It is the final incorporation of the α chain that allows secretion to occur (141).

Of the 45 potential heterotrimer isoforms, only 16 have been confirmed *in vivo* (142), suggesting that differential expression alone is insufficient for specific heterotrimer assembly (141). This specificity of trimerisation has been shown to be dependent on regions of the LCC (137, 138). From the three LCC domains in LM heterotrimer (one LCC domain each from an α, β, and γ chains), it has been experimentally demonstrated that the γ chain's LCC domain provides the highly specific selectivity of which LM heterotrimers are formed (141).

2.3.3 Laminin structure and function - Short Arms

2.3.3a LE Domains

LM epidermal growth factor (EGF)-like (LE) domains are short globular repeats of about 60 residues in the short arms of LM, with 8 highly conserved Cys residues (143). The conserved Cys residues create multiple loops through disulphide linkages in the LE repeats (91, 144). These disulphide linkages limit the flexibility of the LE arrays in the LM short arms (91). The major role of LE repeats therefore appears to be as rod-like spacers between the short arm globular domains (91). These LE-spacers vary in length from chain to chain, with the α3A chain containing only three LE repeats, and the α5 chain containing 22 LE repeats (112). The variance between the lengths of spacer LE repeats means that the length of the short arm of the 11 different LM chains differ in a much greater way compared with the long arms.

2.3.3b L4/F Domains

Within the stretches of LE repeats in the LM short arms lies L4 domains (or LF in the β1 and β 2 short arm) (112, 145). The L4 domains are globular domains (146), inserted between the 3rd and 4th cysteine residues in one LE domain, enlarging the LE domain. The L4 domains are possibly the least well understood domain in the LM chain, with their functions still largely unknown (145). However, there is an obvious importance to these highly conserved domains, as highlighted in patients with in-frame deletions of 63 residues in the LMα2 L4 domain presenting with congenital muscular dystrophy, with hypotonia, poor head control and

stumbling (147). Although a lot milder than patients who suffer a lack of the full protein (147, 148), these findings highlights an important function of the L4 domains.

2.3.4 The LN Domains and their interactions

LN domains are found at the amino terminus of the α1, α2, α3B, α5, β1, β2, β3, γ1 and γ3 laminin. These are globular domains of 252 to 264 amino acids, within which there is strict conservation of six cysteine residues. There is a 72 % overall sequence identity between α1 and α2 and 77 % between α3B and α5, 72 % between LMβ1 and LMβ2 LN domains, and 64 % between LMγ1 and LMγ3 LN domains. Lowest conservation is between LMβ3 and the β1 and β2 LN domains (38 % and 42 % respectively) (149).

The LN domains are essential to the LM-LM interactions that mediate LM polymerisation. A number of diseases have been associated with the inhibition of LN-LN domain interactions, and this will be discussed in detail below. However, in addition to polymerisation, LN domains are implicated in cell adhesion, neurite outgrowth, perlecan, heparan and heparan sulfate binding (149-152). The LN domain of LMα1, α2, and α5 can interact with integrins α1β1, α2β1, and α3β1, and presumed between LMα3b and integrin α3β1 based on antibody inhibition (153-157). These interactions are lower affinity than LG domain interactions and likely are involved in localisation to allow polymerisation rather than signal propagation (1). Nevertheless, there is still much to learn about the roles of LN domains, besides their role in LM-LM polymerisation and network formation.

2.3.5 LN-LN interactions

Laminins interactions have been studied over many years with important early work establishing a “three-arm” model; polymerisation can only occur when all three constituent short arms contain an LN domain (79, 158). Moreover, interactions must be heterotypic, involving an α, β and γ LN domain coming together into a ternary node (159). The process of LM polymerisation and network assembly can be divided into a temperature-dependent oligomerisation step and a calcium-dependent polymerisation step. Calcium ions are required to induce a conformational change in the LN domains, allowing them to interact with one another (160).

In line with the three-arm model, LMs that lack one or more LN domain cannot polymerise independently (79). These include LM332 and LM411, which are abundantly expressed in many epithelial and endothelial BMs. For these LMs, alternative methods of interaction with other LM isoforms may be required for BM assembly. For LM332, incorporation into skin BM can be partly explained by an interaction between LM332’s β3LN domain with the LE domain of α3 in LM311. These LM dimers could then self-associate into higher order networks (161, 162). Non-network forming LM BM incorporation likely also depends on compensatory interactions with other BM/ECM components, such as the β3LN domain binding of the NC1 domain of type VII collagen, or could rely on nidogen binding to γ1 LE repeats for LM411 (132, 162, 163).

LM111 is able to drive polymerisation of other LN containing trimers, however, no self-aggregation or co-aggregation with LM111 was seen for LM3a32 or LM3a11 (164).

A comprehensive analysis of LM short arm interactions detected binary interactions with dissociation constants in the 0.01–1 μM (Kd) range for the majority of α-α, α-β, α-γ and β-γ pairings, indicating that the LM networks might be less dependent on the classical ternary node formation previously thought (165), although to date this is the only study to detect these homotypic interactions. This unusual finding is possibly due to the fusion tag added to these recombinant mouse LN domains for purification (165) that were not present in other studies. It is likely that the homotypic interaction seen in the one study was an artefact of the purification of the murine LN domains (165), where His_6 and Strep II-tagged LN domains were used. Earlier studies using proteolytic LM111 fragments found only a single interaction of measurable affinity, that being the binary β1-γ1 or the ternary α1-β1-γ1 (166). A more recent study failed to detect the reported α5-α5, α5-β1 and α5-γ1 interactions, finding only weak interactions between the β1 and γ1 short arms (Kd ≥5 μM) using surface plasma resonance (167).

In vitro analyses have shown that the αβγ ternary node assembly involves rapid but unstable formation of βγ pairs that are then stabilised through integration of an αLN domain (Figure 2.3) (167). Specifically, a stable complex was observed only when all three short arms (α5, β1 and γ1) were added together (Kd ≥0.8 μM) (Figure 2.3) (167). While in experiments with recombinant LM111 heterotrimers,

deletion of any single LN domain or replacement of β1 LN or γ1 LN with α1 LN abolished polymerisation (159). Moreover, it was shown that a chimeric protein in which the LM α1 LN-LEa1-4 region was fused to the LM γ1 chain-binding region of nidogen could restore polymerisation to a LM lacking the α1 LN domain, but not to one lacking the β1 or γ1 LN domain (10). All of which combine to support the three-arm model.

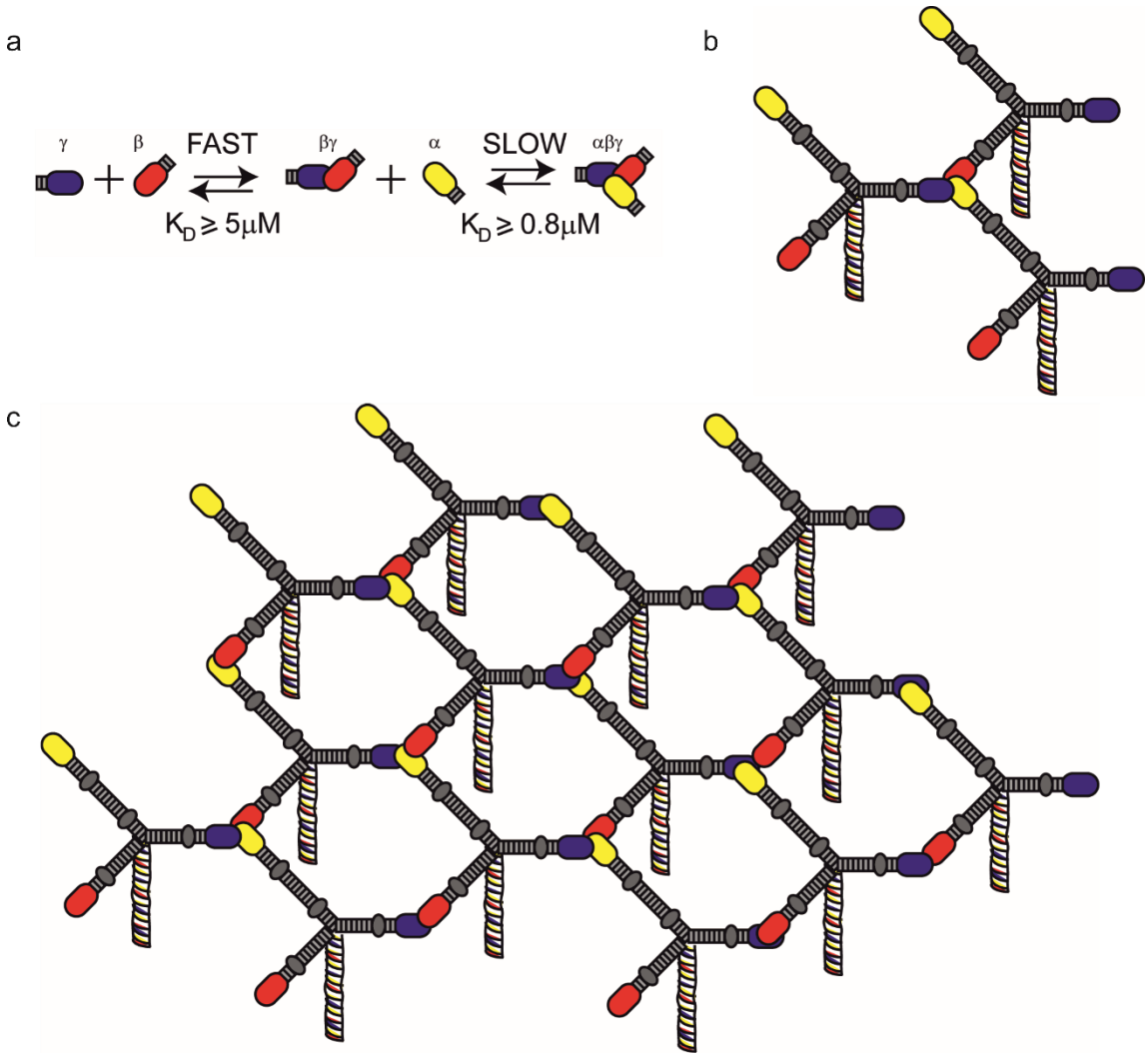

Figure 2.3: LM ternary node and network formation. a) The 2-step interaction that results in the formation of the ternary node. βLN and γLN domains come together in a rapid intermediate reaction that is relatively unstable. Following this intermediate reaction, an αLN domain binds to the interacting β-γ LN domains, to stabilise the interaction and form a stable ternary node. This is the basis of the 3-arm model (b), which expands to give a LM network (c).

2.3.6 Crystal Structure of the LN domain

The crystal structures of α5, β1, γ1 LN domains have been solved, and these combined with conservation of residues between chains (Figure 2.4) allows inferences as to which regions are involved in domain folding and which are involved αβγ ternary node formation. The crystals revealed a similar overall

structure of an antiparallel β sandwich with eight β sheets forming a jelly roll motif held in conformation by cysteines C200 and C220 (167, 168).

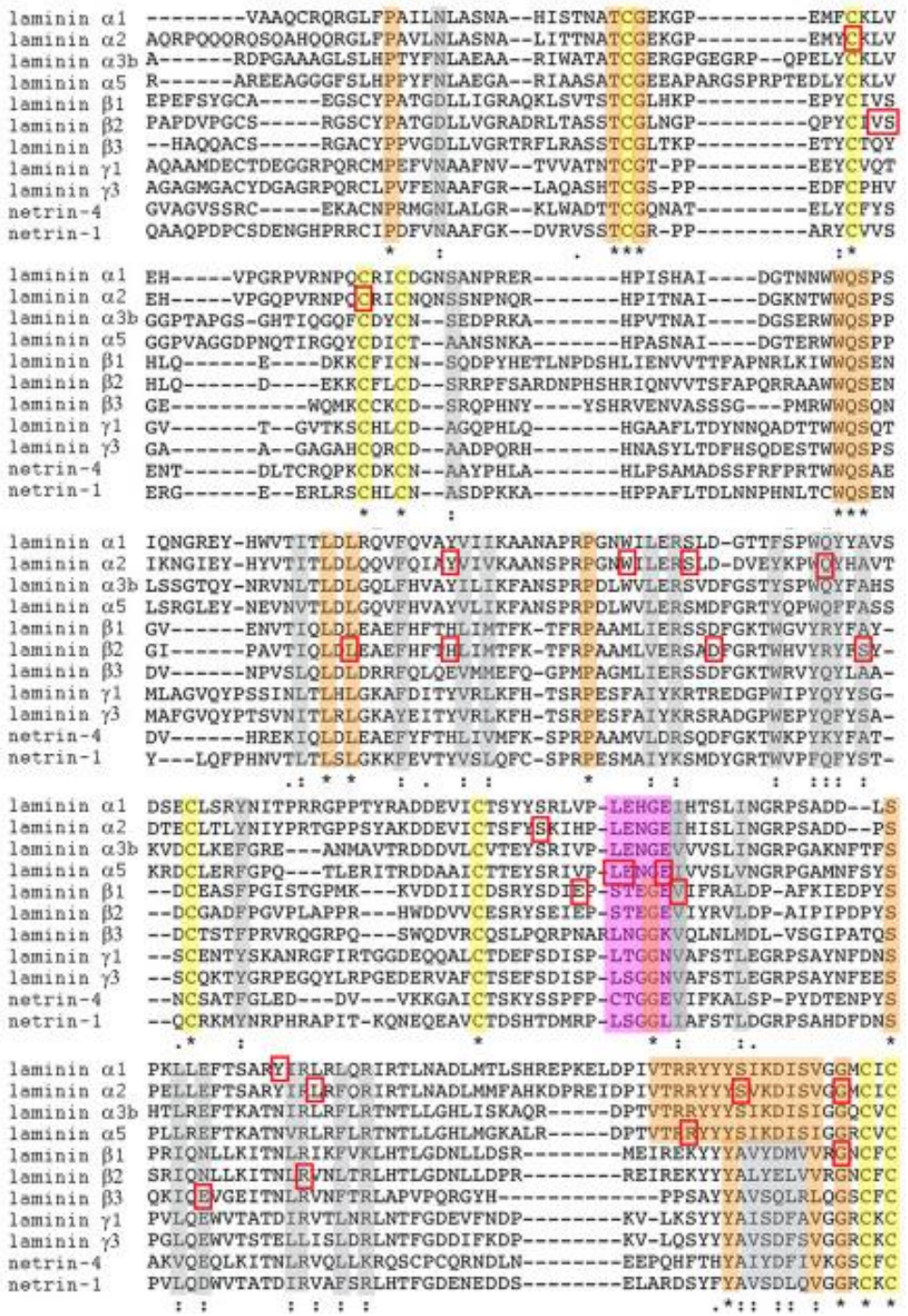

Figure 2.4. Conservation of LN domains across the human LM chains and netrins. Sequence alignments of LN domains from human LM chains, netrin-1 and netrin-4. Yellow, orange and grey highlights indicated conserves cysteines, fully conserved residues or partially conserved residues. Magenta highlights identify the highly conserved LENGE sequence, and red squares indicate pathogenic missense mutation sites. * = conserved residue, : = conservation of residues with strongly similar properties,. = conservation of residues with weakly similar properties

In the α5LN domain, two conserved motifs, Patch 1 and Patch 2, are of particular relevance (167). Patch 1 within the conserved β1-β2-β7-β4-β5 “back face” consists of E178, P189, R265, and R267. These residues are blocked by a glycan attached to N148 (167), suggesting that Patch 1 plays a structural, non-polymerizing role (168). Patch 2 is located across the β6-β3-β8 “front face,” residues W132 and N168, and the β5-β6 loop, residues P229, L230, and E231. Patch 2 is not glycosylated nor conserved with β- or γ-chains but is important for polymerisation as mutation the Leucine, proline or glutamic acid residues within a highly conserved PLENGE residues in the β5-β6 loop all result in inhibition of polymerisation in *in vitro* assays (167, 168).

The β-sandwiches of β1LN and γ1LN domains have similar structure with the main differences in peripheral regions (168). β1LN contains two particular regions of functional importance: the βa-βb hairpin and the β7-α4 loop. The βa-βb hairpin sits at the top of the domain with S80 a key residue for β-γ LN interactions (122). One notable difference in γ1LN domain is a calcium binding site located within a short α-helix and flanked by highly conserved D106 and T114 (168). Testing inferences about residue function is a laborious task but elegant *in vitro* analyses using LN domain fusion proteins have been performed and improve interpretation of clinical findings, these are discussed in context below (169).

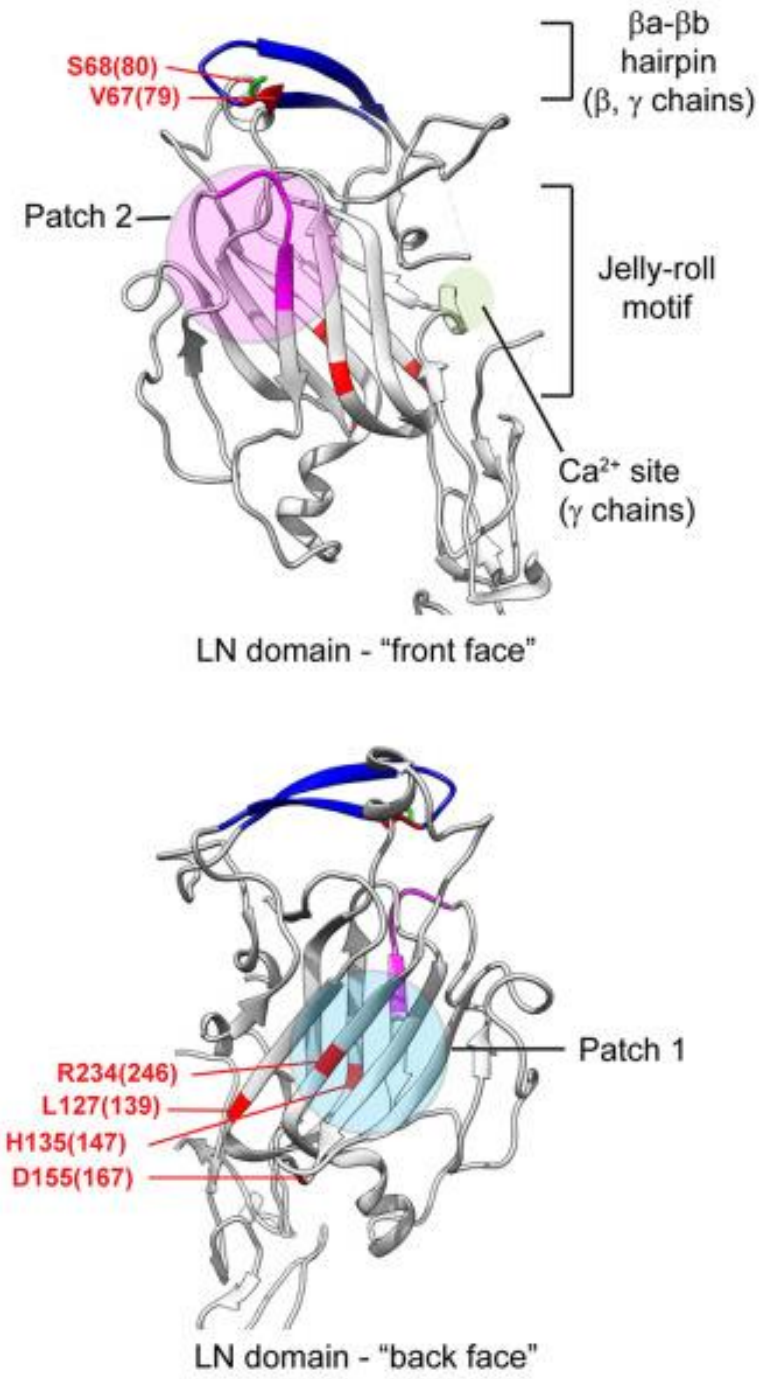

Figure 2.5. Crystal Structure of LN domains. View of the front and back face of the β1 chain is shown with features of conserved patches involved in LN-interaction (patch 2) and required for domain folding (patch 1). Amino acids associated Pierson syndrome mutations are indicated numbered based on LMβ1 with LMβ2 equivalent in parenthesis. Crystal structures derived from (167, 168) and rendered using UCSF chimera (170).

2.3.7 Cell-to-laminin short arm-dependent interactions

2.3.7a Laminin binding integrins

Within the wider integrin family, lies a subfamily of LM-binding integrins, integrins α3β1, α6β4 α6β1, α7β1and α9β1, with high specificity for LM long arm binding (129). In addition, Integrins α1β1 and α2β1 contain an I domain, an independent ligand-binding motif, which allows the integrins to bind to LMs through the LM short arms (153, 171). This was demonstrated through use of short arm recombinant protein fragments and not the native protein and, to date, there is no evidence of the short arm-integrin interaction occurring when in the presence of LM C-terminal LG domains, consistent with the C-terminal domains containing a much higher affinity for the integrins than the short arm. Integrin α1β1 can bind only to the α2-chain short arm (153), but integrin α2β1 has a more promiscuous binding potential, with binding sites for α, β and γ LN domains (153, 171, 172).

2.3.7b Heparan Sulphates and Sulphatides

Heparan sulphates (HS) are a collection of linear polysaccharides found in all animal tissues that also occurs as a proteoglycan (HSPG's) found in the ECM (173). One HSPG shown to interact with the fragmented LM γ2 short arm is syndecan-1 (174). Syndecans are a family of cell surface HSPG's, well known to cooperate with integrins to regulate actin cytoskeleton organisation and cell adhesions (174). It has been reported that the LMγ2 short arm contains binding sites for heparan sulfatides, fibulins and nidogens (175, 176). Interestingly, inhibition of syndecan-1 expression was shown to block the cell adhesion

activities of the LMγ2 short arm, as well as preventing integrin β4 phosphorylation (174), suggesting an important interaction between syndecan-1 and the LMγ2 short-arm. In terms of HSPG's that interact with the LMα chain short arm, a protein of particular interest to this study is perlecan (HSPG2) which was shown to bind to the recombinant LN and LE domains of LMα1 (154).

2.4 LN domains and genetic disease

The biochemical interactions of LM's with each other, and other BM components, have been extensively studied and characterised over the last 40-50 years, and for great reason. What would happen if these LM LN interactions were to fail, preventing polymerisation? The answer to this question has come from the study of human disease and mice models.

A number of severe inherited diseases have been identified as a result of mutations to LM genes, but of particular interest to the focus of this thesis, are the diseases that occur due to a mutation in the LN domain. Mutations in this region can prevent the polymerisation of LM either through loss of LN domain/whole protein or through disrupting the folding of LN domain, or could impact LM function through disrupting specific interactions made by the LN domain. Beyond *in vitro* biochemical assays, studies of these diseases provide evidence of the where, when and why LN-LN domain interactions are important. This becomes clear when considering the variety of mutations within the LN domains which lead to severe disease in humans, or where targeted mutations in mice lead to severe defects or death (Table 2.1). Thankfully, LN-domain related diseases are rare, though due the tissue-specific laminin composition of BMs, different syndromic

disorders are observed depending on which laminin isoform harbours the mutation.

Table 2.1: Pathogenic LN domain mutations

Protein	Mutation	Effect	Phenotype	Refs
LMα1	Y265C	LN interaction	[mouse] Retinal vasculopathy	(177)
LMα2	C79R	LM poly/ fold[c]	[mouse] mild muscular dystrophy	(178)
	C86Y	fold[p]	MDC1A	(179)
	Y138H	LM poly[p]	MDC1A	(179)
	W152G	fold[p]	Limb-girdle–type dystrophy	(180)
	S157F	fold[p]	MDC1A	(181)
	Q167P	LM poly[c]	Limb-girdle–type dystrophy	(182)
	S204F	fold[p]	Mild muscular dystrophy, mild proximal weakness	(183)
	L243P	fold[p]	Mild MDC1A	(180)
	S277L	fold[p]	MDC1A	(184)
	G284R	LM poly[p]	limb-girdle–type dystrophy	(180)
LMα5	R286L	LM poly[c]	Focal segmental glomerulosclerosis, hearing loss, craniofacial dysmorphism, limb development	(185)
LMβ1	E215K	LM poly[c]	[fly] heart development defects	(186)
	V226E		[fly] heart development defects	(186)
	G286R		[fly] heart development defects	(186)
LMβ2	R246W	LM Secretion	/End-stage renal disease, nephrotic proteinuria, diffuse mesangial sclerosis, focal and	(16, 187,
	R246Q	Fold	segmental glomerulosclerosis, microcoria, lens abnormalities, nystagmus hypotonia, cognitive defects, muscle delay	188)
	V79del	LM poly[p]	Retinal detachment, cataracts, progressive vision loss, diffuse mesangial sclerosis, end-stage renal disease	(189)
	S80R	LM poly[c]	Nephrotic proteinuria, atypical diffuse mesangial sclerosis, myopia, retinal detachment. [mouse S83R] Detrimental on Alport syndrome background	(190, 191)
	H147R	LM fold[p]	Nephrotic proteinuria, diffuse mesangial sclerosis, proliferative glomerulonephritis, hypertension, heart failure, microcoria, retinal detachment, lens abnormalities	(192)
	D167Y	LM Secretion [p]	End-stage renal disease, myopia, retinal detachment, severe visual impairment	(193)
	L139P	LM fold[p]	Diffuse mesangial sclerosis, lens abnormalities, severe visual impairment, hypotonia, muscle delay, cognitive deficits	(16)
	S179F	LM fold[p]	End-stage renal disease, focal and segmented glomerulosclerosis, retinal detachment, severe visual impairments	(194)
LMβ3	E210K	Splicing[c] + fold[p]	Skin fragility, nail dystrophy, alopecia	(195)

[p]predicted [c]confirmed in vitro assays

2.4.1 MDC1a

Based on the two-step model of LM polymerisation, mutations that affect an α LN domain would be predicted to impair the stabilisation step of ternary node assembly. The most well understood example is merosin-deficient congenital muscular dystrophy type 1A (MDC1A), which is caused by mutations to *LAMA*2 (LMα2) (196) and therefore affects the LM211 and LM221 heterotrimers, the most abundant LMs in skeletal muscles (197), peripheral nerves, astrocytes and pericytes in the brain (198).

In LMα2 knockout conditions, MDC1A presents with disabilities of the proximal and distal limb muscles, with patients unable to walk more than a few steps unaided (199, 200). Weakness in facial muscles result in reduced sucking and swallowing capabilities, life-threatening problems can arise from failure of the respiratory muscles (201), and cases with intellectual disability and epilepsy have been reported (200-202). In knockout situations, LM411 replaces LM211 in muscle BMs (203). LMα4 lacks an LN domain and is unable to polymerise, which almost certainly is responsible for a weakened BM. However, LMα4 and LMα2 also differ in their receptor binding interaction repertoire and affinities (204), for example, LMα2 binds integrin α7β1 whereas LMα4 cannot, and LMα4 also has weaker affinity for α-dystroglycan (172).

Comparison between missense mutations and knockout mutations allows for some differentiation between polymerisation and receptor-mediated effects, although these inferences are complicated by not every affected tissue expressing LM411.

Many mutations have been reported throughout *LAMA2*'s 65 exons in MDC1A and are catalogued in *LAMA2* gene variant database (179). The LN domain contains a cluster of missense and in frame deletions (178, 179). For example, a point mutation in the highly conserved CxxC motif, C79R, led to a milder form of MDC1A, which affects the myelination of Schwann cells in spinal roots and the stability of the skeletal muscles (178). This amyelination was not attributed to a change in LM211 abundance or mislocalisation, and *in vitro* polymerisation assays confirmed a dramatic effect on LM polymerisation (169). Other pathogenic missense variants include Q167P, Y138H, G284R on the surface of α2 LN domain and C86Y, W152G, S157F, S277L, S204F, L243P in the interior (205). The S204F mutation lies at one extreme of the phenotypic spectrum, whereby the patient was misdiagnosed with a peripheral neuropathy, presenting with mild proximal weakness. Muscle biopsy revealed depletion of LMα2 in intramuscular nerve, subtly depleted LMα2 expression in muscle BMs and diffusely upregulated LMα5 expression (183). To the other extreme, Q167P maps to near the polymerisation face, and consistent with this, causes a 60% drop in *in vitro* polymerisation capability. This mutation led to ambulatory muscular dystrophy (169). More severe still, G284R caused proximal weakness, with a loss of functional gait with age accompanied by frequent falls, and epilepsy. This mutation effect on protein function is yet to be confirmed in biochemical assays, but is predicted to inhibit LM polymerisation (180).

2.4.2 Other LMα LN domain diseases

LMα5 is almost ubiquitous to all adult BMs (79). Unsurprisingly, knockout mice die before birth with a failure in neural tube closure, and no human knockouts

have been reported (206). However, a patient with R286L in LMα5 LN has been identified. They presented with a complex syndromic disease characterised by defects in kidney, craniofacial and limb development (185). The affected residue (R286L) in this case lies adjacent to the highly-conserved PLENGE sequence required for LM polymerisation (167), and abrogated *in vitro* polymerisation potential (185). However, it should be noted that these polymerisation studies utilised recombinant truncated LN-LE domains (167), and not the full-length native protein.

It is not possible to compare the R286L LN mutation against a knockout phenotype; however, a patient with V3140M in the LG3 domain allows comparison of the effects on polymerisation vs cell-surface receptor binding (207). Both the LG3 mutation and R286L led to complex syndromic disorders with similarity in tissues affected but with notable differences. Specifically, in the skin V3140M caused alopecia, lack of eyebrows and body hair, features not present in the R286L patient. V3140M patients also had retinal rod degeneration whereas the R286L had hearing loss but no sight abnormalities. Kidney defects were common to both with R286L presenting with atypical focal segmental glomerulosclerosis progressing to end stage kidney disease compared with floating kidney syndrome in V3140M. Finally, R286L presented with numerous dysmorphic issues include craniofacial dysmorphism, syndactyly, and pyloric web (1). Therefore, the importance of R268, to the function of the LN domain cannot be understated, as well as the importance of its conserved counterparts in all LN-domain containing LMα chains.

2.4.3 Pierson Syndrome

Pierson Syndrome has become somewhat of a universal term for congenital nephrotic syndrome as a result of *LAMB*2 mutations. Despite studies predicting that *LAMB*2 mutations are the cause of 2.5% of all congenital nephrotic syndrome diagnosed within the first year of life (208). Missense, nonsense, and splice mutations have all been identified, with most mutations producing a premature stop codon and complete knockout of *LAMB*2 (16). These mutations have been found as both compound heterozygous and homozygous mutations in patients with severe and milder forms of the disease. Mutations that create premature stop codons are evenly distributed along the *LAMB*2 gene (16). However, the presence of recessive indel mutations in the LN domain of LMβ2 have resulted in milder forms of the disease, with many patients surviving into adolescence and early adulthood (16). Indeed, it seems point mutations and small in-frame deletion cluster in the LN domain (16).

Whereas nephrotic syndrome and ocular abnormalities are commonalities of Pierson Syndrome, the spectrum of related phenotypes arising from mutations in the *LAMB*2 gene is vast. Approximately 50 mutations of *LAMB*2 from 40 unrelated families have been identified, and most of the missense mutations cluster in or near the LN domain (16). Mutations found within the β2 LN domain include S80R, L139P, H157R, D167Y, S179F and R246 Q/W (16). Evidence that specific mutations to the LN domain of laminin β2 are pathogenic was elegantly demonstrated by Mckee et al. (169), whereby laminin-nidogen chimeric fusion proteins that bind to recombinant non-polymerizing laminins to

provide a missing functional LN domain were used to identify non-LN domain binding mutant residues.

The arginine at position 246 in the LN domain is a hot-spot for Pierson syndrome causing mutations. Analysis of patients with mutations to R246 suggest that it may reduce the presence of the LM in the BM. R246W was independently observed in five unrelated families. These mutations led to reduction in protein expression, as determined by immunofluorescence (188). Some of this reduction is explained by heterozygous inheritance along with a nonsense mutation. However, the level of reduction may also suggest that protein processing may be disturbed by this mutation (16). A further mutation, R246Q, observed within one family, and this change also impaired the secretion of LM, as determined confocal microscopy of rat derived R246Q-*LAMB*2 protein (209), which together supports that this arginine residue has a key role in protein folding.

Responsible for a milder form of Pierson Syndrome, the S80R mutation has proven to be of particular interest in resolving the crystal structure of domains involved in LM polymerisation. Located within the βa-βb hairpin on the top surface of the βLN domain and with high conservation across LMβ1 and LMβ2, this mutation was found to be responsible for inhibiting LM polymerisation in fragmented LN domains (168). In a recombinant test, it was shown that equivalent mutations in LMβ1 (S68R), resulted in a similar inhibition of LM polymerisation (122), highlighting the importance of this conserved hairpin loop.

It is likely that the number of mutations with genotype-phenotype correlations is underreported, owing to Pierson Syndrome being such a severe disease and because genomic sequencing is either not available, or is not carried out before death. The majority of reported Pierson Syndrome cases are from Western countries, and it was not until 2013 that the first typical case from Asia was reported (210), which showed that the phenotype due to *LAMB*2 mutations appears to be similar between different ethnic groups (211). Considering this, it is easy for one to imagine how cases of Pierson Syndrome may go undiagnosed in economically deprived areas of the world.

2.4.4 Junctional Epidermolysis Bullosa

LMβ3 is expressed in most epithelial tissues where it forms part of LM3a32 and LM3b32 (212, 213). The resulting heterotrimers have either one or two LN domains and are unable to polymerise independently (158, 164). Therefore, one might predict that LN domain mutations are tolerated for this LM chain unless they influence protein secretion. However, patients were identified where the pathogenic mutation leads to E210K and results in a phenotype of trauma-induced blisters, nail dystrophy and alopecia (mild junctional epidermolysis bullosa) (17, 195, 214). In comparison, homozygous knockout of LMβ3 leads to much more extensive skin blistering complications and early lethality (215-218).

Interpretation of the E210K mutation is complicated; the affected base pair is at a splice junction and in a knock-in mouse model led to skipping of the out-of-frame exon, and no detectable LMβ3 in the skin (195). However, in humans, miss-splicing has been reported for some, but not all patients, and which can also be rescued by second-site mutations (219). Numerous alternative splice

products are produced, including some full-length transcripts. The most common in-frame deletion is predicted to remove several of the central β-strands and disrupt the fold. Modelling of E210K indicates it is unlikely to be required for laminin polymerisation but also is not predicted to affect protein folding or secretion (18). Overall, the evidence from these patients does not point toward a LM polymerisation effect but does suggest a role for the LMβ3 LN domain in protein function.

Direct evidence for the importance of the LMβ3 LN domain has been obtained from keratinocytes expressing either full-length or LN domain-deleted LMβ3 and grafted as skin equivalents onto immunodeficient mice (220). Here, the LN deleted versions displayed subepidermal blistering, erosions, and prominent granulation tissue, not associated with reduced LM332 deposition and pointing LN domain roles beyond polymerisation in this context (1).

2.5 Unresolved questions

The LN-domain associated diseases are an important model in our understanding of the importance of LM polymerisation. They have formed the basis of mouse models, used to directly confirm the drastic affects these mutations have on different tissues. However, the murine models do not allow mechanism-level resolution. They are unable to provide answers to questions about how the different roles of the BM might be affected by the mutation; for example, how is signalling, structure and biophysical resistance at the cellular level affected by these mutations? Moreover, recombinant protein biochemical models are also not sufficient for answering these questions. Indeed, although incredibly valuable, the biochemical assays have tended to not use the full-

length protein, rather a recombinant truncated version. These truncated proteins do not mimic the entire physiological relevance of a native full length LM heterotrimer, with its functionally diverse domains interacting with a dynamic ECM.

In this thesis I approached these questions through generating genome-edited cell model to provide the resolution needed for the finer biological details, whilst still retaining the physiological relevance of a full length native LM. To do so, I used CRISPR-Cas9 genome editing.

2.6 CRISPR-Cas9

Clustered regularly interspace short palindromic repeats (CRISPR) are a family of DNA sequences found in the genome of bacteria, derived from DNA fragments of bacteriophages that had an infected the bacteria previously. These DNA sequences act as a rudimentary immune system for the bacteria (221). These sequences allow for the identification of potential infections, similar to the acquired immunity system of complex multicellular eukaryotes. CRISPR-associated protein 9 (Cas9) is an endonuclease that is guided by the CRISPR sequences to complimentary viral DNA, where the enzyme then introduces a double stranded DNA cleavage (221). This natural mechanism has formed the basis of the genome-editing technique CRISPR-Cas9.

Modern CRISPR-Cas9 technology exploits the guidance of the Cas9 enzyme, using two factors; trans-activating RNA (trRNA) and CRISPR RNA (crRNA) (222). crRNA is used to guide the Cas9 machinery to foreign DNA using complimentary base pairing. To achieve site-specific DNA

cleavage, trRNA is required to complex with the Cas9 and crDNA (221, 222). This process has been simplified somewhat by fabrication of chimeric oligonucleotides combining the crRNA and trRNA sequences into single “guide RNA” (gRNA) molecules (222). These gRNA have simplified CRISPR-Cas9 genome techniques to a two-step process, requiring only a gRNA and Cas9 (221, 222). The complex is guided to a specific Protospacer Adjacent Motif (PAM) sequences, where the Cas9 nuclease introduces a double strand break six nucleotides downstream (221). The most common PAM sequence used in CRISPR genome editing is the 5’-NGG-3’ sequence. This two-step process is the simplest form of CRISPR-Cas9, and disrupts the targeted locus through non-homologous end joining (NHEJ), resulting in indels (Figure 2.6a).

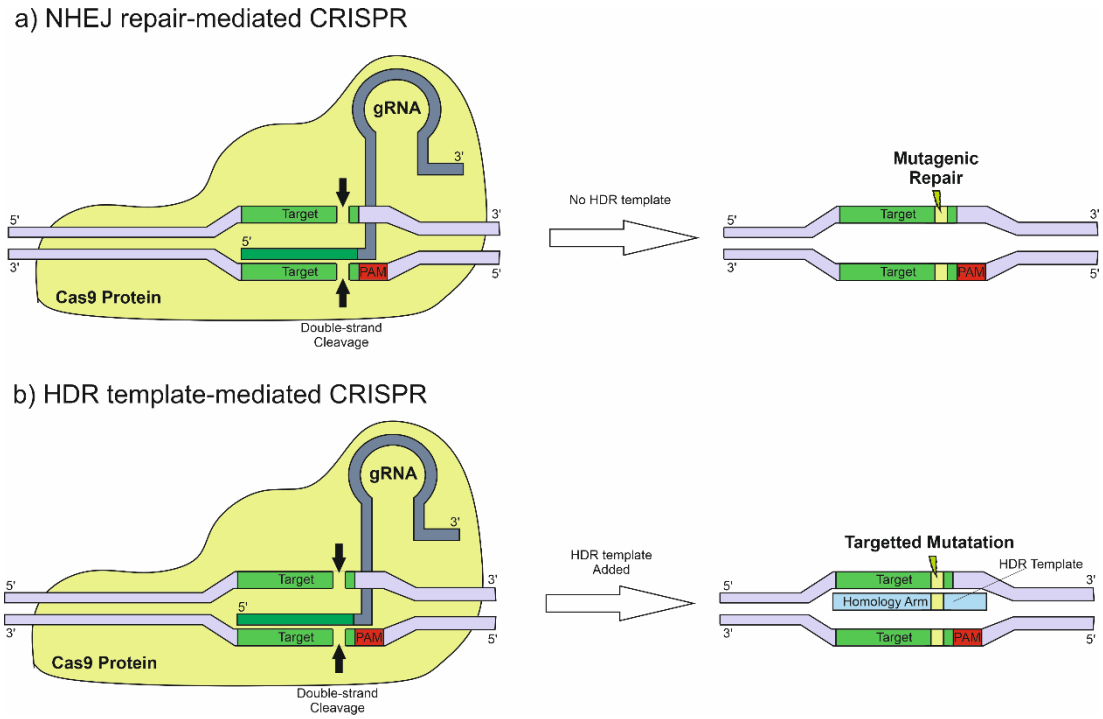

Figure 2.6: NHEJ and HDR-mediated CRISPR genome editing. a) Non-homologous end joining (NHEJ) repair-mediated CRISPR involves just 2 components of gRNA and Cas9 protein, and introduces a random mutation due to mistakes in the NHEJ machinery after a double strand cleavage is introduced 6 nucleotides downstream of PAM sites. b) Homology directed repair (HDR) template-mediated CRISPR involves an additional component in the form a HDR template, which introduces a targeted mutation, by binding through homology arms around the mutation site.

By adding a third component to the process, a more controlled means of introducing mutations can be achieved. The addition of a donor template with homology to the targeted locus, the double strand break can be repaired using homology directed repair (HDR) (223-225). Although less efficient than NHEJ, HDR-based CRISPR-Cas9 allows for more precise replacement mutations, as it provides the template for mutation, rather than relying on the natural errors made by the cellular machinery in NHEJ (Figure 2.6b) (223). The donor template can be in the form of short single- or double-stranded oligonucleotides for point mutations, or in the form of a plasmid for larger inserts (226). For the purposes of this work, a single-stranded oligonucleotide

was used to introduce mutations via HDR CRISPR-Cas9 genome editing, while a plasmid was used for tagging with a fluorescent protein.

While CRISPR-Cas9 transfection systems are one of the simpler genome-editing techniques, compared to more traditional methods such as zinc finger nucleases (227), they are not without their pitfalls. One of the principle concerns with the use of CRISPR-Cas9 genome editing is the propensity of off-target effects, which been difficult to control for, although these problems are not exclusive to CRISPR techniques (228). Mismatches occur when the CRISPR-Cas9 complex binds to a section of DNA that doesn't have a 100% complimentary match to the gRNA, introducing a double strand break in an undesired locus (228). However, methods have been adapted to reduce the chance of these undesirable off-target effects. For example, limiting the time the Cas9 endonuclease is active within cells has been shown to reduce the off-target cutting of the complex (229-231). In addition to this, in silico off-target prediction tools are now available, aiding in the design phase of the genome-editing (232)

Initial developments in this genome-editing tool involved transfecting Cas9 into the cell in the form of a plasmid, and using the cells' natural transcriptional and translational machinery to produce the Cas9 protein (221). This transfection method meant it was difficult to control the amount of Cas9 in the cell at any time while the plasmid was actively expressed (233). To tackle this issue, Cas9 protein with a nuclear localisation signal (NLS) was purified, and transfected in lieu of the plasmid (233). This improvement meant not only could the amount of protein present in the cells be controlled in terms concentration, but also the short half-

life of the protein ensured Cas9 was only present in the cell from 4 to 24 hours (229, 231). Transfection of pure protein reduces the editing efficiency of the CRISPR-Cas9 complex; however, it also reduces the risk of the complex binding to non-complimentary sequences and thereby reduces the frequency of off-target effects (231).

2.7 Thesis aims

In this thesis, my aim was to use CRISPR-Cas9 genome editing to create two new cell lines; a non-polymerizing LN domain mutant cell line (Chapter 4) and fluorescently tagged laminin protein line (Chapter 6). The mutant cell line would create a robust cellular model of the diseases of the LN domain and allow for the study of the important, but as of yet not well understood, mechanistic analyses of the impact of LM polymerisation (Chapter 5). The second line would allow live super-resolution microscopy and analysis of dynamics and half-life of a tagged laminin.

Chapter 3: Materials and Methods

3.1 Cell culture

A549 lung adenocarcinoma cells (ATCC® CCL-185™) (234) and Human Embryonic Kidney 293a (HEK293) cells (235) (ATCC® CRL-1573™) were maintained at 37 °C, 5% CO_2 in high glucose (4.5 g/L) Dulbecco's Modified Eagle Media with 2 mM L-glutamine (Sigma-Aldrich, St. Louis, Missouri, USA), supplemented with 10% foetal calf serum (FCS) (LabTech International Ltd, Heathfield, UK). A549 cells were used as they predominantly expressed LM511. HEK293 cells were used as a control, producing minimal LM of their own, but expressing the integrins necessary for LM-cell binding. For sub-culturing and seeding, cells were washed with Dulbecco's Phosphate-Buffered Saline (DPBS) (Sigma-Aldrich) and incubated with 1 x trypsin EDTA (0.05 % trypsin, 0.02 % EDTA w/v) (Sigma-Aldrich). Upon detachment, the trypsin was neutralised using FCS-containing media, cells pelleted by centrifuging at 1000 rpm for 5 min and re-suspended in normal growth medium. In the experiments detailed below, equal numbers of cells were seeded 24 h prior to assay unless stated otherwise. Cells were kept in culture for no longer than 6 passages after thawing.

3.2 Laminin RT-qPCR

Primers and cDNA were donated by Dr Lee Troughton (University of Liverpool, UK). For cell line comparisons, each cell type was seeded into six-well plates (GreinerBioOne) at a density of 2.5 x 10^5 cells/well, and RNA extracted after 24 h. RNA was extracted for isoform-specific RT-qPCR using RNeasy mini-prep spin columns from Qiagen (Qiagen, Venlo, Netherlands). RNA quantities

and purities were measured using a Nanodrop 2000™ (ThermoFisher) accepting an optical density 260/280 ratio of between 1.9 and 2.1. 1 µg of total RNA was reverse transcribed using Precision nanoScript™ 2 Reverse Transcriptase (Primerdesign, Camberley, UK) using random hexamers and oligo-DT primers under the following conditions: 65 °C for 5 min, 25 °C for 5 min, 42 °C for 20 min, 75 °C for 10 min. 5 ng of cDNA was used for each 10 µL qPCR reaction, made up of: 1 µM primer pair (Table 3.1), 5 µL Precision Plus qPCR Mastermix (Primerdesign), 5 ng cDNA, and H_2O to 10 µL. The following run protocol was used for all qRT-PCR reactions: 1 cycle of 95 °C for 2 min, 40 cycles of 95 °C 15 s, 60 °C 1 min, with a final melt curve analysis. All RT-qPCR was perform using Roche Lightcyler 480™ or Lightcycler 96™ (Roche, Basel, Switzerland).

Table 3.1: Primer Sequences, location and amplicon size of LM genes and reference transcripts for isoform specific RT-qPCR (Dr Lee Troughton, University of Liverpool, UK)

Isoform	Direction	Sequence	Location	Amplicon Size
*LAMA*1	Forward	5'- GGCTCTGTGACTGCAAACCAAACGTG– 3'	Ex 20-21	88 bp
	Reverse	5'- CAGCCATGGCCTGAGTCCAGC– 3'		
*LAMA*2	Forward	5'- CCTCTTGTGTCGCAGAAGGACTTGACG– 3'	Ex 31-32	114 bp
	Reverse	5'- GCCTGGACTGCCAGTATAGCCAG– 3'		
*LAMA*3A	Forward	5'- GCCTCCCGGTCAAAGTCAACTGC– 3'	Ex 39-40	118 bp
	Reverse	5'- GCAGGGAACACACCGTCCGGTATAC– 3		
*LAMA*3B	Forward	5'- GCCACCTGTGTCTCCTTGGCC– 3'	Ex 27-28	181 bp
	Reverse	5'- CCAGGTGTGGTACACGTCCTCTCA– 3		
*LAMA*3LN1	Forward	5'- GGTGGAGGGGTCTGCATTAACTGTCA– 3'	Ex 8-9e	170 bp
	Reverse	5'- CGCTGAGGCAGTACACACAGGC– 3'		
*LAMA*4	Forward	5'- CCAGACTCAGTGATGCCGTTAAGCAAC– 3'	Ex 17-18	95 bp
	Reverse	5'- GGCTTCCTCGGTGATCAGTCTAGACTGC– 3		
*LAMA*5	Forward	5'- AGCGGTGTGACGTGTGTGCC– 3'	Ex 10-12	132 bp
	Reverse	5'- CTGCCGCGCTGCAGTCACAAT– 3'		
*LAMB*1	Forward	5'- CATGAGACCCTGAATCCTGACAGCC– 3'	Ex 4-6	190 bp
	Reverse	5'- GCATAGCAGCTGGACGGAATGTCTTGAAAGTC– 3'		
*LAMB*2	Forward	5'- GCCTGTGTGGGCATTTGGTGC– 3'	Ex 15-16	132 bp
	Reverse	5'- CCACTTCAGATGCAGCTTGTAGGAGA – 3'		
*LAMB*3	Forward	5'- GGAGAAAGAACGGCAGAACACACAGC– 3'	Ex 1-3	91 bp
	Reverse	5'- GGCAGGGCAAAACACAAGAGGAAGAA– 3'		
*LAMC*1	Forward	5'- CCCAGCTCCATCAACCTCACGC– 3'	Ex 1-2	141 bp
	Reverse	5'- CCGTGTGCGCTTGTAAATGGCAAAGC– 3'		
*LAMC*2	Forward	5'- CTGCCTCTGCTTCTCGCTCCTC– 3'	Ex 1-2	85 bp
	Reverse	5'- CTGCCAGGAGTTCCCATTGCTTAGACAGA– 3'		
*LAMC*3	Forward	5'- CCAGCATGGCACCTGTGACC – 3'	Ex 12-13	96 bp
	Reverse	5'- CCATAGAAACCTGGCAAACAGCGTTC – 3'		

RPLP0	Forward	5'- GGTGGAGGGGTCTGCATTAACTGTCA– 3	Ex 6-7	98 bp
	Reverse	5'- GGTGGAGGGGTCTGCATTAACTGTCA– 3'		
SOX9	Forward	5'- CTTTGGTTTGTGTTCGTGTTTTG – 3'	Ex 3	101 bp
	Reverse	5'- AGAGAAAGAAAAAGGGAAAGGTAAGTT– 3'		

3.3 CRISPR-Cas9 genome editing

A549 cells were transfected using 400 ng of one of two gRNA's (gRNA1 CGTGCCCCTGGAGAACGGAG, gRNA2 CGCATCGTGCCCCTGGAGAA), 2 µg of Cas9 2×Nuclear Localisation Signal (GeneMill, Liverpool, UK), in a final volume of 7 µL of Neon™ R Buffer (ThermoFisher, Waltham, Massachusetts, USA). Cas9-gRNA solutions were incubated at room temperature for 20 min, 1.2×10^5 A549 cells and 600 ng HDR donor template (GGCCATCTGCACCACCGAGTACTCACGCATCGTGCCCCTTAAGAACGG AAAGGTGGGCCGGGGAGGGGCAGGGCGGTACGGG) were added, and the solution electroporated using the Neon™ 10 µL Transfection Kit (ThermoFisher) with 4 × 20 ms 1200 V pulses, then seeded onto pre-warmed 24-well plate.

3.4 Clonal Expansion

A549 cells transfected with gRNA's were expanded, and plated to generate single cell clones (0.4 cell/well in 6 x 96-well Corning® TC-treated plates (Sigma-Aldrich)). Single cell clones were expanded then dissociated using trypsin and transferred to a Corning® TC-treated 24-well plate (Sigma-Aldrich) for DNA extraction.

3.5 DNA Extraction

Cells were pelleted and digested in 100 µl DNA lysis buffer (50 mM Tris-HCl pH 8.0, 0.1 M NaCl, 1% SDS, 20 mM EDTA (All Sigma-Aldrich)) and 10 µl of proteinase K (10 mg/ml, all Sigma Aldrich) for 3 h at 55°C (236). Samples were cooled, spun at 13,000 rpm for 3 min and the supernatant transferred to clean 1.5 ml tubes (Eppendorf, Hamburg, Germany). An equal volume of isopropanol (Sigma Aldrich) was added, gently inverted and span at 13,000 rpm, and supernatant discarded. Pellets were washed with 500 µl of 70% EtOH (Sigma Aldrich), then air-dried for 10 min, and resuspended in 20 µl ddH_2O.

3.6 Screening

Single cell clones were screened using a dual method: firstly, using PCR to detect the PLENGK mutation (forward primer AAAGCGTGCAAGGGAGAG, reverse CCCACCTTTCCGTTCTTA, amplicon 224 bp) in unison with a DNA quality control PCR (forward primer AAAGCGTGCAAGGGAGAG, reverse primer GTAGGAGAAATTCATGGCGC, amplicon 537 bp). 25 µL PCRs were run using 1 ng of genomic DNA, 1 µM primers, 12.5 µL REDTaq® ReadyMix™ PCR Reaction Mix (Sigma-Aldrich), with the protocol; 95 °C for 5 min, 35 cycles of 95 °C for 30 s, 60 °C for 45 s and 72 °C for 1 min, ending with 7 min at 72 °C using a Veriti Dx Thermal Cycler™ (ThermoFisher). Products were separated by electrophoresis on a 2 % w/v agarose/TAE gel, and analysed using a BioRad Gel Doc XR+ System (BioRad, Hercules, California, USA). Positive hits from the initial screen where then analysed using the heteroduplex melt-curve analysis (forward primer

GGACTGTCTGGAGCGGTTC, reverse primer CACCTTTCCCTTCTCCAGCC, amplicon 205 bp) 10 uL high-resolution melt-curves were run using 1 ng of genomic DNA, 1 µM primers, 5 µL SYBR® Green PCR Master Mix (ThermoFisher), with the protocol; 50 °C for 2 min, 95 °C for 2 min, 40 cycles of 95 °C for 15 s (ramp rate: 4.4 °C/s) and 60 °C for 1 min (ramp rate: 2.2 °C/s), ending with 1 cycle of 95 °C for 1 min, 40 °C for 1 min, 65 °C for 1 s and 97 °C for 1 s (ramp rate: 0.07 °C/s).

3.7 DNA Sequencing

PCR products from the clones identified as potentially containing the mutant sequence were prepared for DNA sequencing. PCR products were run on a 2 % w/v agarose/TAE gel and bands were purified using Monarch® DNA Gel Extraction Kit (New England Biolabs, Ipswich, Massachusetts, USA) then sequenced by DNASeq (University of Dundee, Dundee, Scotland).

3.8 Primary and Secondary Antibodies

Table 3.2: Antibodies used for Immunoblotting, Immunocytochemistry and Flow Cytometry

Application	Primary antibodies (species)	Supplier	Secondary antibodies	Supplier
Immunoblotting	LM α5 2F7 (Mouse) 0.1 µg/mL	Sigma-Aldrich WH0003911M1	IRDye® 800cw Goat-anti Mouse, 0.05 µg/ mL	LiCor Biosciences 926-32210
	LM β1 (Rabbit) 1 µg/mL	ThermoFisher PA5-27271	IRDye® 680rd Goat-anti Rabbit, 0.05 µg/mL	LiCor Biosciences 925-68071
	LM β2 CL2979 (Mouse) 1 µg/mL	Abcam ab210956	IRDye® 800cw Goat-anti Mouse, 0.05 µg/ mL	LiCor Biosciences 926-32210
Immunocytochemistry	LM α5 4C7 (Mouse) 1 µg/mL	Gifted by Prof Albrechtsen and Prof Wewer	Alexa Flour 488™, Goat-anti mouse IgG (H+L), 2.4 µg/mL	ThermoFisher A-11001
	Paxillin (Rabbit) 0.4 µg/mL	Abcam (Cambridge, UK) ab32084	Alexa Flour 594™, Goat-anti rabbit IgG (H+L), 4 µg/mL	ThermoFisher A-11037
	Vinculin Vin-54 (Mouse) 1 µg/mL	Abcam ab130007	Alexa Flour 488™, Goat-anti mouse IgG (H+L), 2.4 µg/mL	ThermoFisher A-11001
	Zyxin 2D1 (Mouse) 1 µg/mL	Abcam ab58210	Alexa Flour 488™, Goat-anti mouse IgG (H+L), 2.4 µg/mL	ThermoFisher A-11001
	YAP1 (Rabbit) 2 µg/mL	ThermoFisher PA1-46189	Alexa Flour 594™, Goat-anti rabbit IgG (H+L), 4 µg/mL	ThermoFisher A-11037
	TAZ M2-616 (Mouse) 5 µg/mL	BD BioSciences (Franklin, New Jersey, USA) 560235	Alexa Flour 488™, Goat-anti mouse IgG (H+L), 2.4 µg/mL	ThermoFisher A-11001
	Alexa Fluor™ 488 Phalloidin 1.65 µM	ThermoFisher A12379	-	-
Flow cytometry	Integrin α3 ASC-1 (Mouse) 1 µg/mL	Abcam ab228425	Alexa Flour 488™, Goat-anti mouse IgG (H+L), 5 µg/mL	ThermoFisher A-11001
	Integrin α6 MP 4F10 (Mouse) 1 µg/mL	Abcam ab20142	Alexa Flour 488™, Goat-anti mouse IgG (H+L), 5 µg/mL	ThermoFisher A-11001
	Integrin αv 272-17E6 (Mouse) 1 µg/mL	Abcam ab18821	Alexa Flour 488™, Goat-anti mouse IgG (H+L), 5 µg/mL	ThermoFisher A-11001
	Integrin β1 12G10 (Mouse) 1 µg/mL	Abcam ab30394	Alexa Flour 488™, Goat-anti mouse IgG (H+L), 5 µg/mL	ThermoFisher A-11001
	Integrin β4 M126 (Mouse) 1 µg/mL	Abcam ab29042	Alexa Flour 488™, Goat-anti mouse IgG (H+L), 5 µg/mL	ThermoFisher A-11001

3.9 Immunoblotting

Cells were seeded in 100 mm tissue culture dishes for 24, 48, 72 or 96 h to obtain a final population of 2.0×10^6 at point of harvest (1.0×10^6, 5.0×10^5, 2.5×10^5 and 1.25×10^5 seeded per timepoint, respectively). For whole cell lysates, cells were scraped into 90 µL urea-SDS lysis buffer: 10 mM Tris–HCl pH 6.8, 6.7 M Urea, 1 % w/v SDS, 10 % w/v glycerol, 7.4 µM bromophenol blue, 50 µM phenylmethylsulfonyl fluoride, 50 µM *N*-methylmaleimide, sonicated and 10 % v/v β-mercaptoethanol added (all Sigma-Aldrich). For ECM preparations, cells were removed with 2 % v/v ammonium hydroxide (Sigma-Aldrich) solution prior to scraping into urea SDS lysis buffer. Conditioned media was collected and concentrated using a 40% w/v ammonium sulfate (Sigma-Aldrich) cut.

Table 3.3: Recipe for self-made 7.5 % acrylamide/bis-acrylamide gels

Component (all Sigma-Alrich)	Resolving gel (mL)	Stacking gel (mL)
Acrylamide/Bis-acrylamide, 30%	2	0.75
Tris, 0.5M, pH 6.8	0	1.25
Tris, 1.5M, pH 8.8	2	0
ddH_2O	4	3
APS, 10 % w/v	0.1	0.1
TEMED	0.004	0.005

Samples were separated by SDS-PAGE on a 7.5% acrylamide/bis-acrylamide gel (Table 3.3), transferred to 0.2 µm nitrocellulose membrane (Biorad) (100 V, 2.5 h), blocked for 1 h in 5% w/v Marvel® Milk (Premier Foods, Hertfordshire, UK) or Odyssey® Blocking Buffer (TBS) (LiCor Biosciences, Lincoln, Nebraska, USA), then probed overnight at 4 °C with primary antibodies (Table 3.2). Membranes were washed 3 × 5 min in PBS with 0.1%

v/v Tween 20 (Sigma-Aldrich), and probed for 1 h at room temperature in the dark with IRDye® secondary antibodies (Table 3.2, LiCor Biosciences). Membranes were washed for 3 × 5 min with PBS-Tween20 0.1% v/v, rinsed with PBS then imaged using an Odyssey® CLX 9120 infrared imaging system (LiCor Biosciences).

3.10 Laminin Polymerisation assay

Cells were seeded at a density of 1.0 x 10^7 in Nunc™ TripleFlask™ treated cell culture flasks (ThermoFisher) and grown to confluence in normal media. Once confluent, media was changed to α-lactose containing, low serum media: DMEM High Glucose, 1 % FCS, 2 mM L-Glut and 30 mM α-lactose. After 5 days, media was harvested and concentrated with a 40 % ammonium sulfate cut. Concentrated media was dialysed into Tris Buffer Saline (TBS, 50 mM Tris, 150 mM NaCl, pH 7.2) with 0.1 % v/v Triton® X-100 (all Sigma-Aldrich). Protein concentration was determined by QuickStart Bradford Assay (Biorad).

Polymerisation assays were performed in 0.6 mL tubes at a volume of 100 µL with 1 mg/mL of concentrated conditioned media, 5 mM $CaCl_2$ (Sigma-Aldrich) in TBS-Triton X-100, as described previously (121). Tubes were incubated at 37 °C for 3 h then centrifuged at 10,000 g for 15 min to pellet precipitant. Supernatant was carefully removed, and Urea-SDS lysis buffer with 10 % v/v β-mercaptoethanol was added to both the pellet and supernatant. Samples were run on 7.5 % SDS-PAGE and immunoblotted for the presence of laminin α5.

3.11 Immunofluorescence

2×10^4 cells were seeded on glass coverslips, then fixed using either 100% ice-cold methanol (University of Liverpool, UK) for 10 min and air-dried for staining with LMα5 antibodies or fixed in 3.7% v/v paraformaldehyde in PBS for 10 min and permeabilised in 0.1 % v/v Triton X-100 (all Sigma-Aldrich) in PBS for 5 min. For ECM analyses, cells were removed by 2% v/v ammonium hydroxide treatment for 10 min prior to fixation as described previously (237). Primary antibodies (Table 3.2) were diluted in 5% normal goat serum (Sigma-Aldrich) PBS and incubated at 37 °C for 2 h. Coverslips were washed 3 × 5 min with PBS then probed 1 h at 37 °C with Alexa Fluor® secondary antibodies (Table 3.2**,** ThermoFisher) diluted in PBS at 2.4 µg/mL. Coverslips were washed in PBS with 0.05 % v/v Tween20 then mounted using VECTASHIELD® Mounting Medium with DAPI (Vectorlabs, Murarrie, Australia) and fixed with nail varnish (Coco Chanel, Paris, France). Images were obtained using Zeiss LSM800 confocal microscope (Zeiss, Oberkochen, Germany), and processed using Zen Blue (Zeiss) and ImageJ (NIH, Bethesda, Maryland, USA).

3.12 Focal adhesion analysis

Images obtained from focal adhesion immunocytochemistry were exported using Zen Blue and analysed using Image J. To analyse focal adhesions, images were converted to 8-bit, and threshold was *auto-adjusted*. The *Analyse particles* function was used to obtain individual measurements for each focal contact, as well as a summary of results for each image. Unpaired *T* test was

carried out using GraphPad Prism 6 (GraphPad Software, La Jolla, California USA).

3.13 Migration, morphology and scratch assay

For cell morphology analyses and low-density migration assays, cells were seeded at 2.0 x10^4 cells/ well onto uncoated 24-well plates (Corning, Sigma-Aldrich). For morphological analyses, 20X phase contrast images were acquired on a Nikon Eclipse Ti-E fluorescent microscope (Nikon, Tokyo, Japan) and cell perimeters of individual cells were manually traced to define cell area using Image J software. For low density migration assays, cells were imaged every 2 min over a 2 h period using a 20X objective on a Nikon Eclipse Ti-E fluorescent microscope adapted for live cell imaging. Individual cells were then tracked using the MTrackJ plugin on image J, to allow calculation of migration speed (total distance travelled / time), and cell processivity as a measurement of migration directionality persistence; defined as total distance migrated/ distance moved from origin.

For gap closure assays, cells were seeded in a 6-well plate (Corning, Sigma-Aldrich) at 6.0 x 10^4 cell/ well. Plates were carefully scratched with a 200 µL tip after 16 h, cell debris washed away, and the gap margin imaged using a Nikon TiE epifluorescence microscope with a 10X objective at 0 and 16 h. Gap closure was measured as a percentage relative to starting area using the freehand tool in image J.

3.14 Cell cycle analysis

Cells were serum starved for 24 h then seeded at a density of 2.5×10^5 per well of a 6-well dish. 24 h later, cells were dissociated, pelleted, washed, fixed

in 70% ethanol for 5 min, then re-suspended in 150 µL of RNase A (0.5 mg/mL) (Sigma-Aldrich). 150 µL of propidium iodide (ThermoFisher) (100 µg/mL) was added and incubated at 37 °C in the dark for 30 min. Cells were analysed using BD Accuri C6 flow cytometer (BD Biosciences, Franklin Lakes, New Jersey, USA). Multiple *T* test using the Holm-Sidak method was carried out using GraphPad Prism 6 (237).

3.15 Rapid Cell Adhesion Assay

Cells were seeded at 2.0 x 10^6 in a T75 flask, 24 h prior to assay for synchronisation. Cells were dissociated and plated at 1.0 x 10^5 cells/ well in TC-treated 96 well plates, with 1 plate per timepoint and at least 5 technical replicates per plate. After incubation for 5, 10, 20, 30, 45 or 60 min at 37 °C, 5 % CO_2, unattached cells were removed by flicking, and attached cells were fixed at room temperature for 10 min using 3.7 % paraformaldehyde. Plates were then stained with 0.5 % Crystal Violet solution with 20% methanol (both Sigma-Aldrich) for 30 min at room temperature and washed extensively with ddH_2O. Plates were dried and then treated with 100µL/ well 1 % SDS for 1 hour at room temperature. Absorbance at 595 nm was measured using SPECTROstar Nano plate reader (BMG Labtech, Aylesbury, UK), and data were analysed using GraphPad 6.

For rapid adhesion onto cell-derived matrices, A549 and 13C1 cells were seeded in TC treated 48-well plates (Corning, Sigma-Aldrich) at a density of 1.0 x 10^5/ well, and incubated at 37 °C, 5 % CO_2 for 120 h. Cells were then removed with 2 % ammonium hydroxide treatment, and cellular debris was removed with extensive sterile DPBS washes. HEK293 cells were seeded onto

the cell-derived matrices at a density of 2.5 x 10^5/ well, with the rapid adhesion assay then being carried out as described above.

3.16 Detachment Assay

A549 and 13C1 cells were seeded in a TC-treated 48 well plate at a density of 1.0 x 10^5 cells/well and incubated for 48 h at 37°C, 5 % CO_2. Wells were then treated with dilute trypsin EDTA (0.0005 % trypsin, 0.0002 % EDTA w/v or 0.00025 % trypsin, 0.0001 % EDTA w/v) for 1, 2, 5, 10, 20, 30, 45 and 60 min. After each timepoint, trypsin EDTA solution was removed carefully without irrigation, neutralised in serum-containing media and cells were counted. Data was analysed using GraphPad 6.

For detachment from cell-derived matrices, A549 and 13C1 cells were seeded in TC treated 48-well plates at a density of 1.0 x 10^5/ well, and incubated at 37 °C, 5 % CO_2 for 120 h. Cells were then removed with 2 % ammonium hydroxide treatment, and cellular debris was removed with extensive sterile DPBS washes. HEK293 cells were seeded onto the cell-derived matrices at a density of 2.5 x 10^5/ well, and incubated for 48 h at 37 °C, 5 % CO_2. Detachment assay was then being carried out as described above.

3.17 Cross-Matrix Experiments

A549 and 13C1 cells were seeded at density of 1.0 x 10^5 in TC-treated 48 well plates for 120 h at 37 °C, 5 % CO_2. Cells were removed with 2 % ammonium hydroxide and washed extensively with sterile DPBS to remove cellular debris, leaving behind A549 cell-derived matrices and 13C1 cell-derived matrices. A549 and 13C1 cells were then seeded onto 13C1 cell-derived matrices and

A549 cell-derived matrices respectively, for rapid attachment and detachment assays.

3.18 Cell surface integrin analysis

A549 and 13C1 cells were seeded in TC-treated 6 well plate (Corning, Sigma Aldrich) at a density of 5.0 x 10^5 and incubated for 24 h at 37 °C, 5 % CO_2. Cells were dissociated, resuspended in 100 µL of primary antibodies (Table 3.2) with 5 % normal goat serum in PBS, and rotated for 45 min at room temperature. Cells were pelleted at 100 g for 2 min, supernatant was removed and cells were washed with 3 x 5 min sterile DPBS. Cells were resuspended in 100 µL of secondary antibodies dilution (Table 3.2) and rotated for 45 min at room temperature in darkness. Cells were again pelleted and washed, before being fixed with 0.5 % PFA and analysed using the BD Accuri C6 flow cytometer.

3.19 Traction Force Microscopy (TFM)

3.19.1 Amino-salination of dishes

Glass bottom dishes (35 mm, ø13 mm, No. 1, MatTek, Ashland, Massachusetts, USA) were treated with 0.1 M NaOH at room temperature for 5 min. Once dried, dishes were treated with 3-aminopropyltrimethoxysaline (Sigma-Aldrich) for 2.5 min at room temperature before being extensively washed with PBS, followed by extensive ddH_2O washes. Dishes were treated with 200 µL of 0.5 % glutaraldehyde (Sigma-Aldrich) and incubated at room temperature for 30 min. Dishes were extensively washed with ddH_2O before being air dried in a dust cabinet.

3.19.2 Coverslip preparation

13 mm coverslips, No. 0 (SLS, Nottingham, UK) were washed extensively with Rain-X (Kraco Car International, Ellesmere Port, UK), and then left to incubate in Rain-X at room temperature overnight. Coverslips were then washed twice in 70 % ethanol and air-dried in a dust cabinet

3.19.3 Polyacrylamide gel preparation

20 µL of FluoSpheres Carboxylate-Modified Microspheres, 0.2 µm, yellow-green fluorescent (505/515 nm), 2 % solids (ThermoFisher) were added to 500 µL of polyacrylamide gel solution (5 % and 21 % polyacrylamide), and vortexed for 1 min. Setting agents (APS and TEMED) were added to solutions, and 6 µL of gel solution was added to the amino-silinated glass bottom dishes. Treated coverslips were placed on top of gel solution to create an ultrathin polyacrylamide gel (100-150 µm), and gels were turned upside down to set for 30 min at room temperature. Coverslips were removed with forceps, and gels were washed extensively with sterile DPBS to remove residual non-polymerised polyacrylamide.

3.19.4 Polyacrylamide coating

150 µL of 0.2 mg/mL sulfo-SANPAH (Sigma-Aldrich) was uniformly added to the polyacrylamide gels, and gels were then exposed to 365 nm UV light at a distance of 10 cm for 20 min. Gels were rinsed briefly with sterile filtered HEPES buffer (50 mM pH 8.5, Sigma-Aldrich). Rat-tail collagen I (100 µg/mL in HEPES buffer) was added to the gels and incubated overnight at 4 °C. Gels were washed sterile DPBS and sterilised using 365 nm UV light for 20 min.

3.19.5 TFM seeding, image acquisition and analysis

A549 and 13C1 cells were seeded at a density of 2.0 x 10^4 on collagen I coated polyacrylamide gels, and incubated for 24 h at 37 °C, 5 % CO_2. Cells were imaged at 30 designated positions in the brightfield channel, as well as a *z*-stack in the 488nm laser channel, using a 3i Olympus Spinning Disk confocal microscope (Olympus Life Sciences, Waltham Massachusetts, USA). Cells were then rapidly removed using 20 % SDS, and *z*-stacks were again taken in the 30 positions. Images were processed in ImageJ using the TFM macros "GenerateParameterFile" and "AlignCropPIVForce" as described previously (238).

3.20 Scanning Electron Microscopy

5 mm x 5 mm silicon wafer chips (AGG3390, Agar Scientific, Essex, UK) were sonicated in distilled water to remove dust, then sonicated in acetone and dried on a hotplate at 100 °C. Hot chips were plunged in acetone and dried again on the hotplate. Clean chips were mounted on aluminium studs (Agar Scientific) and dried on the hotplate. When dry, chips were plasma cleaned in the Tescan S8000G Fusion Ion Beam/ Scanning Electron Microscope (Tescan, Brno, Czech Republic), using an oxygen plasma to improve wetting. The chips were placed in a storage box and allowed to fully dry in a desiccator, before a final 70 % ethanol wash for cell seeding.

A549 and 13C1 cells were seeded at a density of 2.0 x 10^4 onto the wafer chips and incubated at 37 °C, 5 % CO_2 for 120 h. Cells were then removed using 2 % ammonium hydroxide solution, and cellular debris was removed with extensive DPBS washes. Remaining cell-derived matrices were treated

with either 4 M guanidine hydrochloride overnight at 4 °C with gentle rocking, or 0.1 mg/mL Collagenase A with 1 µg/mL proteinase inhibitor cocktail (P1860 cocktail, Sigma-Aldrich) overnight at 37 °C with gentle rocking. Treated matrices were fixed with 4 % paraformaldehyde 0.1 % glutaraldehyde (Sigma-Aldrich) in PBS at 4 °C for 2 h.

Samples were treated with chromium sputter for 15 s whilst under rotation, to achieve a coating thickness of 5-10 nm. The specimens were studied in the Tescan S8000G Fusion Ion Beam/ Scanning Electron Microscope at an accelerating voltage of 2 kV and a beam current of 15 pA. Micrographs were acquired at 10 µm, 5 µm and 2 µm field of view (length of horizontal axis) using the ET detector. The working distance was approximately 4 mm.

3.21 Liquid Chromatography – Mass Spectrometry (LC-MS)

3.21.1 LC-MS Sample preparation

Cells were synchronised by seeding 4 x 10^6 cells in T175 flasks in DMEM High Glucose media containing 1 % FCS and 2 mM L-Glutamine. After 24 h, 2 x 10^6 cells were seeded in 2 x 100 mm dishes in 1 % FCS media, then transferred to serum free media for 22 h. Cells were removed used 2 % v/v ammonium hydroxide for 10 min on ice, and washed with PBS x 5 to remove cellular debris. Remaining proteins on the two dishes were lysed with 90 µL of Clear Urea-SDS lysis buffer (6.7 M Urea, 10 mM Tris-HCl, 1% w/v SDS, 10% w/v glycerol) and snap frozen using liquid nitrogen (n = 4). Sample preparation from this point was carried out by the Centre of Proteomics Research (University of Liverpool, Liverpool, UK). Samples were normalised to the lowest protein concentration. 7 µg of protein was diluted to a total volume of

75.3 µL using ammonium bicarbonate, and samples were denatured for 10 min at 95 °C. Cysteine reduction was performed using 5 µL Dithiothreitol solution (11.1 mg/mL) for 10 min at 60 °C, 600 rpm. Samples were cooled to room temperature and alkylation was performed by adding 5 µL iodoacetamide (46.6 mg/mL) and incubated for 30 min in the dark. 20 ng of SP3 beads were added to the protein solution, followed by 365.2 µL of ethanol (80% final volume of ethanol). Beads were gently mixed by pipetting and incubated for 15 min. Samples were placed onto a magnetic rack and left to settle for 5 min. The eluent was removed and samples were then washed 3 x 5 min with 200 µL of 80 % ethanol. In-solution digestion was carried out by adding 1 µL 0.02 µg/µL trypsin in 40 µL 25 mM Ambic and incubated at 37 °C overnight at 1000 rpm. Samples were placed onto a magnetic rack and left to settle for 5 min. The solution was removed and acidified with 1 µL of trifluoroacetic acid. Peptide solutions were dried in a vacuum centrifuge and re-suspended in 20 µL of 97:3 water: acetonitrile + 0.1 % TFA for LC-MS analysis.

3.21.2 LC-MS Analysis

Injected samples were analysed using an Ultimate 3000 RSLC™ nano-system (Thermo Scientific) coupled to a Q Exactive™ mass spectrometer (Thermo Scientific). The sample was loaded onto the trapping column (Thermo Scientific, PepMap100, C18, 300 µm x 5 mm), using partial loop injection, for seven minutes at a flow rate of 12 µL/ min with 0.1 % v/v FA. The sample was resolved on the analytical column (Easy-Spray C18 75 µm x 500 mm 2 µm column) using a gradient of 96.2 % A buffer (0.1 % formic acid): 3.8 % B buffer (79.95 % acetonitrile, 19.95 % water, 0.1 % formic acid) to 50 % A: 50 % B

over 90 min at a flow rate of 0.3 µL/min (2 h program). The data-dependent program used for data acquisition consisted of a 60,000-resolution full-scan MS scan in the orbitrap (AGC set to 3e6 ions with a maximum fill time of 100 ms). The 16 most abundant peaks per full scan were selected for HCD MS/MS (30,000 resolution, AGC set to 1e5 ions with a maximum fill time of 45 ms) with an ion-selection window of 2 *m/z* and normalised collision energy of 30 %. Ion selection excluded singularly charged ions and ions with equal to or a greater than +6 charge state. Samples were analysed in random order.

3.21.3 LC-MS Data analysis

Raw MS data files were analysed by Progenesis QI label-free quantitative software. Peptide lists were exported and searched using the Mascot search engine (v 2.7) against the neXtProt database of human reviewed proteins (42,368 sequences; accessed: 09/08/2021) adjusted to a false discovery rate (FDR) of 1 %. The data were searched with the variable modification of methionine oxidation and a fixed cysteine carbamidomethylation modification, limited to 1 missed cleavage. Peptide mass and fragment mass tolerances were defined at ±10 ppm and ±0.01 Da, respectively.

3.22 Cell signalling arrays

Cells were prepared for use with the Human/Mouse AKT Pathway Phosphorylation Array C1 and the Human RTK Phosphorylation Array C1 (RayBiotech, Peachtree Corners, Georgia, USA). A549 and 13C1 cells were seeded at a density of 1.0 x 10^5 in a 6-well TC treated dish and incubated for 120 h at 37 °C, 5 % CO_2 then the cells were removed with 2 % ammonium hydroxide treatment to reveal the ECM. Onto the remaining cell-derived

matrices, HEK293 cells were seeded at a density of 3.0 x 10^5 and incubated for 24 h. Cells were lysed under gently rocking for 30 min at 4 °C in 200 µL of Cell Lysis Buffer (RayBiotech), and protein concentration determined by QuickStart Bradford Assay. Signalling array membranes were blocked with Blocking Buffer (RayBiotech) for 1 h at room temperature. 300 µg of protein lysis was loaded onto the membranes and incubated overnight at 4 °C. Membranes were washed extensively with Wash Buffer 1 and Wash Buffer 2 (RayBiotech) before incubation with the AKT and RTK primary antibody cocktails (RayBiotech) for 2 h at 37 °C. Membranes were washed with Wash Buffer 1 and 2 then incubated with HRP secondary antibody cocktails (RayBiotech) for 2 h at room temperature. Membranes were washed for a final time before being developed with Detection Buffer (RayBiotech) and imaged on a BioRad Gel Doc XR+ System. Densitometry was performed using Image J.

3.23 RNA Sequencing

3.23.1 Sample preparation

A549 and 13C1 cells were seeded at a density of 1.0 x 10^5 in a 6-well plate and incubated for 120 h at 37 °C, 5 % CO_2. HEK293 cells were synchronised by seeding 2.0 x 10^6 cells in a T75 flask 24 h prior to use. After 120 h, cells were removed with ammonium hydroxide and 3.0 x 10^5 HEK293 cells were seeded onto the cell-derived matrices for 24 h. RNA was than extracted from cells using the Monarch® Total RNA Miniprep Kit (New England Biolabs, Ipswich, Massachusetts, USA), and RNA was sent to Genewiz (Azenta Life Sciences, Leipzig, Germany) for RNA sequencing.

3.23.2 RNA Library Preparation and NovaSeq Sequencing

Samples were processed by Genewiz from this point onwards. RNA samples were quantified using Qubit 4.0 Fluorometer (Life Technologies, Carlsbad, CA, USA) and RNA integrity was checked with RNA Kit on Agilent 5300 Fragment Analyzer (Agilent Technologies, Palo Alto, CA, USA). RNA sequencing libraries were prepared using the NEBNext Ultra RNA Library Prep Kit for Illumina following manufacturer's instructions (NEB, Ipswich, MA, USA). Briefly, mRNAs were first enriched with Oligo(dT) beads. Enriched mRNAs were fragmented for 15 min at 94 °C. First strand and second strand cDNAs were subsequently synthesized. cDNA fragments were end repaired and adenylated at 3'ends, and universal adapters were ligated to cDNA fragments, followed by index addition and library enrichment by limited-cycle PCR. Sequencing libraries were validated using NGS Kit on the Agilent 5300 Fragment Analyzer (Agilent Technologies, Palo Alto, CA, USA), and quantified by using Qubit 4.0 Fluorometer (Invitrogen, Carlsbad, CA). The sequencing libraries were multiplexed and loaded on the flowcell on the Illumina NovaSeq 6000 instrument according to manufacturer's instructions. The samples were sequenced using a 2x150 Pair-End (PE) configuration v1.5. Image analysis and base calling were conducted by the NovaSeq Control Software v1.7 on the NovaSeq instrument. Raw sequence data (.bcl files) generated from Illumina NovaSeq was converted into fastq files and de-multiplexed using Illumina bcl2fastq program version 2.20. One mismatch was allowed for index sequence identification.

3.23.3 RNA sequencing Data analysis

After investigating the quality of the raw data, sequence reads were trimmed to remove possible adapter sequences and nucleotides with poor quality using Trimmomatic v.0.36. The trimmed reads were mapped to the Homo sapiens reference genome available on ENSEMBL using the STAR aligner v.2.5.2b. The STAR aligner is a splice aligner that detects splice junctions and incorporates them to help align the entire read sequences. BAM files were generated as a result of this step. Unique gene hit counts were calculated by using feature Counts from the Subread package v.1.5.2. Only unique reads that fell within exon regions were counted. After extraction of gene hit counts, the gene hit counts table was used for downstream differential expression analysis. Using DESeq2, a comparison of gene expression between the groups of samples was performed. The Wald test was used to generate p-values and Log2 fold changes. Genes with adjusted p-values < 0.05 and absolute log2 fold changes > 1 were called as differentially expressed genes for each comparison. A gene ontology analysis was performed on the statistically significant set of genes by implementing the software GeneSCF. The goa_human GO list was used to cluster the set of genes based on their biological process and determine their statistical significance. A PCA analysis was performed using the "plotPCA" function within the DESeq2 R package. The plot shows the samples in a 2D plane spanned by their first two principal components. The top 500 genes, selected by highest row variance, were used to generate the plot.

Chapter 4: Results and Discussion 1: Creating a CRISPR-Cas9 generated LMα5 mutant cell line

4.1 Introduction

Biological models of non-polymerizing LM diseases such as the Pierson syndrome, MDC1a and JEB have revealed much about the importance of LM polymerisation to tissue and organism-level functions. Likewise, biochemical studies have identified the mechanisms involved in laminin polymerisation and the residues involved in the process. However, these studies have largely not addressed an important middle ground, the gap between the biochemical studies and the tissues; the cells. This middle ground is important. The mouse models do not have the resolution to differentiate between the multiple potential contributing mechanisms behind the disrupted tissue functions, whereas the biochemical assays, due to the fragmented nature of the LN domains used, also cannot answer how a cell responds to a mutant LM matrix.

The aim of this chapter was to produce a cell model where the full-length mutant protein is produced in a biologically-relevant model and which would also allow for more subtle questions, including cell mechanotransduction and signalling, to be addressed. My objectives were to establish a mutant LN domain model, assess its phenotype in 2-dimensional cultures, and address how cells respond to a non-polymerizing LM mutation.

For this study, LMα5 was selected as the crystal structure for the LN had been solved and this crystal identified the critical Patch 2 motif and individual residues within that motif that are essential to LM polymerisation (167).

Specifically, the β5-β6 loop and the PLENGE sequence (Figure 4.2.3b). Substitution of glutamic acid 234 to a lysine residue was sufficient in in vitro assays to prevent LN-LN domain interactions in LN domain fragments (167). Specifically, it was shown that a LMα5 LN domain-containing protein fragment was able to prevent pellet formation in a LM polymerisation assay, whereas the protein fragment containing the E234K mutation could not do so (167). I targeted this same E234K mutation within exon 4 of *LAMA*5 for my studies.

This mutation targets the second stage of LM ternary node formation; the stabilisation step, based on the crystal structure and biochemical assay data. β and γLN domains would still be able to interact in the fast-intermediate step of ternary node formation. The hypothesised outcome would be an unstable, easily disrupted network. However, in a cellular context the effect of this change was unknown (Figure 4.1), specifically the implications for cell-to-matrix interaction and cellular responses to a LN domain mutant matrix.

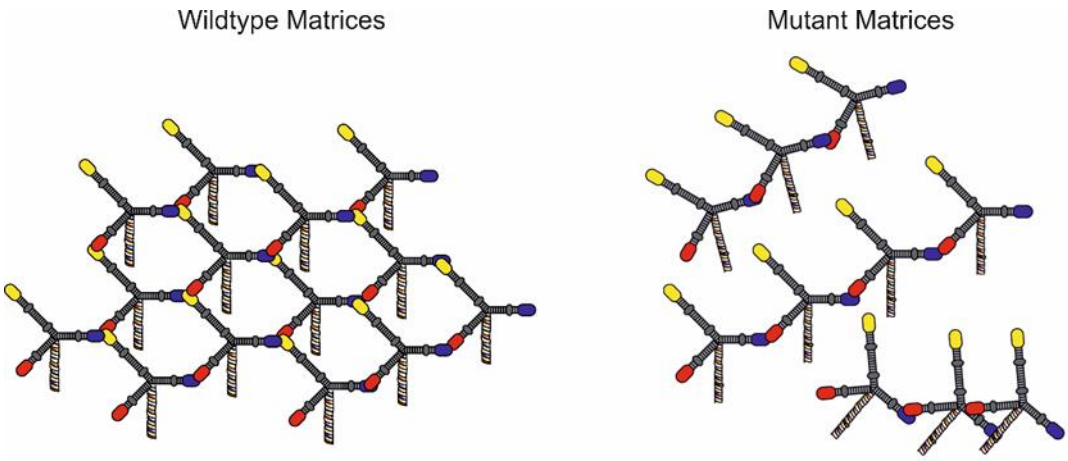

Figure 4.1. Wildtype vs LMα5 LM511 matrices. Wildtype LM511 is likely to form stable ternary nodes in an ordered network conformation, whereas non-polymerizing LMα5 mutant matrices will only be able to form the rapid intermediate β-γ LN domain interaction leading to weak/unstable networks.

4.2 Creating the cell line

4.2.1 Selecting an appropriate cell line

Before design could start on the CRISPR-Cas9 gRNA's and donor templates, an appropriate cell line needed to be selected so that the CRISPR system could be designed specifically to the selected cell-line's genome. Here, a cell line with high expression of the LMα5, LMβ1 and LMγ1 chains, and low expression of other LM chains was desired to reduce the potential impact of other confounding variables by limiting the number of other network-forming LM heterotrimers present.

RT-qPCR was performed to analyse the expression levels laminin genes in different immortalised cell lines. Primers and cDNA from A549 (lung adenocarcinoma cells (234)), HCT-116 (colon cancer cells (239)), MCF-7 (invasive breast ductal carcinoma cells (240)) and MDA-231 (breast adenocarcinoma (241)) cells (Figure 4.2.1), four cell lines known to express *LAMA*5, were kindly donated by Dr Troughton (University of Liverpool). RT-qPCR analysis showed that of the cell lines tested, A549 cells expressed high levels of *LAMA*5, *LAMB*1 and *LAMC*1, while also expressing comparatively low levels of *LAMB*2. Analysis suggested LM511 would be the predominant LM heterotrimer expressed in these cells, with relatively low levels of LM3b32, LM3a32 and LM521 also present. In comparison, HCT 116 expressed a mixture of *LAMA*5, *LAMA*4 and *LAMA*3A, MCF7 expressed *LAMB*2 at high levels, and MDA-231 expressed a mixture of *LAMB*1, *LAMB*2 and *LAMB*3 and a larger fraction of *LAMC*2 (Figure 4.2.1).

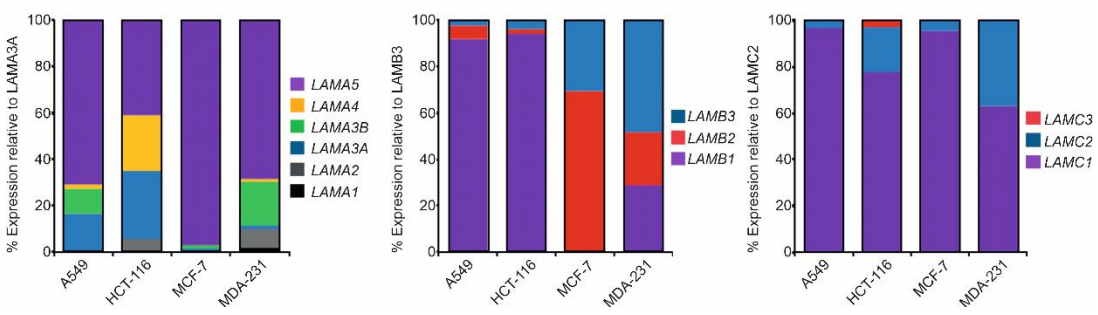

Figure 4.2.1. Relative mRNA expression of the LM chains in different immortalised cell lines. A549, HCT-116, MCF-7 and MDA-231 immortalised cell lines were analysed for their relative levels of each LM chain by RT-qPCR. Expression of *LAMA* genes was quantified relative to *LAMA*3A expression, *LAMB* genes relative to *LAMB*3, and *LAMC* genes relative to *LAMC*2.

Western blots were then performed on cell lysates prepared from A549 cells for LMα5, LMβ1 and LMβ2, with the cell lysate controls of ARPE19 (retinal pigment epithelial), A431 (epidermoid carcinoma) and HaCaT (immortalised keratinocytes) cells. These analyses analysis confirmed the LMα5 and LMβ1 chains as the predominant LMα and β chains in A549 cells, and no detectable LMβ2 (Figure 4.2.2). Together, these data show that A549 cells predominantly express LM511, and, for this reason, A549's was chosen for the CRISPR-Cas9 model cell line.

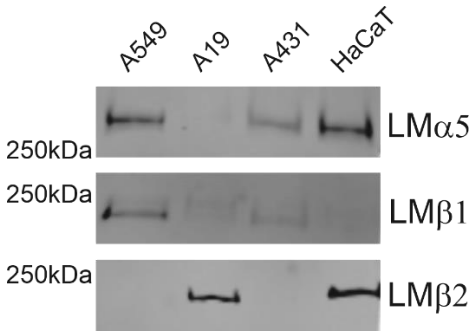

Figure 4.2.2. A549 cells express high levels of LMα5 and LMβ1. Total cell lysates were processed by western immunoblotting with anti-LMα5 (mouse), LMβ1 (rabbit) and LMβ2 (mouse) antibodies. A19, A431 and HaCaT lysates were included as positive controls for each LM chain analysed.

4.2.2 CRISPR Design and Transfection

Two gRNA's specific to PAM sites within and around LMα5 exon 4 were designed (167) (Figure 4.2.3). These gRNA's were screened for potential off-target loci as part of the design process in attempt to minimise off-target effects using the Integrated DNA Technologies' CRISPR-Cas9 gRNA Design Checker (Supplemental Table 1). An oligonucleotide was used as the HDR template to introduce the E234K mutation. A549 cells were electroporated with one of the two gRNA's in a complex with Cas9 protein (231) and the HDR template. Transfected populations were screened by PCR for the presence of E234K (Figure 4.2.4), and gRNA 1 was selected to proceed for single cell expansion and cloning.

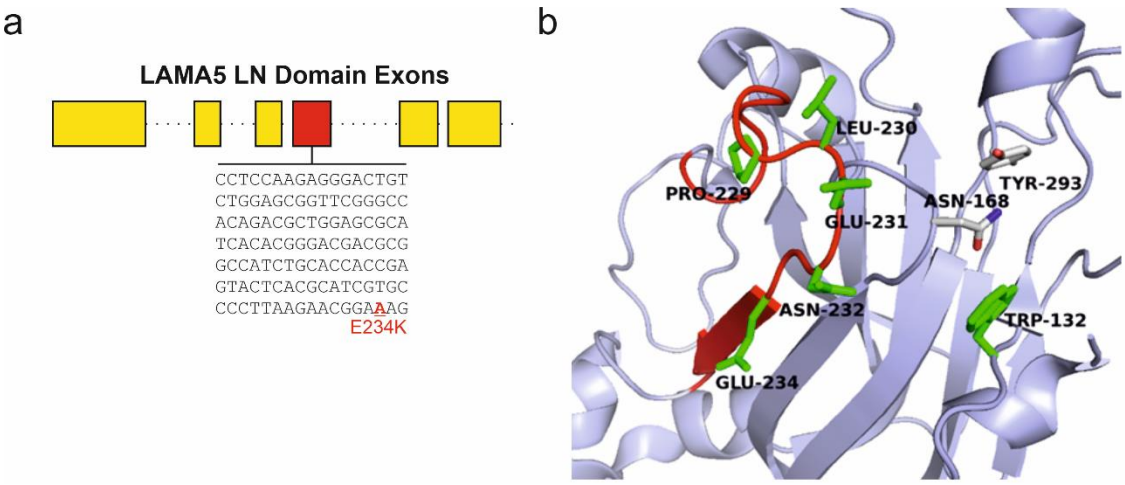

Figure 4.2.3. CRISPR-Cas9 targets with *LAMA*5. a) CRISPR-Cas9 gRNA's were designed to target exon 4 (red) of *LAMA*5, to introduce the E234K mutation (red, underlined). b) This mutation would target the key β5-β6 loop (residues labelled) in Patch2 of the αLN domain. E234K lies within the PLENGE residues (red). Crystal structure based on (167).

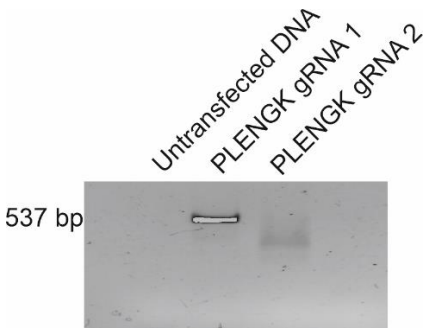

Figure 4.2.4. Population screen for E234K mutant. CRISPR-Cas9 transfected populations were screened for the E234K point mutation through PCR using primers designed to only amplify if the E234K mutation.

4.2.3 Gel screening of clones highlighted potential mutations

Single cell colonies were expanded from gRNA1 transfected populations then screened by endpoint PCR with one set of primers providing a DNA quality check control (Figure 4.2.5, top gels) to ensure DNA was present, and a second set of primers designed to detect the presence of the E234K mutation (Figure 4.2.5, bottom gels).

Initial screening highlighted 12 clonal populations as potential mutants (Figure 4.2.5 red lettering). These positive hits were then screened by heteroduplex analysis.

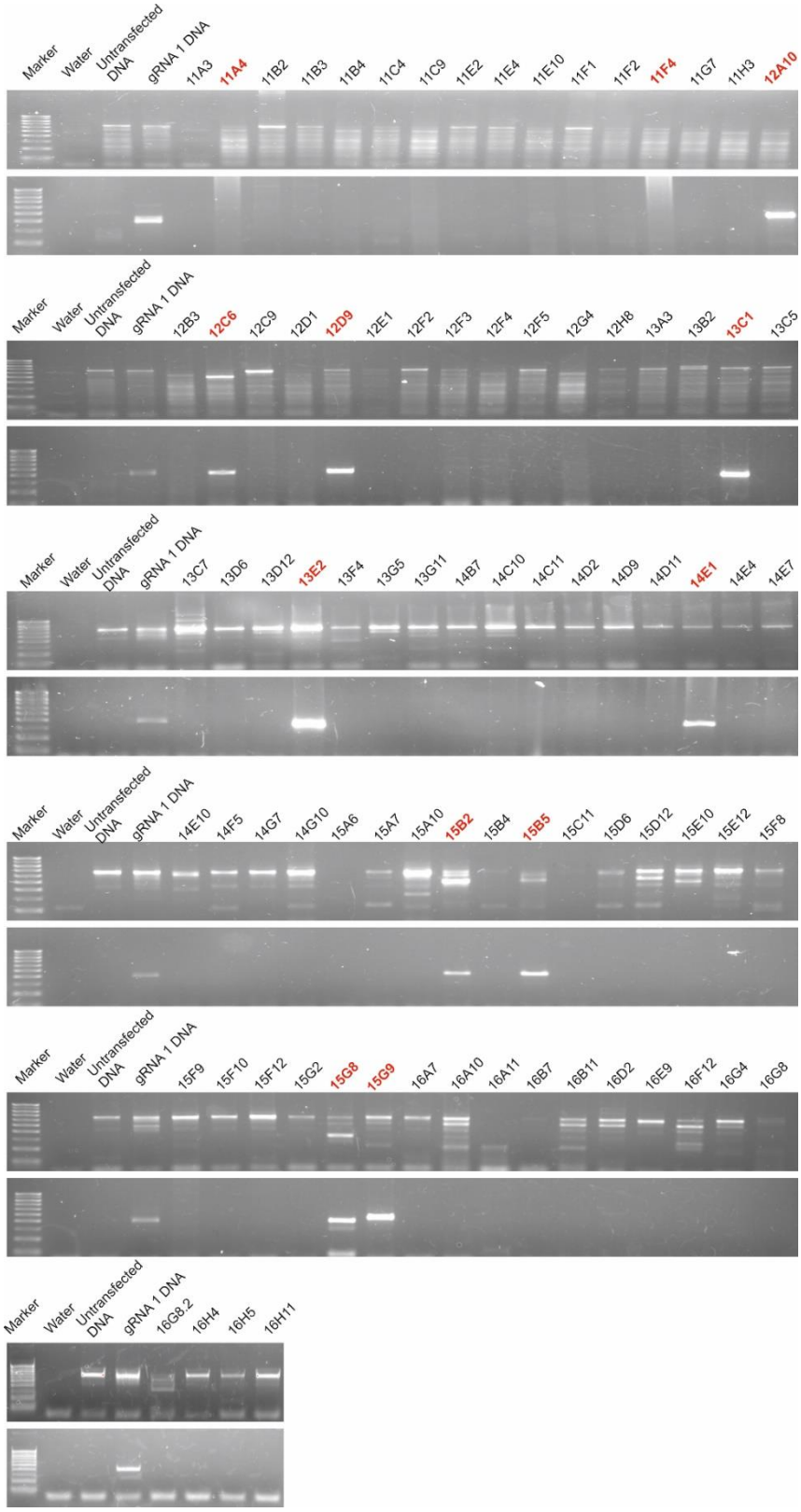

Figure 4.2.5. LMα5 mutant screen. DNA was extracted from all single cell clones and PCR performed to detect the presence of E234K mutation. Top gels represent a general *LAMA*5 DNA check, to ensure DNA was successfully extracted, with lower gels identifying the E234K mutation. Positive hit clones are highlighted in red.

4.2.4 Heteroduplex analysis and sequencing of potential mutants identified the 13C1 LMα5 mutant cell line

As the successfully edited cells would have substituted a GC base pairing (3 covalent bonds) for an AT base pairing (2 covalent bonds), any *LAMA*5 PCR products from a mutant cell would have a lower melting temperature (T_m) than the equivalent product from a wild-type cell. A high-resolution melt-curve was conducted on all positive hits from the PCR screen (Figure 4.2.6a). This analysis showed a reduction in T_m for one clone, 13C1, as well as identifying the presence of heterozygous double peak in clone 12A10, while other clones produced the same melt curve profile as wild-type cell (Figure 4.2.6b). DNA sequencing of the 13C1 clone then confirmed the presence of the homozygous presence of the E234K mutation (Figure 4.2.7).

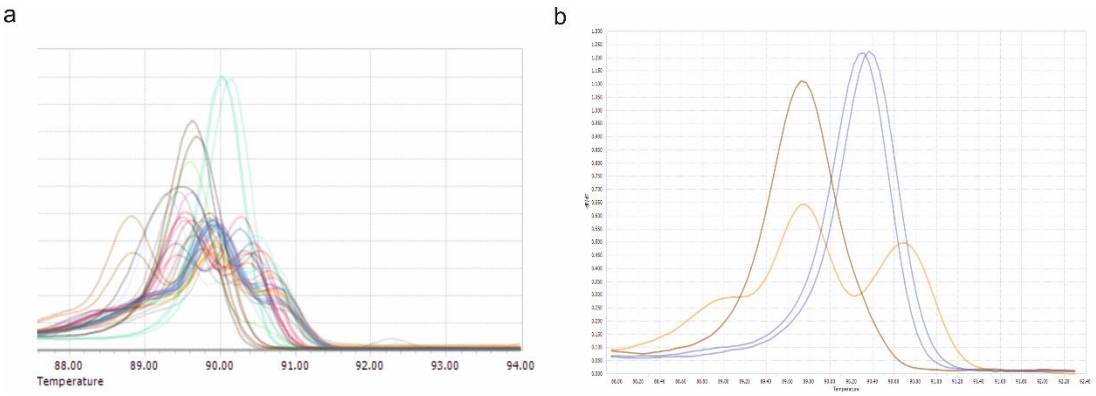

Figure 4.2.6. Heteroduplex analysis of positive hits. a) qPCR products from all "positive hits" were analysed in triplicate using a high-resolution melt curve. b) Example melt-curves from a homozygous mutant in red, a heterozygous population in yellow and wildtype clones in blue.

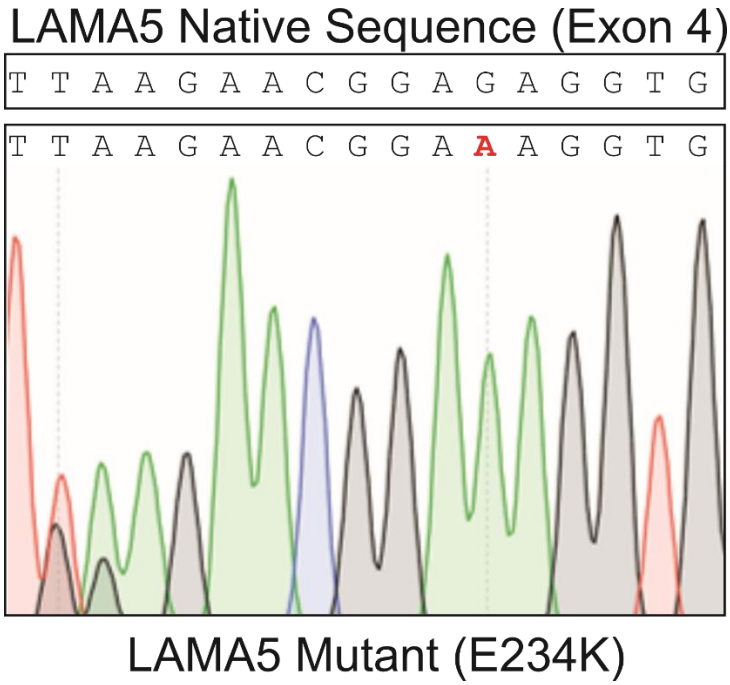

Figure 4.2.7. Sequencing of 13C1 clone confirmed the presence of the E234K mutation. Positive clone 13C1 was sequenced to confirm the presence of the E234K point mutation, highlighted in red. Sequence is shown in SnapGene.

4.2.5 Implementation of the E234K mutation in LMα5 results in a loss of LM polymerisation

A polymerisation assay was performed using conditioned media generated 13C1 cells or wildtype A549 and cells and concentrated through ammonium sulfate cut. The concentrated protein was then incubated for 3 hours at 37 °C and the polymerised fraction pelleted by centrifugation then analysed by immunoblotting. These studies identified a reduction in polymerised LMα5 to near undetectable levels in the pellet of 13C1 cells, ~15 % less compared to the wildtype cells in the same assay (Figure 4.2.8).

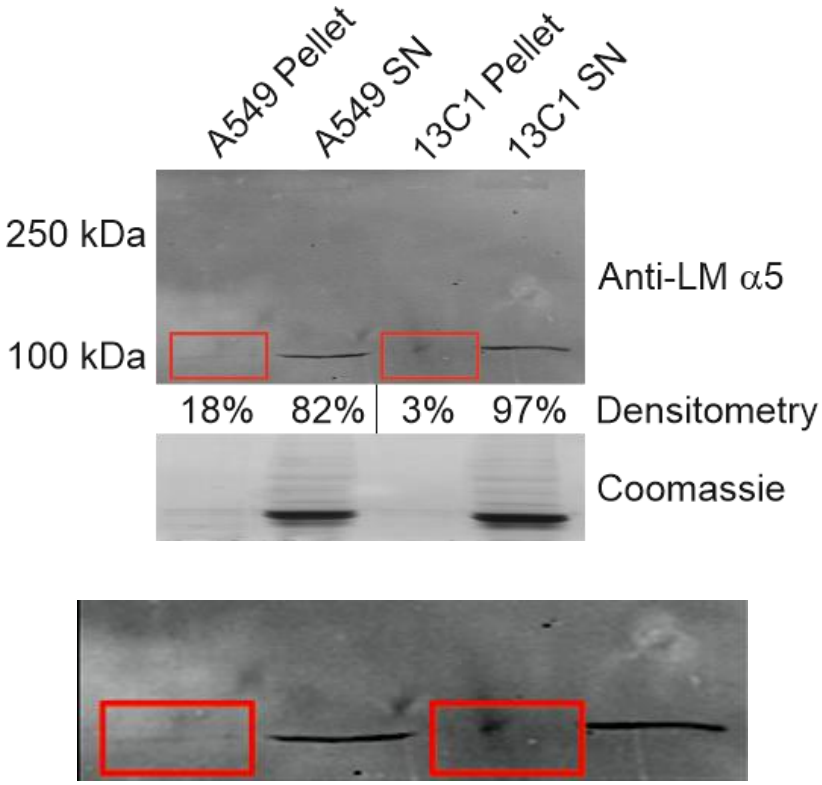

Figure 4.2.8. Polymerisation assay of wildtype and mutant LM. Conditioned media from A549 and 13C1 cells was concentrated using ammonium sulfate cut then incubated at 37C for 3h. The resultant pellet and supernatant (SN) were analysed by immunoblotting with mouse monoclonal antibodies to LMα5 (2F7) and quantified by densitometry. Red boxes indicate LMα5 pellet bands analysed in densitometry, with Coomassie blue staining of total protein shown below.

4.3 13C1 Phenotype analysis

4.3.1 LMα5 mutant cells display a reduced LM511 in the ECM

Next, I examined how the overall protein levels of LMα5 were affected by introduction of the mutation. This was analysed over 96 hours in total cell lysate, in conditioned media extracts and in ECM extracts through immunoblotting for LMα5 and LMβ1.

These analyses revealed no differences between the A549 and 13C1 LMα5 mutants in terms of LMα5 expression in the total cell lysates cells after 96 hours (Figure 4.3.1), although a slight decrease in LMβ1 across all time points was noted in the mutant cells (Figure 4.3.1). There were also no differences in

LMα5 or LMβ1 in the conditioned media lysates for A549 and 13C1 cells, suggesting that LM511 was secreted at consistent levels (Figure 4.3.2). However, there was a pronounced reduction in LMα5 protein in the ECM extracts generated from the mutant cells compared with wild-type A549 at all time points (Figure 4.3.3).

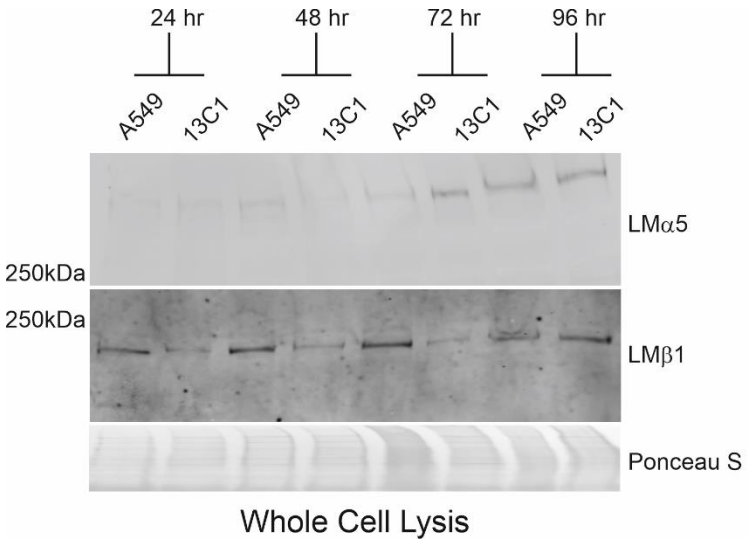

Figure 4.3.1. LMα5 and LMβ1 expression in the whole cell lysates. Cell lysates for A549 and 13C1 cells at 24, 48, 72 and 96 hours after plating were prepared through scraping and analysed through immunoblotting. Blots were probed with mouse monoclonal anti-LMα5 (top) and rabbit polyclonal anti-LMβ1 (middle) antibodies, with protein load balancing Ponceau S stain shown below.

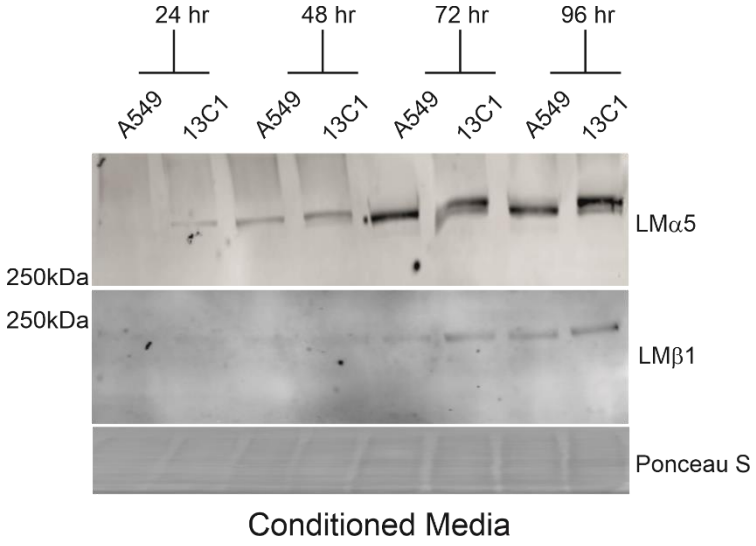

Figure 4.3.2. LMα5 and LMβ1 expression in the conditioned media. Conditioned media for A549 and 13C1 cells at 24, 48, 72 and 96 hours of culture was concentrated and analysed through immunoblotting. Blots were probed with mouse monoclonal anti-LMα5 (top) and rabbit polyclonal anti-LMβ1 (middle) antibodies, with protein load balancing Ponceau S stain shown below.

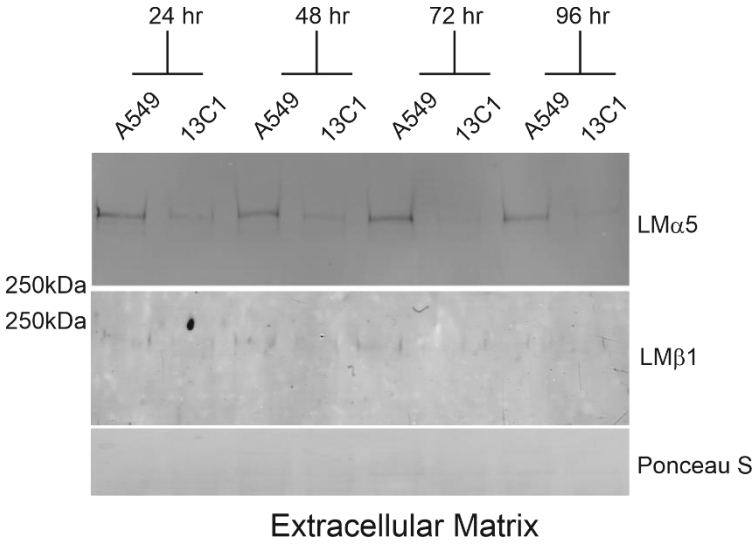

Figure 4.3.3. LMα5 expression in the ECM is reduced. Extracellular matrix preparations for A549 and 13C1 cells after 24, 48, 72 and 96 hours of culture were prepared through ammonium hydroxide-mediated osmotic removal of cells. The remaining ECM was scraped and analysed through immunoblotting. Blots were probed with mouse monoclonal anti-LMα5 (top) and rabbit polyclonal anti-LMβ1 (middle) antibodies, with protein load balancing Ponceau S stain shown below.

4.3.2 LMα5 mutant cells display reduced proliferation rates

During routine handling of the cell lines, I noted a reduced growth rate of the edited 13C1 cells. To formally examine this, cell-cycle analysis was performed. Wildtype A549 and LMα5 mutant 13C1 cells were serum starved and cultured for 24 hours then processed for cell-cycle analysis by flow cytometry (Figure 4.3.4). The 13C1 cells had a ~10% larger proportion of cells in G0/G1 phase compared to the wildtype cells (A549 mean = 49.9 % ± 1.1 SD, 13C1 = 59.8 % ± 1.0 SD, p = 0.01, two-tailed unpaired t-test). There was also an observed 8.5 % decrease in G2/M phase but this did not reach statistical significance at a type I error rate of 0.05 (A549 = 25.6 % ± 2.4 SD, 13C1 = 17.1 % ± 1.6 SD, p = 0.08, two-tailed unpaired t-test). The proportion of cells in S phase were largely unchanged (A549 = 24.5 % ± 3.6 SD, 13C1 = 23.2 ± 0.6 SD, p = 0.79, two-tailed unpaired t-test). These data together suggest that although cells are preparing to undergo mitosis, edited cells are not dividing as quickly as their wildtype counterparts. However, it is unclear whether this is a matrix-driven (i.e. LM) or cell-driven (off-target CRISPR effect) phenotype.

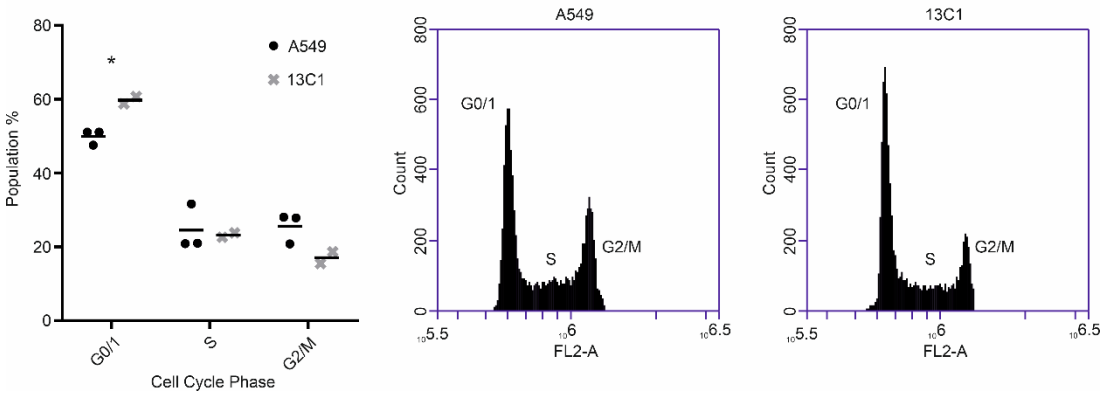

Figure 4.3.4 LMα5 mutants display a reduced proliferation. Wildtype A549 (circles) and LMα5 mutant 13C1 (crosses) cells were synchronised and cultured for 24 hours and then processed for cell cycle analysis by flow cytometry. Detected using propidium iodide, recorded in the FL2-A channel. Percentage of the cell population in each stage of the cell cycle was plotted, with representative Fl2-A count plots from flow analysis also shown. Asterix's (*) highlight statistically significant differences ($p < 0.05$, two-tailed unpaired t-test).

4.3.3 LMa5 mutant cells showed no difference in cell area relative to wildtype cells

As the LMα5 mutant 13C1 cells were not dividing as quickly as the wildtype cells, it was important to ensure the mitosis deficiencies were not having a negative effect on the overall health of the cells. Hypertrophy is characterised by the halt in the cell cycle, with continued production of cellular proteins, which subsequently leads to an increase in cell size (242). To ensure the mutant cells were not undergoing hypertrophy, cell 2D area was analysed for both cell types. Wildtype A549 and LMα5 mutant 13C1 cells were seeded at a low density and imaged using a phase contract microscope after 24 hours (Figure 4.3.5). There was no difference between the cell area of the wildtype and mutant cell lines (A549 mean 820 $\mu m^2 \pm$ 280 SD, 13C1 mean 870 $\mu m^2 \pm$ 270 SD, $p = 0.35$, two-tailed unpaired t-test).

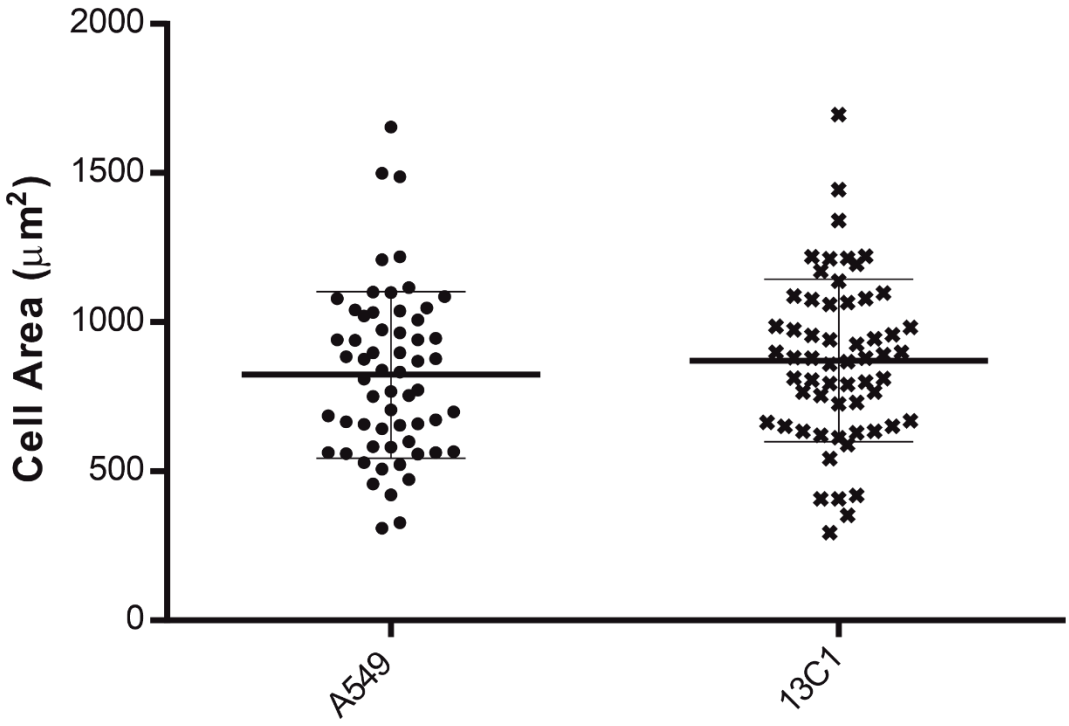

Figure 4.3.5. Cell area comparison between A549 and 13C1 cells. A549 and 13C1 cells were seeded at a density of 2 x 10^4 cells/well (24-well plate) for 24 hours then phase contrast images were taken. Cell perimeters for individual cells were manually traced to define cell area, with each cell representing a technical replicate and data point (n=2 independent experiment, 30 cells per experiment). Mean cell area (horizontal line) and standard deviation (error bars) shown.

4.3.4 LMα5 mutant cells close scratch wounds slower than wildtype cells

Scratch wound closure of the A549 wildtype and LMα5 13C1 mutant cells was observed in a 6-well plate, scratched after 16 hours and the gap margin imaged from 0 and 24 hours (Figure 4.3.6). These assays revealed an ~82 % increase in the mean gap closure time of 13C1 cells compared to the wildtype A549 cells (A549 mean gap closure time = 10.8 hours ± 1.4 SD, 13C1 mean 19.7 hours ± 2.4 SD, p = 0.045, two-tailed unpaired t-test).

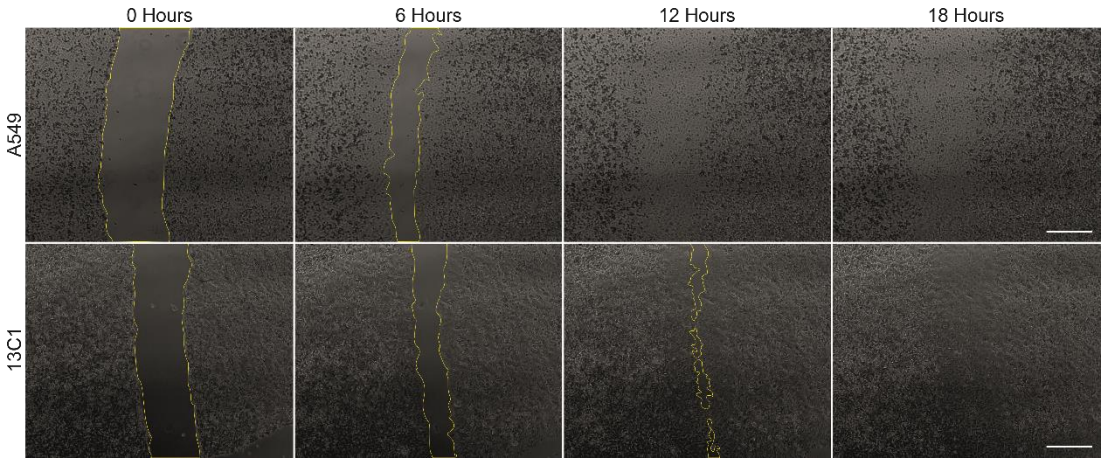

Figure 4.3.6. 13C1 cells display a reduced wound healing rate. A549 and 13C1 cells were seeded at a density of 6.0 x 10^5 for 16 hours then carefully scratched with a 200 µL pipette tip and imaged over 24 hours. Representative images at 0, 6, 12 and 18 hours are shown for A549 (top) and 13C1 (bottom) cells. Yellow boxes indicate gaps in the cell monolayer at each time point. Scale bar is 500 µm.

4.3.5 LMa5 mutant cells displayed reduced migration processivity

A549 and LMα5 mutant 13C1 cells were seeded in a 24-well plate allowed to attach for 6 hours then imaged for 5 hours (Figure 4.3.7). Two measurements of the migration were analysed, speed (total distance/ time) (Figure 4.3.7a) and processivity (distance migrated from origin/ total distance migrated) (Figure 4.3.7b). There was no difference between the speed of the wildtype A549 and mutant 13C1 cells (A549 mean speed= 0.37 µm/min ± 0.10 SD, 13C1 mean = 0.32 µm/min ± 0.08 SD, p = 0.062, two-tailed unpaired t-test). However, there was a 29.1 % reduction in the cellular processivity of the mutant 13C1 cells (A549 mean = 0.73 ± 0.28 SD, 13C1 mean = 0.53 ± 0.29 SD, p = 0.016, two-tailed unpaired t-test). These data indicate that mutant cells were migrating in a more circular or tortuous manner rather than the generally more linear patterns of control cells (Figure 4.3.7c-d).

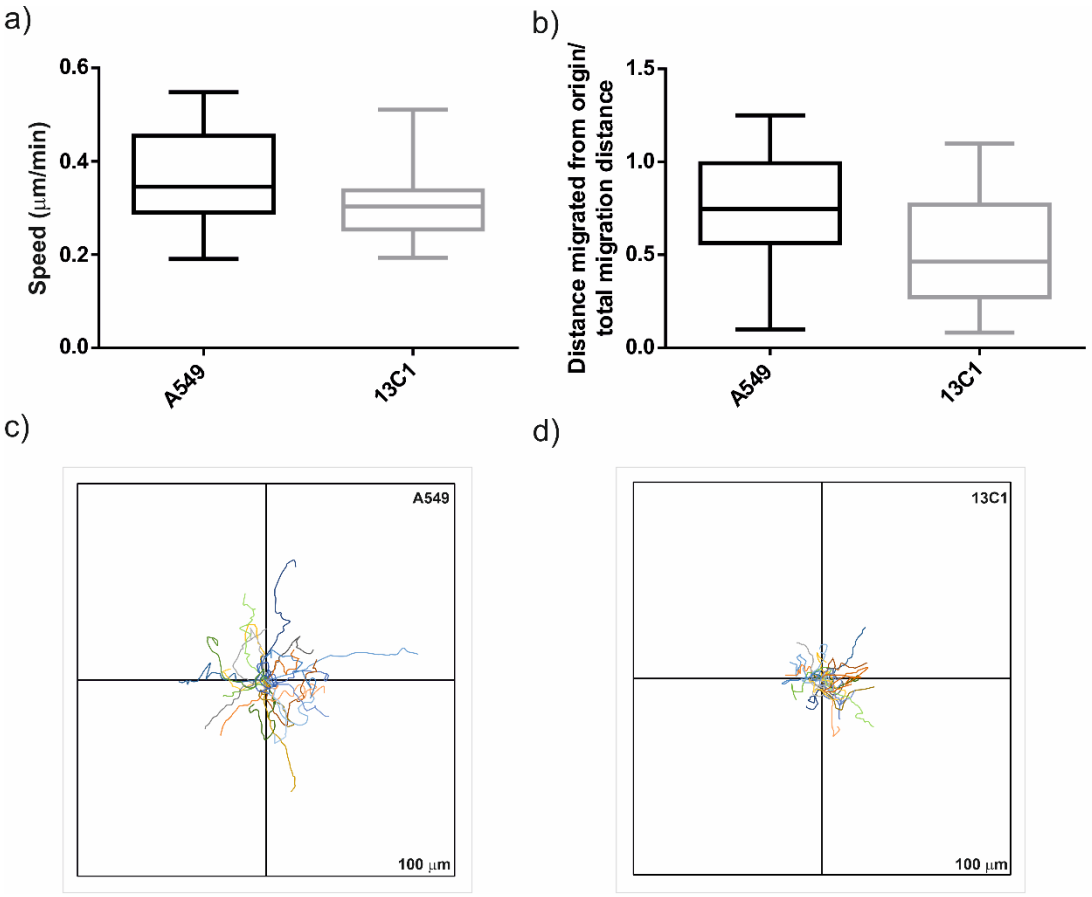

Figure 4.3.7. Mutant cells displayed a reduced cellular processivity. A549 and 13C1 cells were seeded at a density of 2 x 10^4 cells/well (24-well plate) for 6 hours, and migration paths of individual cells were tracked manually. a) Cell speed was calculated as total distance/ time (μm/min), and b) cell processivity was calculated as distance migrated from the origin/ total migration distance. Cell migration tracks plotted as rose plots for wildtype A549 (c) and mutant 13C1 (d) cells. Axis scale = 100 μm.

4.3.6 LMα5 mutant cells show a decrease in rapid adhesion rate

Wildtype A549 and LMα5 mutant 13C1 cells were seeded into 96-well plates for a series of time points over 60 minutes. At each time point, attached cells were fixed then stained with crystal violet (Figure 4.3.8). Overall, 13C1 cells reached 50 % attachment 3 minutes slower than the wildtype A549 cells (31.8 min and 34.8 min respectively) (Figure 4.3.8c). In each of the two independent experiments, the 13C1 cells attached more slowly than the A549 cells, however, this did not reach the threshold for statistical significance (Mean of

differences 4.25 % ± 2.0 SD, p = 0.075 two-tailed paired t-test) (Figure 4.3.8 a-b). These data suggest that the mutant cells are still able to attach to culture plastic effectively, although possibly at a slower rate compared to the wildtype cells.

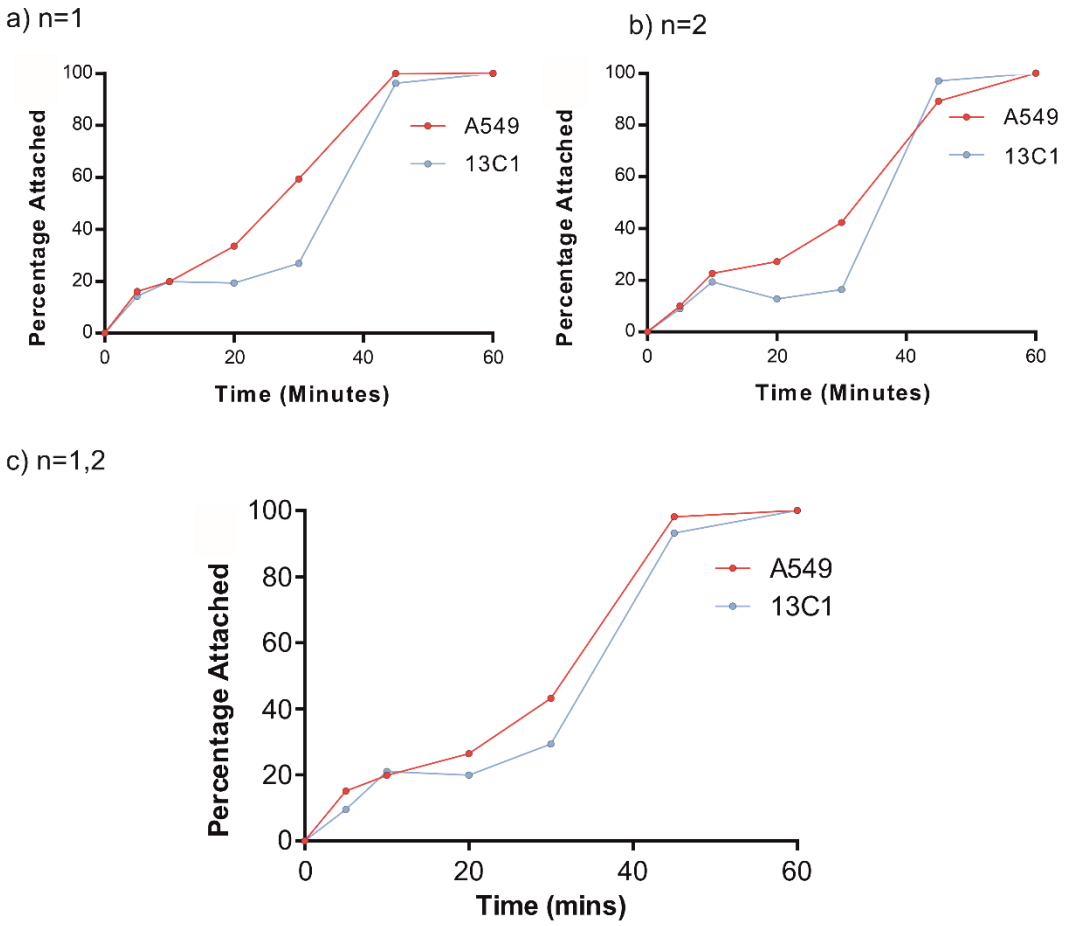

Figure 4.3.8. Rapid cell attachment assay showed a reduced rapid attachment rate in the LMα5 mutant cells. Wildtype A549 (red) and mutant 13C1 (blue) cells were plated in 96-well dishes and incubated for 5, 10, 20, 30, 45 and 60 min, with remaining cells after each time point quantified. Percentage attached was plotted against time since seeded, a) and b) are biological replicates and c) mean of the two experiments.

4.3.7 LMα5 mutant cells displayed a reduced trypsin resistance

The attachment assays assessed the impact of the LN domain mutation on the cells' ability to rapidly attach to plastic. However, this experiment did not assess whether the mutant cells are able to form functional adhesions on their

mutant cell-derived matrix. To assess this, I measured the relative ability of the cells to resist trypsin dissociation as a crude indicator of adhesion strength/efficacy. Wildtype A549 and LMα5 mutant 13C1 cells were cultured for 120 hours to allow for the deposition of LM511 and then were treated with diluted trypsin at either 1 in 200 or 1 in 100 (2.5×10^{-4} or 5×10^{-4} % respectively, Figure 4.3.9a-c). At both concentrations, the LMα5 mutant 13C1 cells detached more rapidly than the wildtype cells (1 in 200: mean of differences 6.2 % ± 2.5 SD $p = 0.04$, 1 in 100: mean of differences 8.1 % ± 2.8 SD, $p= 0.02$, two-tailed paired t-test analysis). Specifically, the time to 50 % detachment decreased by 15 % for the 1 in 200 dilution and 25 % for the in 1 in 100 dilution (A549 mean 18.2 min, 15.5 min respectively, 13C1 mean 15.4 min, 11.6 min respectively) (Figure 4.3.9d).

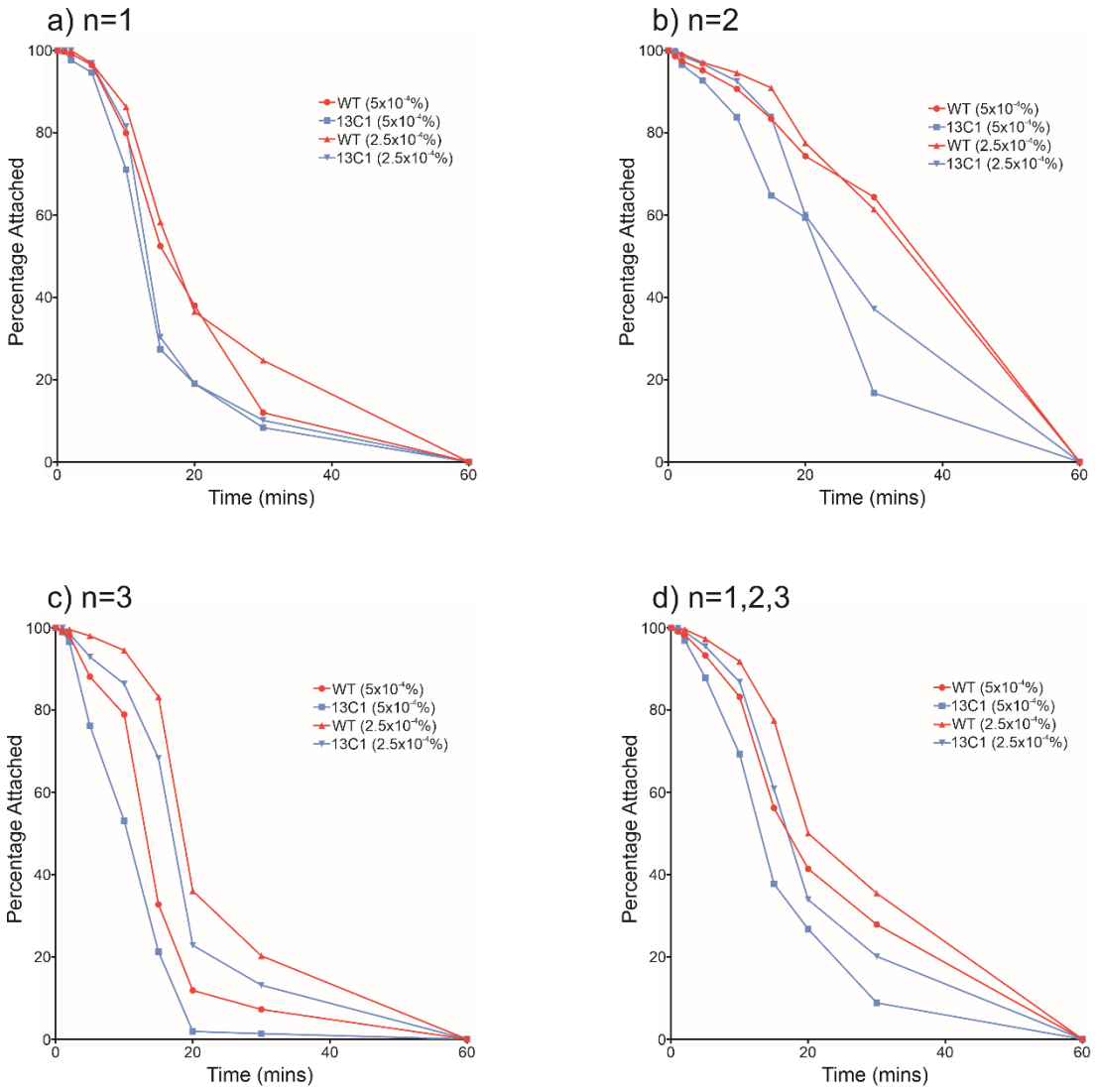

Figure 4.3.9. LMα5 mutant cells have a reduced resistance to trypsin. Wildtype A549 (red) and LMα5 mutant 13C1 (blue) cells were cultured for 120 hours then treated with diluted trypsin ($5x10^{-4}$ and $2.5x10^{-4}$ %). At each timepoint, supernatant was removed and cells were counted. The percentage of cells attached was plotted against the time since trypsin was added. a-c) are independent biological repeats, d) mean from the three experiments.

4.3.8 LMα5 mutant cells displayed a reduction in cellular traction force exerted

As the LMα5 mutant cells displayed an apparent reduced strength of attachment in the crude trypsin-resistance assays, I next compared the forces the cells were exerting, and whether a change in culture substrate might

amplify these strength of attachment phenotypes. Traction force microscopy was conducted under two conditions; hard and soft substrate. Wildtype A549 and mutant 13C1 cells were cultured onto 5 % and 21 % microbead polyacrylamide gels cross-linked with rat-tail collagen I (stiffness of approximately ~5000 and ~85000 Pa respectively (243-245)) for 24 hours (Figure 4.3.10a). After incubation, cells and the fluorescent microbeads in the gel were imaged, and then cells were removed with 20 % SDS and the microbeads imaged again (Figure 4.3.10b). The displacement from the “with cells” image compared with without cells images was used to calculate total displacement magnitude (Figure 4.3.10c).

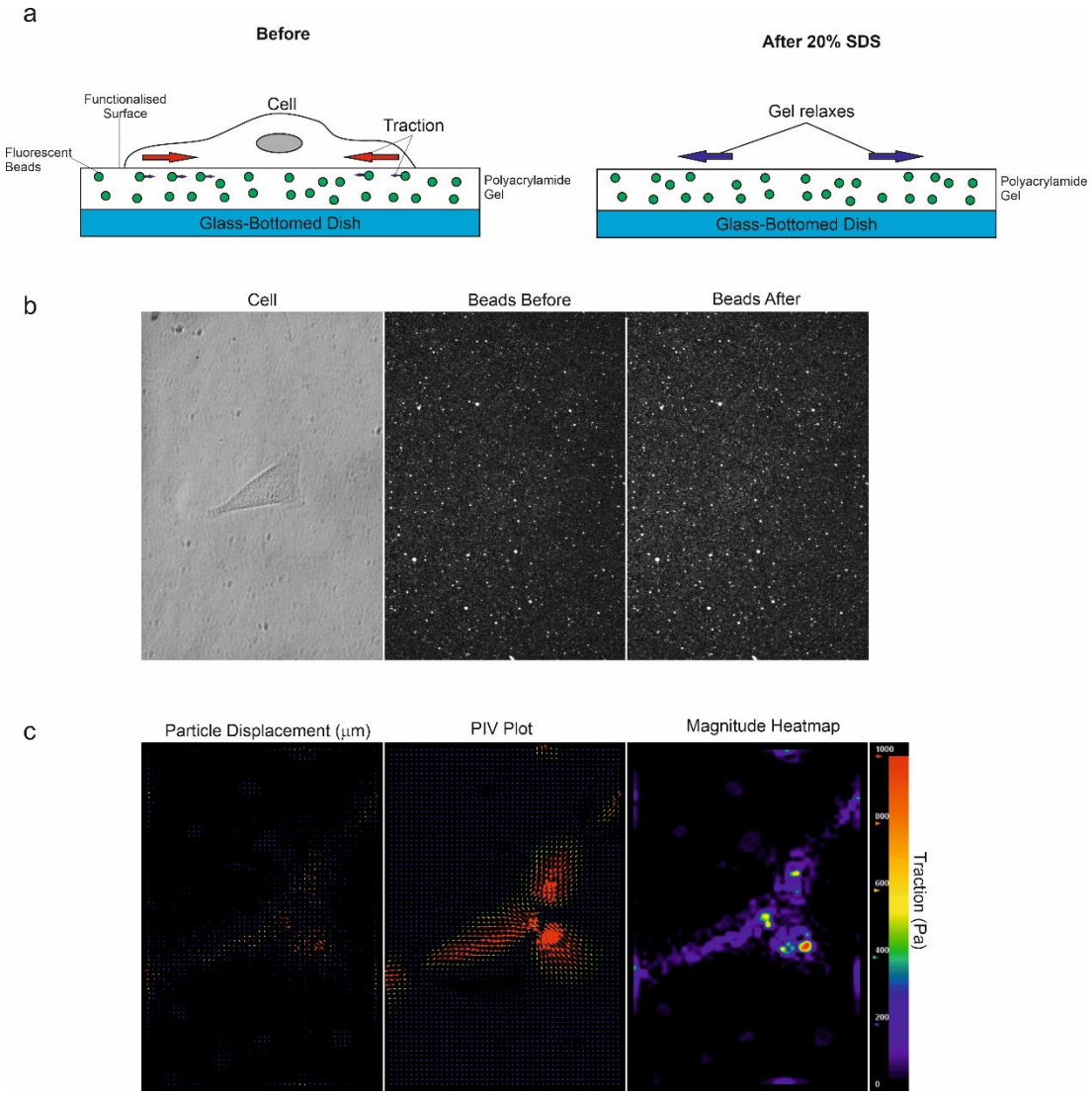

Figure 4.3.10. An overview of traction force microscopy methods. a) Cells seeded onto thin polyacrylamide gels with a functionalised surface (cross-linked with rat-tail collagen I), containing fluorescent microbeads. After 24 hours, single cells were imaged along with the beads below (b), before cells were removed with SDS and again after the cell were removed (b). The total displacement of the microbeads used to calculate particle displacement, PIV plots and total magnitude and traction of the cells (c).

On the stiffer 21 % polyacrylamide substrate, there was no difference between the total displacement magnitude of A549 and LMα5 mutant 13C1 cells (A549 mean = 0.20 mPa ± 0.08 SD, 13C1 mean = 0.23 mPa ± 0.09 SD, p = 0.173, two-tailed unpaired t-test) (Figure 4.3.11). However, on the softer 5 % polyacrylamide substrate (Figure 4.3.12), there was a 42 % decrease in total displacement magnitude in the 13C1 cells compared to the A549 cells (A549

mean = 0.55 mPa ± 0.29 SD, 13C1 mean = 0.32 mPa ± 0.15 SD, $p < 0.01$, two-tailed unpaired t-test).

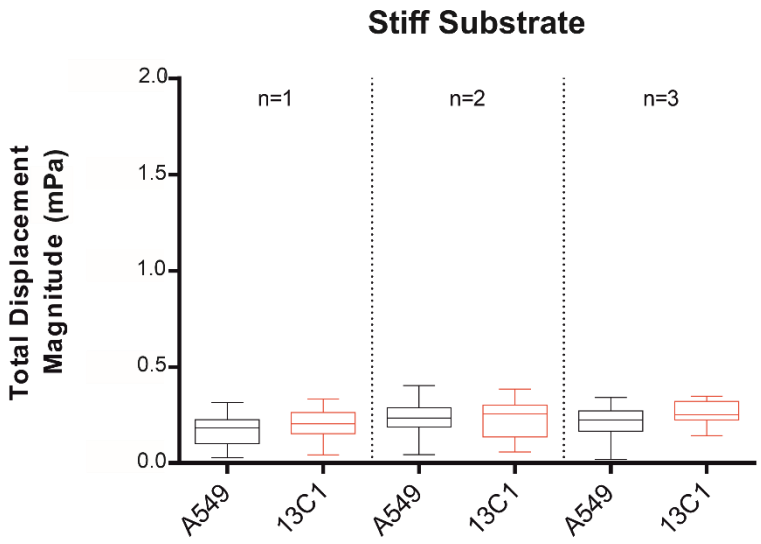

Figure 4.3.11. Traction force microscopy of cells on a stiff polyacrylamide substrate. A549 and 13C1 cells were seeded onto microbead-containing 21 % polyacrylamide gels, functionalised with cross-linked rat-tail collagen I. Cells were incubated for 24 hours and gels were imaged before and after cell removal to measure microbead displacement (Total Displacement Magnitude). Each pair of results represents a set of independent experiments (20 cells per condition per experiment), with box and whisker plots representing the range, interquartile range and mean of A549 (black) and 13C1 (cells).

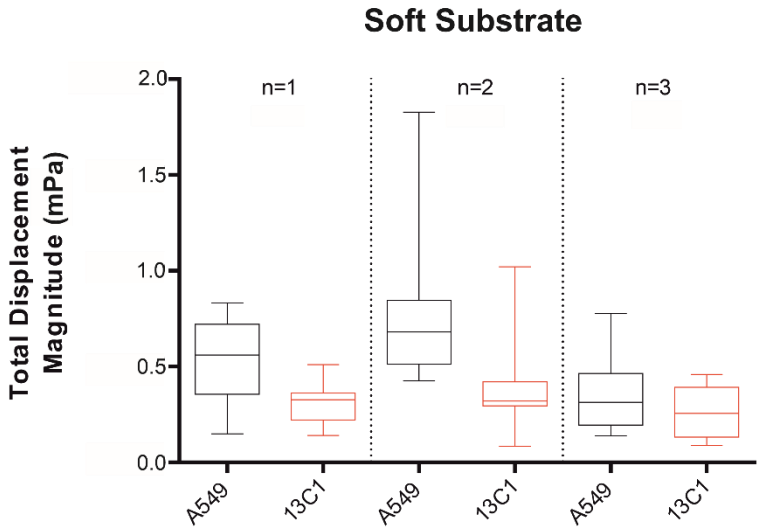

Figure 4.3.12. Traction force microscopy of cells on a soft polyacrylamide substrate. A549 and 13C1 cells were seeded onto 5 % microbead-containing polyacrylamide gels, functionalised with cross-linked rat-tail collagen I. Cells were incubated for 24 hours and gels were imaged before and after cell removal to measure microbead displacement (Total Displacement Magnitude). Each pair of results represents a set of independent experiments (20 cells per condition per experiment), with box and whisker plots representing the range, interquartile range and mean of A549 (black) and 13C1 (cells).

4.3.9 LMα5 mutant displayed reduced cell surface LM-binding integrin expression

The reduced attachment rate and attachment strength of the 13C1 mutant cells implied a defect in cell-to-matrix attachment. To investigate whether this was associated with changes in cell surface integrin expression, wildtype A549 and LMα5 mutant 13C1 cells were cultured for 24 hours and then processed for flow cytometry (Figure 4.3.13). Analysis revealed a reduced expression of α3, α6 and β1 integrin on the cell surface of the mutant cells, while there was no reduction in expression of αv and β4 integrin. Integrin α3, α6 and β1 are well-established as required for rapid attachment of A549s to LM (246), whereas integrin β4 has been implicated in more long-term attachment and

hemidesmosome formation (22), and integrin αv's preferred ligands in these cells are vitronectin and fibronectin (247). These findings suggest that the reduced attachment could be due to reduced LM-binding integrin surface level expression.

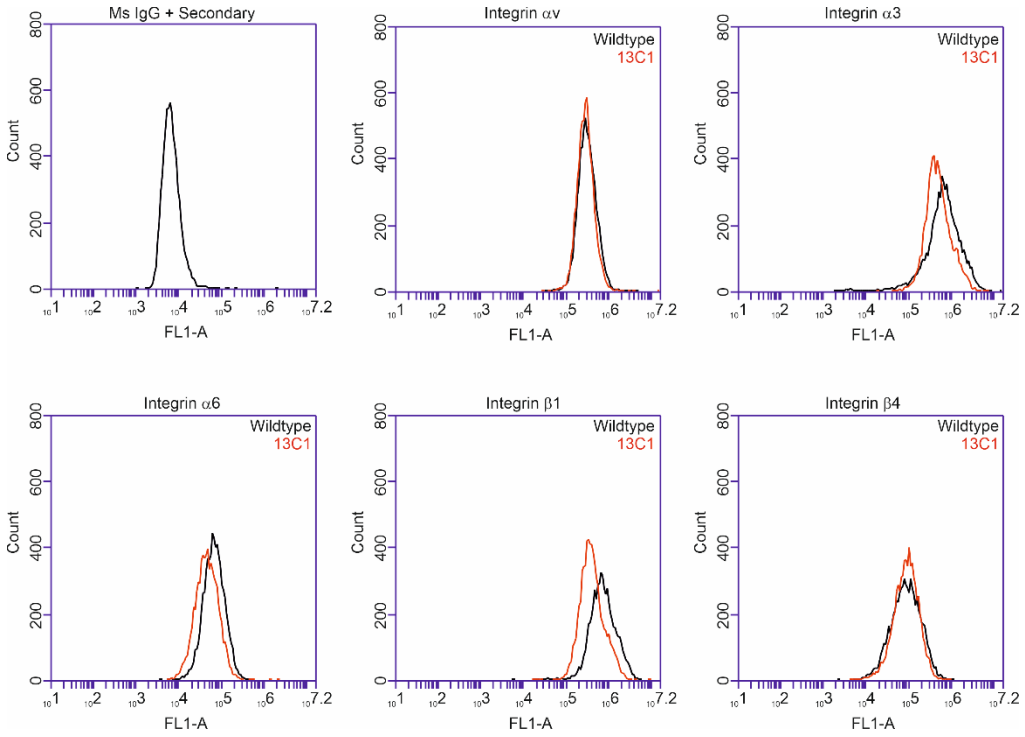

Figure 4.3.13. LMα5 mutant displays reduced cell surface α3, α6 and β1 integrin expression. Wildtype A549 and LMα5 mutant 13C1 cells were cultured for 24 h and then processed for flow cytometry with antibodies against integrin αv, α3, α6, β1 or β4. Mouse IgG with FITC-conjugated secondary antibodies were used as a negative control. FL1-A-count plots. Representative plots of two independent experiments.

4.3.10 LMα5 mutant cells show no difference in paxillin localisation

The combined flow cytometry and adhesion evidence pointed in the direction of an integrin/focal adhesion defect as a result of the LMα5 mutation. To analyse this further I performed a series of indirect immunofluorescence microscopy analyses of established focal adhesion proteins. In each case,

wildtype A549 and LMα5 mutant 13C1 cells were seeded at a low density onto coverslips, incubated for 24 hours then processed with the target antibodies.

Paxillin is a major component in the formation of nascent focal adhesions, and it induces the recruitment of several enzymes and structural molecules that control cell movement and migration (248). Analysis of paxillin distribution (Figure 4.3.14) revealed that there was no difference between in focal contact area of the A549 and 13C1 cells (A549 mean paxillin area = 0.78 μm^2/cell ± 0.26 SD, 13C1 mean paxillin area = 0.77 μm^2/cell ± 0.22 SD, p = 0.88, two-tailed unpaired t-test).

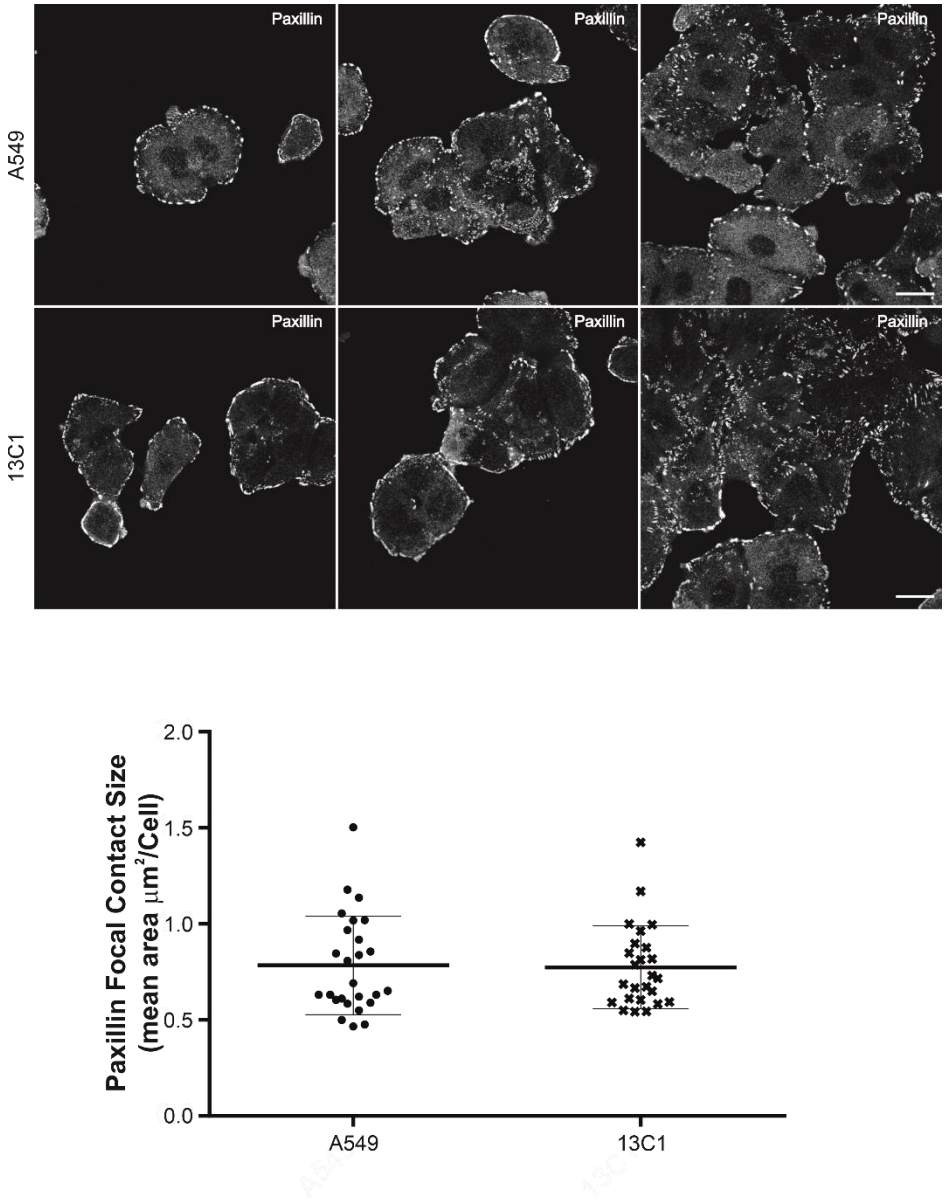

Figure 4.3.14. Paxillin focal contact size does not change as a result of the LMα5 mutation. A549 and 13C1 cells were seeded onto glass coverslips for 24 hours, fixed and processed for indirect immunofluorescence with rabbit polyclonal antibodies raised against paxillin. Image panels are representative image of paxillin staining at a low, medium and high cell density for A549 (top) and 13C1 cells (bottom), with a 20 µm scale bar. Paxillin focal contact size was measured as paxillin area (μm^2) per cell, and each point represents the mean cellular paxillin measurements per image (field of view).

4.3.11 LMα5 mutant cells display a reduced level of active vinculin

Another major focal adhesion scaffold protein is vinculin, which unlike paxillin, changes length upon activation (38). Vinculin is a protein that transmits,

transduces and regulates mechanical force between the cytoskeleton and adhesion receptors (249). Focal adhesion analysis showed that there was a 16 % reduction the average area of vinculin in 13C1 cells compared to A549 cells (Figure 4.3.15, A549 mean vinculin area = 0.49 μm^2/ cell ± 0.10 SD, 13C1 mean vinculin area = 0.41 μm^2/ cell ± 0.08 SD, p = 0.004 two-tailed unpaired t-test). With vinculin length directly relating to activation of the vinculin, these data could suggest that more activated vinculin is being recruited to the cell-to-cell junctions and cell-adhesion receptor junctions in wildtype cells than LMα5 mutant cells.

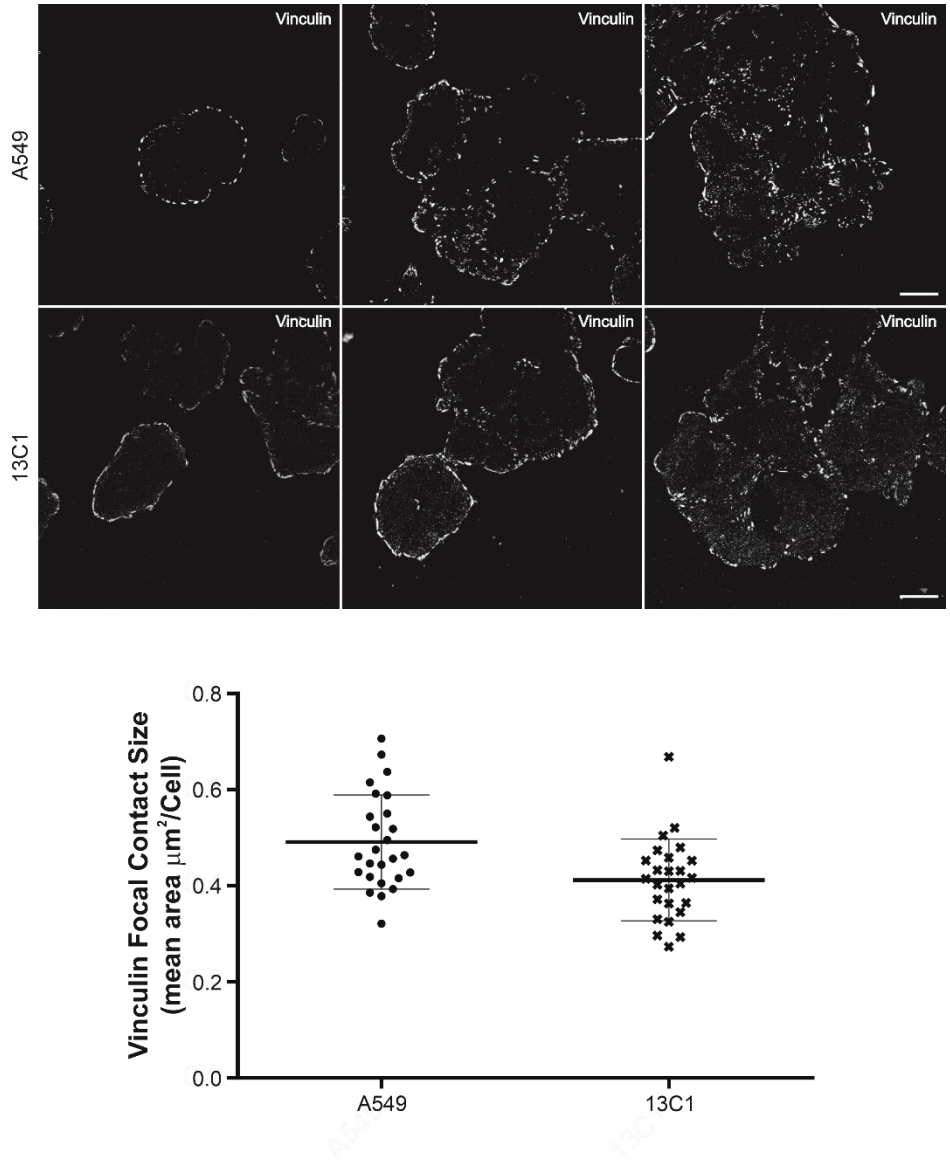

Figure 4.3.15. Vinculin focal contact size is reduced in mutant cells. A549 and 13C1 cells were seeded onto glass coverslips for 24 hours, fixed and processed for indirect immunofluorescence with mouse monoclonal antibodies raised against vinculin. Image panels are representative image of vinculin staining at a low, medium and high cell density for A549 (top) and 13C1 cells (bottom), with a 20 μm scale bar. Vinculin focal contact size was measured as vinculin area (μm^2) per cell, and each point represents the mean cellular vinculin measurements per image (field of view).

4.3.12 LMα5 mutant cells display reduced zyxin recruitment in focal adhesions

I next assessed how the mutation affected coupling of the extracellular matrix to the actin cytoskeleton. Zyxin is a focal adhesion protein that is recruited later in assembling focal adhesions than paxillin and vinculin, and also can form clusters at actin-polymerisation complexes, which are distributed along F-actin fibres (194, 250). Zyxin activity, unlike that of paxillin and vinculin, is directly related to tensional forces in the extracellular matrix, with lower tensions resulting in zyxin unbinding from focal adhesion complexes (251).

Focal adhesion analysis showed that there was a 16 % reduction in the mean area of zyxin in of 13C1 cells compared to A549 cells (Figure 4.3.16. A549 mean zyxin area = 0.63 μm^2/ cell ± 0.26 SD, 13C1 mean zyxin area = 0.46 μm^2/ cell ± 0.11 SD, p = 0.024, two-tailed unpaired t-test). It was also noted that zyxin distribution in A549 cells was more akin to mature focal adhesions with zyxin distribution perpendicular to the cell membrane in A549 cells, whereas in the 13C1 cells, zyxin was distributed more along the cell membrane (Figure 4.3.16). These data when taken with the vinculin and traction force microscopy data imply that the LMα5 mutant cells are taking longer to form mature focal adhesions.

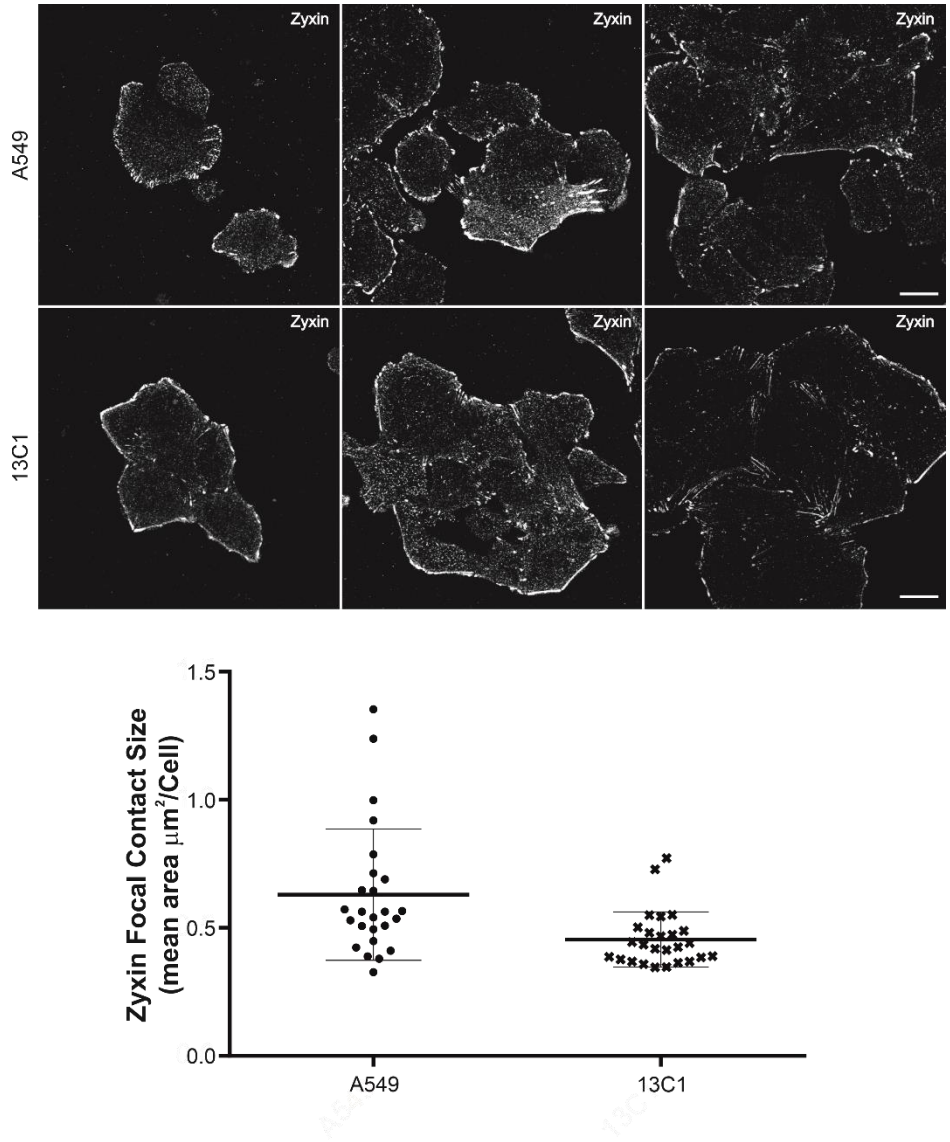

Figure 4.3.16. Zyxin focal contact intensity is reduced in mutant cells. A549 and 13C1 cells were seeded onto glass coverslips for 24 hours, fixed and processed for indirect immunofluorescence with mouse monoclonal antibodies raised against zyxin. Image panels are representative image of zyxin staining at a low, medium and high cell density for A549 (top) and 13C1 cells (bottom), with a 20 µm scale bar. Zyxin focal contact size was measured as zyxin area (μm^2) per cell, and each point represents mean cellular zyxin measurements per image (field of view).

4.3.13 F-actin abundance is unaffected by the LMα5 mutant

As zyxin is known to cluster at actin-polymerisation complexes that are periodically distributed along F-actin, I next investigated whether F-actin was influenced in response to the changes to vinculin and zyxin. One common way

to assess F-actin distribution is through the toxic cyclic peptide phalloidin. Phalloidin binds to and stabilises F-actin fibres and prevents depolymerisation of the actin fibres, due to its high specificity and tight binding to filamentous actin (252). Wildtype A549 and 13C1 cells were processed with fluorophore conjugated phalloidin (Figure 4.3.17). There was no difference between the F-actin intensity in wildtype and LMα5 mutant cells (A549 mean F-actin intensity = 88 AU ± 67 SD, 13C1 mean F-actin = 99 AU ± 65 SD, $p = 0.56$, two-tailed unpaired t-test). However, it was noted that at lower cellular densities (left and centre panels, Figure 4.3.17), A549 cells had a more intense F-actin clustering at and just within the cell membrane, where zyxin binding is likely to cluster (251). This finding may suggest weaker focal adhesion maturity and therefore less tension.

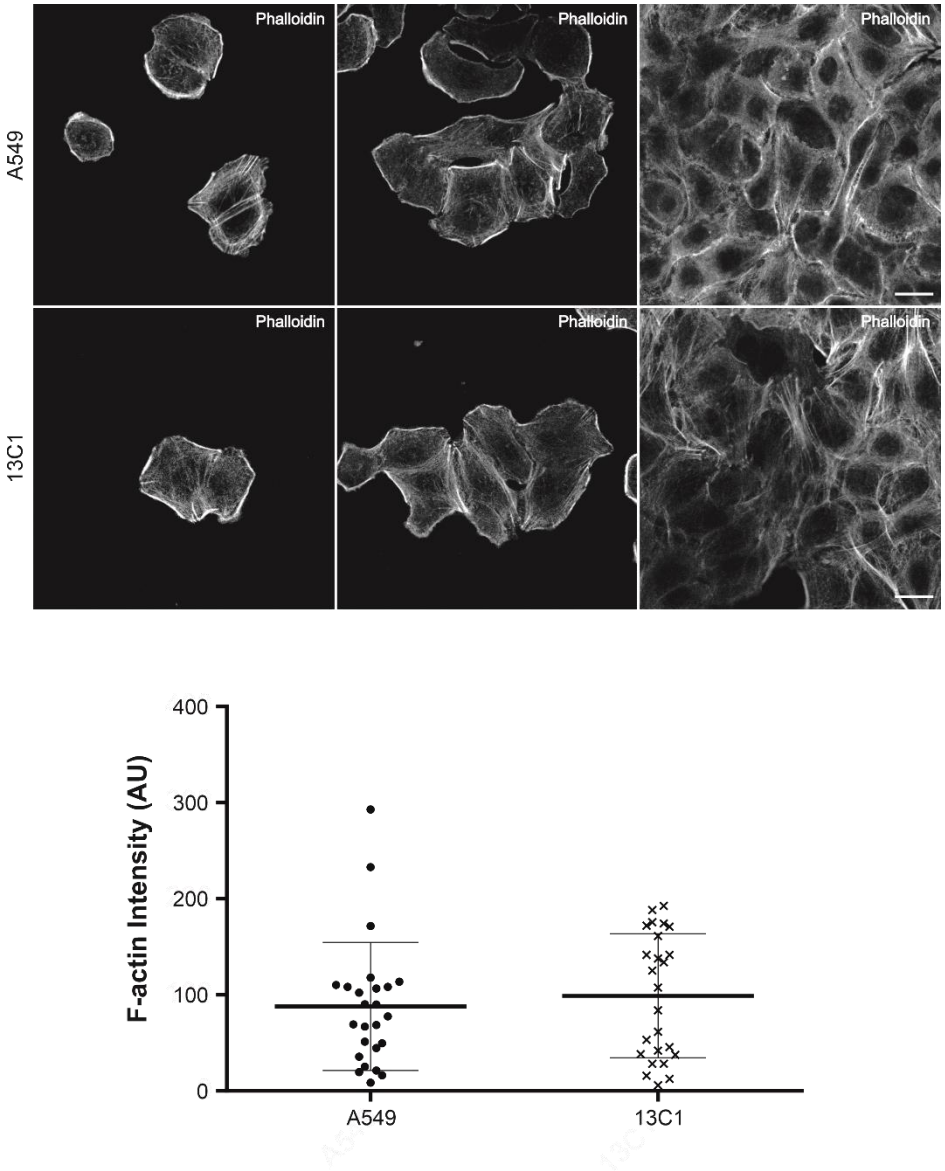

Figure 4.3.17. F-actin intensity in mutant cells remains unchanged. A549 and 13C1 cells were seeded onto glass coverslips for 24 hours, fixed and processed for indirect immunofluorescence with 488-conjugated phalloidin. Image panels are representative image of phalloidin staining at a low, medium and high cell density for A549 (top) and 13C1 cells (bottom), with a 20 µm scale bar. Phalloidin was measured as F-actin intensity (AU) per cell, and each point represents mean cellular F-actin intensity measurements image (field of view).

4.3.14 LMα5 mutant cells display an increase in nuclear YAP/TAZ

Thus far, a picture was developing where the LMα5 mutant cells displayed a decreased ability to respond to their extracellular matrix, but questions still remained as to what implications this had upon the signalling pathways that

allow cells to respond to their environment. An answer could lie within the YAP/TAZ-Hippo signalling cascade. Yes-associate protein 1 (YAP) and transcriptional co-activator with PDZ-binding motif protein (TAZ) are transcriptional co-activators involved in cell proliferation and suppressing apoptotic genes (253, 254). YAP/TAZ are the primary sensors of the cell's physical nature, and respond to the mechanical signals surrounding the extracellular matrix (255). YAP/TAZ lie at the centre of a complex signalling nexus known to control cell behaviour in response to shape, location and environment, by acting as the effectors for the Hippo signalling cascade (255).

Wildtype A549 and 13C1 cells were processed for indirect immunofluorescence with antibodies against YAP and TAZ (Figure 4.3.18). Localisation analysis revealed that there was a 27 % increase in nuclear YAP intensity and 14 % increase in nuclear TAZ intensity in the 13C1 cells relative to the wildtype A549 cells (YAP: A549 mean nuclear localisation = 20.0 % ± 4.3 SD, 13C1 mean nuclear localisation = 25.4 % ± 4.2 SD, $p < 0.001$; TAZ: p = A549 mean nuclear localisation = 33.3 % ± 4.9 SD, 13C1 mean localisation = 37.8 % ± 6.3 SD, $p = 0.017$, two-tailed unpaired t-test). These data indicate that the LMα5 mutant cells have an increased nuclear localisation of YAP/TAZ, which implies reduced Hippo signalling (255).

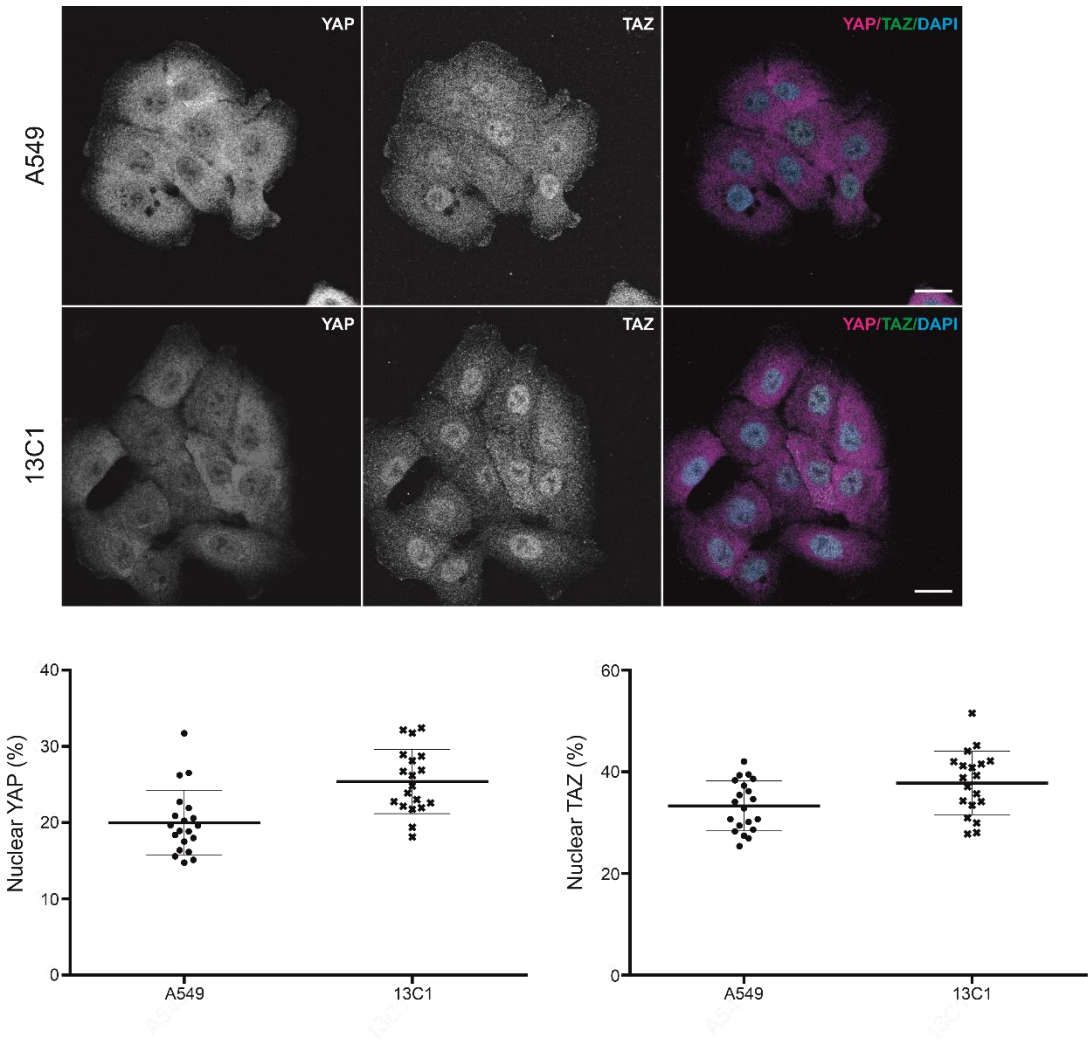

Figure 4.3.18. Nuclear YAP and TAZ localisation are increased in 13C1 cells. A549 and 13C1 cells were seeded onto glass coverslips for 24 hours, fixed and processed for indirect immunofluorescence with mouse monoclonal antibodies raised against TAZ and rabbit polyclonal antibodies raised against YAP. Image panels are representative image of YAP (left) and TAZ (middle) and a channel merge of YAP (magenta) and TAZ (green) with a DAPI co-stain (blue). A549 (top) and 13C1 cells (bottom), with a 20 µm scale bar. YAP and TAZ intensity were measured for the entire cell area, with the staining localised to the nucleus also measured as a percentage. The average nuclear YAP and TAZ measurements per image (field of view) were plotted for analysis.

4.4 Discussion

In this chapter, I have detailed the work undertaken to establish and characterise a new non-polymerizing LM cell line. Using CRISPR-Cas9-HDR genome editing techniques, I was able to successfully introduce a glutamic acid to lysine mutation (E234K) into the genome of A549 cells, giving rise to the clonal 13C1 cell line. After heteroduplex analysis and sequencing data displayed that these LMα5 mutant cells contained a homozygous point mutation, it was then confirmed that the mutant LMα5 was not polymerizing using a polymerisation assay. Phenotypic analysis revealed that the LMα5 mutant cells displayed a reduced proliferation rate, migration processivity, scratch wound closure speed, attachment rate, strength of attachment and reduced force exertion by TFM analysis. At the protein level, the mutant cells had reduced surface integrin level compared to the wildtype cells and a reduction in key focal adhesion proteins at the contact points of the cell. This data collectively would indicate that the mechanotransduction mechanisms of the cell which sense the extracellular environment are in some way compromised. The most likely mechanism of mechanotransduction to be compromised in the LMα5 mutant cells is the LM binding integrins.

There was a reduction in the surface level of three LM-binding integrins in the LMα5 mutant cells; integrin α3, α6 and β1. Integrin α6β1 is the integrin known to have the highest affinity to LM511 of the 24 mammalian integrins (256). Integrin α3β1 not only binds LM511, but is also reported as the most highly expressed integrin in wildtype A549's, as determined by cDNA microarrays and flow cytometry (246, 256). The cellular findings of the newly developed cell model align well with data from previous MDC1a models, where dy/dy

mouse models with low levels of LMα2 expression exhibit reduced levels of integrin α7β1 (257), and the dy2J/dy2J mouse model with αLN domain mutations also shows a reduced expression integrin α7β1 (257-259). The findings here might suggest that the reduction in surface level integrins is a result of the reduced level of LM511 in the ECM of mutant cells, and therefore a reduction in engaged cell surface receptors for LM511.

The importance of the integrins to the LMα5 mutant cell phenotype cannot be understated. Although, it was LMα5 that the mutation targeted, this extracellular protein would be useless to a cell if there were no ways for the cell to sense it. Here the direct LMα5 mutation could be considered as an indirect mechanism to inhibit / reduce to integrin activity. Integrin β1 silencing in A549 cells highlighted the importance of integrin β1 in migration (260). Additionally, integrin β1 has been shown as a driver of proliferation of lung cancer cells (261), so a reduction in integrin β1 in the LMα5 mutant cells may be the cause of the cells reduced proliferation rate. Both integrin β1 heterodimeric partners, α3 and α6 (37), were also reduced in the mutant cells. Integrins act as a cells major adhesion molecule (262, 263), so a reduction in the cells major adhesion molecules would result in a weaker attachment.

The reduced focal adhesion phenotype is most likely a consequence of this reduction in integrin activity. It was initially surprising to see no difference in paxillin distribution in the 13C1 cells, but upon consideration of the mechanism of paxillin activation, this can be explained. Paxillin is typically activated through phosphorylation, and this direct activation is through the integrin associated FAK (focal adhesion kinase) (248), so perhaps localisation studies

were not sufficient to analyse paxillin activation. However, the data from the vinculin and zyxin analysis addressed this point.

Vinculin interacts with paxillin at focal adhesions upon paxillin phosphorylation, through the C-terminal tail of the former (264). Upon vinculin's phosphorylation at Y1065, it converts to its open confirmation (38). This "open" active confirmation is longer than inactive "closed" formation (250), so the decrease in the vinculin staining length may suggest that 13C1 cells have a reduced level of active vinculin. The decrease in active vinculin also indirectly suggests that the LMα5 mutant cells have lower levels of phosphorylated paxillin.

The decrease in active zyxin recruitment to mature focal adhesions in the LMα5 mutant 13C1 cells ties the focal adhesion and TFM data together. Zyxin is recruited much later than paxillin and vinculin to focal adhesions, and is closely associated to a focal adhesion interaction with F-actin (250, 251). Zyxin is also the main focal adhesion protein responsible for transmitting tension-based signals inside the cell (250). The reduction in zyxin in the LMα5 mutant cells indicates two findings; firstly, that these cells are slower in their maturation of focal adhesions, and secondly that the mutant cells have a reduced ability to exert and sense tension on the extracellular matrix substrate. This triangulates what was observed in the TFM, where on softer substrates, the LMα5 mutant cells had a reduced total magnitude displacement. This could have possibly been the case in the stiffer substrates also, with the softer substrate just amplifying any affects observed. The 5 % polyacrylamide gels have a stiffness of around 5 kPa, similar to skin, whereas the 21 % polyacrylamide gels have a stiffness of 85 kPa, closer to tissue culture plastic or glass (265, 266), meaning that the findings from the 5 % polyacrylamide

gels could be considered as the more physiologically relevant for most normal tissue. Indeed, if all the assays were performed on this softer substrate, the other observed phenotypes of the mutant cells may have been even more pronounced.

The YAP/TAZ analysis was a somewhat surprising result, and one more difficult to explain in the context of other results. YAP/TAZ co-localisation to the nucleus is generally accepted as a marker of proliferation upregulation and apoptosis suppression (255). When one considers that the LMα5 mutant cells had a reduced proliferation in the cell cycle analysis, their increase in nuclear YAP/TAZ doesn't make sense at first glance. However YAP/TAZ are part of a very complex signalling array, and besides their role as the effectors of the Hippo pathway, not much else is well understood about their mechanism (255). The YAP/TAZ data here could simply indicate that the Hippo pathway in the LMα5 mutant cells is inactive, which controls cell proliferation and apoptosis through YAP/TAZ inhibition (255). It could indicate that the wildtype A549 cells are better adapted to control their proliferation, through successful inhibition of YAP/TAZ, and that the proliferation defects of the mutant cells are not YAP/TAZ related. It is a complex question that requires a more complex answer. This answer could come through the analysis of signalling pathways known to inhibit cell proliferation, and whether these signalling pathways are upregulated in an attempt to counteract the extra nuclear YAP/TAZ activity.

Taken together the data in this chapter strongly indicate a clear pattern. The E234K mutation to the LN domain of LMα5 results in a lack of incorporation of LM511 into the mutant cell ECM. This in turn leads to a reduction in the cell surface levels of LM-binding integrins, which could consequently cause a

reduction in active focal adhesion maturation with downstream signalling consequences. The extent of these signalling consequences is addressed in Chapter 5.

It is important to mention that this model is not without flaws. During the establishment of the LMα5 mutant cell line, I was only successful in making one homozygous mutant from >80 different independent single cell populations. The low genome editing success was to be expected, as I used purified Cas9 protein to reduce the half-life of Cas9 in the cells, and therefore reduce off-target effects. However, this low editing efficiency means we cannot be confident whether the effects observed are solely down to the LMα5 mutation, or whether there are additional effects from the cloning process. Off-target effects are likely to be minimised or negligible here, as gRNA sequences were screened for potential off-target loci, the majority of which were non-coding regions (Supplemental Table 1).

One thing that isn't clear from these data alone is whether the effects observed are all due to the matrix-level changes or whether there are any direct cell-level changes that are independent of the matrix. In Chapter 5, I address these questions through analysis of the mutant ECM, and how different cells react in response to the mutant matrix.

Chapter 5: Results and Discussion 2: Analyses of the laminin α5 mutant extracellular matrix

5.1 Introduction

LMα5 LN-domain mutant A549 cells displayed phenotypes of reduced migration speed, proliferation, strength of attachment, surface integrin expression and focal adhesion maturation. However, from those data alone it is not possible to identify whether these effects were due to cell-level changes or a reflection of the mutant extracellular matrix as was hypothesised. Furthermore, the effect of the LMα5 mutation upon the rest of the extracellular matrix was not yet known.

In this chapter, my aim was to analyse the effect the LM α5 LN domain mutation upon other components that make up extracellular matrices and to assess the effects the mutant-cell derived matrix had upon other cells, thereby determining the matrix-specific response.

5.2 Protein-level analysis

5.2.1 Scanning electron microscopy revealed an increase in disorder of the LM and collagen network of LMα5 mutant cells

Immunoblotting analysis of the ECM extracts (Chapter 4.3.1) identified that LMα5 was not being incorporated into the mutant matrix efficiently. To identify gross effects of the mutation on the overall organisation of the remaining LM and collagen networks in the ECM, scanning electron microscopy was performed. A549 and 13C1 cells were seeded onto wafer chips, incubated for 120 hours, then cells removed using ammonium hydroxide. The cell-derived

matrices were then treated with either 4 M guanidine hydrochloride to remove LMs and other proteoglycan material, leaving behind the collagens (267), or the matrixes were treated collagenase A to remove collagens to leave the LMs and proteoglycans (267).

In the collagenase treated ECMs, the remaining LM matrices deposited by wildtype A549 cells contained large, regularly spaced gaps, while in comparison the LMα5 mutant 13C1 cell-derived matrix had smaller, more random gaps in (Figure 5.2.1).

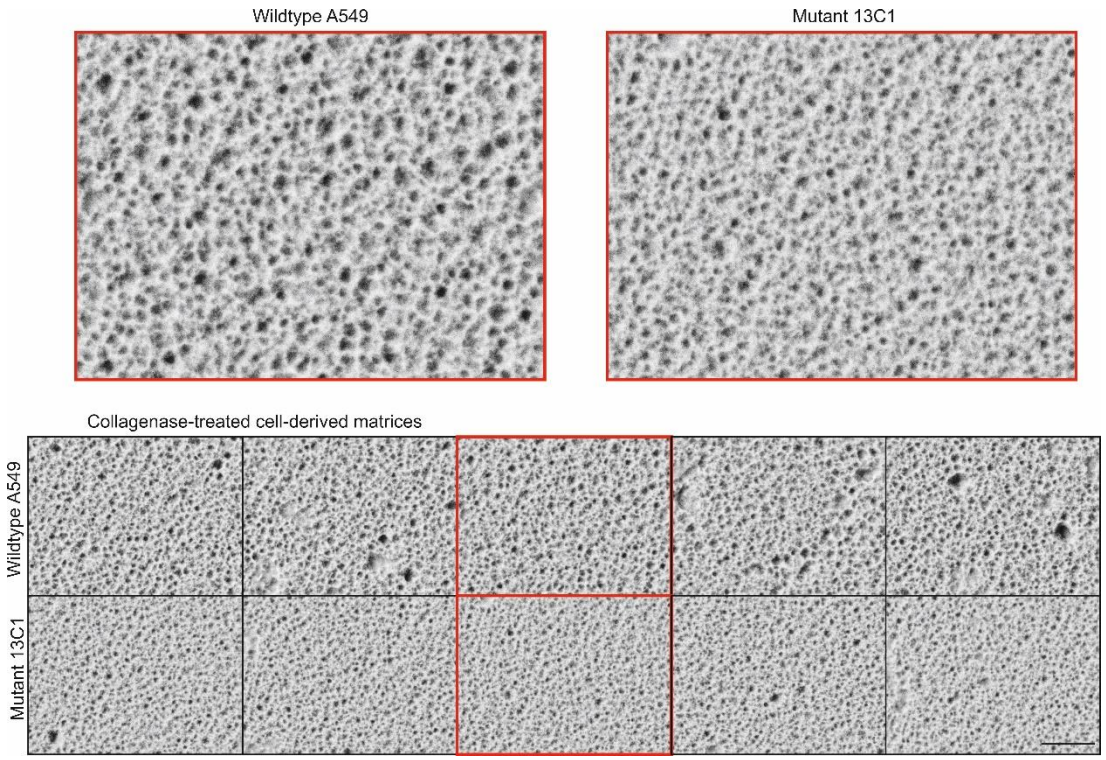

Figure 5.2.1. Mutant LMα5 matrices contain more disorder than the wildtype LM matrices. A549 and 13C1 cells were seeded at a density of 2.0 x 10^4 onto pre-treated wafer chips, incubated for 120 hours. Cells were removed using 2 % ammonium hydroxide solution, and remaining cell-derived matrices were treated with 0.1 mg/mL Collagenase A with 1 µL/mL proteinase inhibitor cocktails. Treated matrices were fixed and processed for SEM. Scale bar = 500 nm. Images with red border are enlarged above.

For the matrices treated with guanidine hydrochloride, the wildtype matrices produced an approximately uniform network of protein (Figure 5.2.2), whereas the mutant matrices had more and larger gaps present throughout (Figure 5.2.2).

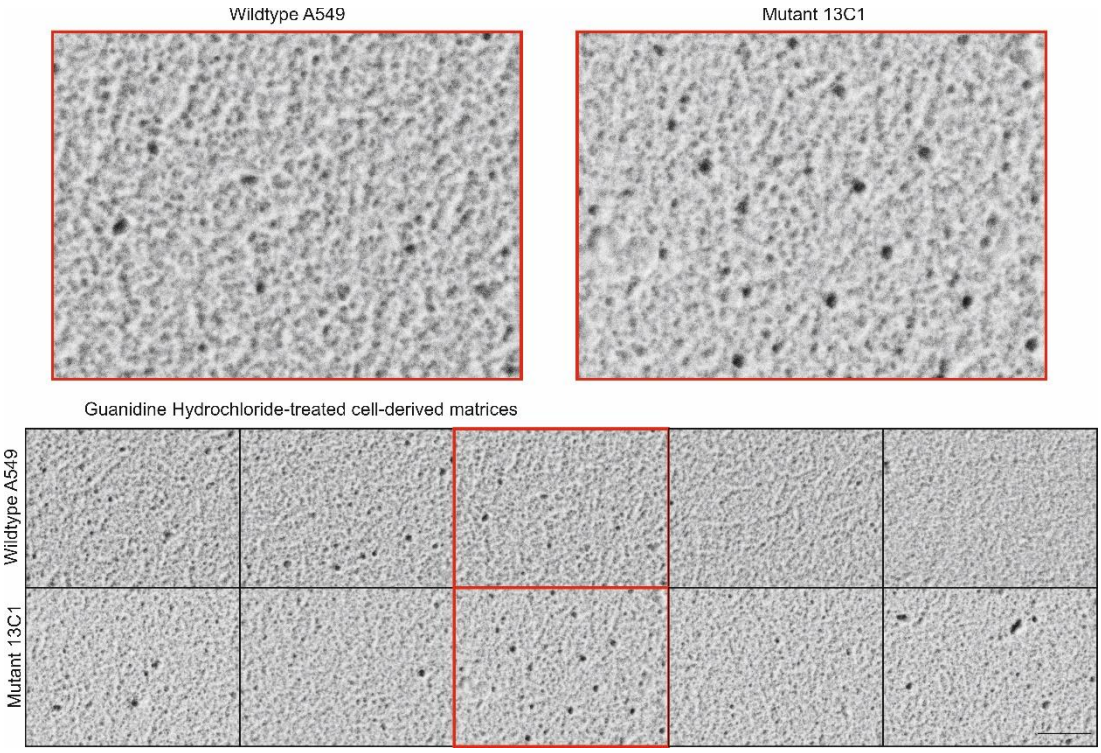

Figure 5.2.2. Mutant matrices contain more gaps in their collagen network than wildtype matrices. A549 and 13C1 cells were seeded at a density of 2.0 x 10^4 onto pre-treated wafer chips, incubated for 120 hours. Cells were removed using 2 % ammonium hydroxide solution, and remaining cell-derived matrices were treated with 4M guanidine hydrochloride overnight. Treated matrices were fixed and processed for SEM. Scale bar = 500 nm. Images with red border are enlarged above.

5.2.2 Mass Spectrometry shows differences between the ECM composition of wildtype and LMα5 cells

A549 and LMα5 mutant 13C1 cells were seeded in low FBS (1 %) and cellular material removed by ammonium hydroxide after 24 hours. The remaining ECM was lysed and processed for LC-MS.

Total Peptide Analysis

Protein hits were grouped into ten categories for analysis. Of the 440 proteins identified by LC-MS, there were 155 plasma membrane proteins (36 % of unique proteins identified, this does not reflect relative abundance), 27 integrin or integrin-associated proteins (6.1 %), 45 ECM proteins (10 %), 6 LMs (1.4 %), 11 collagen or collagen binding proteins (2.5 %), 34 growth factors, binders and receptors (7.7 %), 71 secretory proteins (16 %), 39 cell junction proteins (8.9 %), 36 actin and actin binding proteins (8.2 %), and 13 cytoskeletal proteins (3.0 %) (Figure 5.2.3).

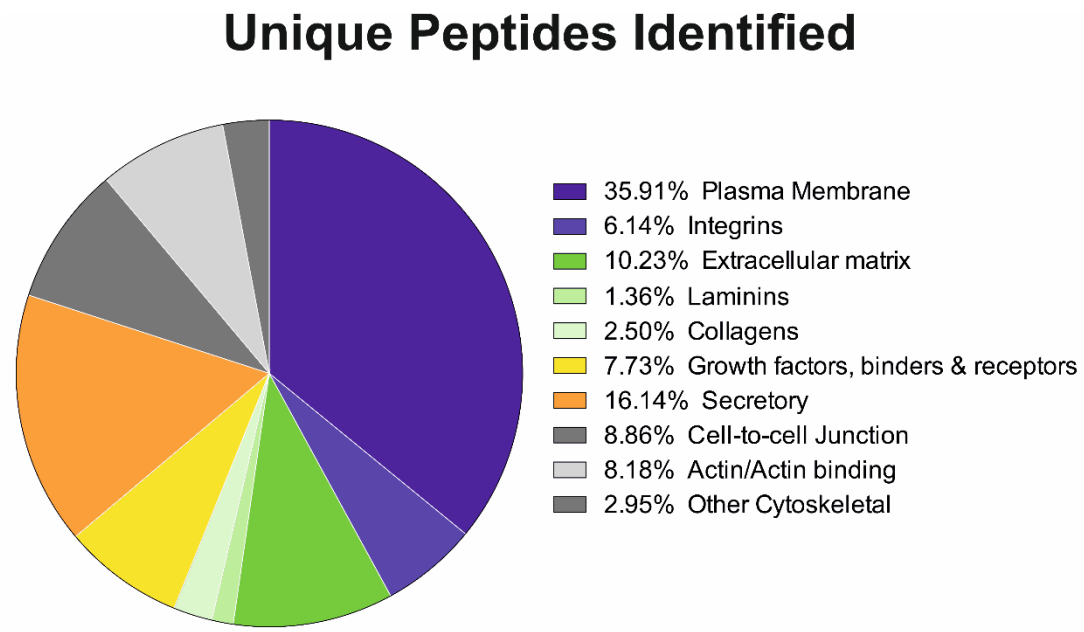

Figure 5.2.3. All peptides detected by LC-MS were sorted into 1 of 10 groups based on similarity. Pie chart representing the distribution of unique proteins detected by LC-MS.

Next, proteins were sorted by total abundance (peptide intensity) in each cell derived matrices (Figure 5.2.4). By abundance of the proteins observed in the matrices preparations (Figure 5.2.4a, b), plasma membrane proteins comprised more than a quarter of the total mass in the wildtype and mutant samples (27 % and 23 % respectively), likely predominantly matrix-bound

membrane left behind by the ammonium hydroxide treatment of the cells (268). Extracellular matrix proteins, laminins and collagens represented nearly a quarter of the total mass in the wildtype matrices (25 % total), with a slightly lower proportion in the mutant matrices (23 %). Growth factors and their receptors comprised a large proportion of the total mass of the wildtype matrices (17 %), but it was this subgroup that was the most abundant in the mutant matrices (23 %). Integrins, secretory proteins and actin/actin binding proteins also combined to 26 % of the total sample mass of wildtype matrices (7 %, 9 % and 10 %, respectively). However, in the mutant matrices, integrins, secretory proteins and actin/actin binding proteins comprised 31 % of the total mass observed (5 %, 11 % and 15 % respectively). The “Other cytoskeletal” subgroup was negligible in both samples (A549 = 0.26 %, 13C1 = 0.27 %).

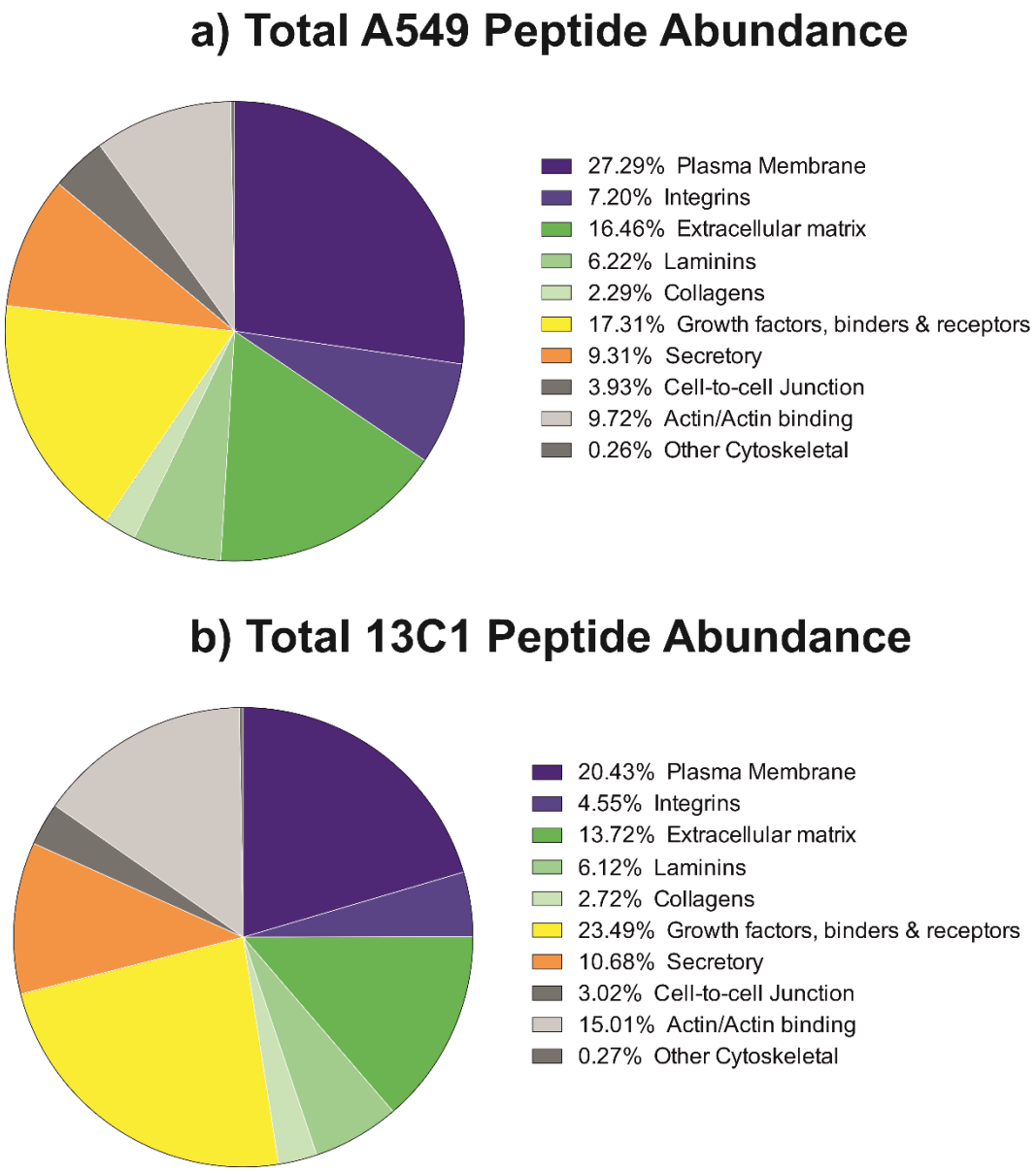

Figure 5.2.4. Peptides abundance by peptide intensity in the A549 and 13C1 cell-derived matrix. Pie chart representing the total abundance of 10 different groups in the wildtype matrices, as detected by LC-MS analysis. 440 peptides total.

144 peptides were increased in the LMα5 mutant matrices

144 peptides were increased in the LMα5 mutant 13C1 samples compared with A549 (Figure 5.2.5). Of the increased proteins in the mutant samples, 35 were secretory proteins, 20 extracellular matrix proteins, 8 collagens, 2 LM's and 5 integrin related proteins. Additionally, 14 of the detected growth factors and their binding proteins were increased in the mutant matrices.

Within the 20 most increased proteins in the mutant matrices, of particular note are one LM chain (*LAMB*3: 2.3-fold increase, p = 0.02) and three collagen chains COL12A1 (4.4-fold, p = 0.02), COL4A2 (4-fold, p < 0.01) and COL4A1 (3.2-fold, p = 0.07). Olfactomedin-like protein 3 (OLFML3), an extracellular matrix scaffold protein, had the highest fold increase relative to the wildtype sample (7.5-fold increase, p < 0.01, Table 5.1).

Other proteins of interest in this group, were the growth factor related proteins LTBP2 (2.1-fold, p = 0.002), ILF2 (2.0-fold, p =0.002) and TGFB1 (1.9-fold, p = 0.002), all of which play important roles in cellular processes including proliferation and cell response to the matrix (65, 99, 269, 270).

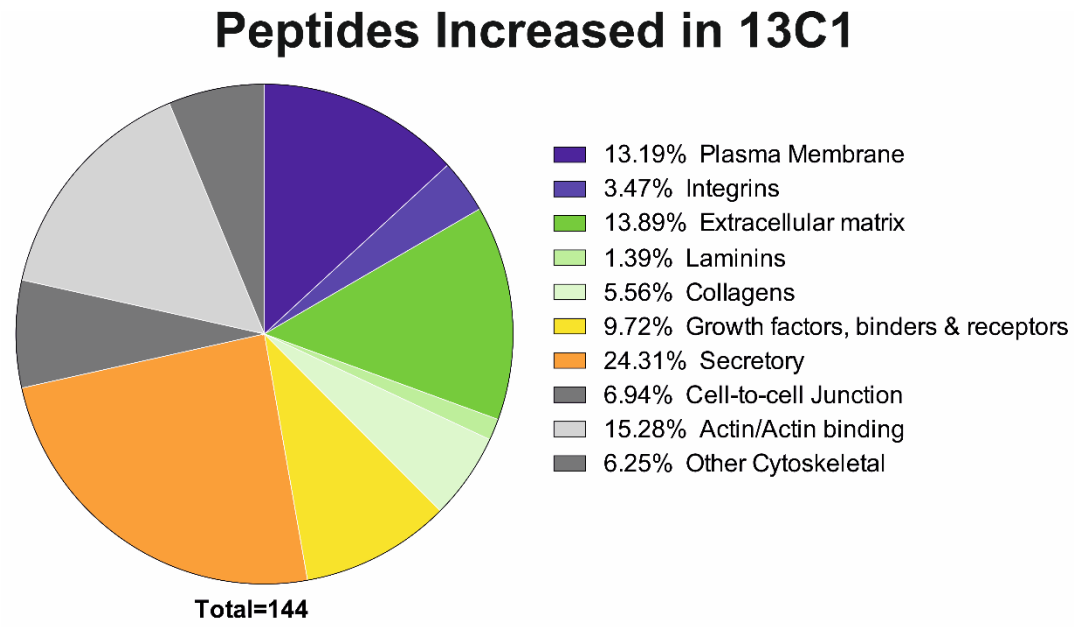

Figure 5.2.5. Peptides increased in the 13C1 cells. Pie chart representing the 144 peptides that were increased in the mutant matrices, as detected by LC-MS analysis.

Table 5.1: Proteins with the highest fold increase in mutant matrices

Group	Protein (Gene code)	Mean Fold Increase	*p* value
Extracellular matrix	OLFML3	7.5	<0.001*
Collagens	COL12A1	4.4	0.019*
Collagens	COL4A2	4.0	<0.001*
Cell-to-cell Junctions	DSG1	3.6	0.163
Secretory/ Integrin binding	EDIL3	3.4	<0.001*
Actin/Actin Binding	FLNB	3.3	<0.001*
Collagens	COL4A1	3.2	0.070
Actin/Actin Binding	MYO1F	2.8	<0.001*
Cell-to-cell Junctions	CDH6	2.6	0.009*
Plasma Membrane	HSP90AB1	2.6	0.257
Secretory	PAM	2.3	0.045*
Actin/Actin Binding	RDX	2.3	0.035*
Actin/Actin Binding	KIF23	2.3	0.020*
Laminins	*LAMB*3	2.3	0.024*
Growth Factors/Binders	LTBP2	2.1	0.002*
Growth Factors/Binders	ILF2	2.0	0.002*
Secretory	SLIT3	1.9	0.002*
Actin/Actin Binding	MYH9	1.9	<0.001*
Actin/Actin Binding	EHD2	1.9	0.002*
Growth Factors/Binders	TGFB1	1.9	0.002*

* = p-value <0.05, two-tailed ANOVA

296 peptides were decreased in the LMα5 mutant matrices

296 proteins were decreased in the LMα5 mutant ECM (Figure 5.2.6), of these 140 were plasma membrane associated proteins, 36 secretory proteins, 25 extracellular matrix proteins, 3 collagens, 4 laminins and 22 integrin/integrin

associated proteins. In addition to this, 20 growth factors and growth factor binding proteins were decreased in the mutant samples.

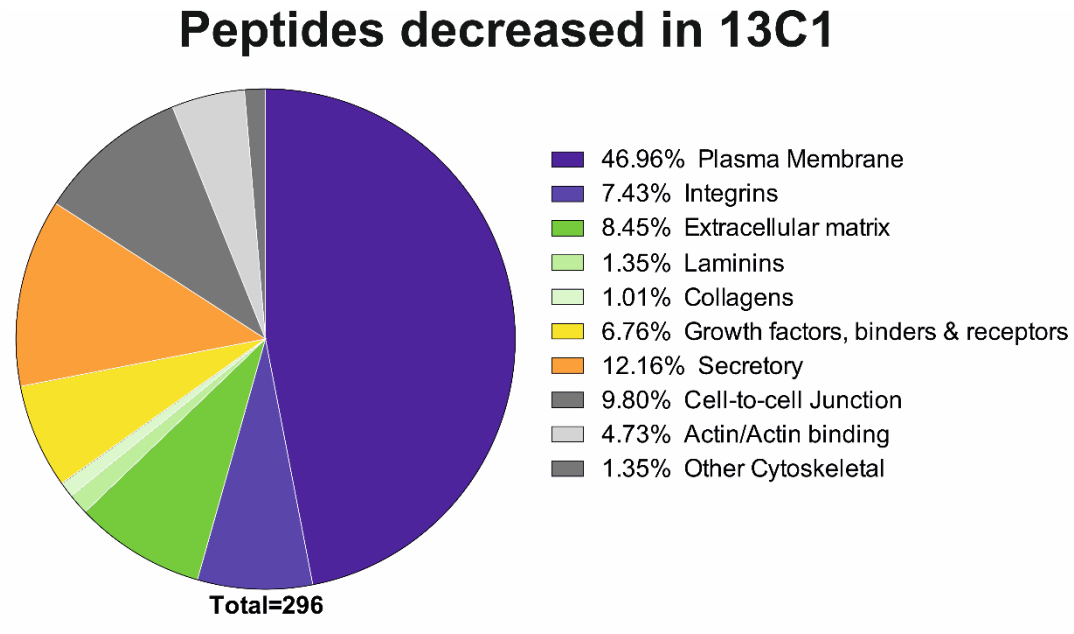

Figure 5.2.6. Peptides decreased in the 13C1 cells. Pie chart representing the 296 peptides that were decreased in the mutant matrices, as detected by LC-MS analysis.

STEAP1B, a cell-to-cell junction protein, showed the largest fold reduction in the mutant matrices (18-fold reduction, $p = 0.083$) (Table 5.2). The second most decreased protein, HHIPL2 (16-fold reduction, $p < 0.001$), is a secreted protein known to interact with heparan sulfates in the extracellular matrix (271, 272). COL4A6, one of the six subunits that make up type IV collagen, showed the third largest fold reduction (14-fold reduction, $p < 0.001$). Other proteins of note that feature in the 20 most decreased proteins included STAM (IL-2 receptor, 7.7-fold reduction, $p = 0.339$), FAS (TNF signalling receptor, 5.8-fold reduction, $p < 0.001$), FGA (fibrinogen, 4-fold reduction, $p < 0.001$), MATN2 (ECM assembly protein, 3.8-fold reduction, $p < 0.001$) and CDH17 (ECM binding protein, 3.7-fold reduction, $p < 0.001$).

Table 5.2. Proteins with the highest fold decrease in mutant matrices.

Group	Protein (Gene code)	Fold decrease	*p* value
Cell-to-cell Junction	STEAP1B	18	0.083
Secretory	HHIPL2	16	<0.001*
Collagens	COL4A6	14	<0.001*
Growth Factor/Binding	STAM	7.7	0.339
Secretory	NTS	7.6	<0.001*
Plasma Membrane	ABCG2	7.1	<0.001*
Growth Factor/Binding	FAS	5.8	<0.001*
Plasma Membrane	SLC6A6	4.7	<0.001*
Plasma Membrane	CEACAM6	4.6	<0.001*
Plasma Membrane	LRRC8D	4.6	<0.001*
Plasma Membrane	SLC12A2	4.1	<0.001*
Extracellular Matrix	FGA	4.0	<0.001*
Plasma Membrane	NT5E	4.0	<0.001*
Plasma Membrane	PODXL	3.9	0.042*
Extracellular Matrix	MATN2	3.8	<0.001*
Plasma Membrane	PLPP2	3.8	0.001*
Extracellular Matrix	CDH17	3.7	<0.001*
Plasma Membrane	GPRC5A	3.5	<0.001*
Actin/Actin Binding	SNTB2	3.4	<0.001*
Plasma Membrane	CALM1	3.4	<0.001*

* = p-value <0.05, two-tailed ANOVA

Laminins were decreased in the mutant matrices

There were five LM chains identified by LC-MS: LMα5, LMβ1, LMβ3, LMγ1 and LMγ2 (Figure 5.2.7). Netrin-4 was also included in this group of proteins due to the presence of an LN domain in netrin (1, 273). Of all LM chains, LMα5 was the most abundant in both the wildtype and the mutant matrices, despite a 1.2-fold reduction in the mutant matrices (A549 matrix mean = 4.5 x 10^8,

13C1 matrix mean = 3.8 x 10^8, p =0.056). The next most abundant in both matrices was LMβ1, with levels similar between the two matrices (A549 matrix mean = 2.1 x 10^8, 13C1 matrix mean = 2.0 x 10^8, p = 0.77). LM γ1 abundance was also similar in both wildtype and mutant matrices (A549 matrix mean = 1.77 x 10^8, 13C1 matrix mean = 1.73 x 10^8, p = 0.81). There was a 1.17-fold increase in netrin-4 in the mutant matrices, but this increase did not reach the statistical significance threshold (A549 matrix mean = 2.2 x 10^7, 13C1 matrix mean = 2.6 x 10^7, p = 0.38). LMβ3 and LMγ2 were detected at much lower levels than LM511, and no LMα3 was detected by this analysis. This suggests that although the A549 cells were shown to have mRNA for the chains comprising LM332 at low levels, this mRNA was not translated to the LM332 protein or none of this protein was present at this timepoint in the ECM.

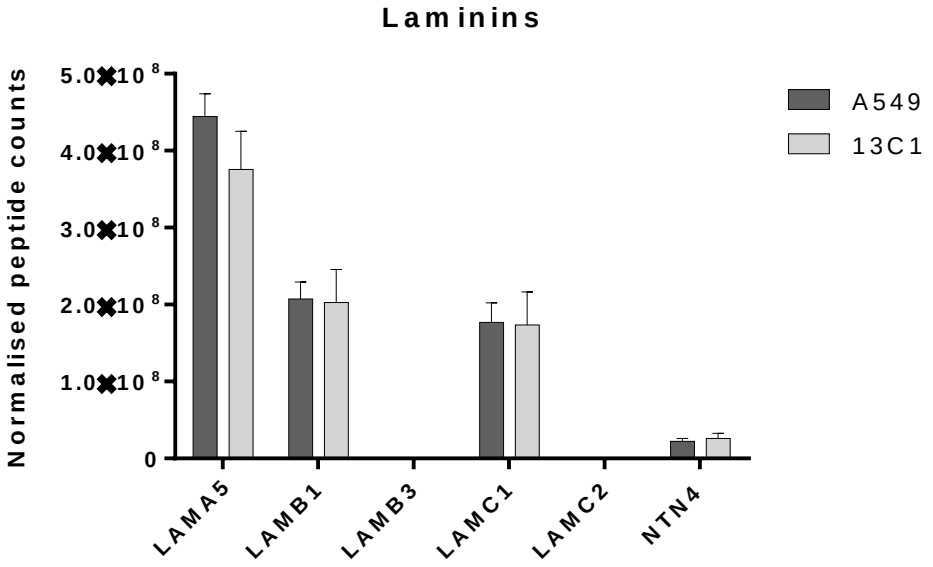

Figure 5.2.7. Most LMs show a reduced abundance in the mutant matrices. Proteins detected in the LC-MS analysis were grouped based on similarity and groups were analysed individually. Darker grey columns represent wildtype A549 matrices, with lighter grey columns representing the LMα5 mutant 13C1 matrices.

All LM-binding integrins were decreased in the mutant matrices

Of the 8 integrin chains identified by LC-MS, all displayed a large reduction in the LMα5 mutant matrices (Figure 5.2.8). The most abundant of the integrins, the non-LM binding integrin αv, showed the smallest fold reduction in the mutant matrices, with a 1.4-fold reduction relative to the wildtype (A549 matrix mean = 2.2×10^8, 13C1 matrix mean = 1.6×10^8, $p < 0.001$). Integrin β1 showed a 2.24-fold reduction in the mutant matrices (A549 matrix mean = 2.1×10^8, 13C1 matrix mean = 9.2×10^7, $p < 0.001$). Integrin α2 and α3 which also displayed large fold reductions in the mutant matrices of 1.7 and 2.2, respectively, (Integrin α2: A549 mean = 6.2×10^7, 13C1 mean = 3.7×10^7, $p < 0.001$. Integrin α3: A549 mean = 8.4×10^7, 13C1 mean = 3.7×10^7, $p < 0.001$). Integrin β4 and α6 also had large fold reductions in the mutant matrices, with a 1.9- and 2.6-fold reduction respectively (Integrin β4: A549 mean = 4.6×10^7, 13C1 mean = 2.5×10^7, $p < 0.001$. Integrin α6: A549 mean = 4.5×10^7, 13C1 mean = 1.7×10^7, $p < 0.001$) as did integrin α5 (1.5- fold reduction, A549 mean = 4.1×10^6, 13C1 mean = 2.7×10^6, $p = 0.014$) and integrin β5 (1.9-fold reduction, A549 mean = 1.3×10^7, 13C1 mean = 6.7×10^6, $p < 0.001$).

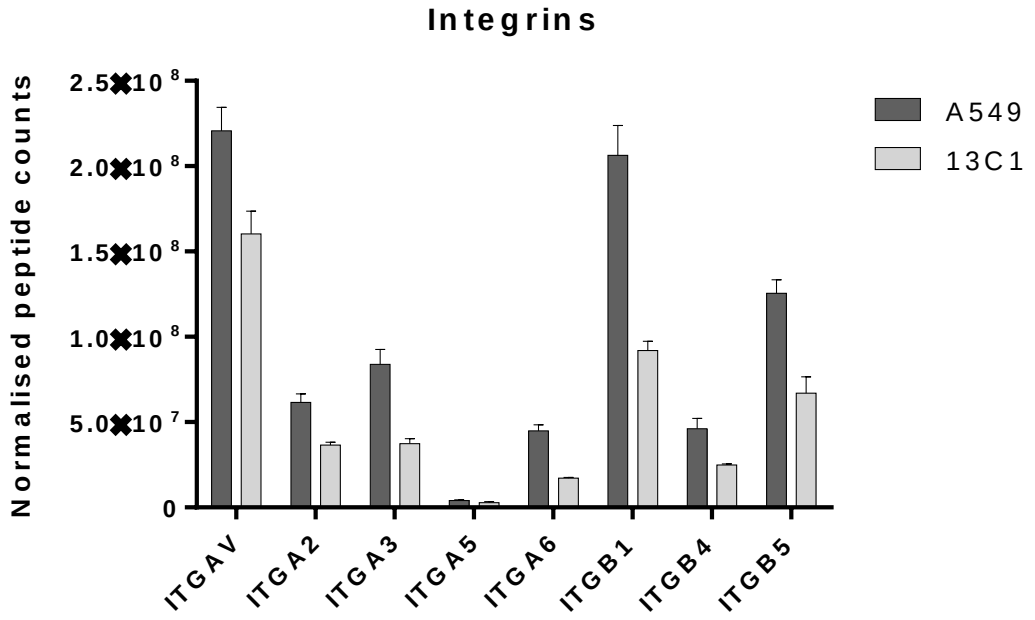

Figure 5.2.8. All integrins showed reduced abundance in the mutant matrices. Proteins detected in the LC-MS analysis were grouped based on similarity and groups were analysed individually. Darker grey columns represent wildtype A549 matrices, with lighter grey columns representing the LMα5 mutant 13C1 matrices.

Most collagens were increased in the mutant matrices

Six collagen chains were identified by LC-MS, and were grouped together for analysis, along with perlecan (HSPG2), an important binder of collagens in the ECM (Figure 5.2.9). Of the six collagens, four were increased in the mutant matrices; COL4A1, COL4A2, COL5A1 and COL12A1. COL4A1 was increased 3.2-fold (A549 mean = 7.8 x 10^4, 13C1 mean = 2.5 x 10^5, p = 0.070) COL4A2 4.0-fold (A549 mean = 2.4 x 10^5, 13C1 mean = 9.4 x 10^5, p < 0.001), COL5A1 1.3-fold (A549 mean = 6.8 x 10^6, 13C1 mean = 9.1 x 10^6, p = 0.136) and COL12A1 4.4-fold (A549 mean = 1.1 x 10^5, 13C1 mean = 4.9 x 10^5, p = 0.019). Two collagens were decreased in the mutant ECM; COL4A6 (14-fold reduction, A549 mean = 8.2 x 10^5, 13C1 mean = 5.9 x 10^4, p < 0.001) and COL6A1 (1.2-fold reduction, A549 mean = 3.0 x 10^6, 13C1 mean = 2.5 x 10^6,

p =0.297). Perlecan was also decreased 2.2-fold in the mutant matrices (A549 mean = 9.8 x 10^6, 13C1 mean = 4.4 x 10^6, p = 0.007).

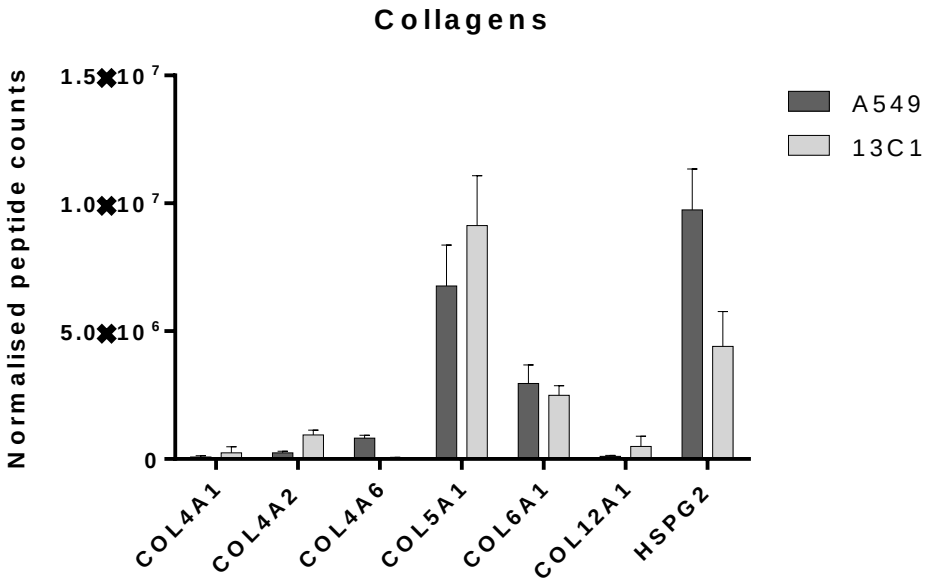

Figure 5.2.9. All collagens except COL4A6 showed an increased abundance in the mutant matrices. Proteins detected in the LC-MS analysis were grouped based on similarity and groups were analysed individually. Darker grey columns represent wildtype A549 matrices, with lighter grey columns representing the LMα5 mutant 13C1 matrices.

Growth Factors, their binders and receptors

Growth factors were also assessed using intragroup comparison (Figure 5.2.10). The most abundant of growth factor detected was insulin growth factor 2 (IGF2) which had similar levels in the wildtype and mutant matrices. Other abundant growth factor-associated proteins included EGFR and IGF binding protein 3, which were both decreased in mutant matrices (1.2- and 1.5-fold reduction respectively), as well as LTBP1 (2.3-fold reduction). TGFβ1 and 2 were both increased in the mutant matrices, with a 1.9- and 1.2-fold increase

in expression respectively, as well at IGFBP2 (1.1-fold increase), LTBP2 (2.1-fold increase), LTBP3 (1.6-fold increase) and LTBP4 (1.2-fold increase).

One of the most striking changes in the growth factor related proteins was that of the TNF receptor and apoptosis regulator FAS, with a 5.8-fold reduction in the mutant matrices. No other signalling protein had a fold change above 2.5 in reduction or increase.

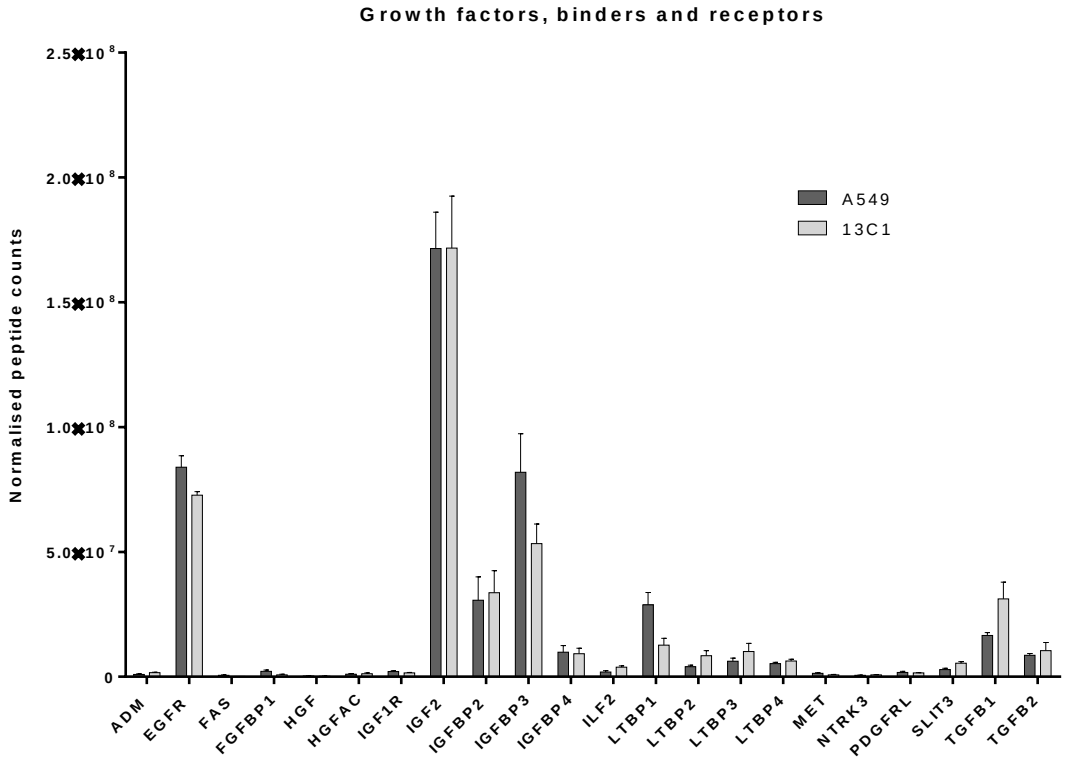

Figure 5.2.10. Growth factors, binders and receptors abundance in the wildtype and mutant matrices. Proteins detected in the LC-MS analysis were grouped based on similarity and groups were analysed individually. Only direct binders and receptors of the growth factors were analysed. Darker grey columns represent wildtype A549 matrices, with lighter grey columns representing the LMα5 mutant 13C1 matrices.

Other ECM proteins were generally decreased in the mutant matrices

The final group assessed from the LC-MS analysis was the remaining ECM proteins. The heatmap constructed from the ECM proteins (Figure 5.2.11) detected shows a difference in expression of all proteins in the wildtype and mutant matrices. In general, the majority of proteins had a positive row Z-score in the wildtype samples, and negative row Z-score in the mutant samples. Of the major ECM/ECM binding proteins detected, there was a reduction in the levels of fibronectin (FN), dystroglycan 1 (DAG1), CCN2, syndecan 1 and 4 (SDC1/4), perlecan (HSPG2), vitronectin (VTN), and versican (VCAN) in the LMα5 mutant matrices (Figure 5.2.12). These data indicate that the majority of the ECM proteins were decreased in the mutant matrices compared to the wildtype matrices.

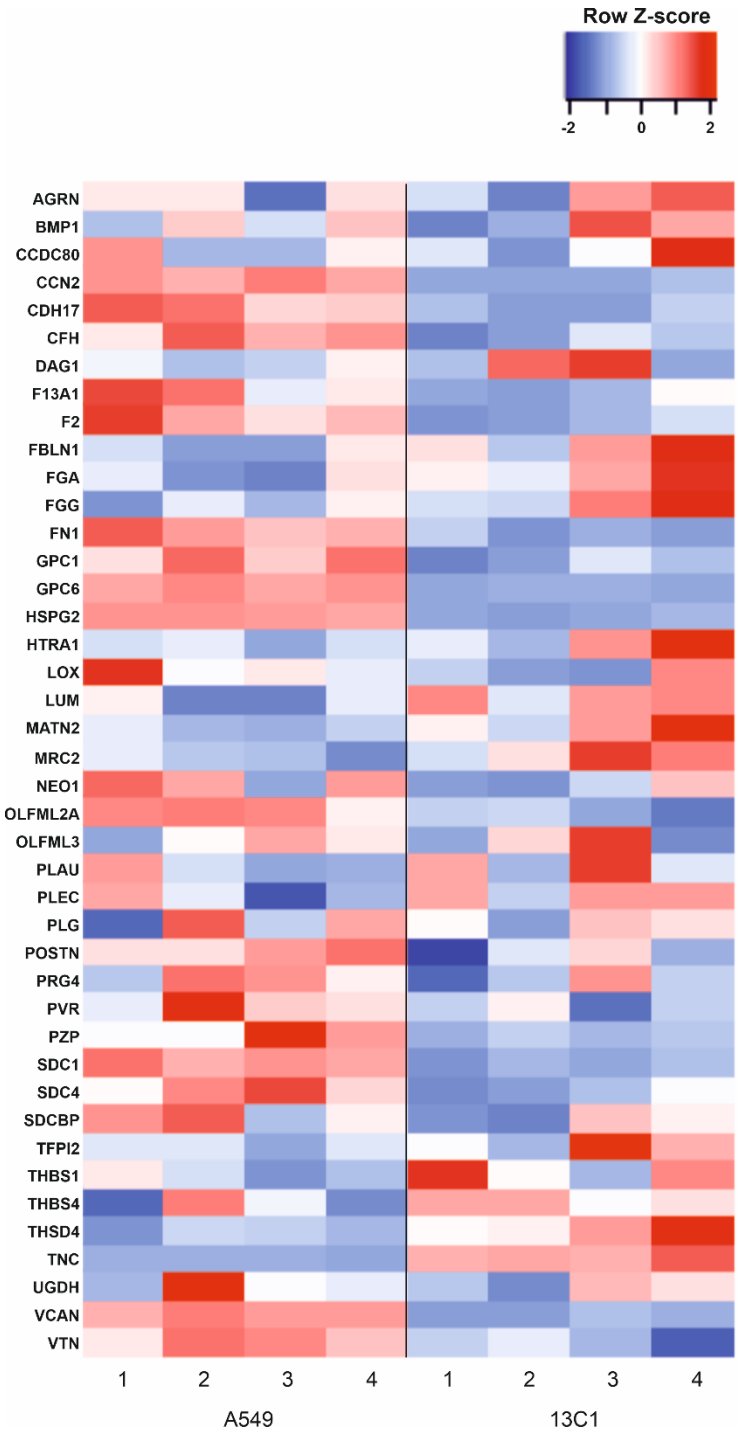

Figure 5.2.11. Heatmap visualisation of differences in peptide counts for ECM proteins detected by LC-MS. Peptides in red indicate an increase from the mean up to 2 SD, whereas blue indicates a decrease from the mean up to 2 SD.

5.3 Cellular response to the mutant matrices

Next, I performed a series of analyses to study how cells respond when plated onto either the wild-type or LMα5 mutant cell-derived matrixes. The control cell line used here was the human embryonic kidney HEK293 cells (235). HEK293 cells do not deposit high levels of their own LMs (274-276), but do express the integrins necessary to bind LMs (277, 278), making them a useful tool for study into preformed matrices. In these experiments, A549 or the LMα5 mutant 13C1 cells were cultured for 120 hours to allow for the deposition of their matrices then the cells were removed with ammonium hydroxide treatment as in other experiments (Figure 5.3).

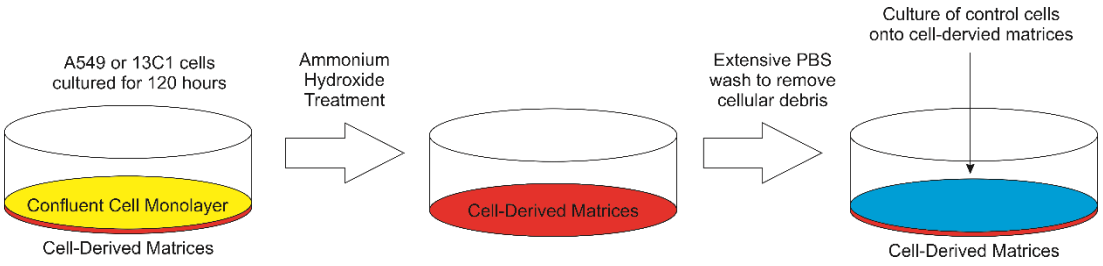

Figure 5.3. Ammonium hydroxide treatment for isolation of cell-derived matrices. A549 or 13C1 cells were cultured for 120 hours to allow for the formation of a confluent cell monolayer and the deposition of their cell-derived ECM. After 120 hours, cells were removed using 2 % ammonium hydroxide treatment for 10 minutes, leaving behind a cell-derived matrix. After extensive washes with PBS to remove cellular debris, control cells such as HEK293 cells were cultured onto the remaining cell-derived matrices.

5.3.1 HEK293 cells reach 50 % attachment more slowly to the LMα5 mutant matrices

HEK293 cells were used in a rapid adhesion assay onto the preformed cell-derived matrixes on the wildtype matrices, HEK293 cells reached 50 % attachment faster on the wildtype matrix than on the mutant matrices, with a 12 % increase in attachment time on mutant matrices (HEK293 on wildtype matrix = 18.3 min, HEK293 on mutant matrix = 20.5 min, Figure 5.3.1).

However, there was no difference in overall attachment rate between the HEK293 cells grown on wildtype and mutant matrices (Mean of differences = 0.6 % ± 6.3 SD, p = 0.84, paired two-tailed t-test). Both conditions reached 100% attachment after 60 min. These data suggest that initial rapid attachment of HEK293 cells is better facilitated on the wildtype LM matrix, but is still possible on the mutant LM matrix.

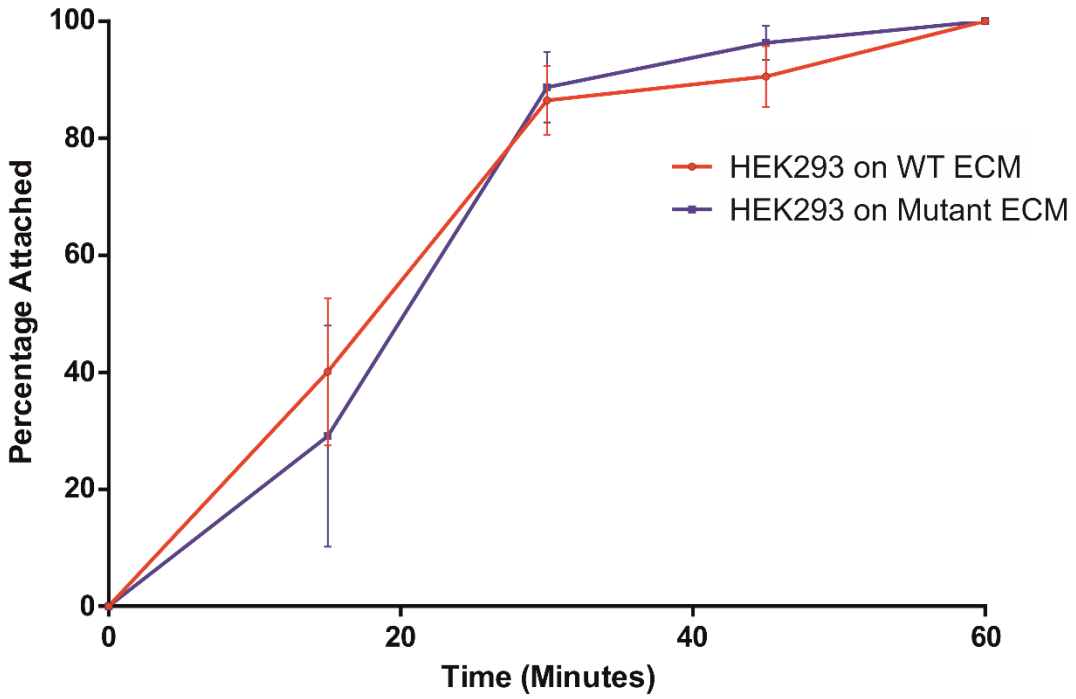

Figure 5.3.1. HEK293 cells attach more rapidly to the wildtype LM matrices. Wildtype A549 (red) and LMα5 mutant 13C1 (blue) cells were cultured for 120 hours then removed with ammonium hydroxide. HEK293 cells were then used in a rapid adhesion assay onto the pre-formed wildtype (WT) and mutant ECM. Error bars represent standard deviation.

5.3.2 Cells cultured on the mutant ECM display reduced trypsin resistance

HEK293 cells were cultured for 48 hours on the ECM derived from either A549 or the LMα5 mutant 13C1 cells, then a resistance to trypsinisation detachment

assay performed (Figure 5.3.2). HEK293 cells on the mutant ECM displayed a reduced resistance to trypsin compared with those on the wildtype A549 ECM (1 in 200: mean of difference 6.1 % ± 8.3 SD, p = 0.03, 1 in 100: mean of differences 5.0 % ± 7.4 SD, p = 0.01). Specifically, the time to 50 % attachment was reduced by 16.6 % in the 1 in 200 dilution, and 13.5 % in the 1 in 100 dilution (A549 16.2 and 14.5 min respectively, 13C1 14.0 and 12.1 min respectively). These data, together with the mutant-cell detachment data, suggest that the mutation to the LMα5 N-terminal domain results in an ECM that is sub-optimal for strong cell attachment.

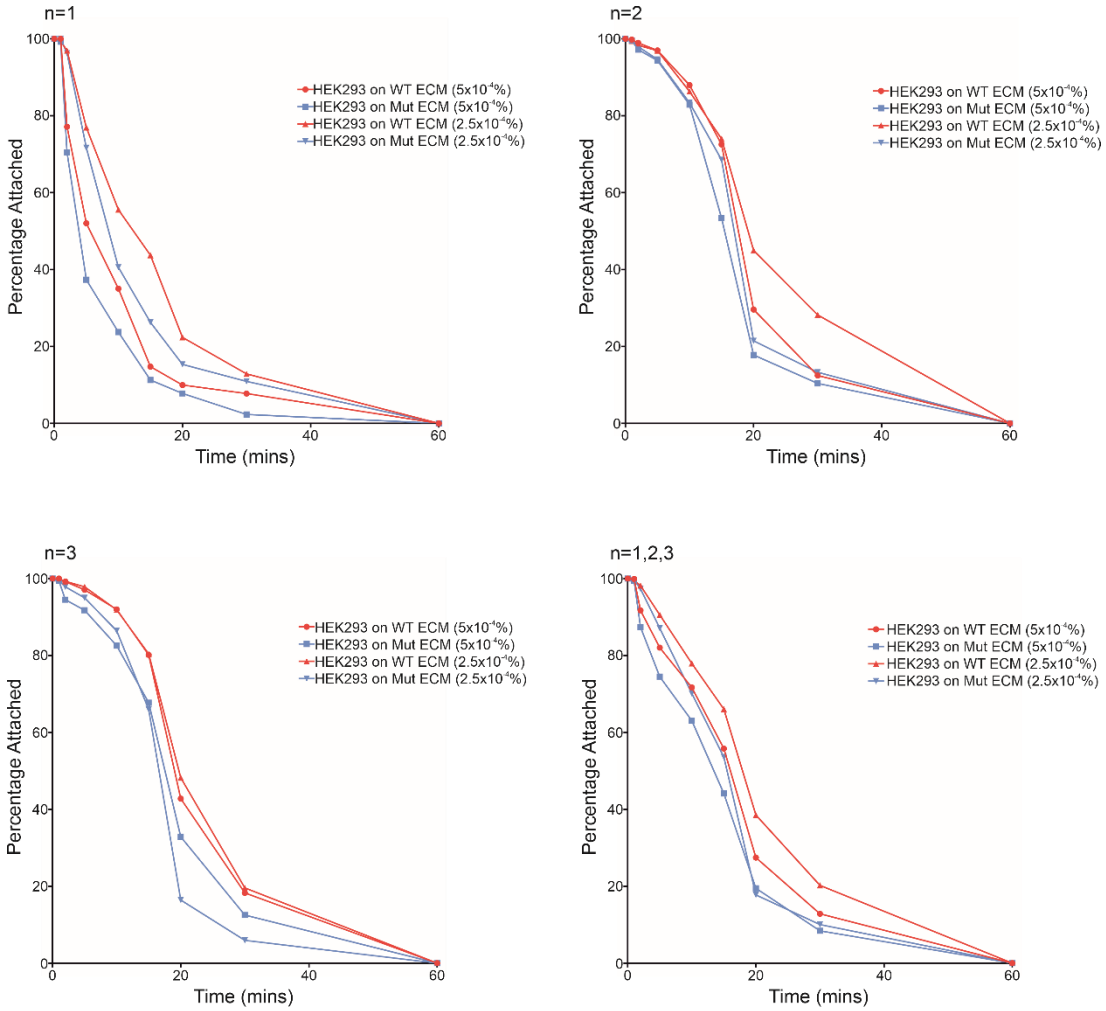

Figure 5.3.2. HEK293 cells cultured on LMα5 mutant ECM have a reduced resistance to trypsin. Wildtype A549 (red) and LMα5 mutant 13C1 (blue) cells were cultured for 120 hours then removed with ammonium hydroxide. HEK293 cells were then cultured on the remaining ECM for 48 hours before being treated with diluted trypsin. Trypsin concentrations at $5x10^{-4}$ and $2.5x10^{-4}$ %. At each timepoint, supernatant was removed, and cells were counted. The percentage of cells attached was plotted against the time since trypsin was added. a-c) are independent biological repeats, d) mean from the three experiments.

5.3.3 Wildtype matrix rescues adhesion phenotype of LMα5 mutant cells

I hypothesised that aspects of the LMα5 mutant cell phenotype that were matrix dependent could be rescued by culturing them on wildtype matrices. To test this, a cross-matrix rapid attachment assay was performed using A549 or

13C1-derived ECMs then seeding fresh A549 or 13C1 cells onto these ECMs (as in Figure 5.3). All four conditions had similar attachment rates, with all conditions reaching 50% attachment between 43.5 and 45.1 min (Figure 5.3.3). These data indicate that there was no difference in the ability of the A549 and the 13C1 cells to attach to pre-formed matrix.

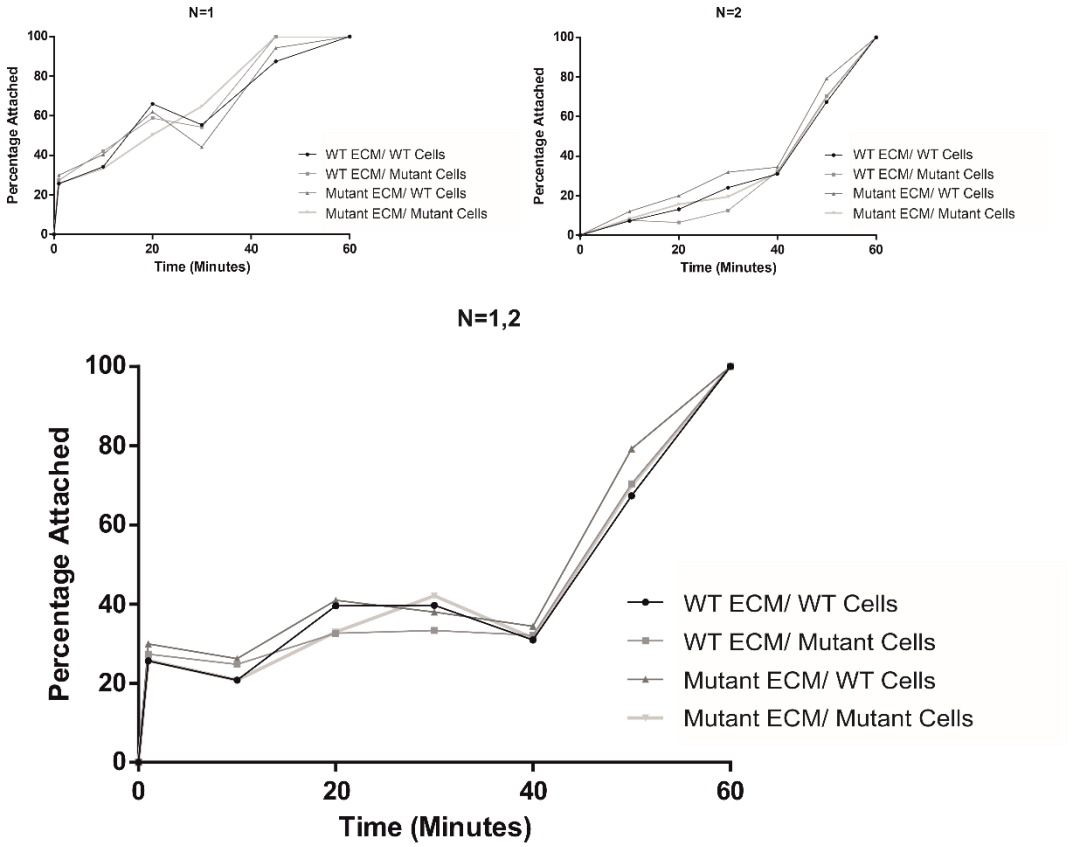

Figure 5.3.3. Cross-matrix attachment assay showed no differences in attachment rate onto pre-formed matrices. Wildtype A549 and LMα5 mutant 13C1 cells were cultured for 120 hours before being removed with ammonium hydroxide. A549 and 13C1 cells were then used in a rapid adhesion assay onto the pre-formed wildtype (WT) and mutant LM ECM.

5.3.4 Wildtype matrix rescued the strength of attachment phenotype of LMα5 mutant cells

I next determined whether the culture of the LMα5 mutant 13C1 cells onto wildtype LM matrices would recue their adhesion strength defect. A549 or

13C1 cells were cultured on to wild-type of LM α5 mutant cell-derived matrices and a detachment assay performed with 0.00025 % trypsin-EDTA (Figure 5.3.4). Wildtype A549 cells on wildtype ECM had the slowest detachment rate (50 % detachment = 41.1 min). However, mutant cells cultured on the non-mutant ECM were slower to detach than those cultured on their native mutant ECM (mean of differences: 4.2 % ± 2.3 SD, p = 0.003). Indeed, mutant cells cultured on wildtype matrices had a similar trypsin resistance to A549 cells cultured on mutant matrices (mean of differences = 1.6 % ± 2.3 SD, p = 0.176), with almost identical 50 % detachment times (Wildtype ECM/ Mutant cells = 37.9 min, Mutant ECM/ Wildtype cells = 37.6 min).

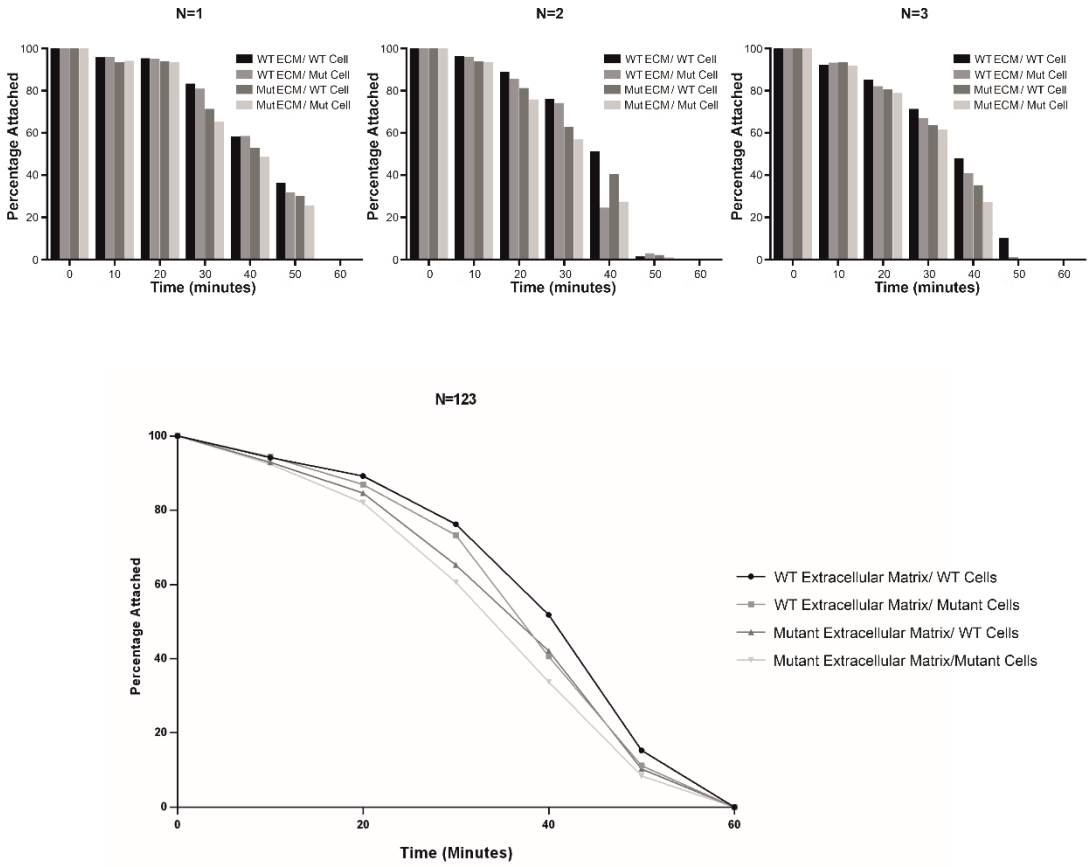

Figure 5.3.4. Wildtype ECM rescues some of the reduced trypsin resistance in 13C1 cells. Wildtype A549 and LMα5 mutant 13C1 cells were cultured for 120 hours before being removed with ammonium hydroxide. Wildtype (WT) A549 and mutant cells (WT membrane/WT cells, WT membrane/Mutant cells, Mutant membrane/ WT cells, Mutant membrane/Mutant cells) were then cultured on the remaining ECM for 48 hours before being treated with diluted trypsin ($2.5x10^{-4}$ %). At each timepoint, supernatant was removed, and cells were counted. The percentage of cells attached was plotted against the time since trypsin was added. Top bar graphs are independent biological repeats, with line graph below representing mean from the three experiments.

5.3.5 No statistically significant differences were observed in the gene expression of cells grown on the LMα5 mutant and wildtype matrices

Together the results had indicated that the LMα5 mutant matrix induced a detrimental phenotype upon cells cultured upon that matrix. To determine if these effects were direct or indirect, I next assessed the effects of the mutant matrix upon gene expression. RNA sequencing was performed on HEK293 cells grown for 24 hours on cell-derived matrices from A549 or the LMα5

mutant 13C1 cells. Gene hit counts were then normalised within each sample using DESeq2 (Figure 5.3.5). The normalised box plots showed highly similar expression values and ranges across samples, indicating that normalisation was successful.

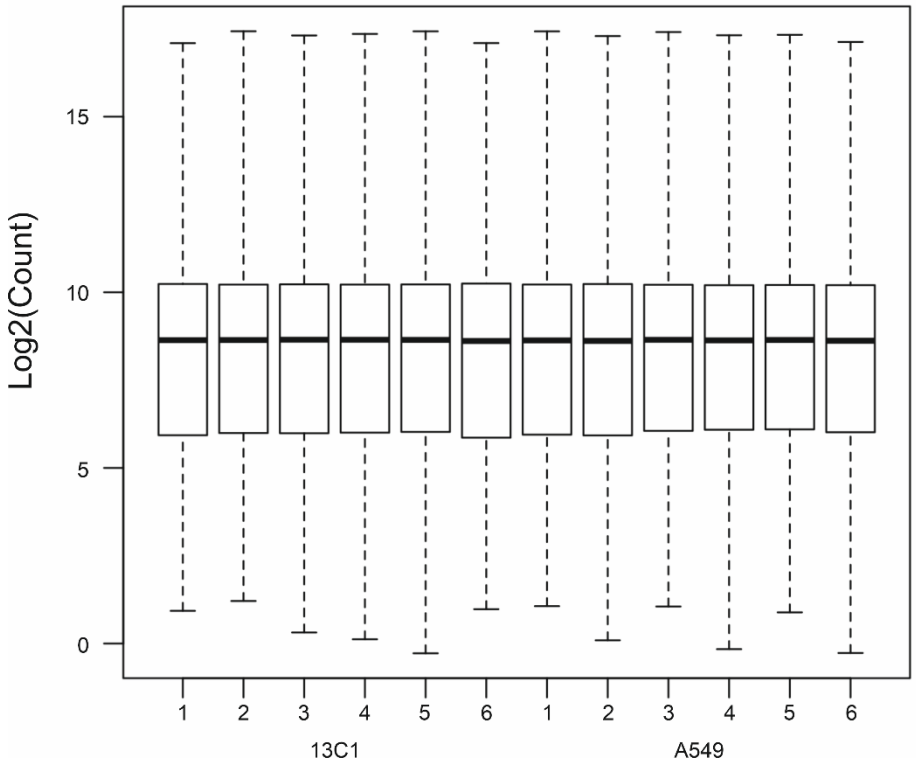

Figure 5.3.5. Distribution of normalised reads count for genes. The original read counts were normalised to adjust for factors such as variations of sequencing yield between samples. These normalised read counts were used to determine differentially expressed genes.

After normalisation, similarity in gene expression values between the two samples and their biological repeats were analysed using sample-to-sample distances (Figure 5.3.6). Sample-to-sample distance showed little variation between the six biological repeats for the HEK293 cells grown on wildtype matrix or LMα5 mutant matrix. These analyses also highlighted the global

similarities in gene expression between cells grown on wildtype and mutant matrices.

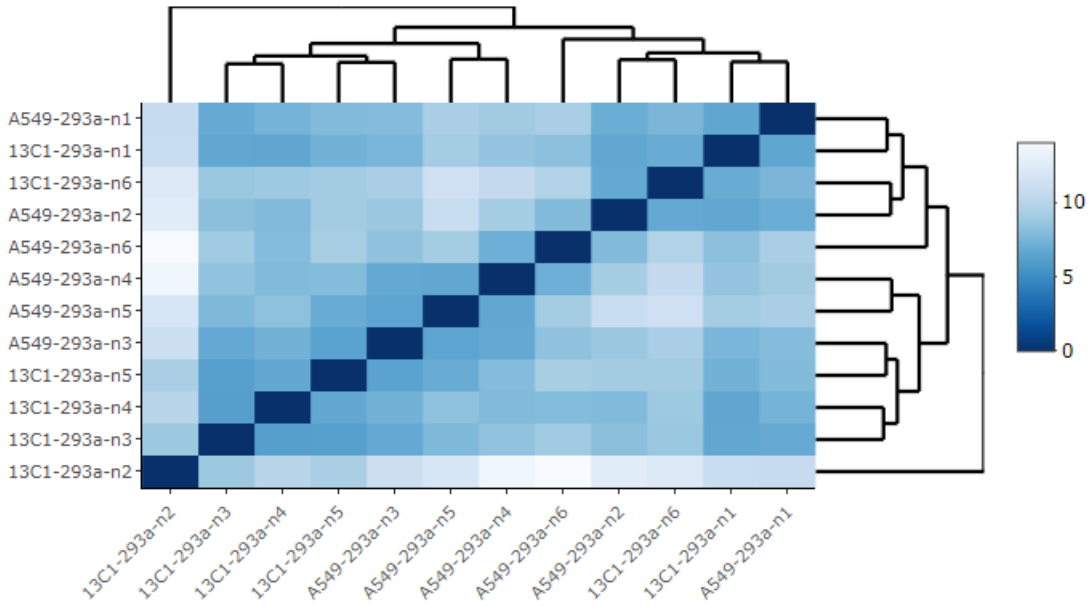

Figure 5.3.6 Heatmap of sample-to-sample distance. The overall similarity among samples were assessed by the Euclidean distance between samples. This method was used to examine which samples are similar/different to each other and if they fit to the expectation from the experiment design (279). The shorter the distance, the more closely related the samples are. Samples were then clustered using the distance.

This similarity in gene expression is also apparent by the volcano plots (Figure 5.3.7). No genes in the mutant samples showed a log2 fold reduction of more than 0.34, or a log2 fold increase of more than 0.27. Only one gene showed a change that reached a statistical significance threshold of 0.05 (KRT17, log2 fold change = -0.34, $p_{adj} < 0.001$).

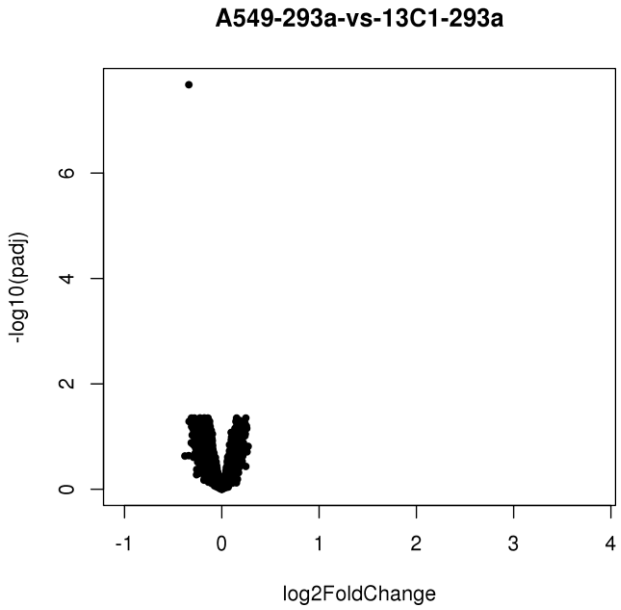

Figure 5.3.7. Volcano plot indicates there is no change in differential gene expression. Each data point in the scatter plot represents a gene. The log2 fold change of each gene is represented on the x-axis and the log10 of its adjusted p-value is on the y-axis. Black dots indicate gene changes with a p-value > 0.05.

The top 30 most differentially expressed genes were compared across all samples (Figure 5.3.8). Even within these 30 genes, all samples showed similar expression of each gene, with little variation between samples. Together, these data indicate that LMα5 mutant matrix compared with WT-ECM does not induce major change in gene expression in HEK293 cells exposed to that matrix for 24h.

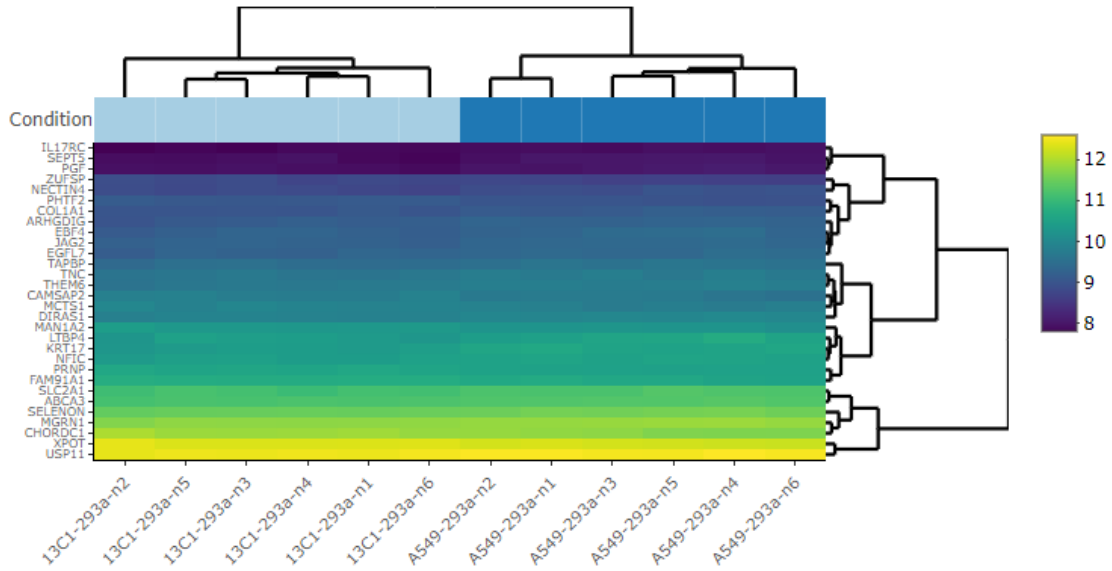

Figure 5.3.8. Heatmap of top 30 differentially expressed genes. Bi-clustering heatmap was used to visualise the expression profile of the top 30 differentially expressed genes sorted by their adjusted p-value by plotting their log2 transformed expression values in samples. Yellow colours indicate higher relative expression, while blue colours indicate lower relative expression.

5.3.6 LMα5 mutant matrices induce a reduction in phosphorylation of signalling pathways

Next, I investigated whether WT or LMα5 mutant ECM induces differential activation of cell-matrix signalling pathways. As previously, HEK293 cells were cultured on cell-derived matrices from A549 and 13C1 cells for 24 hours, then lysed for analysis.

First, I analysed a broad spectrum of receptor tyrosine kinases using an array designed to detect changes in phosphorylation of proteins related to receptor tyrosine kinases (RTKs) (Figure 5.3.9).

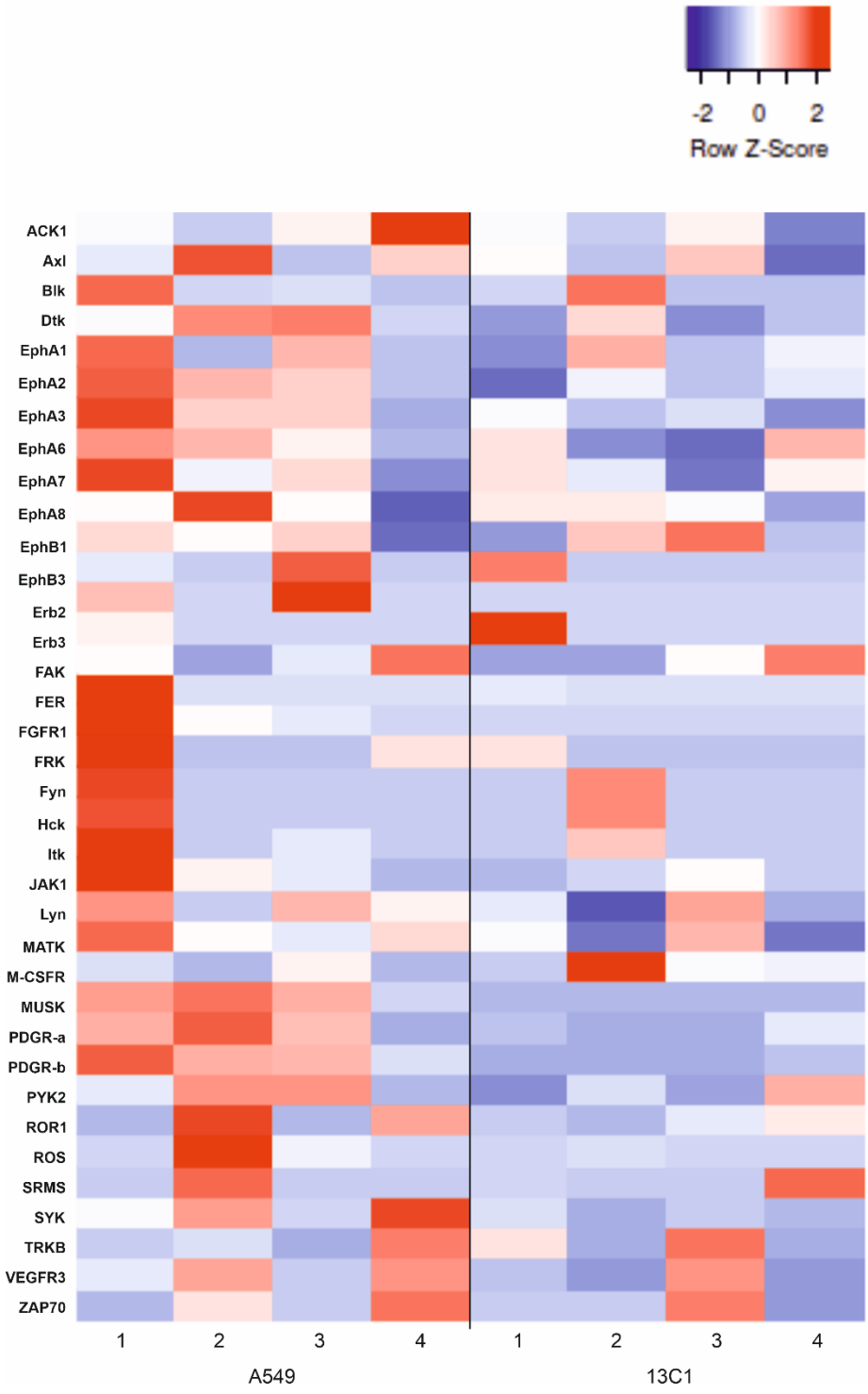

Figure 5.3.9. Mutant matrices result in a reduction of phosphorylation of many signalling molecules responsible for receptor tyrosine kinase signalling. Heatmap used to visualise changes in phosphorylation of signalling components in RTK signalling cascades. Proteins in red indicate increased phosphorylation relative to the protein signal mean, whereas blue indicates a decrease from the mean.

Changes to the phosphorylation state of these targets were subtle and frequently varied from assay to assay (Figure 5.3.10-12). However, generally, phosphorylation of most detected targets in the array were downregulated in the cells grown on the mutant matrices (Figure 5.3.9). Of particular note was the downregulation of phosphorylation in focal adhesion kinase (FAK), Janus Kinase 1 (JAK1) and Fyn Kinase in the mutant matrix cells, with a 66 %, 88 % and 35 % reduction, respectively (Figure 5.3.10, 5.3.11, 5.3.12). All three kinases play an important role as some of the first kinases involved in detecting extracellular ligand binding to cell surface receptors (45, 46, 280-282).

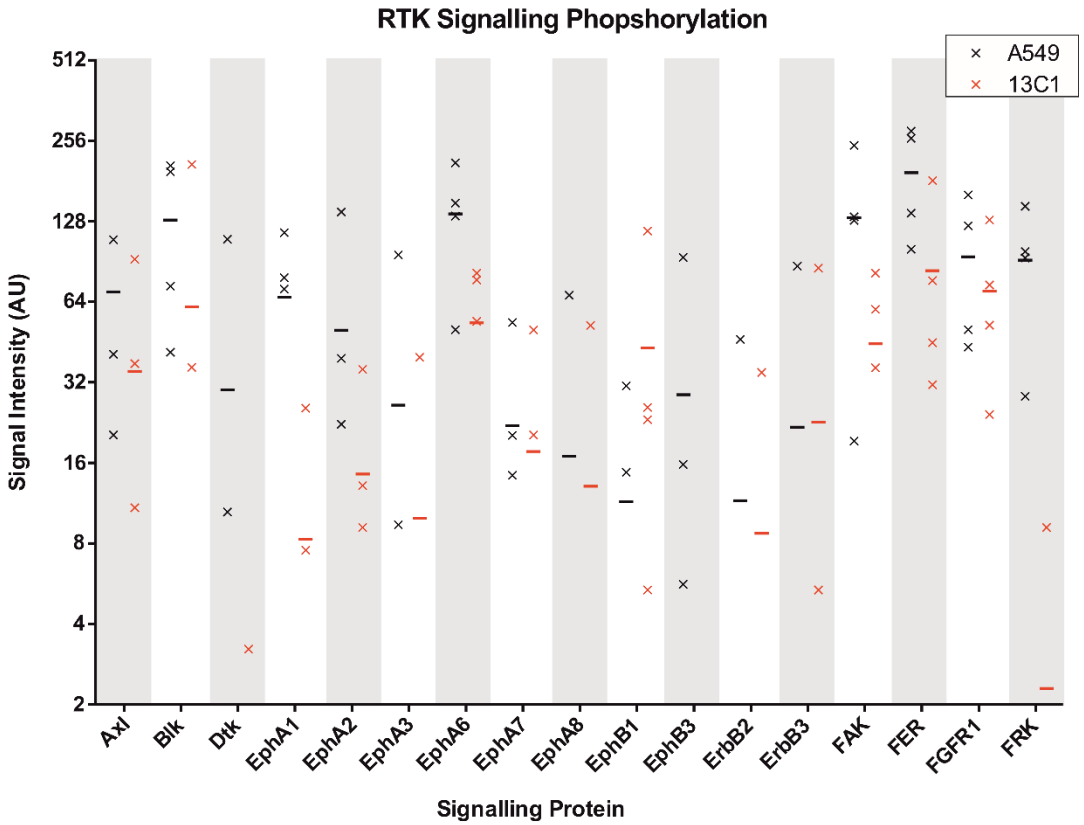

Figure 5.3.10. Mutant matrices induce a reduction in phosphorylation in many RTK signalling pathways (Axl-FRK). Wildtype A549 and mutant 13C1 cells were seeded for 120 hours, before removal with ammonium hydroxide. HEK293 cells were then seeded onto the remaining cell-derived matrices and incubated for 24 hours before being processed for phosphorylation analysis. Points represent the phosphorylation signal intensity obtained from each independent experiment, with a line to represent the median for HEK293 cells grown on A549 (black) and 13C1 (red) cell-derived matrices. Proteins shown alphabetically from Axl-FRK.

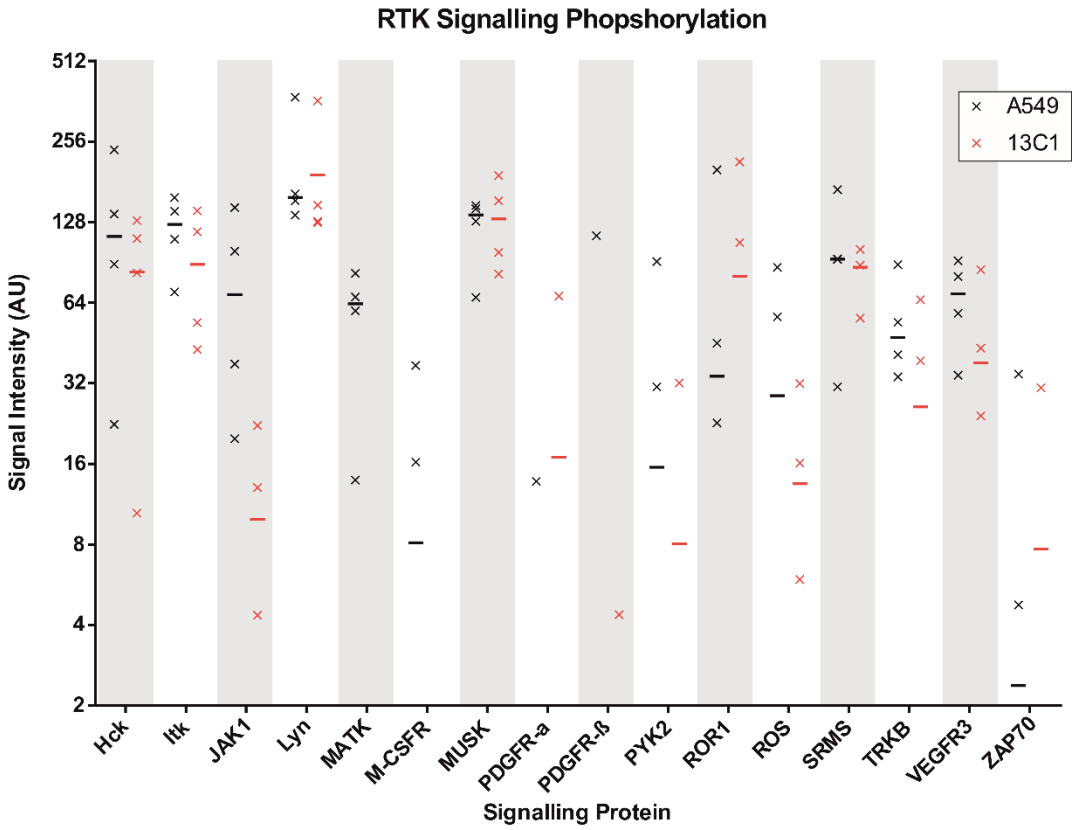

Figure 5.3.11. Mutant matrices induce a reduction in phosphorylation in many RTK signalling pathways (Hck-ZAP70). Wildtype A549 and mutant 13C1 cells were seeded for 120 hours, before removal with ammonium hydroxide. HEK293 cells were then seeded onto the remaining cell-derived matrices and incubated for 24 hours before being processed for phosphorylation analysis. Points represent the phosphorylation signal intensity obtained from each independent experiment, with a line to represent the median for HEK293 cells grown on A549 (black) and 13C1 (red) cell-derived matrices. Proteins shown alphabetically from Hck-ZAP70.

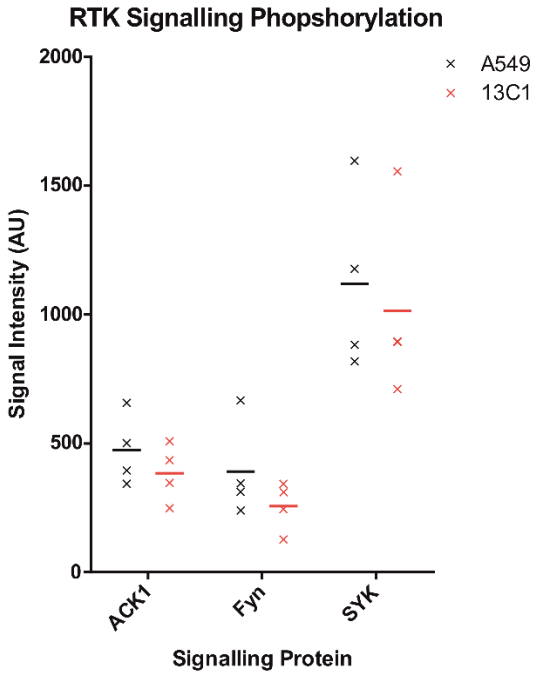

Figure 5.3.12. Mutant matrices induce a reduction in phosphorylation for Fyn Kinase. Wildtype A549 and mutant 13C1 cells were seeded for 120 hours, before removal with ammonium hydroxide. HEK293 cells were then seeded onto the remaining cell-derived matrices and incubated for 24 hours before being processed for phosphorylation analysis. Points represent the phosphorylation signal intensity obtained from each independent experiment, with a line to represent the median for HEK293 cells grown on A549 (black) and 13C1 (red) cell-derived matrices. Proteins shown are the three strongest signals.

One of the major signalling pathways responsible for cellular response to extracellular environment in the AKT signalling pathway (44, 46, 47, 283), so I performed an additional analysis focused on this pathway using a Phospho-AKT signalling array assay (Figure 5.3.13). HEK293 cells cultured on the mutant LMα5 cell-derived matrices showed a 39.1 % reduction in AKT phosphorylation (HEK293 on wildtype matrix mean = 3100 AU ± 2200 SD, HEK293 on mutant matrix mean = 1900 AU ± 1600 SD). The phosphorylation of AKT acts as the central activation point of the signalling cascade, which affects the phosphorylation of all the other components analysed by this array (46) (Figure 5.4.2). These data, therefore, suggest that the reduction of AKT

phosphorylation in mutant cells leads to a subtle downregulation of the other components of the AKT signalling pathway.

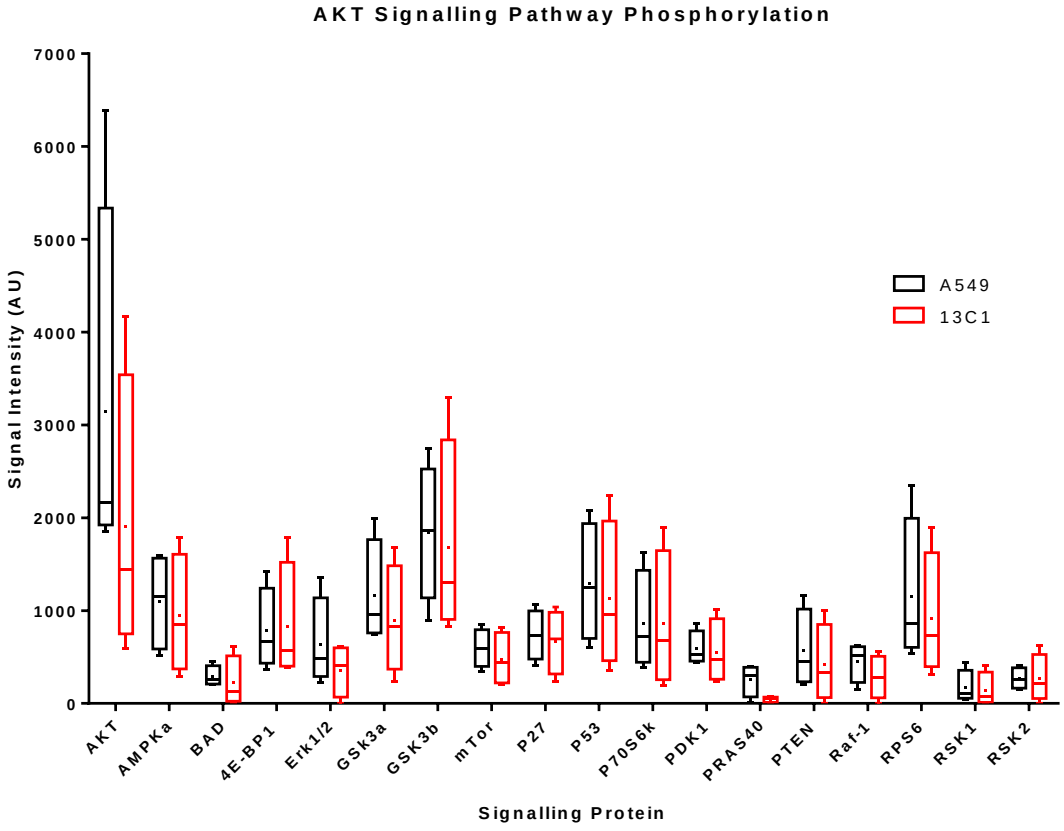

Figure 5.3.13. Mutant matrices induce a reduction in phosphorylation in the AKT signalling pathway. Wildtype A549 and mutant 13C1 cells were seeded for 120 hours, before removal with ammonium hydroxide. HEK293 cells were then seeded onto the remaining cell-derived matrices and incubated for 24 hours before being processed for phosphorylation analysis. Boxplots represent the minimum and maximum phosphorylation signal intensity for HEK293 cells grown on A549 (black) and 13C1 (red) cell-derived matrices. Dots represent the mean phosphorylation signal intensity value.

5.4 Discussion

The results in this chapter have demonstrated that the matrix deposited by LMα5 LN domain mutant cells differs in organisation and composition compared with wild-type counterparts, that cells interacting with that matrix display slower adhesion and reduced adhesion strength and that signalling cascades activation of cells interacting with the mutant matrix is altered. Moreover, these results demonstrate that the mutant cells can be rescued at least as far as adhesion and migration, by provision of a preformed non-mutant matrix, indicating that at minimum these aspects of the phenotype are likely predominantly matrix-dependent. On a wider scale, these collective results indicate that the network forming aspect of LMs are not only structurally important but also play a wider role in defining matrix composition and in modifying signalling. Indeed, these roles are likely tightly intertwined.

The HEK293 assays and cross-matrix rescue assays are particularly important to the story of the LMα5 mutant. One of the main concerns following the phenotypic analysis of the 13C1 cells was whether the observed phenotype was cell-driven (i.e. a result of the genome editing and clonal expansion) or matrix-driven (i.e. a result of the mutant matrix alone). The findings described in this chapter that the HEK293 cells showed a similar phenotype in response to mutant matrix as the 13C1 cells did themselves provides a robust indication that the cellular phenotype was likely to be matrix-driven rather than artifactual.

Knowing that the matrix behaves differently, warranted a deeper investigation of the reason behind those differences. The SEM analyses indicated a clear difference in the LM network formed in the mutant matrices. A difference in the

LM preparation was, of course, anticipated; however, at a first glance, the decrease in gap size in the mutant network might suggest that a more ordered rather than less polymerised network is being formed. To interpret these data, we must consider how SEM sample preparation occurs. Here, sample coatings were achieved by low-angled heavy metal sputter, a standard procedure for SEM (284). However, SEM typically has a spatial resolution of around 50-100 nm (285), so while useful for 70 nm x 40 nm LM heterotrimers that are perfectly perpendicular to the surface, any angled heterotrimer would produce a loss in resolution (286, 287). One might expect that if a LM heterotrimer cannot polymerise, such as from the mutant cells, the abundance of LMα5-containing heterotrimers perpendicular to the wafer chip would be decreased. This would present as smaller gaps in the network, as in the SEM images. Therefore, although the images may ostensibly indicate a more ordered environment, I believe that these outcomes could also be explained by the LM network being, actually, more disordered.

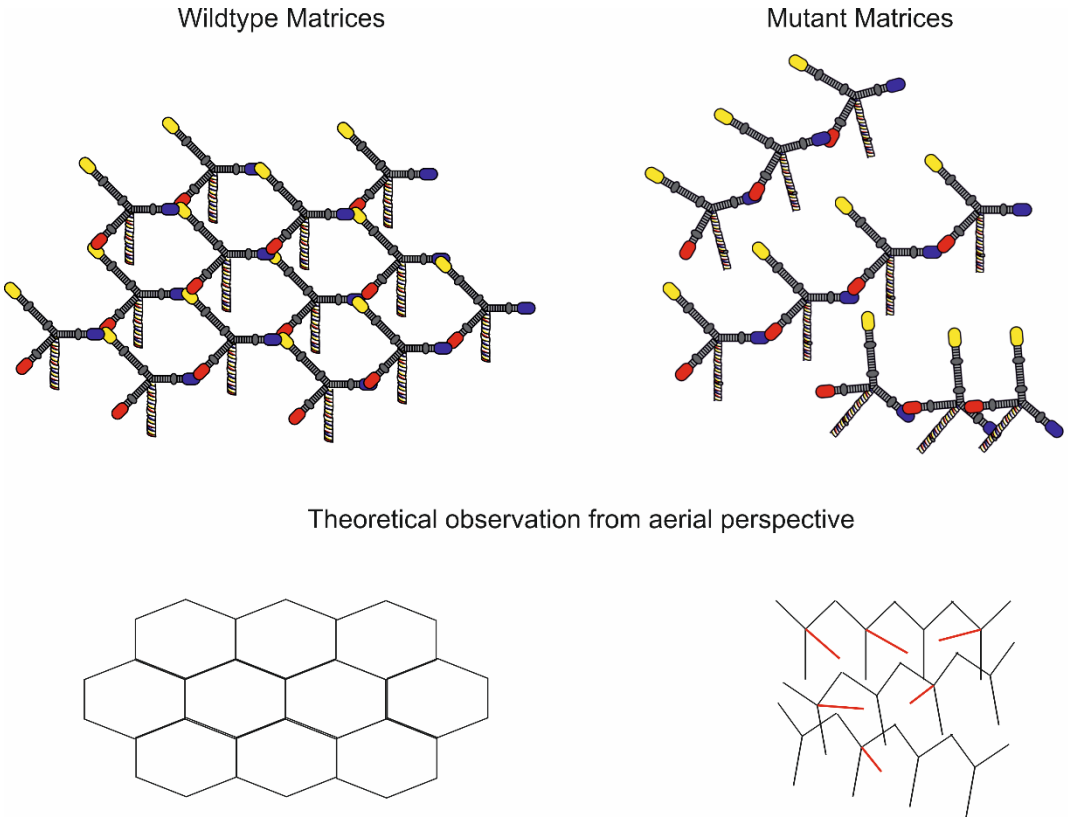

Figure 5.4.1. Theoretical matrices formation and how these matrices would be observed from an aerial perspective, as with an upright microscope. Wildtype matrices are able to form successful ternary nodes, and these stable ternary nodes in the LM network almost lock the laminin long arm into a perpendicular angle to the substrate. Compare that to the mutant matrices, whereby no stable ternary node is formed. This lack of a ternary node allows the long arm (shown in red) more freedom in its angular distribution, making it less likely to be perpendicular to the substrate. When observing this from an upright perspective, such as SEM would, this will theoretically result in regular gaps in the wildtype matrices, whereas the mutant matrices is likely to have less regular and smaller gaps in its network, particularly at the spatial resolution capable with an SEM.

A disordered LM network could also explain the reduced abundance of LMα5 in the ECM of 13C1 cells. I will refer to this as *The Bookshelf Hypothesis*. When imagining a bookshelf, if one stacks the books perpendicular to the bookshelf in an ordered manner, more books can fit on the shelf than if they were not stacked perpendicular to the bookshelf. With the wildtype LMα5, the tight ternary nodes could force the long arm of the LM heterotrimer into a perpendicular orientation, allowing for a tighter packing of LM within the network. Compare this to the mutant LMα5, whereby ternary nodes are not

able to form and even binary interactions are not stabilised, which then allows the long arm of the heterotrimer more angular freedom. This angular freedom increases the disorder in the LM network, the “books” are placed onto the shelf randomly, and as such, less space is available to pack the network with LM (Figure 5.4.1). The Bookshelf hypothesis could consequently partly explain the reduced surface integrin phenotype in the 13C1 cells. If we posit that fewer LM heterotrimer long-arms are in a conformation perpendicular to the substrate, with the substrate here being the cell surface, then fewer LM-binding integrins would be required to bind to the reduced number of LG-domains presented to the cell surface. This is under the assumption that LM is first secreted and then later incorporated into the basement membrane (288, 289), which the data from the conditioned media blots in Chapter 4 supports.

The lack of space for LM in the ECM provides an explanation for the reduced levels of ECM proteins observed in the mutant matrices. Accepting the current dogma that LM is sequentially the first BM protein incorporated and thus its dynamics controls the later assembly of BM components (7), then a reduction in LM would also lead to a reduction of other basement membrane components. By reducing the amount of LM present in the mutant’s ECM, the available scaffold space for the other ECM components to assemble upon has been diminished. This simple explanation holds for the majority of the changed proteins, including perlecan, a core BM and LM-collagen linker protein (94) and one type IV collagen, COL4A6, which showed a dramatic 14-fold downregulation. However, there was an unexplained upregulation of most other collagens in the 13C1 matrices. One explanation could be that the 13C1 cells overcompensate their collagen expression to aid cellular adhesion. This

excess of collagen could also explain why rapid attachment of A549 and 13C1 cells to mutant and wildtype matrices showed no difference in the phenotypic rescue experiments; although the mutant matrices were atypical, they still supported cell attachment. A future experiment to test this might involve antibody inhibition of collagen and laminin binding integrin to ascertain whether there is differential requirement of these integrins when attaching to the different matrixes. The overexpression of other collagens also supports the increase in disorder seen in the SEM collagen data. The LM-perlecan-collagen interactions likely drive basement membrane orientation, so with a reduction in the LM and perlecan, an increase in collagen disorder is likely. To further assess this in the future, picrosirius red stain (290) or two-photon microscopy could be used to study the orientation of the collagen networks in the LMα5 mutant cells.

The proteomics findings could also explain the observed downregulation in matrix-mediated signalling, but in a possibly more nuanced way than first thought. My initial hypothesis was that growth factors held in the ECM would be downregulated by disrupting the LM network, and that this would affect cellular signalling. Looking at points of particular interest, the increase of latent transforming growth factor binding proteins (LTBPs) in the mutant matrices agrees with the increase in TGFβ1 and 2, as they act as extracellular storage for latent but secreted TGFβ. However, the decrease of LTBP1 in the mutant cells would be consistent with these finding when one considers it is involved in the apoptosis pathway (291, 292). The reduction in mutant levels of FAS in the matrix, as well as the YAP/TAZ data, could suggest that the mutant cells have a loss of regulation of apoptosis, something which I did not formally

analyse. However, while it was true that some growth factors were present at reduced or elevated levels in the mutant matrices, in general, most growth factor levels stayed consistent.

Interestingly, two groups or proteins in particular were almost exclusively downregulated in the mutant matrices; the integrins (in agreement with the flow cytometry data from the 13C1 cells) and the plasma membrane proteins. Both of these groups play a critical role in signalling. Integrins role in signalling is controlled by focal adhesion kinase (FAK), a kinase also strongly linked to perlecan, as well as vinculin and paxillin in focal adhesions (103, 264). FAK was also shown to have a reduced phosphorylation in the receptor tyrosine kinase signalling data, which could be explained by the reduction of integrins present in the mutant samples and, again, agrees with the focal contact indirect immunofluorescence analyses of Chapter 4. Other receptor tyrosine kinases were also downregulated in terms of phosphorylation and also as part of the plasma membrane group in proteomics.

The biggest effects, in terms of signalling, were clearly within the AKT signalling cascade. The AKT pathway is one of the most diverse and complex signalling cascades, and is highly conserved across eukaryotes (47). It controls a multitude of cell behaviours including behaviours observed to be altered in the 13C1 cells including as proliferation, migration, as well others including metabolism, autophagy and cell survival (44-47) (Figure 5.4.2). The activation of this single kinase can control all of these cell behaviours, whilst also interacting with other signalling pathways through cross-talk and feedback mechanisms (293). The activation of AKT can be controlled by FAK upon integrin activation (283), so a downregulation of surface integrin in

mutant cells, and subsequent downregulation of FAK activation was likely to lead to a downregulation of AKT activation. Indeed, the level of AKT phosphorylation reduction was extremely high and this one observation can substantively explain many of the phenotypes observed in response to the mutant matrices.

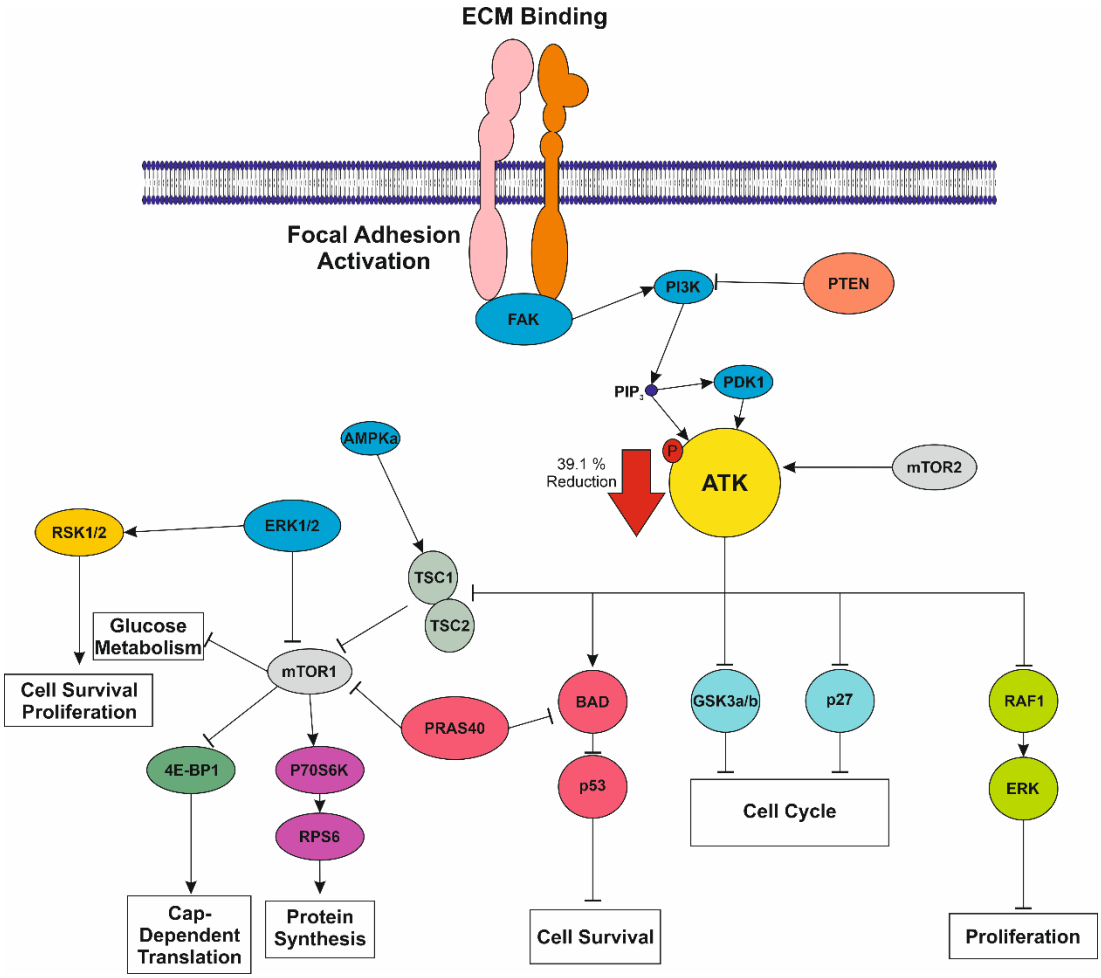

Figure 5.4.2. Reduction in AKT phosphorylation leads to a reduction in phosphorylation and activation of downstream signalling kinases. An overview of the downstream signalling kinases affected by a reduction in AKT phosphorylation, and the cell processes likely to be affected (white boxes).

The findings here combine to a produce a model where without LM polymerisation, cell adhesion receptors on the cell surface have a reduced access to LG domains at the C-terminal of the LM heterotrimer. With this

reduced access to LG domains, surface level integrins reduce, focal adhesions mature more slowly, and this reduces the ability of FAK and other RTK's to induce a signalling cascade. This ultimately results in the detrimental phenotypes seen in both in the 13C1 cells and in the HEK293 cells grown upon the mutant matrix.

The work outlined in this chapter acts as a triangulation of all data shown so far in this thesis, and highlights the importance of LM polymerisation to the overall function of the cell and the tissues. This work has shown that LM polymerisation is essential not only to the cell as a scaffold on which a sufficient basement membrane can form, but also on a molecular and signalling level. One could summarise this as: If the scaffold structure that cells and tissues are built upon is faulty, then the way in which the cells and tissue react to the scaffold will be detrimental to the phenotype. A solid foundation is essential for the cell, and the data here clearly shows that the non-polymerising LMα5 mutant weakens that foundation.

Chapter 6: Making Laminin β1::Dendra2

6.1 Introduction

In this chapter, I describe my attempts to create the first endogenously-expressed, fluorescently-tagged LM for use in live imaging experiments with advanced microscopy techniques. Before describing the work undertaken, I will introduce how LM research has been advanced by the ever-developing field of microscopy. I will then introduce the fluorescent tools currently available and in use within the LM field, and how these tools were adapted to generate my construct. The results part of the work in this chapter has been published in BMC research notes (237) which can be found in Chapter 9: Appendix 1.

6.1.1 LM microscopy: the formative years

Advancements in super resolution microscopy provide an exciting opportunity for those in the field of basement membrane research. In the 1970s and 80s, brightfield and electron microscopy (EM) were a researcher's primary tools for the visualisation of cells and tissue (294). However, the optical resolution of a brightfield microscope, typically 0.25 μm (295), is not small enough to reveal finer details such as structural features of the ECM (296). The core structure of LMs that we understand today were generated using high resolution rotary shadowing EM (166, 276, 297, 298). Rotary shadowing is variant of transmission EM (TEM) that works by coating a sample from one direction with a heavy metal, to produce a shadow, before visualising the sample (296). Areas where the coating is thickest scatter the electrons creating dark areas,

whereas thinly coated areas produce a brighter area (299). This scattering allowed the determination the core structure of LM111 (117, 127, 287, 300).

The high resolution of EM provided the vital foundations of LM research; many principal understandings that still stand to this day, but it is not without its caveats. One of the major requirements of any traditional EM technology was the removal of water molecules from the sample on the EM matrix (301). This sample manipulation can result in artefacts or inadvertent changes. When one considers that roughly 60-80% of human anatomy comprises of water (302), observing proteins in a dehydrated environment is akin to comparing grapes to raisins. Although the level of detail that can be observed by TEM can be staggeringly complex, the preparation conditions can also lead to structures observed being misleading.

Fluorescence microscopy brought about the next paradigm-shift in the understanding of the cell and it's ECM. In the early years of LM research this took the form of widefield fluorescence microscopy which uses a halogen-lamp to visualise tagged proteins or antibodies (303-307). Early work using widefield microscopy focused on visualising LM within whole tissue, while visualising other components of the ECM such as ColIV and FN (308). These methods typically involved the illumination of the entire sample (Figure 6.1.1a). Although limited by today's standards, this work was one of the earliest to use antibodies to distinguish between ColIV and LM in tissue and look at their co-deposition. However, techniques quickly advanced and tools were developed that allowed a more detailed understanding of LMs.

Throughout the latter half of the twentieth century, many attempts were made to improve the resolution of conventional widefield fluorescent microscopy. The development of high intensity lasers and electronic sensors sensitive enough to collect high-resolution information ultimately gave rise to the first laser scanning confocal microscopes (309). Confocal microscopy differs from widefield fluorescence in two important ways. Firstly, by focusing the light from a single point illumination source and scanning the sample this limits the traditional “flooding” of light used in widefield and aids XY resolution (Figure 6.1.1a) (310). Secondly, the confocal microscope has a pinhole in front of the detector, which allows only a single plane of light to be detected (311), which drastically reduces the out-of-focus signal produced in widefield microscopes, improving resolution in the Z (axial) direction. When used optimally, with high quality lenses, confocal microscopy can achieve a maximum resolution of approximately 180 nm laterally and 500 nm axially (312).

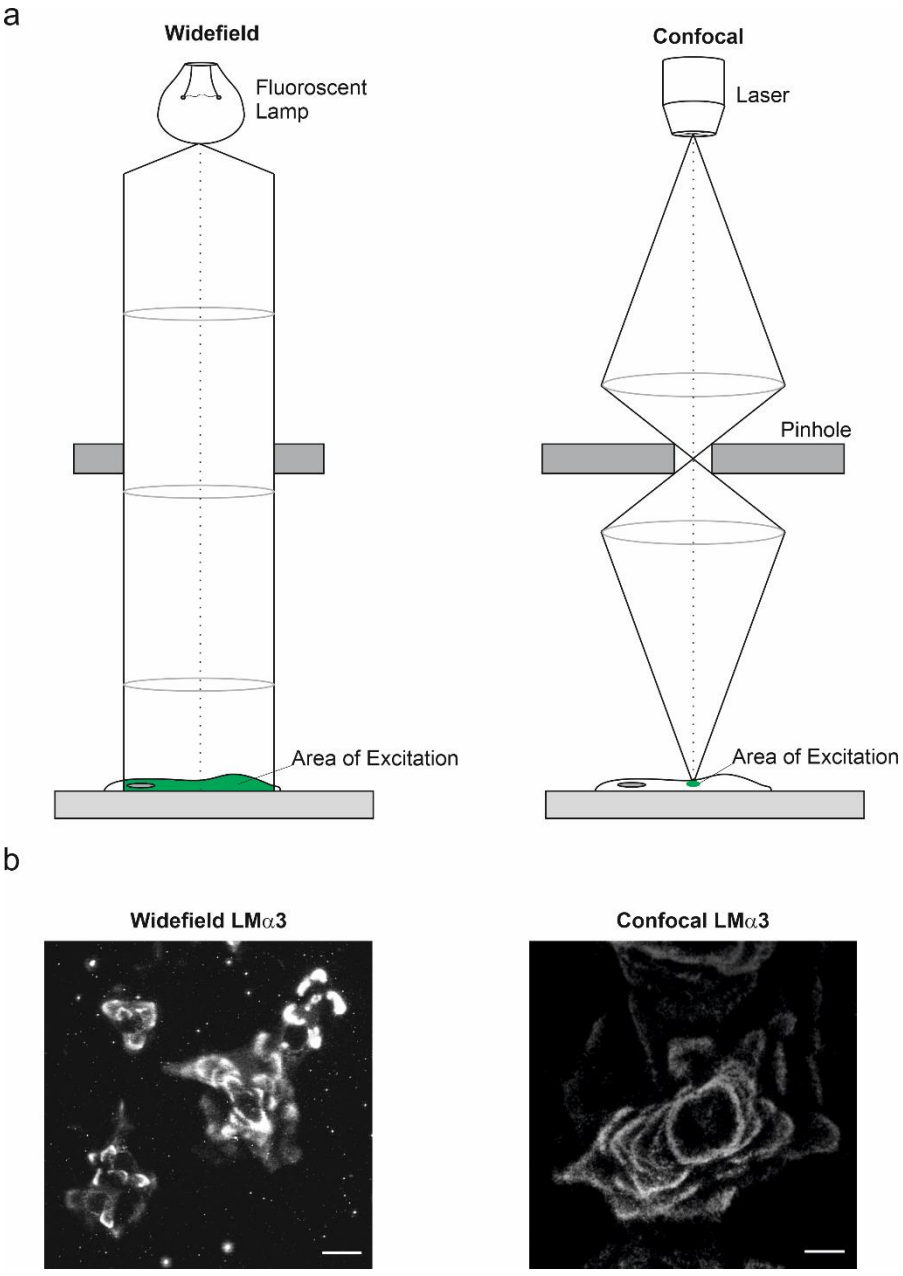

Figure 6.1.1: Widefield vs Confocal differences in sample illumination and resolution. a) With widefield illumination, the whole sample is exposed to light from a halogen lamp-source, resulting in a relatively large area of excitation. With confocal microscopy, from the laser is focused through a pinhole for illumination, resulting in a relatively area of excitation in the sample (310, 311). b) Human corneal epithelial keratinocytes plated on glass coverslips then processed for indirect immunofluorescence microscopy with antibodies against LMa3, visualised with widefield and confocal microscope. Scale bar represents 20 µm.

The development of confocal microscopy was of particular value to the ECM field as it allowed for targeted visualisation of specific areas of the basement

membrane in more natural conformation. Confocal microscopy allowed for the targeted antibodies probing of the ECM components in fixed cells and tissues, which were then visualised using fluorescent secondary antibodies (313, 314) This allowed observations into the distribution of LMs, such as the archetypal rose-like distribution of LM332 deposited by keratinocytes (Figure 6.1.1b), as well as the other core components of basement membrane and LM-binding proteins (174, 315-319). The ability to process samples for multiple proteins at the same time enabled the visualisation of protein distribution patterns *in vitro* and provide support for predicted interactions identified through biochemical techniques (320, 321) . However, much like with EM, confocal microscopy is not without its disadvantages.

One of the main limitations of confocal microscopy is the potential for contamination of signals into other detection channels when the spectral profiles of fluorophores overlap, commonly known as “bleed through” (312). However, this can be combatted through careful selection of appropriate fluorophores with narrow spectral peaks (312). Poor antibody specificity however cannot be combatted by peak selection, with non-specific staining an issue that researchers must consider when using antibodies with a confocal microscope. The issue of non-specific antibody staining is typically tackled with a blocking step prior to staining after fixation (322), but this is not always successful with particularly promiscuous or poorly optimised antibodies. Another area of caution is the potential for oversaturation of samples, which could result in the loss of data, and is a common mistake when using confocal microscopy (323). As such, there is a degree of reality checking that must always be carried out with confocal microscopy. All detection settings should

be evaluated to minimise the risk of confocal artefacts being produced, with a suitable control vital to ensure specificity. Although a powerful tool in a researcher's arsenal to the present day, confocal images should always be used in conjunction with other means of analysis to validate the evidence provided by these microscopes.

Advancements have been made in the development of tools for live-cell LM experiments. In human cells, adenoviral-mediated expression of the two smallest LMs, LMβ3 and LMγ2, with C-terminal fluorescent tags have been performed (324, 325). These constructs have proven to be a useful tool, allowing studies into how cells secrete matrix towards the leading edge of the cells and leave behind a "snail-trail" of matrix as they migrate over their substrate (324). However, these constructs are at the adenoviral packaging limit, around 35 kb (326), making it impossible for larger LMs, such as LMα5, to be tagged using this method. Additionally to this, the adenoviral transduction allows only for the transient expression of the tagged LM's (326). Further to this, the adenoviral vector, containing a strong promoter, such as CMV (324), results in overexpression of the tagged LM in transduced cells. These transduced cells still express non-tagged LM through their own native expression, so any potential matrices are likely to have a mix of fluorescently-tagged and non-tagged LM. What this work does highlight though, is that a C-terminal fluorescent tag of around 26 kDa is a feasible target when designing future fluorescently tagged-LM models.

6.1.2 LM microscopy: a super-resolution revolution

In recent years, the development of stochastic super-resolution microscopy has seen an increase in the resolution possible by commercial microscopes,

as well as the ability to now view live samples with a resolution higher than that of confocal microscopy. By using photoswitchable or photoactivatable fluorophores these new techniques can achieve an optimal resolution of 20 nm on the XY axis and 50 nm on the Z axis (327, 328). Taking into consideration the dimensions of LMs (~80-100 nm long arm, with ~20-40 nm short arms) (112), with appropriate tools, super resolution approaches will allow questions that were previously impossible to answer to now be addressed.

The majority of confocal microscopes require the fixation and staining of a sample with fluorescent antibodies onto glass slides, resulting in the death of the cells during fixation (329). Even where live imaging is possible, the damage caused to the cell from the intensity of the laser itself and the photobleaching effects of the laser on the fluorophore restricts the ability to view live cell dynamics especially when slow processes such as laminin dynamics require long-term imaging (330). Advancements in super resolution microscopy limit photobleaching through the use of photoactivatable fluorophores (331, 332). With laser intensity limited to periodic bursts of intensity and no need for fixation, it has become possible to view cell dynamics in real time.

The super-resolution technique of particular interest to this project is photo activated localisation microscopy (PALM). PALM makes use of fluorophores with controllable photochromism, such as photoactivatable GFP (paGFP) (331, 332). Using a widefield excitation source, PALM is based on collecting a large number of images with a just a few active fluorophores isolated to each image (328). The low number of fluorophores activated in a dense

environment of each image allows for higher resolution, as fluorophores localisation becomes more precise (Figure 6.1.3) (333).

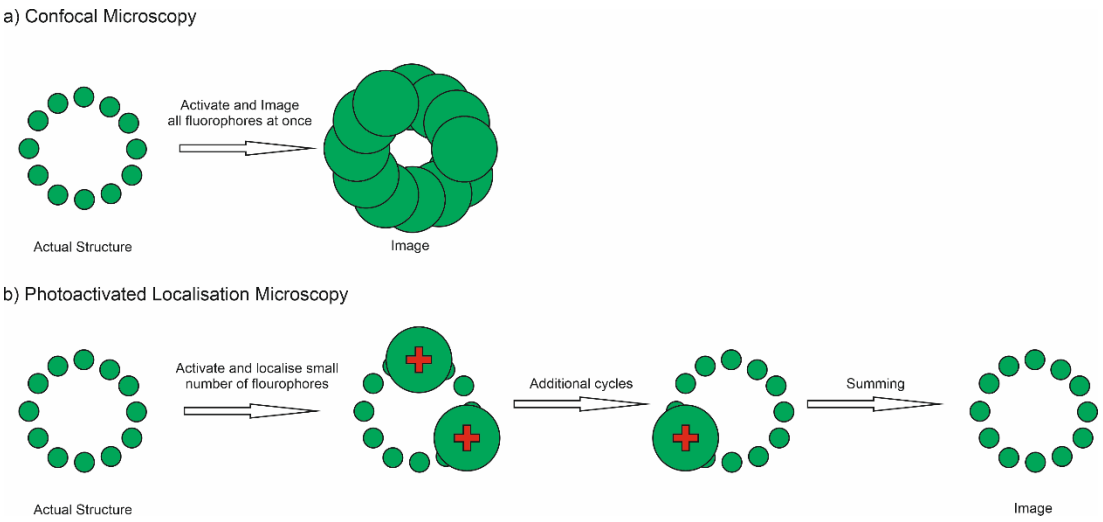

Figure 6.1.2: Differences between sample observation with confocal and photoactivation localisation microscopy. a) Confocal microscopy involves the activation of all fluorophores in a specific area. This total excitation of the area results in a loss of image resolution which could distort the final images structure. b) Photoactivated localisation microscopy combats this problem by only activating a small number of fluorophores with in a set region, focusing these fluorophores, and then repeating cycles of activation until a more resolute structure is visible. (Adapted from (333)).

Originally developed as 2D imaging method, PALM quickly developed 3D capability through the use of a light sheet excitation (334-336). This development allowed for the temporal activation of the Z-plane of a sample, with a resolution of a few hundred nanometres. The employment of multicolour fluorophores in PALM has enabled the observation of specific interaction between small molecules at a resolution that previously had not been distinguishable (336). PALM has been able to show substantive progress in the real-time observation of slower processes (seconds to tens of seconds),

such as the reorganisation of focal adhesions (327). PALM provides the tools to answer some of the lingering questions about the dynamics of LM turnover and remodelling during development, maturation and tumour invasion.

6.1.3 Dendra2, LMs and PALM

Dendra2 is a protein that emits a green fluorescence similar to GFP under blue light (331). However, Dendra2 is distinct from GFP in that brief exposure of short wavelength light (e.g. 405nm) irreversibly photoconverts the Dendra2 protein from green to red (331). In addition to all the standard uses of a fluorophore for spatial tracking, this photoconversion allows for tracking of aspects of protein dynamics such as half-life and turnover (328, 331). Dendra2, under PALM illumination, photobleaches and “blinks” quickly, which also makes it suitable for PALM-based experiments (328).

The power of using Dendra2 to study LMs has been demonstrated in a series of elegant experiments in nematode worms where the C-terminus of the worm LMβ chain ortholog was tagged with Dendra2, GFP or mCherry (337-339). These genome edited nematodes allowed for *in vivo* observation of basement membrane turnover, sliding and remodelling during the process of anchor cell invasion (337, 338, 340). These studies identified a hitherto unknown transient and non-enzymatic disruption of the basement membrane that could not have been observed without the advanced imaging tools. However, *lam-1* has only a 40.8% identity match to human equivalent LM. More fundamentally, the molecular complexity of *C. elegans* BMs are dramatically less than mammalian equivalents, meaning that the findings using the nematode model may not necessarily or completely translate fully to the understanding of mammalian LM deposition and turnover.

6.1.4 Aims

In the *C. elegans* model, the *lam-1::Dendra2* constructs were stably expressed after injection of plasmids to produce a transgenic line. This was non-targeted integration into the *C. elegans* genome with expression driven by part of the lam-1 promoter, which, while functional, could have implications for expression level compared with endogenous proteins. In starting my project, the advancements in genome-editing techniques such as CRISPR-Cas9, meant it was possible to integrate a construct into the genome of cell lines, which would allow expression to remain under the native gene control mechanisms, ensuring expression at near endogenous levels.

Here, I aimed to generate a stable human line incorporating the Dendra2 fluorescent tag in the human ortholog of *lam-1*; *LAMB*1. In this line and in combination with PALM, it would be possible to visualise live dynamics of the LM network, its development and maturation. Furthermore, if applied to an invasive cancer line, the nature of BM remodelling during tumour progression could be observed.

6.2 Chapter Specific Methods

6.2.1. Dendra2 conversion test

HEK293 cells (ATCC® CRL-1573™) were transfected using 2.5 µL Lipofectamine2000 (ThermoFisher) with a LifeACT Dendra2 plasmid (200ng) (Addgene, Plasmid #54694, Watertown, MA, USA) in serum free DMEM High Glucose media (4.5 g L^{-1}) supplemented with 2 mM L-Glutamine for 6 hours. After 6 hours, media was replaced with serum containing media (10 %). 5 x 10^4 transfected cells were seeded onto uncoated 35 mm glass bottomed

dishes (MatTek Corporation, Ashland, Massachusetts, USA) for 16 hours and imaged using a BioAFM (Zeiss).

BioAFM was setup in confocal mode running Zen Black (Zeiss), with the 63x 1.4NA oil lens. Two channels (Dendra2-Green and Dendra2-Red) were made using very low laser power (1%) and a fully open pinhole. Scan area was set at 1024x1024. A range of switching parameters were tried, including changing the laser (405 nm, 488 nm), laser power (5, 10,100 %) and scan speed (speed = 4 or 5).

6.2.2 CRISPR-Cas9 gRNAs and HDR template

A HDR plasmid template (total length 2.7 kb) was designed containing homology arms for the genomic sequence surrounding *LAMB*1 exon 34, with the sequence for a 15 amino acid linker sequence and the Dendra2 cDNA inserted immediately before the translational stop site of *LAMB*1.

Three gRNAs were designed to target different PAM sequences around exon 34 of *LAMB*1 human (Table 6.1). Design of gRNA's was assisted by Dr James Johnson (GeneMill). gRNA's were designed relative to the genomic sequence of the lung adenocarcinoma cell line, A549.

Table 6.1: gRNA Sequences and their target region within *LAMB*1 (79439 bp)

gRNA	Sequence	Target Region
1	ATAGCACATGCTTGTAACAG	*LAMB1:* 79289 - 79308
2	AAAAATGGCTGAGGTGAACA	*LAMB1:* 79318 - 79337
3	TTATATCCTTTAGGAGTGAA	*LAMB1:* 79251 - 79270

LMβ1::Dendra2 HDR-Donor Plasmid was generated by GeneMill (GeneMill) and provided as a purified plasmid. This plasmid was transformed into TOP10 competent E. coli (ThermoFisher, Waltham, Massachusetts, USA) and expanded in LB broth before extracting and purifying using the NEB miniprep kit (New England BioLabs, Ipswich, Massachusetts, USA).

6.2.3 PCR Screening

Populations were screened using PCR to detect the *LAMB*1-Dendra2 insert (forward primer TGGGTCTTTTCACACAGGCT, reverse CAGGGCCATGTTGATGTTGC, amplicon 785 bp). Single cell clones were generated by seeding 0.4 cells/well and expanding, then screened using PCR primers in *LAMB*1 exon 34 and 3′ untranslated region (3′UTR) (Forward GGAGAAGTCCGTTCACTCCT, reverse AAGGGATTCATCAACAATCAGTGA: 274 bp amplicon in non-edited cells, 967 bp with Dendra2 insert). 25 µL PCRs were run using 1 ng of genomic DNA, 1 µM primers, 12.5 µL REDTaq® ReadyMix™ PCR Reaction Mix (Sigma-Aldrich), with the protocol; 95 °C for 5 min, 35 cycles of 95 °C for 30 s, 60 °C for 45 s and 72 °C for 1 min, ending with 7 min at 72 °C using a Veriti Dx Thermal Cycler™ (ThermoFisher). Products were separated by electrophoresis on a 2% agarose/TAE gel, and PCR bands purified using Monarch® DNA Gel Extraction Kit (New England Biolabs, Ipswich, Massachusetts, USA) then sequenced by DNASeq (University of Dundee, Dundee, Scotland).

6.3 Results

6.3.1 Dendra2 imaging test

Before embarking on a genome-editing process I first confirmed that I could visualise and photoconvert dendra2 tagged proteins. HEK293a cells were transfected with a Dendra2-LifeACT plasmid, and photoconverted from green to red using the 405nm laser at 5% power (Figure 6.3.1.). Cells with a high expression of Dendra2-LifeACT were easy to convert, attempts to activate the lower expressing cells using up to 100% laser power resulted in photobleaching (not shown). However, it was possible to fully photoactivate a whole cell with high levels of Dendra2 expression.

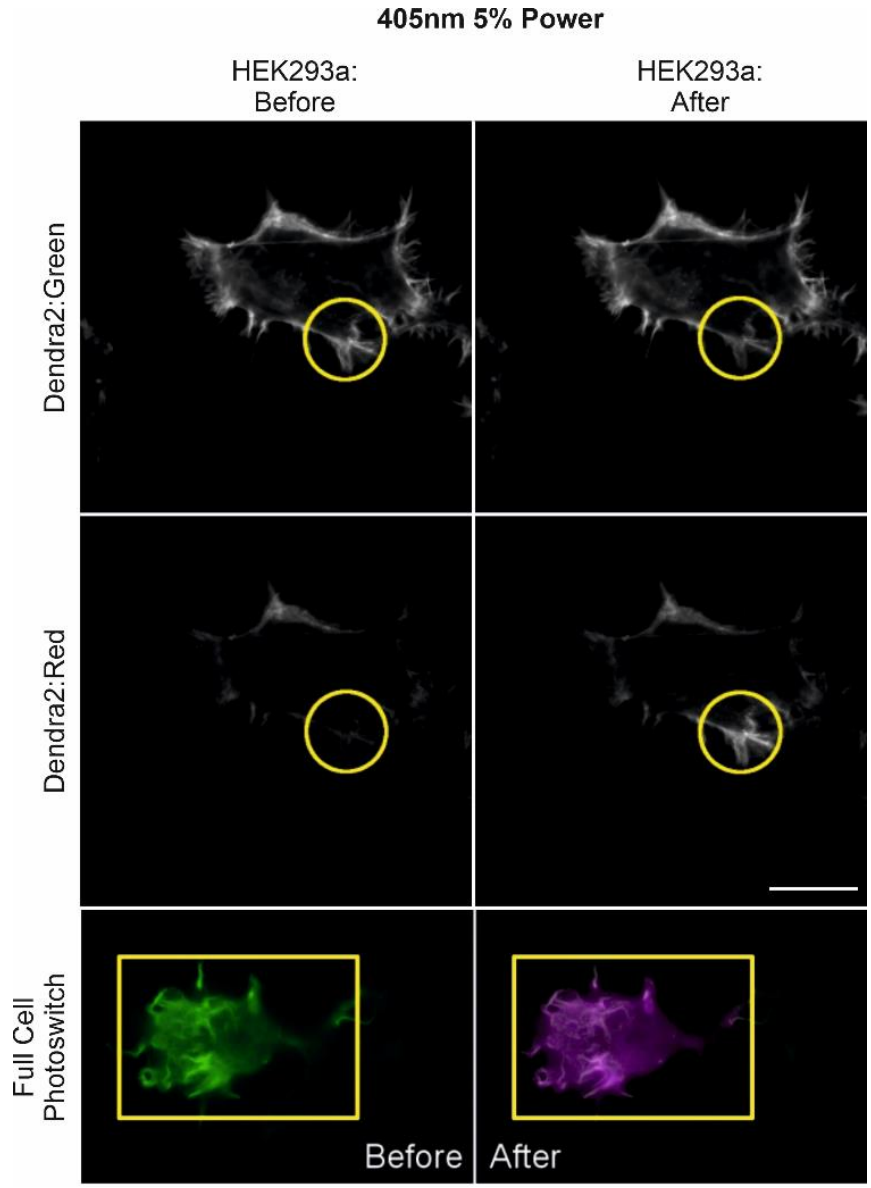

Figure 6.3.1: Photoconversion of Dendra2-LifeACT. HEK293A cells transfected with dendra2-LifeACT were seeded onto glass-bottomed dish and subject to a 405nm laser at 5% power. Regions of the HEK293a Dendra2-LifeACT transfected cell were photoconverted (shown in yellow), with before (left panels) and after (right panels) the photoconversion shown for both Dendra2:Green (top panels) and Dendra2:Red (middle panels). An example of a full cell photoswitch is also shown (bottom panels). Scale bars represent 20 µm.

6.3.2 LMβ1::Dendra2 design

Two important design considerations were made to generate the LMβ1::Dendra2 construct. Firstly, the position of the tag, with two obvious options; the N-terminus or C-terminus of LMβ1. Interference with the LM network formation had to be avoided, making the N-terminus not an attractive option. However, at the C-terminus, there were potential issues with folding with regard the LCC domain and LG domains. However, in the studies involving the LMβ1 ortholog, *lam-1* in *C.elegans* (340), the Dendra2 and GFP tags were engineered at the C-terminus. As these studies demonstrated that a BM-incorporated protein was produced which worked for super-resolution microscopy, tagging the C-terminus of LMβ1 was selected.

A second consideration in the design was avoiding disruption of the cysteine residue in the 3rd position (119) from the end of the LCC domain of LMβ1. This cysteine is essential for the formation of the LM coiled-coil heterotrimer with the LMα and γ chains, and thus for the secretion of the heterotrimeric protein (289, 341). To help avoid interference with the heterotrimerisation process, a small linker sequence (GSGSNTPGINLIKED) was inserted between the LMβ1 C-terminus and the Dendra2 sequence. This linker sequence was designed to contain a small, mostly non-polar residues to avoid distortion of native protein folding (Figure 6.3.2a).

A549 lung adenocarcinoma cells were selected as I confirmed previously that they expressed mainly LM511 and LM332, with a higher abundance of LM511 (Chapter 4). This means that mutations caused to LM511 are less likely to result in the cells “switching” to a different LM heterotrimer such as LM521.

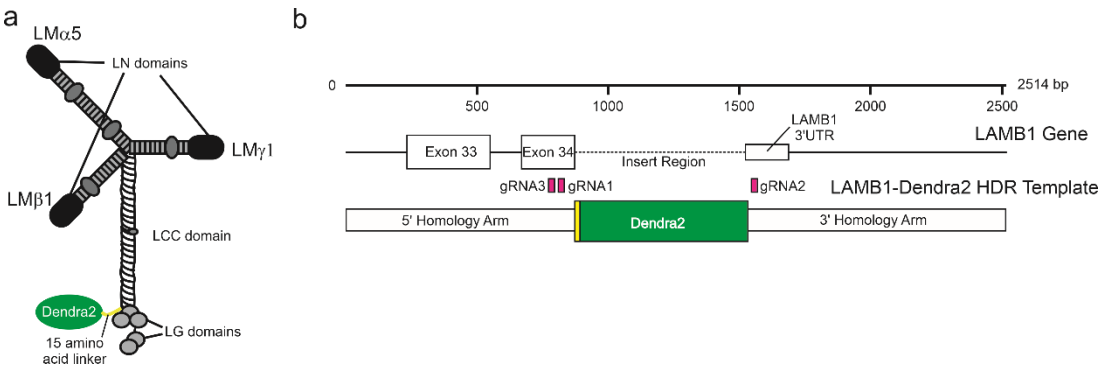

Figure 6.3.2: Design of *LAMB*1::Dendra2 HDR donor template. 1a) Diagram of desired insertion of Dendra2. b) Linearised sequence map of the *LAMB*1-Dendra2 HDR template donor, with gRNA PAM sites highlighted in pink and linker sequence in yellow.

6.3.3 Establishment of LMβ1::Dendra2 clonal line

A549 cells were transfected with a *LAMB*1-Dendra2 HDR donor template and one of three different gRNA, each specific to different protospacer adjacent motif (PAM) sites within exon 34 or 3' UTR of LMβ1 (Figure 6.3.2b). Each gRNA was screened for mismatches and had greater than three mismatches within other genes (Supplemental Table 2)

DNA was extracted from the transfected cells and screened for the presence of Dendra2 between exon 34 and the 3'UTR of the LMβ1 gene. PCR from transfected cells showed a band matching the *LAMB*1-Dendra2 HDR template positive control for gRNA1 and a weaker band with gRNA3 (Figure 6.3.3a). Cells from all three gRNA populations were also visually screened by confocal microscopy, which also indicated that gRNA1 had a higher proportion of green cells compared to the gRNA3 (Figure 6.3.3b).

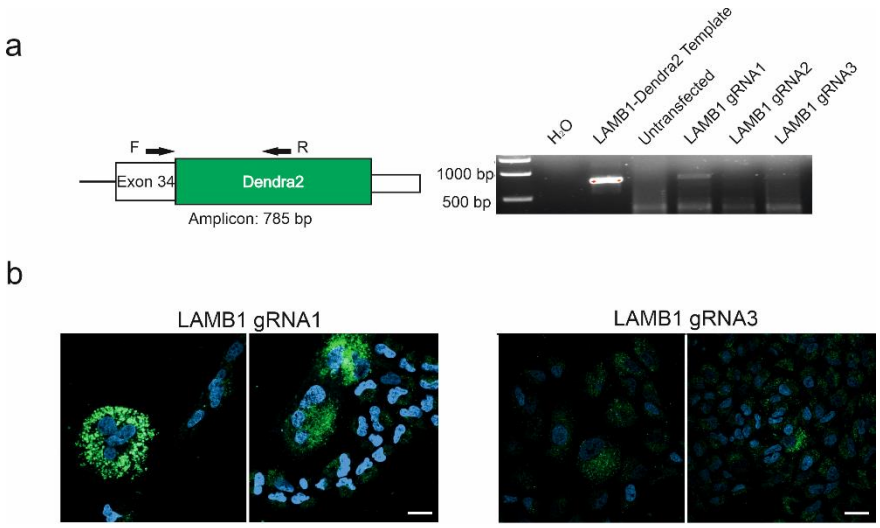

Figure 6.3.3: Transfection and selection of gRNA for cloning. a) Gel image from PCR performed on DNA from transfected cells and using primers designed to amplify only when the Dendra2 sequences was inserted in the appropriate genetic location. c) Transfected cells were seeded onto glass coverslips and fixed 48 h later, then counterstained with DAPI and imaged by confocal microscopy. Scale bars represent 20 µm.

gRNA1 was selected for single cell cloning (Figure 6.3.4a): >500 clonal populations were expanded and screened in a two-step procedure. First, by microscopy for green protein expression (Figure 6.3.4a), then second, by PCR using primers designed to generate two potential products; 967 bp when Dendra2 was located between exon 34 and the 3'UTR, and 274 bp from non-modified *LAMB*1 (Figure 6.3.4b). These primers also allowed detection of whether the clones were heterozygous or homozygous, with heterozygous clones displaying both the 967 bp and 274 bp bands. Despite screening over 500 clones, this screening only identified a single clone, 59B2, as heterozygous for the *LAMB*1-Dendra2 (Figure 6.3.4b). DNA sequencing of the 967 bp band confirmed it to be *LAMB*1-Dendra2 (Figure 6.3.4c).

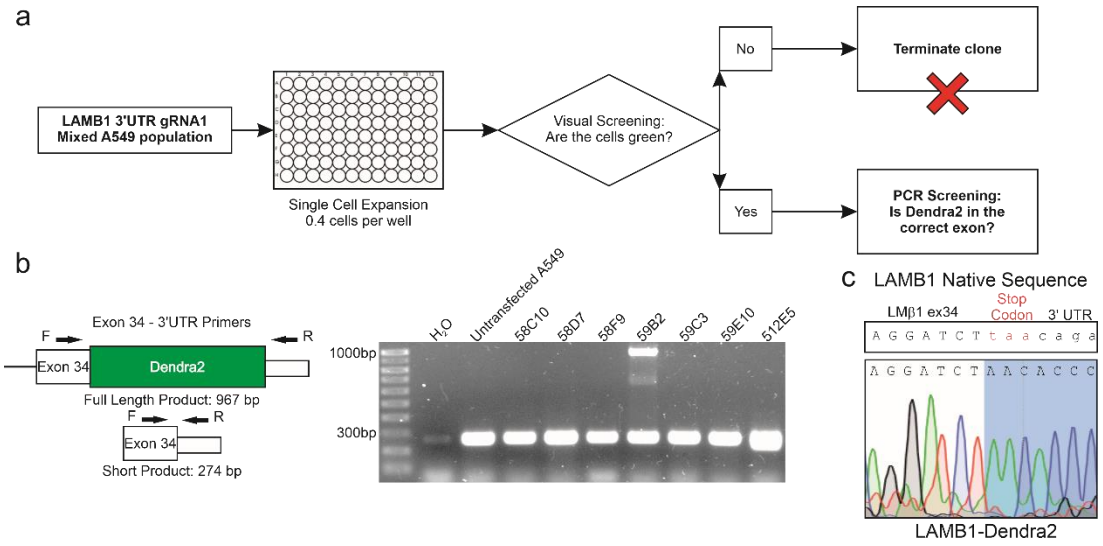

Figure 6.3.4: Establishment of the LMβ1::Dendra2 clonal line. a) Diagram highlighting the screening workflow of >500 single cell clones. Cells were expanded from single cells then screened based on green protein expression. Green clones were expanded then further screened using PCR. b) Representative PCR gel from secondary screen on green clones using primers designed to give two potential products, a short (274 bp) and a full (967 bp) product in successfully edited cells only. c) Positive clone 59B2 was sequenced to confirm for the presence of Dendra2. Start of the Dendra2 insert shown in SnapGene (LMβ1::Dendra2), with the sequence for exon34 and the 3'UTR of LMβ1 shown for reference.

6.3.4 LMβ1::Dendra2 is expressed but not secreted from edited cells

To confirm expression of the LMβ1 protein tagged with the Dendra2, whole cell extracts, matrix only and concentrated conditioned media extracts were collected from wild-type A549 cells and 59B2 LMβ1::Dendra2 cells (Figure 6.3.5a, b). Consistent with heterozygous expression of LMβ1::Dendra2, a second band above the native LMβ1 band was obtained in whole cell extracts from the edited clone but not controls (Figure 6.3.5a). However, in ECM preparations and conditioned media extracts, there was no evidence of the LMβ1::Dendra2 band although LMβ1 was detected, indicating the tagged protein either was not secreted or the tag was proteolytically removed (Figure 6.3.5b).

Next, the green signal from the edited clones was analysed using confocal microscopy. Z stack of images from 59B2 cells revealed the Dendra2 signal to be restricted to within the cytoplasm around the nucleus and translational organelles (Figure 6.3.5c) and not in the characteristic LMβ1 distribution patterns beneath the cells. Moreover, processing with antibodies against LMα5, the major heterotrimeric partner of LMβ1 in A549 cells (342) revealed a similar deposition pattern both in the edited and the control cells (Figure 6.3.5). Finally, cells were removed from coverslips using ammonium hydroxide to visualise the ECM (Figure 6.3.5e). Although LMα5 was detected in the ECM, there was no detectable Dendra2 signal within the ECM of the 59B2 cells (Figure 6.3.5e).

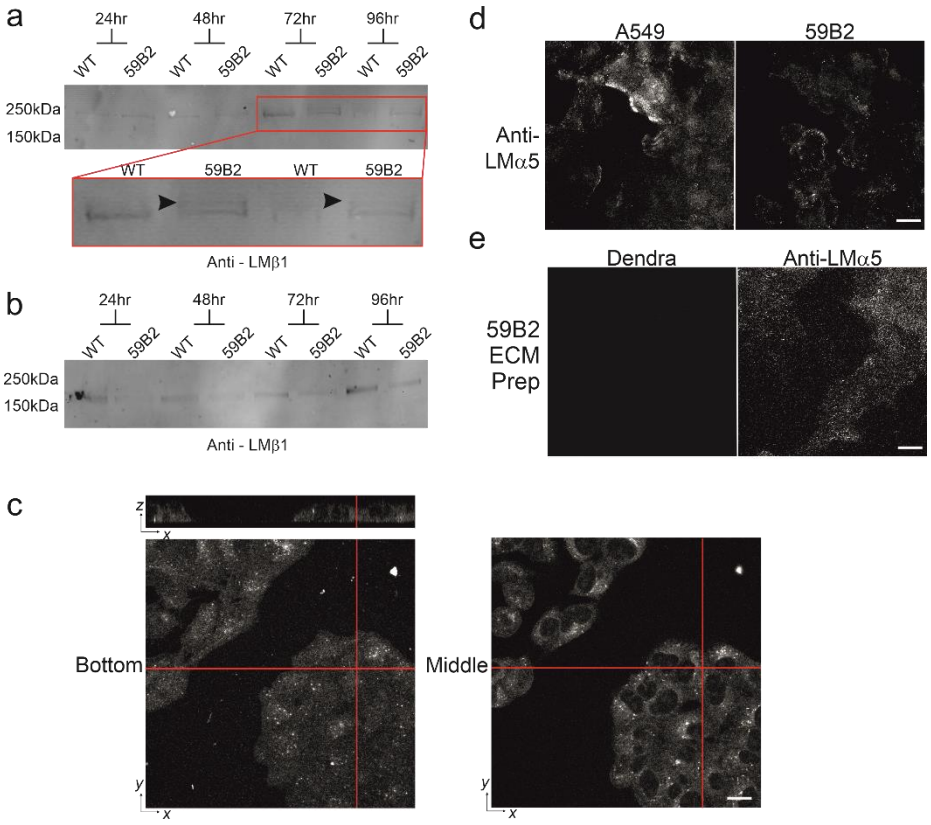

Figure 6.3.5: LMβ1::Dendra2 is expressed inside cells, but no secretion of LMβ1::Dendra2 was observed. a) Total cell lysates from A549 or 59B2 LMβ1::Dendra2 edited cells were processed by western immunoblotting with anti-LMβ1 antibodies. Red box represents an enlarged section of the blot. Arrowed indicates additional upper LMβ1 band consistent with LMβ1::Dendra2. b) Conditioned media and extracellular matrix lysates prepared for the indicated times then processed for immunoblotting with anti-LMβ1 antibodies. c and d) Control A549 or 59B2 cells were seeded on coverslips for 72 h then either fixed and imaged with a z-stack (panel c) or processed for indirect immunofluorescence microscopy with antibodies against LMα5 (panel d). In e), LMβ1::Dendra2 cells were cultured for 72 h on glass coverslips then removed with ammonium hydroxide to reveal only the extracellular matrix, then processed with antibodies against LMα5. All scale bars represent 20 μm.

6.3.5 LMβ1::Dendra2 results in a drop in S and M phase

During routine culture of the edited cells, I became aware that the 59B2 cells appeared to exhibit a reduced growth rate compared with the parental A549 or non-edited clones. Cell cycle analysis confirmed this, revealing a reduced proportion of the LMβ1::Dendra2 cells in S phase and M Phase relative to

A549 (8.6 % ± 0.5 SD, and 8.2 % ± 0.5 SD reduction compared with parental A549 respectively, both p-value < 0.01) (Figure 6.3.6).

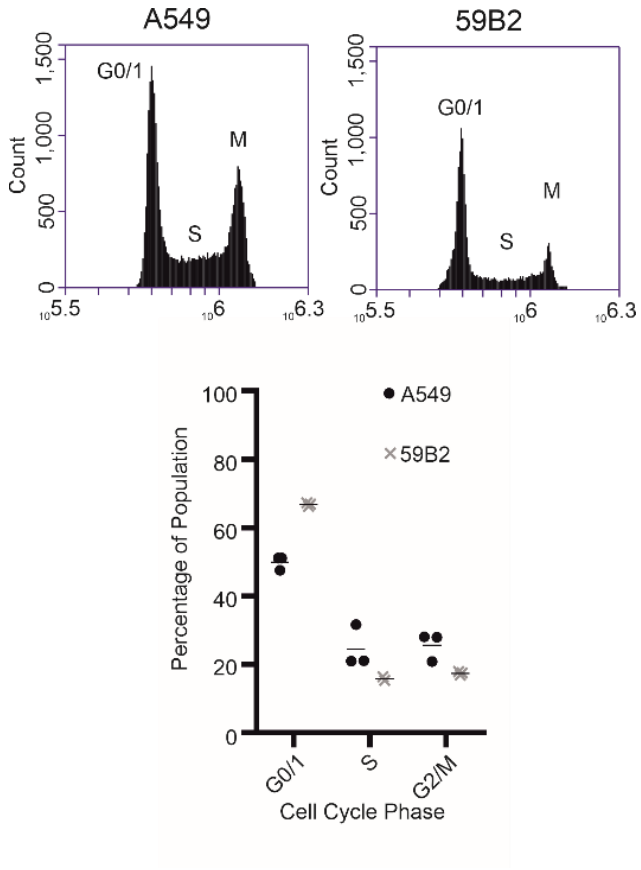

Figure 6.3.6: Cell cycle analysis of 59B2 cells showed a decrease of cells in S and M phase. Cell cycle analysis of 59B2 cells (x's) against wildtype A549 cells (circles) analysed 24 h after serum shock. Proportion of cell population in each phase of the cell cycle was then plotted. Data was plotted in GraphPad.

6.4. Discussion

The findings in this chapter demonstrate that although tagging LMβ1 with Dendra2 at the C-terminus in human cells is possible, the protein is not deposited at detectable levels, which precludes its use for investigating BM assembly and dynamics and which causes detrimental effects to cell proliferation.

There are many potential reasons for the failure in deposition. The most obvious is simply that addition of the Dendra2 tag inhibits either the post-translational processing of the LMb1 protein or interferes with LM trimerisation. Indeed, the presence of LMα5 in the ECM in the edited cells suggests it is only the non-edited LMβ1 that is forming a heterotrimer with LMα5, and, as LM deposition is thought to be driven primarily by the α chain (276), this seems most likely. Note that, based on the C. elegans and human fluorescent LMs studies, the design of the construct included a linker sequence in the LMβ1 C-terminus before the Dendra2, in an attempt to avoid this problem. The ineffective secretion and deposition here suggest a fundamental difference in human LMβ1, but the reason for this difference is unclear. One hypothesis is that the proline in the linker sequence has caused the linker sequence to kink in a way that blocks the C-terminal LCC domain. It is also possible that the linker sequence was not sufficient for the LMβ1 chain, as it was based solely on previous adenoviral work with the LMβ3 chain.

Dendra2 was selected for two reasons. The first is it is a monomeric protein, rather than multimeric like most other fluorescent proteins. This suggests that Dendra2 mediated-self-aggregation was unlikely to be responsible for the observed aggregation of fluorescent proteins inside the 59B2 cells. The second reason was due its high contrast photoconversion, making it possible to distinguish between unconverted and converted fluorescence (331). However, its photoconversion proved to be a challenge. Dendra2 irreversibly converts from green to red upon the breakage of covalent bonds within its monomeric tertiary structure. However, in the edited clones I was unable to produce this photoconversion as in the Life-ACT Dendra2 controls. This could

have been a result of mis-folding of the Dendra2 as a tag, or the stabilisation of the confocal bonds through interactions with either the LM long-arm or the linker sequence. With this taken into consideration, any future work should explore the possibility of other photoconvertible or photoactivatable tags.

In these studies, only a single clone containing the successful LMβ1::Dendra2 edit was obtained, despite screening a large number of clones. This is most likely explained by the cell cycle defect in the edited cells. It appeared that all fluorescent signal was localised within the cell's endoplasmic reticulum (ER), which would have resulted in high levels of ER stress within the cell, consistent with a reduced proliferation (343). An alternative explanation is that the cell cycle defect is due to a reduction in LM511 available to the 59B2 cells (half as much LM511), which could have resulted in reduced outside-in signalling through the AKT signalling pathway, and such a reduced proliferation of the cells, as in Chapter 5. Finally, I cannot rule out an unknown off-target genome edit. To lessen this potential problem, the purified Cas9 protein was used which is known to reduce the frequency of off-target cleavage (229), and gRNAs with low non-specific binding potential. Irrespective of the mechanism, the cell cycle defects would presumably be more severe in homozygous mutants, which could also explain the low number of clones obtained.

If future work were to focus on LMβ1, an alternative to tagging the C terminus would be to insert the tag within the short arm of the protein, thereby preventing any issue with LM trimerisation. This approach would require something which did not disrupt the LN domain or secretion signal and which would leave the LE repeats intact. Intriguingly, recent data suggests that this could be possible. Specifically, the crystal structure of the L4 domain was

solved (146) and it was determined that it was not required for the LE repeats to be folded correctly, Thus, if designed correctly, one could potentially replace the L4 domain with the fluorescent protein or insert the protein within this domain. This concept isn't ideal; although not much is known about the function of the L4 domain, it may have ephrin binding capability. Furthermore, substantial in-frame deletions of the L4 domain in *LAMA*2 has been described in patients with congenital muscular dystrophy (147). However, in these patients the LM containing this mutated L4 domain was still secreted suggesting it is structurally sound, and that any phenotype would be due to the loss of L4 domain function (147, 344). Therefore, although this approach might be effective, the interpretation would have to consider those caveats.

Although ultimately this work was unsuccessful in terms of my primary aim, it was still of value. It demonstrated that it is possible to introduce large protein tags into the LM genome, although it illustrates that where and how those tags are introduced is very important. When one considers that for many years expression of fluorescently tagged LMs has been restricted to plasmid-driven expression, often at or near the packaging limits of viral delivery systems. The concept of stably expressing a fluorescent LM was still very attractive. Thanks to the lessons learned here, the groundwork was laid for the creation of the LMβ3 tagged with photoactivatable GFP, which will be discussed in Chapter 7.

Chapter 7: Discussion

The main questions addressed by the work in this thesis addressed the roles of LM polymerisation; whether polymerisation is important from solely a structural perspective or whether there were additional, more intricate systems at play. The importance of the LM polymerisation was clear, highlighted by the severity of phenotypes in diseases that lack polymerisation such as MDC1a (345), Pierson Syndrome (346) and specifically relevant here, the syndromic disorder caused by a *LAMA*5 LN domain mutation (347). However, little else besides its role as a structural scaffold was well understood. The studies detailed here have established that LM polymerisation affects many important aspects of cell behavior, not only as a structural scaffold, but also as a component of complex signalling cascades.

The data on the LMα5 mutant cell phenotype has shown that the inhibition of LM polymerisation has a severe detrimental effect on a cell's ability to thrive. The LMα5 mutant cells had a reduction in proliferation, migration distance, attachment rate, and strength of attachment. Importantly, HEK293 cells cultured on the mutant cell-derived matrices shared these phenotypes indicating it is a matrix-driven response. These phenotypes can likely be explained by another key observation in this study; the reduced surface abundance of LM-binding integrins, their subsequent focal adhesion maturation and the impacts of this upon downstream signalling in the cells Integrins were known to have a prominent role in signalling processes of the cell (261, 325), as well as acting as the major binder of LM through LG domains

(128), but how the polymerisation state of the LM network affected the role of integrins had not previously been studied.

LM-binding integrins are the ultimate extracellular matrix sensor. They are intimately involved in the attachment of cells to the extracellular matrix (124, 128, 256), the recruitment of focal adhesion proteins to the cell membrane in response to the extracellular matrix (250), and acting as the receptor that signals to activate the AKT signalling cascade (46, 47, 283). Without the integrins, cells would not actually sense any changes to their extracellular environment in the mutant cells. The findings in this thesis strongly indicate that the integrins detected a fault in the extracellular scaffold in the mutant cells, and communicated this to the cell through reduced signalling cascades. Of course, the LN domains bind a multitude of different ECM related proteins that were not tested for in this study such as the heparan, heparan sulphates and sulphatides (348). However, it is unlikely that the binding potential of these proteins would have been affected enough to induce the phenotypic changes seen in the 13C1 cells as LN domains were still present in the mutant ECM.

These data highlight that although there is a strong structural component to the LM, there is much more to the story as a complete system. LMs are the substrate the cell responds to, but it's the integrins that initiate this response. In some ways, an inhibition of LM polymerisation is actually an inhibition of integrin function.

7.1 Interpreting the cell-based experiments relative to MDC1a

One the primary objectives in conducting the cell-based analyses of the LMα5 mutant cells was to help provide mechanistic explanation of the drivers for the

pathology of LN domain mutant patients and animal models. The main symptoms of MDC1a include hypotonia, muscle weakness and muscle wasting (148, 178, 345, 349); all of which can be explained by data seen in the LMα5 mutant cells. In healthy individuals, muscles require a tight control of force generation, with forces dependent on not only the length of the muscle, but also its shortening velocity (350), and muscles are under a constant tensional force, even when resting (350). One might naturally associate this weakness to the structural defect in BMs associated with weak laminin networks. However, the LMa5 mutant cells themselves had reduced strength of attachment and reduced ability to generate force onto their matrixes. From a structural perspective, this force reduction was already anticipated, but a reduced force was also observed on cells platen on collagen gels. Although the time-course from plating to analysis meant that there would be laminin deposited onto those gels, these assays do suggest that at least part of the force reduction phenotype is connected to the cellular-level changes. In a larger tissue system, cellular changes of this type are likely to have a detrimental effect on a muscles ability to exert force, a likely hitherto unknown contributor to the hypotonia and muscle weakness seen in MDC1a patients.

A second key observation that aids the understanding of LN domain disease is the slower maturation of focal adhesions in LM mutant cells. Skeletal muscles can respond to rapid changes in workload (351). These changes are primarily detected through cytoskeletal tension such that appropriate signals can be generated within the cell (351). One of the main transducers of these signals are the focal adhesion complexes which FAK is recruited to (40). In skeletal muscles, focal adhesion complexes are densely located in the

costamere (352, 353) and the myotendinous junction (354), the main transducers of the skeletal muscles. In particular, the costamere transmits forces laterally to the extracellular matrix (351, 353). In the LMα5 mutant cells. I hypothesise that the reduced surface abundance of LM-binding integrins leads to a slower maturation of focal adhesion complexes and therefore signal transduction. This is likely the case in LMα2 deficient MDC1a patients, and a reduced ability to detect changes in tension within the muscles and react accordingly would lead to muscle weakness in patients.

Many MCDC1a patients experience defects in the central nervous system (CNS) (355). LM-integrin interactions are one of the central drivers of development of the CNS through mediation of nerve cell migration and proliferation (356). One of the more unusual symptoms of MDC1a is the hypointensity of white matter in the brain (357). This is still as of yet unexplained, but there are two hypotheses as to the cause. The first is that the abnormal white matter is a result of increased water content due to impaired selective filtration caused by the LMα2 deficiency (358, 359). The second is that these white matter changes are due to structural changes in the white matter tracts, with LMα2-containing heterotrimers playing an integral role in their development (43, 360). However, when one considers that white matter stem cell differentiation into neurons is guided by the ECM, in particular a tight network of collagen fibrils (361), then the increased disorder in the collagen deposited by LMα5 mutant cells could support for the latter hypothesis.

One of the more complex pathological symptoms of MDC1a patients is the increased and somewhat rampant fibrosis (148, 362, 363). In short, an increase in fibrosis drivers such as TGF-β and renin-angiotensin result in

myofibroblast transdifferentiation and matrix remodeling (362). Unlike in Duchenne's muscular dystrophy, where fibrosis develops during the later stages of disease progression, MDC1a patients see a surge of fibrotic inflammation shortly after birth, as early as 20 days after birth (362, 364). It has been posited that this fibrosis is the main driver of the laminin-deficient pathology, severely altering the myomatrix and having a deleterious impact on post-natal muscle growth (365). The data in this thesis supports this increase in fibrosis with an increase of many collagens as seen in the mass spectrometry data in the mutant cells, likely leading to a fibrotic effect in a 3D culture environment. Indeed, one might interpret the SEM findings are the early stages of an almost fibrotic environment.

The proteomics data leads me to a hypothesis that the increase in collagen protein levels in the mutant cells' ECM is a response to the lack of LM network in the ECM. With the lack of a LM network, the strength of attachment in cells is reduced, and this is transduced to the cell through the reduced integrin signalling. In response to this reduction in integrin signalling, I hypothesise that the cells over-compensate the expression other components of the extracellular matrix, such as collagens, to aid in stronger attachment of the cells. However, the degradation rate of this overexpressed collagen is superseded by the rate of secretion of new collagen by the cells, leading to the formation of fibrotic tissue in MDC1a patients. Concurrent with this hypothesis, previous evidence from *Lama*3 lung-specific KO mouse models suggests that a loss of LM in the ECM leads to an increase in TGFβ activity and pulmonary fibrosis (366). This would then have a detrimental effect on the muscle tissue of MDC1a patients, with extensive interstitial connective tissue

and a lack of regenerating fibers, leading to muscle wastage, and weakness. The lack of LM-integrin interactions in the muscle fibers would lead to a reduced focal adhesion complex maturation in MDC1a patients, and this combined with the fibrosis in the muscles of patients, would lead to hypotonia.

Of course fibrosis is considered to be primarily driven by myofibroblasts (362) and the studies highlighted in this thesis have focused on epithelial cell responses to the ECM. Therefore, it is difficult to predict the extent that the observed changes to collagen deposition has upon a patient's pathology. Indeed, BM integrity is likely to be compromised but how this excessive collagen and reduced LM in the mutant cells would affect myofibroblasts is currently unknown. To directly investigate this in the future, it would be valuable to assess the fibrotic response of myofibroblasts in a mutant LMα5 3D culture model with co-culture of the LMα5 mutant cells and THP-1 cells, a monocyte cell line which promotes fibrogenic activity in response to fibrogenic sensitisers (367).

7.2 Translating these findings to other LM diseases

Although this study was into the effects of a point mutation that prevented polymerisation in LMα5, it is possible to extrapolate how these finding might apply to other diseases where the pathogenic mutation affects LM polymerisation, such as Pierson Syndrome. Pierson syndrome is a disease that effects the LMβ2 chain (346), a LM chain responsible for the initial interactions in LM ternary node formation (122). For this reason, one might expect the phenotype of the mutant LMα5 cells to be less severe than the equivalent Pierson syndrome-associated mutation as the latter are unlikely to

have any form of LM network, stable or otherwise (122). This hypothesis is somewhat supported by the more severe morbidity rates of Pierson Syndrome patients, who often don't survive infancy (191), compared to MDC1a patients who often reach late childhood (368), although the different distributions of the affected laminin chains, of course, complicates this comparison. ((369), Figure 7.1), LMβ2 is much more broadly expressed throughout the body.

Without the intermediate LMβ-LMγ interaction, the LM deposition of Pierson Syndrome patients is likely to be even more disordered than in 13C1 cells, with a completely random deposition and orientation of LM heterotrimers. When applying my Bookshelf Hypothesis, this would result in even less space in the ECM for LM, resulting in a severe reduction of LM in the ECM. Considering the severe fibrosis seen in infants with Pierson Syndrome (370), it is likely that this lack of LM in the ECM would be accompanied by an extreme upregulation of collagen following a similar but more dramatic version of overcompensation mechanism outlined above.

a) LMα2

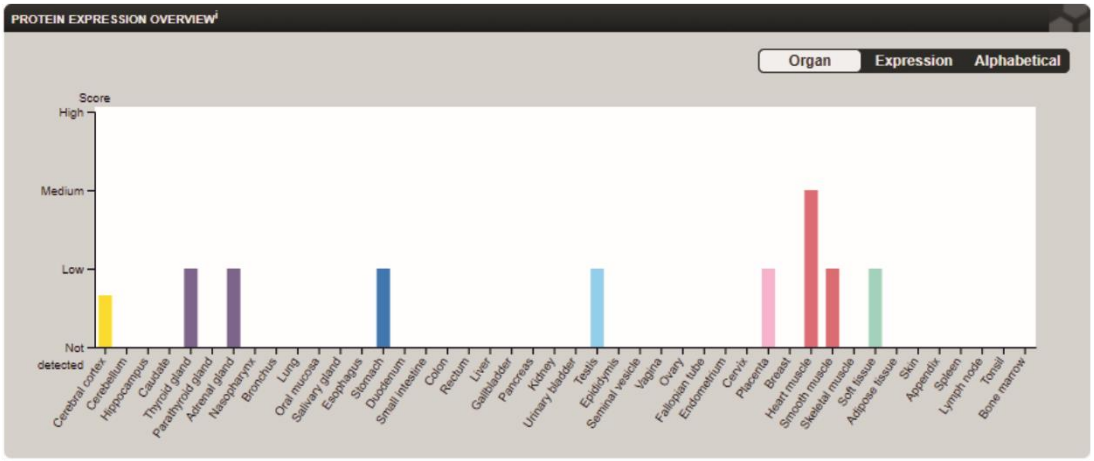

b) LMβ2

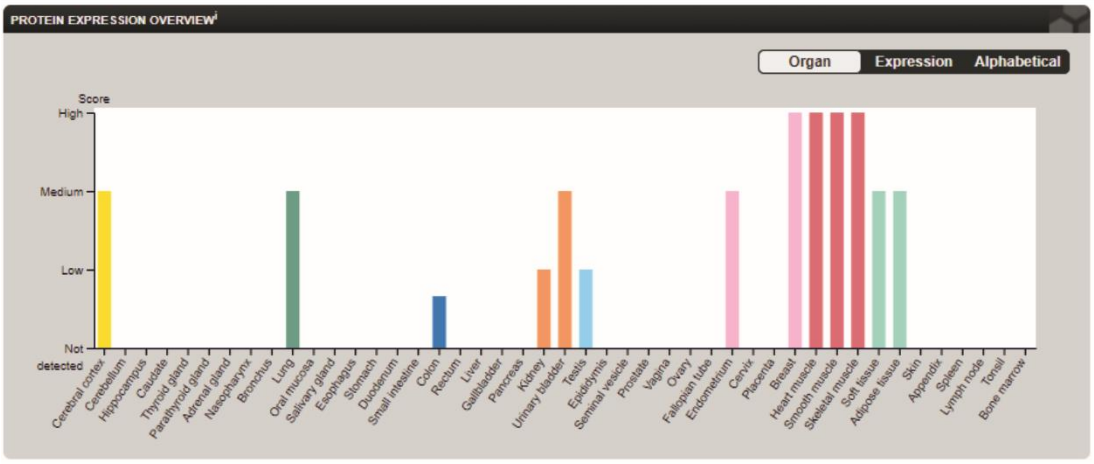

Figure 7.1: LMα2 and LMβ2 expression in different organs. Image credit: Human Protein Atlas (LMα2 (*LAMA*2, top and LMβ2 (*LAMB*2, bottom) images available from proteinatlas.org).

7.3 Relating 13C1 data to existing mouse models

A useful tool in the characterisation of MDC1a pathology were the dy^{3k}/dy^{3k} LMα2 deficient mice (371). These mouse models allowed the study of the effects of LMα2 deficiency in development, muscle morphology (344), organ morphology and disease progression (371), whilst also providing a useful model for potential MDC1a therapeutic studies (355, 372). Whilst an important resource in the understanding of LMα-chain mutations in disease, this model has not been without its limitations from a cell biology standing. Mouse models

do not have the resolution required to investigate the impact on individual cells these diseases cause. Furthermore, many of these models are complete LMα-chain knockouts, so therefore are studies into the absence of LM, rather than the absence of polymerisation (373). Quite interestingly, MDC1a mouse models with complete *Lama*2 KO show a compensatory upregulation of *Lama*4 (374, 375), whereas previous mouse models with α2LN mutations (C79R) do not show this same compensation (178). The LN domain mutant mice had a milder phenotype than models with complete KO, as LMα2 was still present in the BM (178, 373). The model I have made is more a study of LN domain failure than LM absence, and highlights the critical roles controlled by a functioning LN domain. However, the LMα5 LN mutant cell model provides further support for previous findings in these MDC1a mouse models.

One of the findings from the mass spectrometry data was a 1.8-fold increase in the signalling protein TGF-β1 in 13C1 cells. TGF-β1 has been described as the master regulator of fibrosis, responsible for driving fibrosis in most, if not all, forms of chronic kidney disease (376). It has also been identified as a driver of fibrosis in muscles, responsible for inhibiting the regeneration capacity in muscle (377). The new cell data presented in this thesis correlates with LMα2 deficient mouse models, where a substantial increase in TGF-β signalling was detected (378). Interestingly, TGF-β signalling was suppressed by treatment with a losartan derivative (an angiotensin II receptor antagonist), and this was able to reduce fibrosis in the skeletal muscles of the mice (378). It would be interesting if treatment of the 13C1 cells with the losartan derivative could also suppress TGF-β signalling in the cells, and whether this treatment would recover the fibrotic collagen expression in the cells.

One way in which the MDC1a mouse models and the 13C1 cell models differ is in the state of apoptosis within the models. Dy^{3K}/dy^{3K} mice have been shown to have a severe increase in apoptotic cell death, hampering the regeneration of muscle fibers (371). Interestingly the LMα5 mutant cells did not share this phenotype, with no evidence of cell senescence or apoptosis. The LMα5 mutant cells cells did, however, proliferate at a slower rate than the wildtype cells. The likely explanation lies within the mutations present within both models. 13C1 cells simply contain a point mutation in the LN domain of LMα5 that prevents polymerisation. Compare this to the *Lama*2 knockout MDC1a mouse models, where LMα2 is completely absent, and taking into consideration that LMα chains are the driving force for heterotrimer secretion, then is it likely that the abundance of three-armed LM in the ECM of mice is even lower than in the ECM of LMα5 mutant cells. This is despite the upregulation of the two-armed LM411 in the mice models (375). There is also likely a physiological component to this, when considering the dynamic tensions cells are under in a skeletal muscle tissue (379), compared to the relatively constant tension of tissue culture plastic. Perhaps the reduced LM in the LMα5 mutant cells-derived ECM is sufficient for cells on tissue culture plastic to avoid the apoptotic response seen in the mouse models, and that the network formed by the compensatory LM411 is not sufficient for the forces exerted in muscles.

Of particular interest with LMα5 mutant cells is the identification of signalling pathways that have not yet been identified in the MDC1a mouse models. AKT signalling, as well as other receptor tyrosine kinase (RTK) signalling cascades, were downregulated in the LMα5 mutant cells, which provide biochemical

explanations for the MDC1a pathology. These signalling pathways have not yet been identified as drivers for pathology in MDC1a, but the distinct changes in signalling may provide new potential therapeutic avenues. Upregulation of AKT signalling pathways may be difficult due to its over-activation being strongly linked to cancers, but the therapeutic potential of the RTKs could be investigated using the MDC1a mouse models.

7.4 Limitations

Although the results presented herein have added to the understanding of the importance and varied roles of LM polymerisation, the work is not without limitations. It is important to note here that the majority of the experiments in this study were 2-dimensional experiments, done on tissue culture plastic or glass, with the exception being the 2.5-dimensional traction force microscopy experiments. These experiments, while very useful to our understanding of the cellular biology of LM polymerisation, are not the most accurate representations of a physiological structure like a muscle tissue. The glass and plastic substrates used in these experiments have a tensional force much higher than those seen in physiological tissues (265). However, when one considers that many of the phenotypes seen in the LMα5 cells correlate with those seen in mouse models, it is likely that any affects seen on glass and plastic will only be amplified on a softer, more physiologically relevant substrate. It is also worth noting here that a functional physiological tissue contains many different cell types, whereas here, the model was much simpler, containing only one cell type. The most relevant drawback of a monolayer culture system stems from the lack of complex, multicellular

microenvironments that exist within a tissue (380). Future work will likely look at the effects of the LMα5 mutant cells in more complete model systems.

One of the main limitations to this work was the low success rate of the CRISPR-Cas9 genome editing. Steps were taken in the design of this study to limit the off-target effects of the Cas9 by transfecting it as a protein using electroporation. The rationale behind this was that Cas9 enzyme has a relatively short half-life when transfected as a protein compared when expressed from a plasmid (381). By reducing the time the Cas9 enzyme spent in the cell, this should reduce off-target cleavage. However, as well as reducing off-target effects, there was the risk-reward element of a possibly much lower transfection rate and/or lower editing efficiency. Also taking into the relatively low success of HDR editing compared to NHEJ editing by CRISPR-Cas9 (231), this was always likely to be a risk. Having extra clones to support the 13C1 and Dendra-59B2 data, and rule out clonal expansion phenotypes, would have been useful. However, the cross-matrix and HEK293 data, as well as the supporting data in Chapter 5, increases the confidence that the phenotypes observed were matrix-derived and not cell-derived. It would have been ideal to complete the integrin and focal adhesion assays on either the cross-matrix assays or the HEK293 cells. In any future HEK293 integrin assay, it is likely that surface integrin expression will also be reduced as it is in the 13C1 cells and conducting these experiments is a priority.

7.5 LMα5 mutant future work

The work in this thesis has laid the ground for a number of future studies. The most obvious study to follow up this work would be into the establishment of a non-polymerizing LMβ1/2 mutant. A LMβ mutant would triangulate the LMα5 mutant data and further test the hypotheses laid out in this discussion. A LMβ mutant would provide data on the effects of blocking the formation of the intermediate LMβ-LMγ chain interaction and should block the subsequent LMα chain stabilisation and ternary node formation. A S68R LMβ1 mutation was attempted in A549 cells at the beginning of this study, but these attempts proved unsuccessful. This was possibly due to low genome editing success, as seen with the LMα5 mutant. However, the field of CRISPR-Cas9 genome editing is constantly evolving. Future work could attempt to make use a Cas9 protein with selection tool, such as the pSpCas9(BB)-2A-GFP plasmid, which expresses a GFP-tagged Cas9 protein where it is possible to clone in gRNA (382). In addition to this fluorescent tag, this plasmid also contains an ampicillin selection gene (382). Although off-target effects of the genome editing may be increased by use of this plasmid, the increased efficiency of the on-target genome editing would justify this risk.

Once a non-polymerizing LMβ mutant has been established, the next obvious course of action would be to start more complex, physiologically relevant culture models. In particular, the use of 3D culture models for both the LMα5 and LMβ1 mutants could provide a useful tool for the study of LM polymerisation in a more physiologically relevant setting. A549 cells, an alveolar cell line and parental cell line for 13C1's, have been used in 3D culture models previously, forming almost alveolar 3D spheroids over 7 days in a

hanging drop culture (383). It would be interesting to see whether the 13C1 cells could form similar spherical structures in 3D culture, despite their compromised ECM.

Mutant cell models could also be used to investigate the effects of the compromised extracellular matrices on cells of other lineages. Pierson Syndrome and MDC1a are known to affect multiple different tissues and organs (355, 384). These organs were not the central focus of this study, but future work could investigate the effects of the mutant ECMs on cells from the kidney or lens epithelium for example, with organoids from both having been used in the past for BM experiments (95, 385, 386). This work could follow the approach of the cross-matrix and HEK293 cell assays, where cells containing the point mutation were removed for the culture of different cell lines on top of the remaining cell-derived matrices. These assays could even incorporate aspects of the 3D studies. For instance, kidney cells cultured on non-polymerizing LMβ ECM could be used to recreate the interplay seen in the glomerular filter (6, 73, 387). This model could incorporate a flow mechanism over the top of the cells, to study how efficiently the cells cultured on mutant matrices retain macromolecules and cells, but allow the filtration of smaller molecules and water. Another example would be the culture of lens cells on mutant membranes. Bovine lens capsules provide a useful scaffold for the culture of cells, containing many growth factors essential for cell maintenance (388), and having the unique distinction of having a very simple basement membrane (389, 390). This lens basement membrane could be treated with guanidine hydrochloride (as with the SEM work in this thesis and previous studies (391)) to remove the LM but leave the collagen scaffold. The *LAMA*5

mutant cell models could then be cultured until they deposit their own LM, removed as described previously, and lens cells cultured on top to study the effects of mutant matrices on a 3D BM assembly.

With the extensive fibrotic collagen expression of the 13C1 cells, it is likely that the mutant cells are presenting with pro-inflammatory antigens on the cell surface. These antigens, such as IL-8 (392), IL-β (393) and others, could be identified using flow cytometry. The identification of these pro-inflammatory markers could provide new potential therapeutic avenues to target fibrosis in MDC1a and Pierson Syndrome.

On the subject of therapeutic avenues, an interesting finding that requires further investigation was the potential for rescuing the pathological phenotype of the cells. Cross-matrix studies showed a marked improvement in strength of cell attachment. Although not possible to directly recreate in in vivo models, it does support the idea that if the ECM can somehow be rescued, the severity of the disease will be decreased. Two therapeutic options could exist here; LaNt α31 and peptide treatment. Laminin N-terminal domain (LaNt) α31 is naturally produced short protein consisting of an α LN domain with a unique C-terminus that arose from an intron retention and alternative polyadenylation event (125). Previous work has shown that replacing the missing LN domain through short LN domain-containing chimeric proteins has reduced the severity of MDC1a in vivo (394), but LaNt α31 has the benefit of occurring natively. This short protein has the potential to integrate into LM networks and to stabilise the LMβ-LMγ interaction (395), which could provide a therapeutic avenue to lessen the severity of MDC1a. Potential therapeutic avenues could increase the expression of LaNt α31 in a tissue-specific manner (396). With

Pierson Syndrome lacking LMβ2, LaNt α31 would not be a suitable therapeutic. Instead, the rescue of the Pierson Syndrome phenotype could involve the use of peptides based on the βLN domains. Short fragmented βLN domains have been used in the past for in vitro studies (168), and synthetic peptides derived from the α5 LN have been used to enhance cell attachment in the past (397, 398). Recent work suggests that two binding sites (for both the LNα and LNγ domains) rather than one would need to be mirrored in such a peptide, however (399). A peptide could likely disrupt one of the binding sites through competition, but it is unlikely that it would bind to both binding sites and therefore compensate for the loss. One might predict that a peptide based off the βa-βb hairpin loop of βLN domains may be able to bind the LNγ domain, but without the LNα binding site, it is likely to have little therapeutic use.

7.6 LMβ1-Dendra2: Future avenues

In Chapter 6, it was shown the introduction of photoactivatable Dendra 2 tag to the C-terminus of LMβ1 inhibited the secretion of the LM511 heterotrimer. Although ultimately this work was unsuccessful in terms of my primary aim of creating a photoactivatable LM, it was still of value. It demonstrated that it is possible to introduce large protein tags into the LM genome, although it illustrates that where and how those tags are introduced is very important to the formation and secretion of the LM heterotrimer. However, when one considers that for many years expression of fluorescently tagged LMs has been restricted to plasmid-driven expression, often at or near the packaging limits of viral delivery systems, the concept of stably expressing a fluorescent LM was still very attractive. Thanks to the lessons learned here, it paves the avenue for some incredibly exciting future work.

The first interesting avenue to take this work in the future would be to base our photoactivatable fluorescent tag more strongly on the original adenovirus (324). In my study, LM511 was the desired heterotrimer to tag as the data would have connected with the LN domain mutant work. My design was based on work on the introduction of an mCherry tag to LMβ3 (LM332) (324). However, this proved more complicated that initially envisioned, possibly due to the blocking of the cysteines in the LCC domain by the large Dendra2 tag. However, my work had showed it was possible to tag LM using CRISPR-Cas9 for the stable expression of a fluorescent LM, as a permanent natively expressing LM.

Following the initial disappointment, I generated a new design to introduce a PA-GFP tag prior to the 3' UTR of the *LAMB*3 gene, creating a stably expressed LMβ3-PAGFP (Figure 7.2a-b). This design is based directly upon the LMβ3-mCherry adenovirus (324); with a small 20 amino acid linker was introduced prior to the inclusion of the PA-GFP tag (Figure 7.2b). This was designed to result in two tagged LM heterotrimers, the two-armed LM3B32, and the one-armed LM3A32 (Figure 7.2a). Following initial test run transfections, human corneal epithelial cells (hTCEpi cells) were successfully transfected and provided first evidence of a photoactivatable LM that is stably expressed (Figure 7.2c). Due to time constraints, this was as far as this work was carried out by myself, but this work will be continued in the future.

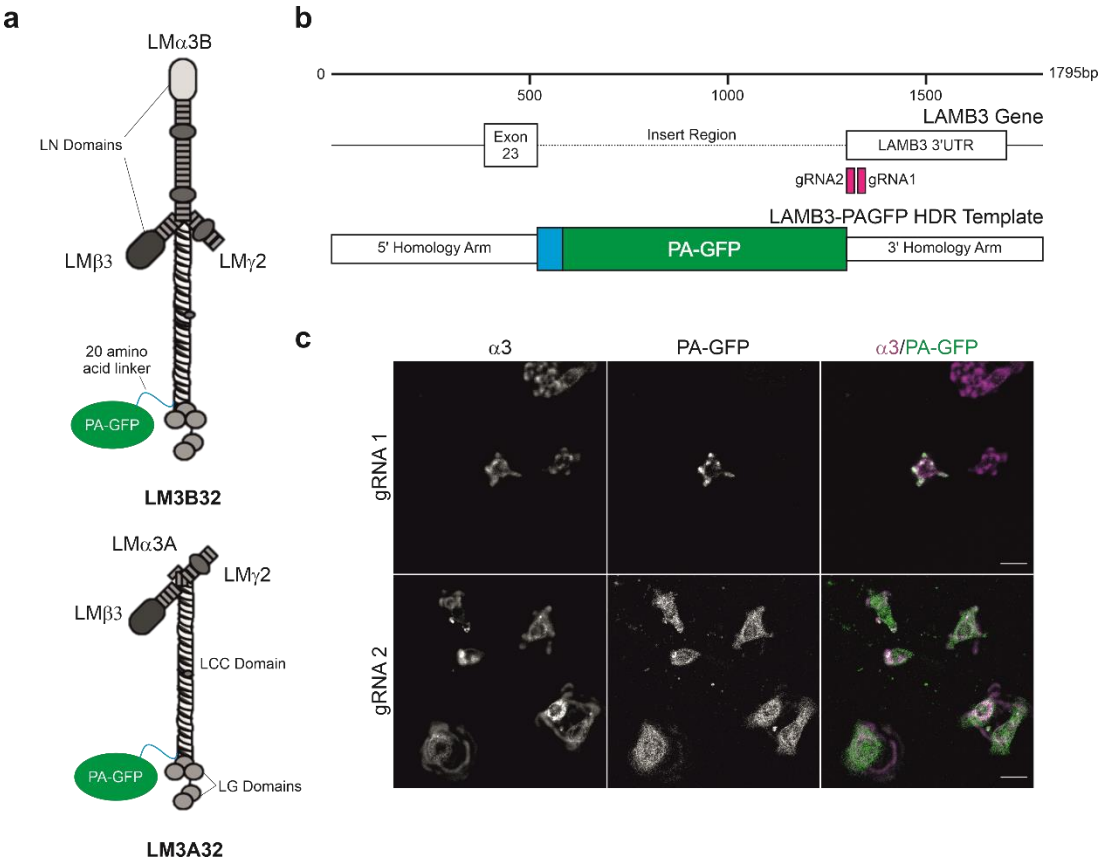

Figure 7.2. CRISPR-Cas9 Design of LMβ3-PAGFP. A) Introduction of a PA-GFP tag to the C-terminal of LM3A32 and LM3B32. B) This was achieved through the introduction of a PA-GFP tag prior to the 3'UTR of the *LAMB*3 gene. Two unique gRNAs were designed for this study. C) This was successfully transfected into hTCEpi cells (middle panels, green). Co-stained with mouse monoclonal antibodies raised against LMα3. Scale bar represents 20 μm.

The work has therefore laid the groundwork for the permanent expression of the photoactivatable LM. An exciting potential for this study lies within the potential use of the tagged LMβ3 as a tool for high throughput drug screening (Figure 7.3). In the severe blistering disease JEB, mutations to the *LAMB*3 gene account for 79 % of all cases, and of these cases, a single point mutation is responsible for 64 % of cases; R635X (400). This hotspot mutation is of particular interest as the introduction of an early stop codon makes it a candidate for treatment with stop-codon read-through drugs (401), although to date, no high-throughput screening method exists. This is one area where a tagged LM could provide an exciting tool.

The prevalence of the R635X mutation as a hotspot mutation has meant in vitro models of this mutation currently exist (Figure 7.3a) (402). It would however it would be unlikely that homozygous mutant cells could survive due to their lack of attachment to tissue culture plastics. Instead, if we were able to create a GFP tagged LMβ3 and then introduce the R635X mutation as a secondary course of genome editing, a tool for high-throughput screening method would arise (Figure 7.3b). R635X-meGFP-LMβ3 mutant cells would be seeded into a multi-well plate and would not immediately fluorescence due to the premature stop-codon. Cells would then be treated with stop-codon read-through drugs, in an attempt to restore expression and thereby generate the meGFP signal (7.3b). Using the JEB hotspot mutation as a model, this tool could be adapted to other diseases caused by hotspot mutations, such as cystic fibrosis (F508X in the *CFTR* gene) or, indeed other laminin knockout mutations (403). The cell-based screening platform would allow for mass compound library screens to identify potential future therapeutic compounds.

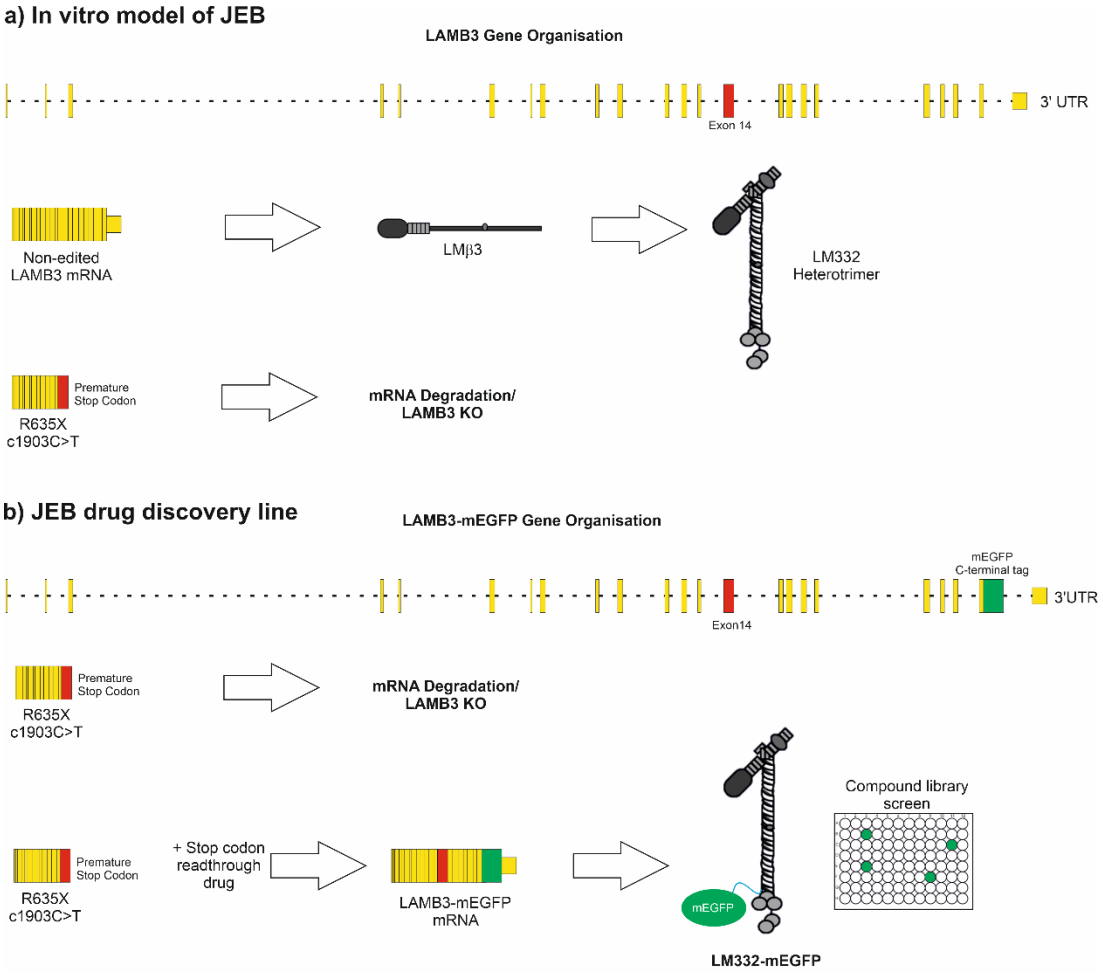

Figure 7.3. Potential model for a JEB drug discovery cell line. a) In vitro models of JEB currently exist using the R635X hotspot mutation, which causes an early stop-codon and premature mRNA degradation and *LAMB*3 knockout (KO). b) However, using what we have learnt about the introduction of fluorescent tags, we could introduce the R635X mutation into the tagged *LAMB*3 gene. This could then be used for the high-throughput screening of stop codon read-through drugs such as gentamicin, in an attempt to recover green signal. This would then be used in compound library screens for potential therapeutics.

7.7 Conclusion

Throughout this scientific adventure, I have investigated the roles of LM polymerisation and the importance of a highly ordered LM network to the maintenance and behaviors of a cell. These cellular behaviors form the basis of all life, and lead to the construction of higher order structures such as

tissues, organs and eventually multi-cellular eukaryotic beings. It is remarkable to think that the interactions of a simple cross-shaped protein has such an important role to play in the development and ability to thrive as an organism. It is hoped that the work outlined in this thesis has gone someway to understanding the intricate and subtle roles that this simple interaction plays in life. A role once thought to be solely structural but is actually part of a much larger and more dynamic picture that we, as a field, have only just really started to fully understand.

Chapter 8: Supplemental data

Supplemental table 1: gRNA sequences and potential off-target loci for the LMα5 PLENGK mutant gRNAs: Off-target sites as identified by Integrated DNA Technologies' CRISPR-Cas9 gRNA Design Checker with mismatches (#MM) threshold set to 3. PAM = Protospacer adjacent motif sequence with only those recognised by purified Cas9 protein (NGG) shown. Off-target genes shown as – represent non-coding regions of the genome.

gRNA	Sequence	PAM	#MM	Gene	Locus
1	**CGTGCCCCTGGAGAACGGAG**	**AGG**		***LAMA*5**	**chr20:-62352243**
	CGTGGCCCATGGAGAACAGAG	AGG	3		chrX:-113262256
	CCTGGCTGTGGAGAACGGAG	CGG	4		chr11:+65915473
	CCTGGCTCTGAAGAACGGAG	AGG	4		chr1:+59540756
	CCCGCCTGTGGAGAACGGAG	AGG	4		chr13:+52933988
	TGTTCCCCTGGGAGAACGGAG	GGG	3		chrY:+1609267
	TGTTCCCCTGGGAGAACGGAG	GGG	3		chrX:+1609267
	AGTGACCCTGAAGGACGGAG	GGG	4		chr13:+111580101
	CATGACCCTGAAGAACGAAG	TGG	4	LOC107986865	chr8:+2665354
	GGGGCCCTTGGAGGACGGAG	TGG	4		chr13:+112176752
	AGTGCCAGTGGAGAATGGAG	AGG	4		chr10:+78650608
	TCTGCCCTTGGAGAAAGGAG	GGG	4		chr10:+101230773
	AGGGCCCATGGAGAACAGAG	AGG	4		chr10:+132107931
	GGTGCCAGGGGAGAACGGAG	GGG	4		chr16:-557195
	CCTGCCCTCTGGAGAAAGGAG	AGG	3		chr15:+33412525

AGTGCCCCTGGAGAGTGGAG	AGG	3		chr15:+81410693
TGTTCCCCGGGAGAACAGAG	AGG	4		chr11:-36279537
ACTGCCACTGGAGAACTGAG	AGG	4		chr2:+138829599
TGTG-CCCTGGAGAACTGAG	CGG	3	RNF223	chr1:+1066832
CCTGCCCCTGAAGAGAGGAG	AGG	4		chr11:+117735460
CGTAACCCTGCAGAACGAAG	AGG	4		chr10:-128864453
CATGGCCCTGCAGAATGGAG	GGG	4		chr1:-205477719
CCTGCCCCTGGAGGACAGTG	TGG	4		chr2:+100819571
CCTCCCCCTGGGGAATGGAG	GGG	4		chr2:-17912639
CGAGGCGATGGAGAACGGAG	CGG	4	CMTM6	chr3:-32502732
CCTGCCCCTGGAGGAAGGAG	GGG	3		chr10:+98294775
ACTGCCCCTTGATAACGGAG	GGG	4		chr2:-121323071
AGTGCCCCTCGAGAATGGAG	TGG	3	LOC107987137	chr9:-134209091
CGCGCCTCGGGAGAGCGGAG	GGG	4		chr2:+96116751
GGTGCCCCTGGGGAGAGGAG	TGG	4		chr18:-9732112
GGTGCTCCTGCAGAACGGAG	TGG	3		chrX:-115906989
CCTGCCACTGGAGAACGGGA	GGG	4		chr8:-38404379
CGAGTCCCTGGAAAAAGGAG	AGG	4		chr17:-57863401
CATCCCCATGGAGAACGGCG	TGG	4	KCNJ11	chr11:-17387361
CGTGTCCCCGGAGGAAGGAG	CGG	4	GXYLT1P3	chr9:+40348677
CGTGTCCCCGGAGGAAGGAG	CGG	4		chr9:+64488678
TCTGCCCCTGGAGAGGGGAG	GGG	4		chr1:+29453640
CGTGTCCCCGGAGGAAGGAG	CGG	4		chr9:-66027620
CGTGACCCTGGGGAACGGTT	AGG	4		chr16:+81676084
TGTGCCTCTGGAGAACAGGG	TGG	4		chr1:-164157348
CGTGCACCTGCAGGACAGAG	AGG	4	LOC105378042	chr6:-146857358

	GGTCCCCCTGGAGAAGGGAA	AGG	4		chr1:+36135431
	GGTGGCCCCGGAGAAGGGAG	AGG	4	ATG2A	chr11:-64909085
	CATGCCCCTGGAGAACCAAG	CGG	3		chr17:+66823119
	CGGGCCCCCAGAGAAAGGAG	TGG	4		chr18:+75863503
	CGTGGCCCTGAAGAAGGGAA	TGG	4		chr19:-14584745
	CGTGGCCCTGAAGAAGGGAA	TGG	4		chr19:-14589006
	CGTGCCCTTGGAGGACACAG	TGG	4		chr12:-53217348
	CGTTGCCATGGAGACCGGAG	AGG	4		chr16:-24686144
	GGTGCCCCTGG-GAACCGAG	GGG	3		chr17:+18968710
	CGTGAGCCTGGAAAACGGAG	GGG	3		chr16:+88158630
	GGTGCCTCTGGAGAAGAGAG	AGG	4		chr20:-23600786
	CTTGCTCCTGAAGAAAGGAG	AGG	4		chr8:-20150922
	CCTGCCCCAGGAGAACAGAT	CGG	4		chr8:+138833247
	CGTGCAACTGGAGAGCGCAG	AGG	4	PFKP	chr10:+3104863
2	**CGCATCGTGCCCCTGGAGAA**	**CGG**		***LAMA*5**	**chr20:-62352248**
	CGGCTCGCGCACCTGGAGAA	GGG	4		chr21:-36693172
	CCCAGCATGTCCCTGGAGAA	GGG	4		chr7:+154775731
	CTAATCATGTCCCTGGAGAA	GGG	4		chr17:-28510977
	TGCACC-TGCCCCTGGAGAA	GGG	3		chr13:-29976796
	AGCCTCGT-CCCCTGGAGAA	CGG	3		chr19:+44792807
	TACATCTTGCCCCTGAAGAA	GGG	4		chr15:-100531313
	CCCAACTTCCCCCTGGAGAA	GGG	4		chr1:+225769505
	AGCTTCCTGCCCCTGGAGAA	GGG	3		chr13:-51801806
	GGCAGCGTGTCCCTGGGGAA	GGG	4		chr16:+11670388
	GGCACCGTGCACCTGGAGAT	CGG	4	B9D2	chr19:-41354745
	CGCTGCGTGTCCCTGGAGAG	GGG	4		chr18:-77342302

CGCTGCCTGCACCTGGAGAA	AGG	4	PDZD3	chr11:+119188065
CTCATCGTCTCCATGGAGAA	GGG	4		chr10:-77526600
GGCCTCTTGCCCCAGGAGAA	GGG	4		chrX:-72354928
CCCATCATTCTCCTGGAGAA	AGG	4		chr1:+224700676
CACAGCGTTCCCCTGGAGAG	AGG	4		chr6:-34110936
CGCACCGGGCCCCAGGAGTA	GGG	4		chr5:-759347
CTCTTCTTGCCCCTGGAGAC	AGG	4		chr1:+47948449
CACATCTGTGCCCCAGGAGAA	TGG	3		chr8:+123678994
CACATCTTGTCCCTGGAGCA	GGG	4		chr4:+107893782
TGCATCGTGCCCTCTGGAGAG	AGG	3		chr16:-67216809
CGCATC-TGCACCTGGGGAA	AGG	3		chr2:-73720264
CGTAT-GTGCCCCTGGAGAG	AGG	3		chr18:-78424091
CCCATCTTGTCCCAGGAGAA	GGG	4		chr11:+133657512
CTCCTCGTGCCCTGGGAGAA	GGG	4		chr12:+130450087
CGAATCTTGTGCCTGGAGAA	GGG	4		chr20:+19391937
CGCACCGTGGACCTGGAGTA	GGG	4		chr15:+96323381
GGCATGGAGCACCTGGAGAA	CGG	4		chr2:-217880995
CGCATTGGGCCCATGAAGAA	TGG	4		chr8:+109379013
AGCCTCGTGCCCCTGGACAT	AGG	4		chr1:-175670204
CTCACCGTGCTCCTGGAGGA	CGG	4		chr2:+236309827
CTCATCCGGCCCCTGGAGCA	AGG	4		chr1:+200888541
CACTTCCTGCCCCTGGAGCA	TGG	4		chr1:-188382651
AGCATCGGACCCCAGGAGAA	AGG	4		chr13:-28819633
TGCAGCCTGCCCCAGGAGAA	AGG	4		chr5:+78639982
AGCATAGTGACCCTGGGGAA	GGG	4		chr20:-48246560
CACATTTTACCCCTGGAGAA	TGG	4		chr8:+50860939

CTCATCGTGCTCCCAGAGAA	AGG	4	chr16:+66236654
CGTATCGTGCCCCTG-AGGA	AGG	3	chr16:-8043924
GGCCTCGTGCCCCTGGACAC	AGG	4	chr6:-3888549
CGCAGCATGCCGCTGGAGGA	TGG	4	chr1:-226890371
CGCACTGTCCTCCTGGAGAA	GGG	4	chr17:-75493405
GGCATCGAGCCACTGTAGAA	AGG	4	chr10:-127447120
GGCATCGTGTCCCAGGAGAG	AGG	4	chr8:+142409375
CTCATCGTGACCTGGGAGAA	GGG	4	chr17:+39139821
CTCATCTTGCCCCTGGTGAG	GGG	4	chr8:-96032639
GGCATCTTGCCCCTTGAGAT	AGG	4	chr5:-81254167

Supplemental table 2: gRNA sequences for *LAMB*1 3'UTR and potential off-target loci: Off-target sites as identified by Integrated DNA Technologies' CRISPR-Cas9 gRNA Design Checker with mismatches (#MM) threshold set to 3. PAM = Protospacer adjacent motif sequence with only those recognised by purified Cas9 protein (NGG) shown. Off-target genes shown as – represent non-coding regions of the genome.

gRNA	Sequence	PAM	#MM	Gene	Locus
1	**ATAGCACATGCTTGTAACAG**	**AGG**	**-**	***LAMB*1**	**chr7:-107923947**
	ATAGCAC-TGTTTGTAACAG	AGG	2	-	chr20:-54489778
	CCAGCA-ATGCTTGTAACAG	GGG	3	-	chrX:-11679804
	ATGGAA-ATGCTTGTAACAG	AGG	3	-	chr2:-132853996
	GTAGC-CTTGCTTGTAACAG	AGG	3	-	chr3:-165621411
	AAAGCACATGCCTGAAACAG	AGG	3	PRAMEF18	chr1:+13223043
	AAAGCACATGCCTGAAACAG	AGG	3	-	chr1:-13005892
	ATGGGACATGCTTGGAACAG	TGG	3	-	chr1:+201360309
	AAAGCACATGCCTGAAACAG	AGG	3	PRAMEF19	chr1:+13368778
	ATAGCCCATCATTGTAACAG	GGG	3	-	chr1:-150169073
2	**AAAAATGGCTGAGGTGAACA**	**AGG**	**-**	***LAMB*1**	**chr7:-107923918**
	AAAAATAGCAGAGGTGAACA	CGG	2	-	chr4:-185889429
	AAACATGGCTGA-GTGAACA	TGG	2	-	chrX:+72314675
	AATAATGGCTGAGGCTGAACA	CGG	2	-	chr22:+18396314
	AATAATGGCTGAGGCTGAACA	CGG	2	-	chr22:+18645927
	AATAATGGCTGAGGCTGAACA	CGG	2	-	chr22:-21349335
	AATAATGGCTGAGGCTGAACA	CGG	2	-	chr22:-18228229

AATAATGGCTGAGGCTGAACA	CGG	2	-	chr22:-18723516
GAACATGGCTGAGGTAAACA	TGG	3	-	chr6:+137830010
AAAAATGCCTAGGGTGAACA	AGG	3	-	chr7:-61764339
AATAAT-ACTGAGGTGAACA	TGG	3	-	chr15:+34472088
AAAAATGCCTAGGGTGAACA	AGG	3	-	chr7:-62183366
AATAATG-CTGCGGTGAACA	TGG	3	-	chr5:-9711216
AATAATG-CTGAAGTGAACA	TGG	3	-	chr3:-192694445
AATCATGGCTGAAGGTGAACA	AGG	3	-	chr11:+69188108
ATACATGGCTG-GGTGAACA	AGG	3	-	chr2:-99577573
AAACTTGGCTGA-GTGAACA	GGG	3	-	chr13:+20246396
AATAAT-GCTGCGGTGAACA	TGG	3	-	chr2:+227929112
AAAAATG-CTGCAGTGAACA	TGG	3	-	chr14:-90224265
AAAAATG-CTGCAGTGAACA	TGG	3	-	chr8:-143542501
AAAAATGCCTATGGTGAACA	AGG	3	-	chr5:-46283174
AATAAT-GCCGAGGTGAACA	TGG	3	-	chr15:+76464689
ATAAATG-CTGTGGTGAACA	TGG	3	-	chr4:-82865451
GAAAATGGCAGAAGTGAACA	TGG	3	-	chr8:+60466821
AATAAT-GCTGAGATGAACA	TGG	3	-	chr9:+2409871
AAAAAT-GCCAAGGTGAACA	AGG	3	-	chr10:+128141546
AATAATGG-TGAAGTGAACA	TGG	3	-	chr6:+39528402
TAAAATGGC--AGGTGAACA	TGG	3	-	chr21:-13962038
TAAAATGGC--AGGTGAACA	TGG	3	ANKRD20A9P	chr13:-18862737

	CAAAATGGCTCACGGTGAACA	AGG	3	-	chr5:+46013513
3	**TTATATCCTTTAGGAGTGAA**	**CGG**	**-**	***LAMB*1**	**chr7:+107923985**
	AAATATCCTTTAGGAGTGAA	GGG	2	-	chr3:-188016088
	AAATATCCTTCAGGAGTGAA	GGG	3	-	chr14:-92066542
	AAATATCCTTCAGGAGTGAA	AGG	3	-	chrX:+72436480
	AAATATCCTTTAGGAATGAA	GGG	3	-	chr19:+33982373
	AAATATCCTTTAGGAATGAA	GGG	3	-	chr2:-46894629
	TAATATT-TTTAGGAGTGAA	AGG	3	-	chr2:-155009215
	TTCT-TCCTTTAGGAATGAA	AGG	3	-	chr18:-27661308
	CTATA-CTTTTAGGAGTGAA	GGG	3	-	chr21:-32994567
	TCATA-CCTTAAGGAGTGAA	TGG	3	-	chr13:+29911258
	CTAGATCCTTTAGGAGAGAA	AGG	3	-	chrX:+13414781
	TAAAATCCTTTAGGAGTTAA	GGG	3	-	chr9:+11381550

Chapter 9: Peer-reviewed publications

Appendix 1: BMC Research Notes 2020

Shaw *et al. BMC Res Notes* (2020) 13:90
https://doi.org/10.1186/s13104-020-04956-z

BMC Research Notes

RESEARCH NOTE Open Access

CRISPR-Cas9-mediated labelling of the C-terminus of human laminin β1 leads to secretion inhibition

L. Shaw*, R. L. Williams and K. J. Hamill

Abstract

Objectives: The laminins (LM) are a family of basement membranes glycoproteins with essential roles in supporting epithelia, endothelia, nerves and muscle adhesion, and in regulating a range of processes including cell migration, stem cell maintenance and differentiation. However, surprisingly little is known about the mechanisms of turnover and remodelling of LM networks due to lack of appropriate tools to study these processes at the necessary resolution. Recently, the nematode *C. elegans* ortholog of human the LMβ1 chain was labelled at the C-terminus with the photo-convertible fluorophore Dendra2. Here we used genome editing to establish a similar system in a mammalian cell line as proof of concept for future mammalian models.

Results: CRISPR-Cas9 was used to introduce the Dendra2 sequence at the C-terminus of LMβ1 in the human lung adenocarcinoma cell line A549. Despite expression of the tagged protein within cells, no detectable LMβ1-Dendra2 protein was deposited to the extracellular matrices or conditioned media of edited cells. Moreover, the edited cells displayed reduced proliferation rates. Together, these data suggest that, in humans, addition of C-terminal Dendra2 tag to LMβ1 inhibits LM secretion, and is not a viable approach for use in animal models.

Keywords: Laminin, Basement membrane, Dendra2, Genome editing, CRISPR-Cas9

https://bmcresnotes.biomedcentral.com/articles/10.1186/s13104-020-04956-z

Appendix 2: Frontiers in Genetics 2021

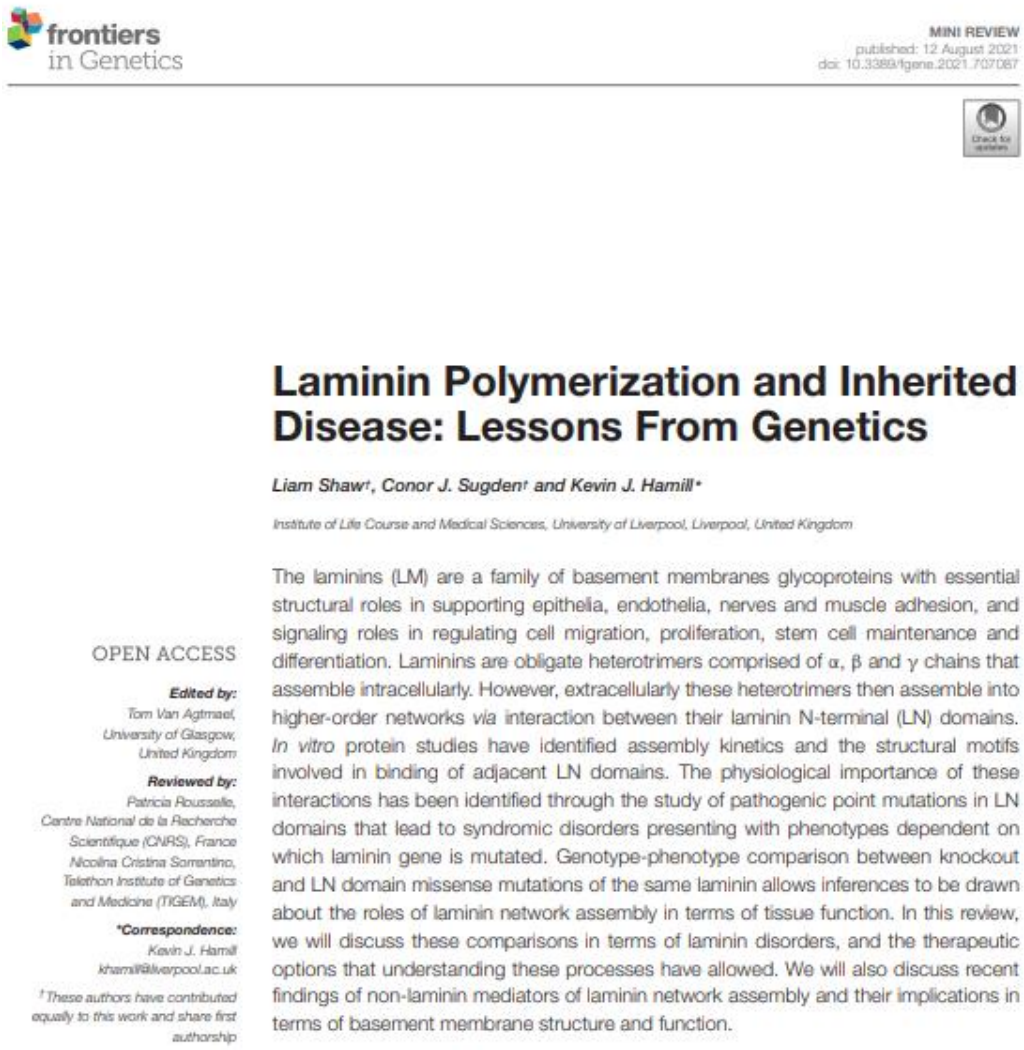

frontiers in Genetics

MINI REVIEW
published: 12 August 2021
doi: 10.3389/fgene.2021.707087

Laminin Polymerization and Inherited Disease: Lessons From Genetics

*Liam Shaw†, Conor J. Sugden† and Kevin J. Hamill**

Institute of Life Course and Medical Sciences, University of Liverpool, Liverpool, United Kingdom

The laminins (LM) are a family of basement membranes glycoproteins with essential structural roles in supporting epithelia, endothelia, nerves and muscle adhesion, and signaling roles in regulating cell migration, proliferation, stem cell maintenance and differentiation. Laminins are obligate heterotrimers comprised of α, β and γ chains that assemble intracellularly. However, extracellularly these heterotrimers then assemble into higher-order networks *via* interaction between their laminin N-terminal (LN) domains. *In vitro* protein studies have identified assembly kinetics and the structural motifs involved in binding of adjacent LN domains. The physiological importance of these interactions has been identified through the study of pathogenic point mutations in LN domains that lead to syndromic disorders presenting with phenotypes dependent on which laminin gene is mutated. Genotype-phenotype comparison between knockout and LN domain missense mutations of the same laminin allows inferences to be drawn about the roles of laminin network assembly in terms of tissue function. In this review, we will discuss these comparisons in terms of laminin disorders, and the therapeutic options that understanding these processes have allowed. We will also discuss recent findings of non-laminin mediators of laminin network assembly and their implications in terms of basement membrane structure and function.

OPEN ACCESS

Edited by:
Tom Van Agtmael, University of Glasgow, United Kingdom

Reviewed by:
Patricia Rousselle, Centre National de la Recherche Scientifique (CNRS), France
Nicolina Cristina Sorrentino, Telethon Institute of Genetics and Medicine (TIGEM), Italy

***Correspondence:**
Kevin J. Hamill
khamill@liverpool.ac.uk

†These authors have contributed equally to this work and share first authorship

https://www.frontiersin.org/articles/10.3389/fgene.2021.707087/full

Appendix 3: PLoS One 2019

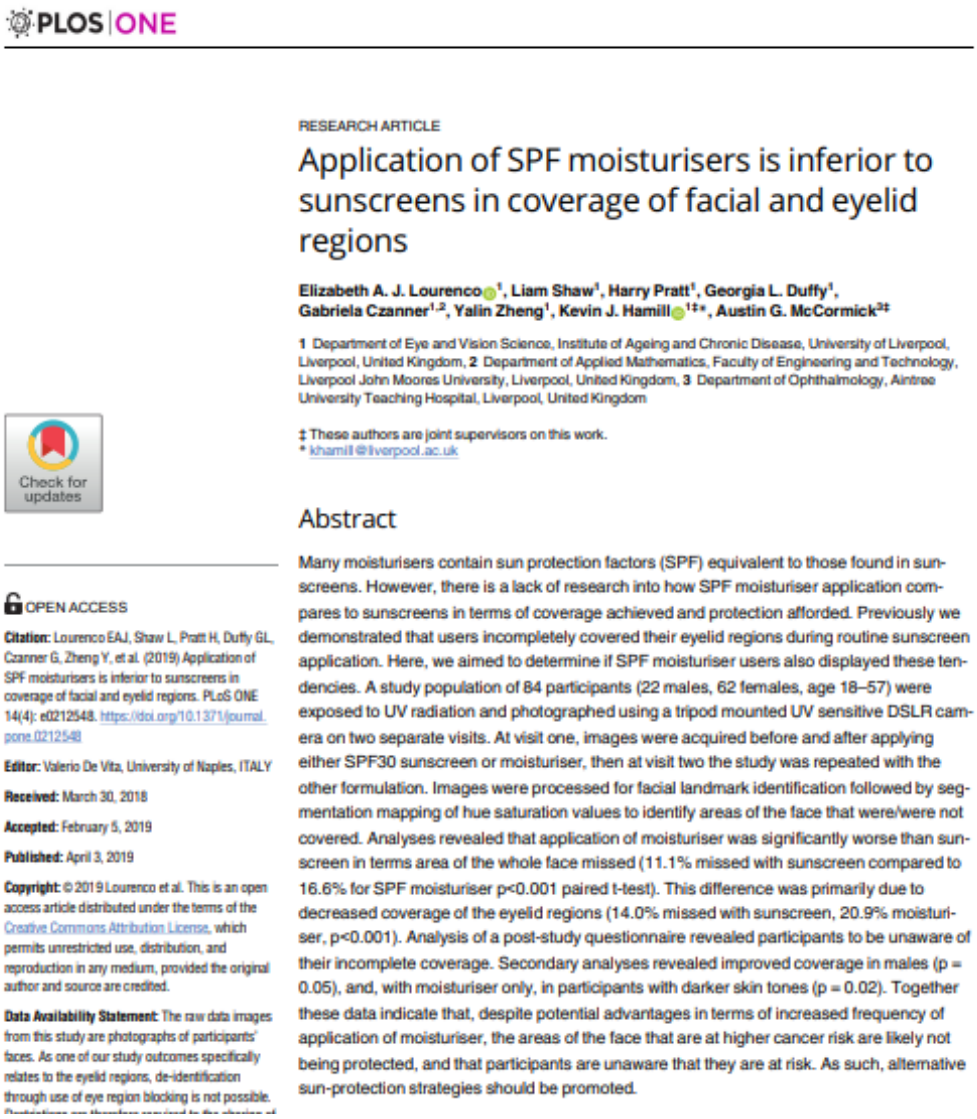

PLOS ONE

RESEARCH ARTICLE

Application of SPF moisturisers is inferior to sunscreens in coverage of facial and eyelid regions

Elizabeth A. J. Lourenco[1], Liam Shaw[1], Harry Pratt[1], Georgia L. Duffy[1], Gabriela Czanner[1,2], Yalin Zheng[1], Kevin J. Hamill[1‡*], Austin G. McCormick[3‡]

1 Department of Eye and Vision Science, Institute of Ageing and Chronic Disease, University of Liverpool, Liverpool, United Kingdom, 2 Department of Applied Mathematics, Faculty of Engineering and Technology, Liverpool John Moores University, Liverpool, United Kingdom, 3 Department of Ophthalmology, Aintree University Teaching Hospital, Liverpool, United Kingdom

‡ These authors are joint supervisors on this work.
* khamill@liverpool.ac.uk

OPEN ACCESS

Citation: Lourenco EAJ, Shaw L, Pratt H, Duffy GL, Czanner G, Zheng Y, et al. (2019) Application of SPF moisturisers is inferior to sunscreens in coverage of facial and eyelid regions. PLoS ONE 14(4): e0212548. https://doi.org/10.1371/journal.pone.0212548

Editor: Valerio De Vita, University of Naples, ITALY

Received: March 30, 2018

Accepted: February 5, 2019

Published: April 3, 2019

Data Availability Statement: The raw data images from this study are photographs of participants' faces. As one of our study outcomes specifically relates to the eyelid regions, de-identification through use of eye region blocking is not possible.

Abstract

Many moisturisers contain sun protection factors (SPF) equivalent to those found in sunscreens. However, there is a lack of research into how SPF moisturiser application compares to sunscreens in terms of coverage achieved and protection afforded. Previously we demonstrated that users incompletely covered their eyelid regions during routine sunscreen application. Here, we aimed to determine if SPF moisturiser users also displayed these tendencies. A study population of 84 participants (22 males, 62 females, age 18–57) were exposed to UV radiation and photographed using a tripod mounted UV sensitive DSLR camera on two separate visits. At visit one, images were acquired before and after applying either SPF30 sunscreen or moisturiser, then at visit two the study was repeated with the other formulation. Images were processed for facial landmark identification followed by segmentation mapping of hue saturation values to identify areas of the face that were/were not covered. Analyses revealed that application of moisturiser was significantly worse than sunscreen in terms area of the whole face missed (11.1% missed with sunscreen compared to 16.6% for SPF moisturiser $p<0.001$ paired t-test). This difference was primarily due to decreased coverage of the eyelid regions (14.0% missed with sunscreen, 20.9% moisturiser, $p<0.001$). Analysis of a post-study questionnaire revealed participants to be unaware of their incomplete coverage. Secondary analyses revealed improved coverage in males ($p = 0.05$), and, with moisturiser only, in participants with darker skin tones ($p = 0.02$). Together these data indicate that, despite potential advantages in terms of increased frequency of application of moisturiser, the areas of the face that are at higher cancer risk are likely not being protected, and that participants are unaware that they are at risk. As such, alternative sun-protection strategies should be promoted.

https://journals.plos.org/plosone/article/comments?id=10.1371/journal.pone.0212548

Chapter 10: References

1. Shaw L, Sugden CJ, Hamill KJ. Laminin Polymerization and Inherited Disease: Lessons From Genetics. Front Genet. 2021;12:707087-.
2. LeBleu VS, MacDonald B, Kalluri R. Structure and Function of Basement Membranes. Experimental Biology and Medicine. 2007;232(9):1121-9.
3. Leblond CP, Inoue S. Structure, composition, and assembly of basement membrane. American Journal of Anatomy. 1989;185(4):367-90.
4. Paulsson M. Basement membrane proteins: structure, assembly, and cellular interactions. Crit Rev Biochem Mol Biol. 1992;27(1-2):93-127.
5. Aumailley M, Bruckner-Tuderman L, Carter WG, Deutzmann R, Edgar D, Ekblom P, et al. A simplified laminin nomenclature. Matrix biology : journal of the International Society for Matrix Biology. 2005;24(5):326-32.
6. Naylor RW, Morais MRPT, Lennon R. Complexities of the glomerular basement membrane. Nature Reviews Nephrology. 2021;17(2):112-27.
7. McKee KK, Harrison D, Capizzi S, Yurchenco PD. Role of laminin terminal globular domains in basement membrane assembly. Journal of Biological Chemistry. 2007;282(29):21437-47.
8. Li S, Harrison D, Carbonetto S, Fassler R, Smyth N, Edgar D, et al. Matrix assembly, regulation, and survival functions of laminin and its receptors in embryonic stem cell differentiation. J Cell Biol. 2002;157(7):1279-90.
9. Li S, Liquari P, McKee KK, Harrison D, Patel R, Lee S, et al. Laminin-sulfatide binding initiates basement membrane assembly and enables receptor signaling in Schwann cells and fibroblasts. J Cell Biol. 2005;169(1):179-89.
10. McKee KK, Capizzi S, Yurchenco PD. Scaffold-forming and Adhesive Contributions of Synthetic Laminin-binding Proteins to Basement Membrane Assembly. J Biol Chem. 2009;284(13):8984-94.
11. McKee KK, Harrison D, Capizzi S, Yurchenco PD. Role of Laminin Terminal Globular Domains in Basement Membrane Assembly *. Journal of Biological Chemistry. 2007;282(29):21437-47.
12. Smyth N, Vatansever HS, Meyer M, Frie C, Paulsson M, Edgar D. The targeted deletion of the *LAMC*1 gene. Ann N Y Acad Sci. 1998;857:283-6.
13. Kalb E, Engel J. Binding and calcium-induced aggregation of laminin onto lipid bilayers. J Biol Chem. 1991;266(28):19047-52.
14. Lu P, Takai K, Weaver VM, Werb Z. Extracellular matrix degradation and remodeling in development and disease. Cold Spring Harbor perspectives in biology. 2011;3(12):a005058.
15. Khalilgharibi N, Mao Y. To form and function: on the role of basement membrane mechanics in tissue development, homeostasis and disease. Open Biology. 2021;11(2):200360.
16. Matejas V, Hinkes B, Alkandari F, Al-Gazali L, Annexstad E, Aytac MB, et al. Mutations in the human laminin beta2 (*LAMB*2) gene and the associated phenotypic spectrum. Human mutation. 2010;31(9):992-1002.
17. McGrath JA, Pulkkinen L, Christiano AM, Leigh IM, Eady RA, Uitto J. Altered laminin 5 expression due to mutations in the gene encoding the beta 3 chain (*LAMB*3) in generalized atrophic benign epidermolysis bullosa. J Invest Dermatol. 1995;104(4):467-74.
18. Mittwollen R, Wohlfart S, Park J, Grosch E, Has C, Hohenester E, et al. Aberrant splicing as potential modifier of the phenotype of junctional epidermolysis bullosa. J Eur Acad Dermatol Venereol. 2020;34(9):2127-34.

19. Schwartz MA. Integrins and extracellular matrix in mechanotransduction. Cold Spring Harbor perspectives in biology. 2010;2(12):a005066.
20. Burridge K, Chrzanowska-Wodnicka M. Focal adhesions, contractility, and signaling. Annual review of cell and developmental biology. 1996;12(1):463-519.
21. Tsuruta D, Gonzales M, Hopkinson SB, Otey C, Khuon S, Goldman RD, et al. Microfilament-dependent movement of the beta3 integrin subunit within focal contacts of endothelial cells. Faseb j. 2002;16(8):866-8.
22. Tsuruta D, Hashimoto T, Hamill KJ, Jones JCR. Hemidesmosomes and focal contact proteins: functions and cross-talk in keratinocytes, bullous diseases and wound healing. J Dermatol Sci. 2011;62(1):1-7.
23. Carter WG, Kaur P, Gil SG, Gahr PJ, Wayner EA. Distinct functions for integrins alpha 3 beta 1 in focal adhesions and alpha 6 beta 4/bullous pemphigoid antigen in a new stable anchoring contact (SAC) of keratinocytes: relation to hemidesmosomes. The Journal of cell biology. 1990;111(6):3141-54.
24. Zhong C, Chrzanowska-Wodnicka M, Brown J, Shaub A, Belkin AM, Burridge K. Rho-mediated Contractility Exposes a Cryptic Site in Fibronectin and Induces Fibronectin Matrix Assembly. Journal of Cell Biology. 1998;141(2):539-51.
25. Baneyx G, Baugh L, Vogel V. Fibronectin extension and unfolding within cell matrix fibrils controlled by cytoskeletal tension. Proceedings of the National Academy of Sciences. 2002;99(8):5139-43.
26. Streuli CH, Bissell MJ. Expression of extracellular matrix components is regulated by substratum. Journal of Cell Biology. 1990;110(4):1405-15.
27. Chiquet M, Renedo AS, Huber F, Flück M. How do fibroblasts translate mechanical signals into changes in extracellular matrix production? Matrix biology. 2003;22(1):73-80.
28. Katsumi A, Orr AW, Tzima E, Schwartz MA. Integrins in mechanotransduction. Journal of Biological Chemistry. 2004;279(13):12001-4.
29. Ross TD, Coon BG, Yun S, Baeyens N, Tanaka K, Ouyang M, et al. Integrins in mechanotransduction. Current opinion in cell biology. 2013;25(5):613-8.
30. Canty EG, Starborg T, Lu Y, Humphries SM, Holmes DF, Meadows RS, et al. Actin filaments are required for fibripositor-mediated collagen fibril alignment in tendon. J Biol Chem. 2006;281(50):38592-8.
31. Isenberg BC, Tranquillo RT. Long-Term Cyclic Distention Enhances the Mechanical Properties of Collagen-Based Media-Equivalents. Annals of Biomedical Engineering. 2003;31(8):937-49.
32. Solan A, Dahl SL, Niklason LE. Effects of mechanical stretch on collagen and cross-linking in engineered blood vessels. Cell transplantation. 2009;18(8):915-21.
33. Zaidel-Bar R, Cohen M, Addadi L, Geiger B. Hierarchical assembly of cell–matrix adhesion complexes. Biochemical Society Transactions. 2004;32(3):416-20.
34. Wehrle-Haller B. Structure and function of focal adhesions. Current Opinion in Cell Biology. 2012;24(1):116-24.
35. Zamir E, Geiger B. Molecular complexity and dynamics of cell-matrix adhesions. Journal of cell science. 2001;114(20):3583-90.
36. Horton ER, Byron A, Askari JA, Ng DHJ, Millon-Frémillon A, Robertson J, et al. Definition of a consensus integrin adhesome and its dynamics during adhesion complex assembly and disassembly. Nat Cell Biol. 2015;17(12):1577-87.
37. Takada Y, Ye X, Simon S. The integrins. Genome Biol. 2007;8(5):215-.
38. Cohen DM, Kutscher B, Chen H, Murphy DB, Craig SW. A Conformational Switch in Vinculin Drives Formation and Dynamics of a Talin-Vinculin Complex at Focal Adhesions*. Journal of Biological Chemistry. 2006;281(23):16006-15.
39. Turner CE, Glenney JR, Jr., Burridge K. Paxillin: a new vinculin-binding protein present in focal adhesions. Journal of Cell Biology. 1990;111(3):1059-68.

40. Schaller MD, Otey CA, Hildebrand JD, Parsons JT. Focal adhesion kinase and paxillin bind to peptides mimicking beta integrin cytoplasmic domains. The Journal of cell biology. 1995;130(5):1181-7.
41. Bellis SL, Miller JT, Turner CE. Characterization of Tyrosine Phosphorylation of Paxillin in Vitro by Focal Adhesion Kinase *. Journal of Biological Chemistry. 1995;270(29):17437-41.
42. Byron A, Morgan MR, Humphries MJ. Adhesion signalling complexes. Curr Biol. 2010;20(24):R1063-R7.
43. Barros CS, Nguyen T, Spencer KS, Nishiyama A, Colognato H, Müller U. β1 integrins are required for normal CNS myelination and promote AKT-dependent myelin outgrowth. 2009.
44. Bhaskar PT, Hay N. The two TORCs and Akt. Developmental cell. 2007;12(4):487-502.
45. Carnero A, Blanco-Aparicio C, Renner O, Link W, Leal JF. The PTEN/PI3K/AKT signalling pathway in cancer, therapeutic implications. Current cancer drug targets. 2008;8(3):187-98.
46. Hers I, Vincent EE, Tavaré JM. Akt signalling in health and disease. Cellular signalling. 2011;23(10):1515-27.
47. Manning BD, Cantley LC. AKT/PKB signaling: navigating downstream. Cell. 2007;129(7):1261-74.
48. Li H, Gao Y, Ren C. Focal adhesion kinase inhibitor BI 853520 inhibits cell proliferation, migration and EMT process through PI3K/AKT/mTOR signaling pathway in ovarian cancer. Discover Oncology. 2021;12(1):29.
49. Kong D, Chen F, Sima N. Inhibition of focal adhesion kinase induces apoptosis in bladder cancer cells via Src and the phosphatidylinositol 3-kinase/Akt pathway. Exp Ther Med. 2015;10(5):1725-31.
50. Wang S, Basson MD. Akt directly regulates focal adhesion kinase through association and serine phosphorylation: implication for pressure-induced colon cancer metastasis. American journal of physiology Cell physiology. 2011;300(3):C657-70.
51. Walko G, Castañón MJ, Wiche G. Molecular architecture and function of the hemidesmosome. Cell and Tissue Research. 2015;360(2):363-78.
52. Hopkinson SB, Jones JCR. The N Terminus of the Transmembrane Protein BP180 Interacts with the N-terminal Domain of BP230, Thereby Mediating Keratin Cytoskeleton Anchorage to the Cell Surface at the Site of the Hemidesmosome. Molecular Biology of the Cell. 2000;11(1):277-86.
53. Hirako Y, Usukura J, Nishizawa Y, Owaribe K. Demonstration of the Molecular Shape of BP180, a 180-kDa Bullous Pemphigoid Antigen and Its Potential for Trimer Formation*. Journal of Biological Chemistry. 1996;271(23):13739-45.
54. Nishie W, Kiritsi D, Nyström A, Hofmann SC, Bruckner-Tuderman L. Dynamic interactions of epidermal collagen XVII with the extracellular matrix: laminin 332 as a major binding partner. Am J Pathol. 2011;179(2):829-37.
55. Zillikens D, Giudice GJ. BP180/type XVII collagen: its role in acquired and inherited disorders or the dermal-epidermal junction. Archives of Dermatological Research. 1999;291(4):187-94.
56. Litjens SHM, Sonnenberg A. Hemidesmosomes. Encyclopedic Reference of Genomics and Proteomics in Molecular Medicine. Berlin, Heidelberg: Springer Berlin Heidelberg; 2006. p. 754-8.
57. Moch M, Leube RE. Hemidesmosome-Related Keratin Filament Bundling and Nucleation. International journal of molecular sciences. 2021;22(4):2130.
58. Wang W, Zuidema A, Te Molder L, Nahidiazar L, Hoekman L, Schmidt T, et al. Hemidesmosomes modulate force generation via focal adhesions. The Journal of cell biology. 2020;219(2).

59. Faham S, Hileman RE, Fromm JR, Linhardt RJ, Rees DC. Heparin structure and interactions with basic fibroblast growth factor. Science. 1996;271(5252):1116-20.
60. Nurcombe V, Ford MD, Wildschut JA, Bartlett PF. Developmental regulation of neural response to FGF-1 and FGF-2 by heparan sulfate proteoglycan. Science. 1993;260(5104):103-6.
61. Lyon M, Deakin JA, Mizuno K, Nakamura T, Gallagher JT. Interaction of hepatocyte growth factor with heparan sulfate. Elucidation of the major heparan sulfate structural determinants. J Biol Chem. 1994;269(15):11216-23.
62. Raines EW, Lane TF, Iruela-Arispe ML, Ross R, Sage EH. The extracellular glycoprotein SPARC interacts with platelet-derived growth factor (PDGF)-AB and -BB and inhibits the binding of PDGF to its receptors. Proceedings of the National Academy of Sciences of the United States of America. 1992;89(4):1281-5.
63. Klein G, Conzelmann S, Beck S, Timpl R, Müller CA. Perlecan in human bone marrow: a growth-factor-presenting, but anti-adhesive, extracellular matrix component for hematopoietic cells. Matrix biology : journal of the International Society for Matrix Biology. 1995;14(6):457-65.
64. Flaumenhaft R, Rifkin DB. The extracellular regulation of growth factor action. Mol Biol Cell. 1992;3(10):1057-65.
65. Taipale J, Keski-Oja J. Growth factors in the extracellular matrix. The FASEB Journal. 1997;11(1):51-9.
66. Schultz GS, Wysocki A. Interactions between extracellular matrix and growth factors in wound healing. Wound Repair Regen. 2009;17(2):153-62.
67. Alon R, Cahalon L, Hershkoviz R, Elbaz D, Reizis B, Wallach D, et al. TNF-alpha binds to the N-terminal domain of fibronectin and augments the beta 1-integrin-mediated adhesion of CD4+ T lymphocytes to the glycoprotein. J Immunol. 1994;152(3):1304-13.
68. Jones JI, Gockerman A, Busby WH, Jr., Camacho-Hubner C, Clemmons DR. Extracellular matrix contains insulin-like growth factor binding protein-5: potentiation of the effects of IGF-I. J Cell Biol. 1993;121(3):679-87.
69. Vukicevic S, Latin V, Chen P, Batorsky R, Reddi AH, Sampath TK. Localization of osteogenic protein-1 (bone morphogenetic protein-7) during human embryonic development: high affinity binding to basement membranes. Biochem Biophys Res Commun. 1994;198(2):693-700.
70. Hecht PM, Anderson KV. Extracellular proteases and embryonic pattern formation. Trends Cell Biol. 1992;2(7):197-202.
71. Lyons RM, Keski-Oja J, Moses HL. Proteolytic activation of latent transforming growth factor-beta from fibroblast-conditioned medium. J Cell Biol. 1988;106(5):1659-65.
72. Kleinman HK, Koblinski J, Lee S, Engbring J. Role of basement membrane in tumor growth and metastasis. Surg Oncol Clin N Am. 2001;10(2):329-38, ix.
73. Miner JH. The glomerular basement membrane. Exp Cell Res. 2012;318(9):973-8.
74. Vaccaro CA, Brody JS. Structural features of alveolar wall basement membrane in the adult rat lung. The Journal of cell biology. 1981;91(2 Pt 1):427-37.
75. Thomsen MS, Routhe LJ, Moos T. The vascular basement membrane in the healthy and pathological brain. J Cereb Blood Flow Metab. 2017;37(10):3300-17.
76. Favor J, Gloeckner CJ, Janik D, Klempt M, Neuhäuser-Klaus A, Pretsch W, et al. Type IV procollagen missense mutations associated with defects of the eye, vascular stability, the brain, kidney function and embryonic or postnatal viability in the mouse, Mus musculus: an extension of the Col4a1 allelic series and the identification of the first two Col4a2 mutant alleles. Genetics. 2007;175(2):725-36.
77. Aumailley M, Battaglia C, Mayer U, Reinhardt D, Nischt R, Timpl R, et al. Nidogen mediates the formation of ternary complexes of basement membrane components. Kidney Int 43:7-12. Kidney international. 1993;43:7-12.

78. Fox JW, Mayer U, Nischt R, Aumailley M, Reinhardt D, Wiedemann H, et al. Recombinant nidogen consists of three globular domains and mediates binding of laminin to collagen type IV. The EMBO journal. 1991;10(11):3137-46.
79. Hohenester E, Yurchenco PD. Laminins in basement membrane assembly. Cell adhesion & migration. 2013;7(1):56-63.
80. Laurie GW, Bing JT, Kleinman HK, Hassell JR, Aumailley M, Martin GR, et al. Localization of binding sites for laminin, heparan sulfate proteoglycan and fibronectin on basement membrane (type IV) collagen. Journal of molecular biology. 1986;189(1):205-16.
81. Reinhardt D, Mann K, Nischt R, Fox JW, Chu ML, Krieg T, et al. Mapping of nidogen binding sites for collagen type IV, heparan sulfate proteoglycan, and zinc. J Biol Chem. 1993;268(15):10881-7.
82. Paralkar VM, Vukicevic S, Reddi AH. Transforming growth factor beta type 1 binds to collagen IV of basement membrane matrix: implications for development. Developmental biology. 1991;143(2):303-8.
83. Paralkar VM, Vukicevic S, Reddi AH. Transforming growth factor β type 1 binds to collagen IV of basement membrane matrix: Implications for development. Developmental biology. 1991;143(2):303-8.
84. Somasundaram R, Schuppan D. Type I, II, III, IV, V, and VI collagens serve as extracellular ligands for the isoforms of platelet-derived growth factor (AA, BB, and AB). J Biol Chem. 1996;271(43):26884-91.
85. Nishi N, Matsushita O, Yuube K, Miyanaka H, Okabe A, Wada F. Collagen-binding growth factors: Production and characterization of functional fusion proteins having a collagen-binding domain. Proceedings of the National Academy of Sciences. 1998;95(12):7018.
86. Tunggal J, Wartenberg M, Paulsson M, Smyth N. Expression of the nidogen-binding site of the laminin γ1 chain disturbs basement membrane formation and maintenance in F9 embryoid bodies. Journal of Cell Science. 2003;116(5):803-12.
87. Aumailley M, Battaglia C, Mayer U, Reinhardt D, Nischt R, Timpl R, et al. Nidogen mediates the formation of ternary complexes of basement membrane components. Kidney International. 1993;43(1):7-12.
88. Chung AE, Dong LJ, Wu C, Durkin ME. Biological functions of entactin. Kidney Int. 1993;43(1):13-9.
89. Erickson AC, Couchman JR. Still more complexity in mammalian basement membranes. The journal of histochemistry and cytochemistry : official journal of the Histochemistry Society. 2000;48(10):1291-306.
90. Reinhardt D, Mann K, Nischt R, Fox J, Chu M, Krieg T, et al. Mapping of nidogen binding sites for collagen type IV, heparan sulfate proteoglycan, and zinc. Journal of Biological Chemistry. 1993;268(15):10881-7.
91. Stetefeld J, Mayer U, Timpl R, Huber R. Crystal structure of three consecutive laminin-type epidermal growth factor-like (LE) modules of laminin gamma1 chain harboring the nidogen binding site. Journal of molecular biology. 1996;257(3):644-57.
92. Noonan DM, Fulle A, Valente P, Cai S, Horigan E, Sasaki M, et al. The complete sequence of perlecan, a basement membrane heparan sulfate proteoglycan, reveals extensive similarity with laminin A chain, low density lipoprotein-receptor, and the neural cell adhesion molecule. Journal of Biological Chemistry. 1991;266(34):22939-47.
93. Iozzo RV. Perlecan: A gem of a proteoglycan. Matrix Biology. 1994;14(3):203-8.
94. Knox SM, Whitelock JM. Perlecan: how does one molecule do so many things? Cellular and Molecular Life Sciences CMLS. 2006;63(21):2435-45.
95. Wu W, Tholozan FM, Goldberg MW, Bowen L, Wu J, Quinlan RA. A gradient of matrix-bound FGF-2 and perlecan is available to lens epithelial cells(). Experimental Eye Research. 2014;120(100):10-4.

96. Brown JC, Sasaki T, Gohring W, Yamada Y, Timpl R. The C-terminal domain V of perlecan promotes beta1 integrin-mediated cell adhesion, binds heparin, nidogen and fibulin-2 and can be modified by glycosaminoglycans. Eur J Biochem. 1997;250(1):39-46.
97. Villar María J, Hassell John R, Brandan E. Interaction of skeletal muscle cells with collagen type IV is mediated by perlecan associated with the cell surface. Journal of Cellular Biochemistry. 1999;75(4):665-74.
98. Melrose J, Roughley P, Knox S, Smith S, Lord M, Whitelock J. The structure, location, and function of perlecan, a prominent pericellular proteoglycan of fetal, postnatal, and mature hyaline cartilages. J Biol Chem. 2006;281(48):36905-14.
99. Nishida T, Maeda A, Kubota S, Takigawa M. Role of mechanical-stress inducible protein Hcs24/CTGF/CCN2 in cartilage growth and regeneration: mechanical stress induces expression of Hcs24/CTGF/CCN2 in a human chondrocytic cell line HCS-2/8, rabbit costal chondrocytes and meniscus tissue cells. Biorheology. 2008;45(3-4):289-99.
100. Chakravarti S, Horchar T, Jefferson B, Laurie GW, Hassell JR. Recombinant domain III of perlecan promotes cell attachment through its RGDS sequence. Journal of Biological Chemistry. 1995;270(1):404-9.
101. Aumailley M, Gerl M, Sonnenberg A, Deutzmann R, Timpl R. Identification of the Arg-Gly-Asp sequence in laminin A chain as a latent cell-binding site being exposed in fragment P1. FEBS letters. 1990;262(1):82-6.
102. Hopf M, Gohring W, Kohfeldt E, Yamada Y, Timpl R. Recombinant domain IV of perlecan binds to nidogens, laminin-nidogen complex, fibronectin, fibulin-2 and heparin. Eur J Biochem. 1999;259(3):917-25.
103. Farach-Carson MC, Brown AJ, Lynam M, Safran JB, Carson DD. A novel peptide sequence in perlecan domain IV supports cell adhesion, spreading and FAK activation. Matrix biology : journal of the International Society for Matrix Biology. 2008;27(2):150-60.
104. Gautam M, Noakes PG, Moscoso L, Rupp F, Scheller RH, Merlie JP, et al. Defective Neuromuscular Synaptogenesis in Agrin-Deficient Mutant Mice. Cell. 1996;85(4):525-35.
105. Groffen AJ, Ruegg MA, Dijkman H, van de Velden TJ, Buskens CA, van den Born J, et al. Agrin is a major heparan sulfate proteoglycan in the human glomerular basement membrane. The journal of histochemistry and cytochemistry : official journal of the Histochemistry Society. 1998;46(1):19-27.
106. Tátrai P, Dudás J, Batmunkh E, Máthé M, Zalatnai A, Schaff Z, et al. Agrin, a novel basement membrane component in human and rat liver, accumulates in cirrhosis and hepatocellular carcinoma. Lab Invest. 2006;86(11):1149-60.
107. Kammerer RA, Schulthess T, Landwehr R, Schumacher B, Lustig A, Yurchenco PD, et al. Interaction of agrin with laminin requires a coiled-coil conformation of the agrin-binding site within the laminin γ1 chain. The EMBO journal. 1999;18(23):6762-70.
108. Miner JH, Abrahamson DR. CHAPTER 25 - Molecular and Cellular Mechanisms of Glomerular Capillary Development. In: Alpern RJ, Hebert SC, editors. Seldin and Giebisch's The Kidney (Fourth Edition). San Diego: Academic Press; 2008. p. 691-706.
109. Ervasti JM, Campbell KP. A role for the dystrophin-glycoprotein complex as a transmembrane linker between laminin and actin. J Cell Biol. 1993;122(4):809-23.
110. Gee SH, Blacher RW, Douville PJ, Provost PR, Yurchenco PD, Carbonetto S. Laminin-binding protein 120 from brain is closely related to the dystrophin-associated glycoprotein, dystroglycan, and binds with high affinity to the major heparin binding domain of laminin. J Biol Chem. 1993;268(20):14972-80.
111. Henry MD, Campbell KP. A role for dystroglycan in basement membrane assembly. Cell. 1998;95(6):859-70.
112. Aumailley M. The laminin family. Cell adhesion & migration. 2013;7(1):48-55.
113. Domogatskaya A, Rodin S, Tryggvason K. Functional Diversity of Laminins. Annual Review of Cell and Developmental Biology. 2012;28(1):523-53.

114. Ferrigno O, Virolle T, Galliano M-F, Chauvin N, Ortonne J-P, Meneguzzi G, et al. Murine Laminin α3A and α3B Isoform Chains Are Generated by Usage of Two Promoters and Alternative Splicing *. Journal of Biological Chemistry. 1997;272(33):20502-7.
115. Hunter I, Schulthess T, Engel J. Laminin chain assembly by triple and double stranded coiled-coil structures. Journal of Biological Chemistry. 1992;267(9):6006-11.
116. Nissinen M, Vuolteenaho R, Boot-Handford R, Kallunki P, Tryggvason K. Primary structure of the human laminin A chain. Limited expression in human tissues. Biochemical Journal. 1991;276(2):369-79.
117. Paulsson M, Deutzmann R, Timpl R, Dalzoppo D, Odermatt E, Engel J. Evidence for coiled-coil alpha-helical regions in the long arm of laminin. The EMBO journal. 1985;4(2):309-16.
118. Utani A, Nomizu M, Timpl R, Roller PP, Yamada Y. Laminin chain assembly. Specific sequences at the C terminus of the long arm are required for the formation of specific double-and triple-stranded coiled-coil structures. Journal of Biological Chemistry. 1994;269(29):19167-75.
119. Zimmerman T, Blanco FJ. The coiled-coil structure potential of the laminin LCC domain is very fragmented and does not differentiate between natural and non-detected isoforms. J Biomol Struct Dyn. 2007;24(4):413-20.
120. Fahey B, Degnan BM. Origin and Evolution of Laminin Gene Family Diversity. Molecular Biology and Evolution. 2012;29(7):1823-36.
121. Cheng Y-S, Champliaud M-F, Burgeson RE, Marinkovich MP, Yurchenco PD. Self-assembly of Laminin Isoforms *. Journal of Biological Chemistry. 1997;272(50):31525-32.
122. Purvis A, Hohenester E. Laminin network formation studied by reconstitution of ternary nodes in solution. The Journal of biological chemistry. 2012;287(53):44270-7.
123. Kalkhof S, Haehn S, Paulsson M, Smyth N, Meiler J, Sinz A. Computational modeling of laminin N-terminal domains using sparse distance constraints from disulfide bonds and chemical cross-linking. Proteins: Structure, Function, and Bioinformatics. 2010;78(16):3409-27.
124. Timpl R, Tisi D, Talts JF, Andac Z, Sasaki T, Hohenester E. Structure and function of laminin LG modules. Matrix biology : journal of the International Society for Matrix Biology. 2000;19(4):309-17.
125. Hamill KJ, Langbein L, Jones JC, McLean WI. Identification of a Novel Family of Laminin N-terminal Alternate Splice Isoforms. Journal of Biological Chemistry. 2009;284(51):35588-96.
126. Sasaki T, Timpl R. Laminins. In: T. Kreis RVE, editor. Guidebook to the Extracellular Matrix, Anchor and Adhesion Proteins. Oxford Oxford University Press; 1999. p. 434-43.
127. Sasaki M, Kleinman HK, Huber H, Deutzmann R, Yamada Y. Laminin, a multidomain protein. The A chain has a unique globular domain and homology with the basement membrane proteoglycan and the laminin B chains. J Biol Chem. 1988;263(32):16536-44.
128. Aumailley M, Gimond C, Rousselle P. Integrin-mediated cellular interactions with laminins. The laminins. 1996;2:127-58.
129. Kikkawa Y, Sasaki T, Nguyen MT, Nomizu M, Mitaka T, Miner JH. The LG1-3 tandem of laminin alpha5 harbors the binding sites of Lutheran/basal cell adhesion molecule and alpha3beta1/alpha6beta1 integrins. J Biol Chem. 2007;282(20):14853-60.
130. Ott U, Odermatt E, Engel J, Furthmayr H, Timpl R. Protease resistance and conformation of laminin. Eur J Biochem. 1982;123(1):63-72.
131. DEUTZMANN R, AUMAILLEY M, WIEDEMANN H, PYSNY W, TIMPL R, EDGAR D. Cell adhesion, spreading and neurite stimulation by laminin fragment E8 depends on maintenance of secondary and tertiary structure in its rod and globular domain. The FEBS Journal. 1990;191(2):513-22.

132. Rousselle P, Golbik R, van der Rest M, Aumailley M. Structural requirement for cell adhesion to kalinin (laminin-5). J Biol Chem. 1995;270(23):13766-70.
133. Carafoli F, Clout NJ, Hohenester E. Crystal structure of the LG1-3 region of the laminin alpha2 chain. J Biol Chem. 2009;284(34):22786-92.
134. Takizawa M, Arimori T, Taniguchi Y, Kitago Y, Yamashita E, Takagi J, et al. Mechanistic basis for the recognition of laminin-511 by α6β1 integrin. Sci Adv. 2017;3(9):e1701497-e.
135. Taniguchi Y, Ido H, Sanzen N, Hayashi M, Sato-Nishiuchi R, Futaki S, et al. The C-terminal region of laminin beta chains modulates the integrin binding affinities of laminins. J Biol Chem. 2009;284(12):7820-31.
136. Arimori T, Miyazaki N, Mihara E, Takizawa M, Taniguchi Y, Cabañas C, et al. Structural mechanism of laminin recognition by integrin. Nature Communications. 2021;12(1):4012.
137. Utani A, Nomizu M, Timpl R, Roller PP, Yamada Y. Laminin chain assembly. Specific sequences at the C terminus of the long arm are required for the formation of specific double- and triple-stranded coiled-coil structures. The Journal of biological chemistry. 1994;269(29):19167-75.
138. Utani A, Nomizu M, Sugiyama S, Miyamoto S, Roller PP, Yamada Y. A specific sequence of the laminin alpha 2 chain critical for the initiation of heterotrimer assembly. J Biol Chem. 1995;270(7):3292-8.
139. Kammerer RA, Antonsson P, Schulthess T, Fauser C, Engel J. Selective chain recognition in the C-terminal alpha-helical coiled-coil region of laminin. Journal of molecular biology. 1995;250(1):64-73.
140. Nomizu M, Utani A, Beck K, Otaka A, Roller PP, Yamada Y. Mechanism of laminin chain assembly into a triple-stranded coiled-coil structure. Biochemistry. 1996;35(9):2885-93.
141. Macdonald PR, Lustig A, Steinmetz MO, Kammerer RA. Laminin chain assembly is regulated by specific coiled-coil interactions. Journal of structural biology. 2010;170(2):398-405.
142. Miner JH. Laminins and their roles in mammals. Microscopy research and technique. 2008;71(5):349-56.
143. Engel J. EGF-like domains in extracellular matrix proteins: localized signals for growth and differentiation? FEBS Lett. 1989;251(1-2):1-7.
144. Mayer U, Nischt R, Poschl E, Mann K, Fukuda K, Gerl M, et al. A single EGF-like motif of laminin is responsible for high affinity nidogen binding. The EMBO journal. 1993;12(5):1879-85.
145. Hohenester E. Structural biology of laminins. Essays in Biochemistry. 2019;63(3):285-95.
146. Moran T, Gat Y, Fass D. Laminin L4 domain structure resembles adhesion modules in ephrin receptor and other transmembrane glycoproteins. Febs j. 2015;282(14):2746-57.
147. Al*LAMA*nd V, Sunada Y, Salih MAM, Straub V, Ozo O, Al-Turaiki MHS, et al. Mild Congenital Muscular Dystrophy in Two Patients with an Internally Deleted Laminin α2-Chain. Human molecular genetics. 1997;6(5):747-52.
148. Gawlik KI, Durbeej M. Skeletal muscle laminin and MDC1A: pathogenesis and treatment strategies. Skeletal Muscle. 2011;1(1):9.
149. Garbe JH, Gohring W, Mann K, Timpl R, Sasaki T. Complete sequence, recombinant analysis and binding to laminins and sulphated ligands of the N-terminal domains of laminin alpha3B and alpha5 chains. Biochem J. 2002;362(Pt 1):213-21.
150. Kunneken K, Pohlentz G, Schmidt-Hederich A, Odenthal U, Smyth N, Peter-Katalinic J, et al. Recombinant human laminin-5 domains. Effects of heterotrimerization, proteolytic processing, and N-glycosylation on alpha3beta1 integrin binding. J Biol Chem. 2004;279(7):5184-93.

151. Nielsen PK, Yamada Y. Identification of cell-binding sites on the Laminin alpha 5 N-terminal domain by site-directed mutagenesis. J Biol Chem. 2001;276(14):10906-12.
152. Nomizu M, Yokoyama F, Suzuki N, Okazaki I, Nishi N, Ponce ML, et al. Identification of homologous biologically active sites on the N-terminal domain of laminin alpha chains. Biochemistry. 2001;40(50):15310-7.
153. Colognato H, MacCarrick M, O'Rear JJ, Yurchenco PD. The laminin alpha2-chain short arm mediates cell adhesion through both the alpha1beta1 and alpha2beta1 integrins. J Biol Chem. 1997;272(46):29330-6.
154. Ettner N, Gohring W, Sasaki T, Mann K, Timpl R. The N-terminal globular domain of the laminin alpha1 chain binds to alpha1beta1 and alpha2beta1 integrins and to the heparan sulfate-containing domains of perlecan. FEBS Lett. 1998;430(3):217-21.
155. Hozumi K, Ishikawa M, Hayashi T, Yamada Y, Katagiri F, Kikkawa Y, et al. Identification of cell adhesive sequences in the N-terminal region of the laminin alpha2 chain. J Biol Chem. 2012;287(30):25111-22.
156. Kariya Y, Yasuda C, Nakashima Y, Ishida K, Tsubota Y, Miyazaki K. Characterization of laminin 5B and NH2-terminal proteolytic fragment of its alpha3B chain: promotion of cellular adhesion, migration, and proliferation. The Journal of biological chemistry. 2004;279(23):24774-84.
157. Pfaff M, Gohring W, Brown JC, Timpl R. Binding of purified collagen receptors (alpha 1 beta 1, alpha 2 beta 1) and RGD-dependent integrins to laminins and laminin fragments. Eur J Biochem. 1994;225(3):975-84.
158. Yurchenco PD, Cheng YS. Laminin self-assembly: a three-arm interaction hypothesis for the formation of a network in basement membranes. Contrib Nephrol. 1994;107:47-56.
159. McKee KK, Harrison D, Capizzi S, Yurchenco PD. Role of laminin terminal globular domains in basement membrane assembly. J Biol Chem. 2007;282(29):21437-47.
160. Schittny JC, Yurchenco PD. Terminal short arm domains of basement membrane laminin are critical for its self-assembly. Journal of Cell Biology. 1990;110(3):825-32.
161. Champliaud M-F, Lunstrum GP, Rousselle P, Nishiyama T, Keene DR, Burgeson RE. Human amnion contains a novel laminin variant, laminin 7, which like laminin 6, covalently associates with laminin 5 to promote stable epithelial-stromal attachment. The Journal of cell biology. 1996;132(6):1189-98.
162. Rousselle P, Beck K. Laminin 332 processing impacts cellular behavior. Cell adhesion & migration. 2013;7(1):122-34.
163. Chen M, Marinkovich MP, Veis A, Cai X, Rao CN, O'Toole EA, et al. Interactions of the amino-terminal noncollagenous (NC1) domain of type VII collagen with extracellular matrix components: a potential role in epidermal-dermal adherence in human skin. Journal of Biological Chemistry. 1997;272(23):14516-22.
164. Cheng YS, Champliaud MF, Burgeson RE, Marinkovich MP, Yurchenco PD. Self-assembly of laminin isoforms. The Journal of biological chemistry. 1997;272(50):31525-32.
165. Odenthal U, Haehn S, Tunggal P, Merkl B, Schomburg D, Frie C, et al. Molecular analysis of laminin N-terminal domains mediating self-interactions. Journal of Biological Chemistry. 2004;279(43):44504-12.
166. Yurchenco PD, Cheng YS. Self-assembly and calcium-binding sites in laminin. A three-arm interaction model. The Journal of biological chemistry. 1993;268(23):17286-99.
167. Hussain SA, Carafoli F, Hohenester E. Determinants of laminin polymerization revealed by the structure of the alpha5 chain amino-terminal region. EMBO reports. 2011;12(3):276-82.
168. Carafoli F, Hussain SA, Hohenester E. Crystal structures of the network-forming short-arm tips of the laminin beta1 and gamma1 chains. PloS one. 2012;7(7):e42473.

169. McKee KK, Aleksandrova M, Yurchenco PD. Chimeric protein identification of dystrophic, Pierson and other laminin polymerization residues. Matrix biology : journal of the International Society for Matrix Biology. 2018;67:32-46.
170. Pettersen EF, Goddard TD, Huang CC, Couch GS, Greenblatt DM, Meng EC, et al. UCSF Chimera—a visualization system for exploratory research and analysis. Journal of computational chemistry. 2004;25(13):1605-12.
171. Calderwood DA, Tuckwell DS, Eble J, Kühn K, Humphries MJ. The Integrin α1 A-domain Is a Ligand Binding Site for Collagens and Laminin*. Journal of Biological Chemistry. 1997;272(19):12311-7.
172. Nishiuchi R, Takagi J, Hayashi M, Ido H, Yagi Y, Sanzen N, et al. Ligand-binding specificities of laminin-binding integrins: a comprehensive survey of laminin-integrin interactions using recombinant alpha3beta1, alpha6beta1, alpha7beta1 and alpha6beta4 integrins. Matrix biology : journal of the International Society for Matrix Biology. 2006;25(3):189-97.
173. Iozzo RV. MATRIX PROTEOGLYCANS: From Molecular Design to Cellular Function. Annual Review of Biochemistry. 1998;67(1):609-52.
174. Ogawa T, Tsubota Y, Hashimoto J, Kariya Y, Miyazaki K. The Short Arm of Laminin γ2 Chain of Laminin-5 (Laminin-332) Binds Syndecan-1 and Regulates Cellular Adhesion and Migration by Suppressing Phosphorylation of Integrin β4 Chain. Molecular Biology of the Cell. 2007;18(5):1621-33.
175. Gagnoux-Palacios L, Allegra M, Spirito F, Pommeret O, Romero C, Ortonne J-P, et al. The short arm of the laminin γ2 chain plays a pivotal role in the incorporation of laminin 5 into the extracellular matrix and in cell adhesion. The Journal of cell biology. 2001;153(4):835-50.
176. Sasaki T, Göhring W, Mann K, Brakebusch C, Yamada Y, Fässler R, et al. Short arm region of laminin-5 γ2 chain: structure, mechanism of processing and binding to heparin and proteins. Journal of molecular biology. 2001;314(4):751-63.
177. Edwards MM, Mammadova-Bach E, Alpy F, Klein A, Hicks WL, Roux M, et al. Mutations in *LAMA*1 disrupt retinal vascular development and inner limiting membrane formation. Journal of Biological Chemistry. 2010;285(10):7697-711.
178. Patton BL, Wang B, Tarumi YS, Seburn KL, Burgess RW. A single point mutation in the LN domain of *LAMA*2 causes muscular dystrophy and peripheral amyelination. Journal of cell science. 2008;121(Pt 10):1593-604.
179. Oliveira J, Gruber A, Cardoso M, Taipa R, Fineza I, Goncalves A, et al. *LAMA*2 gene mutation update: Toward a more comprehensive picture of the laminin-alpha2 variome and its related phenotypes. Hum Mutat. 2018;39(10):1314-37.
180. Gavassini BF, Carboni N, Nielsen JE, Danielsen ER, Thomsen C, Svenstrup K, et al. Clinical and molecular characterization of limb-girdle muscular dystrophy due to *LAMA*2 mutations. Muscle Nerve. 2011;44(5):703-9.
181. Geranmayeh F, Clement E, Feng LH, Sewry C, Pagan J, Mein R, et al. Genotype–phenotype correlation in a large population of muscular dystrophy patients with *LAMA*2 mutations. Neuromuscular disorders. 2010;20(4):241-50.
182. Di Blasi C, Piga D, Brioschi P, Moroni I, Pini A, Ruggieri A, et al. *LAMA*2 gene analysis in congenital muscular dystrophy: new mutations, prenatal diagnosis, and founder effect. Archives of neurology. 2005;62(10):1582-6.
183. Chan SH, Foley AR, Phadke R, Mathew AA, Pitt M, Sewry C, et al. Limb girdle muscular dystrophy due to *LAMA*2 mutations: diagnostic difficulties due to associated peripheral neuropathy. Neuromuscul Disord. 2014;24(8):677-83.
184. Dekomien G, Hoffjan S, Haug V, Anastasopoulos C, Kirschner J. High creatine kinase levels and white matter changes: clinical and genetic spectrum of congenital muscular

dystrophies with laminin alpha-2 deficiency. Molecular and cellular probes. 2013;28(4):118-22.
185. Jones LK, Lam R, McKee KK, Aleksandrova M, Dowling J, Alexander SI, et al. A mutation affecting laminin alpha 5 polymerisation gives rise to a syndromic developmental disorder. Development. 2020;147(21).
186. Hollfelder D, Frasch M, Reim I. Distinct functions of the laminin β LN domain and collagen IV during cardiac extracellular matrix formation and stabilization of alary muscle attachments revealed by EMS mutagenesis in Drosophila. BMC developmental biology. 2014;14(1):1-20.
187. Bredrup C, Matejas V, Barrow M, Bláhová K, Bockenhauer D, Fowler DJ, et al. Ophthalmological Aspects of Pierson Syndrome. American Journal of Ophthalmology. 2008;146(4):602-11.e1.
188. Zenker M, Aigner T, Wendler O, Tralau T, Muntefering H, Fenski R, et al. Human laminin beta2 deficiency causes congenital nephrosis with mesangial sclerosis and distinct eye abnormalities. Human molecular genetics. 2004;13(21):2625-32.
189. Matejas V, Al-Gazali L, Amirlak I, Zenker M. A syndrome comprising childhood-onset glomerular kidney disease and ocular abnormalities with progressive loss of vision is caused by mutated *LAMB*2. Nephrology, dialysis, transplantation : official publication of the European Dialysis and Transplant Association - European Renal Association. 2006;21(11):3283-6.
190. Funk SD, Bayer RH, Malone AF, McKee KK, Yurchenco PD, Miner JH. Pathogenicity of a human laminin β2 mutation revealed in models of Alport syndrome. Journal of the American Society of Nephrology. 2018;29(3):949-60.
191. Matejas V, Hinkes B, Alkandari F, Al-Gazali L, Annexstad E, Aytac MB, et al. Mutations in the human laminin β2 (*LAMB*2) gene and the associated phenotypic spectrum. Human mutation. 2010;31(9):992-1002.
192. Mohney BG, Pulido JS, Lindor NM, Hogan MC, Consugar MB, Peters J, et al. A novel mutation of *LAMB*2 in a multigenerational mennonite family reveals a new phenotypic variant of Pierson syndrome. Ophthalmology. 2011;118(6):1137-44.
193. Kagan M, Cohen A, Matejas V, Vlangos C, Zenker M. A milder variant of Pierson syndrome2008. 323-7 p.
194. Choi HJ, Lee BH, Kang JH, Jeong HJ, Moon KC, Ha IS, et al. Variable phenotype of Pierson syndrome. Pediatric Nephrology. 2008;23(6):995-1000.
195. Mellerio J, Eady R, Atherton D, Lake B, McGrath J. E210K mutation in the gene encoding the beta3 chain of laminin-5 (*LAMB*3) is predictive of a phenotype of generalized atrophic benign epidermolysis bullosa. The British journal of dermatology. 1998;139(2):325-31.
196. Helbling-Leclerc A, Zhang X, Topaloglu H, Cruaud C, Tesson F, Weissenbach J, et al. Mutations in the laminin alpha 2-chain gene (*LAMA*2) cause merosin-deficient congenital muscular dystrophy. Nat Genet. 1995;11(2):216-8.
197. Ehrig K, Leivo I, Argraves WS, Ruoslahti E, Engvall E. Merosin, a tissue-specific basement membrane protein, is a laminin-like protein. Proceedings of the National Academy of Sciences of the United States of America. 1990;87(9):3264-8.
198. Voit T, Sewry CA, Meyer K, Hermann R, Straub V, Muntoni F, et al. Preserved merosin M-chain (or laminin-alpha 2) expression in skeletal muscle distinguishes Walker-Warburg syndrome from Fukuyama muscular dystrophy and merosin-deficient congenital muscular dystrophy. Neuropediatrics. 1995;26(3):148-55.
199. Jones KJ, Morgan G, Johnston H, Tobias V, Ouvrier RA, Wilkinson I, et al. The expanding phenotype of laminin alpha2 chain (merosin) abnormalities: case series and review. J Med Genet. 2001;38(10):649-57.

200. Philpot J, Sewry C, Pennock J, Dubowitz V. Clinical phenotype in congenital muscular dystrophy: correlation with expression of merosin in skeletal muscle. Neuromuscul Disord. 1995;5(4):301-5.
201. Mendell JR, Boue DR, Martin PT. The congenital muscular dystrophies: recent advances and molecular insights. Pediatr Dev Pathol. 2006;9(6):427-43.
202. Muntoni F, Voit T. The congenital muscular dystrophies in 2004: a century of exciting progress. Neuromuscul Disord. 2004;14(10):635-49.
203. Ringelmann B, Röder C, Hallmann R, Maley M, Davies M, Grounds M, et al. Expression of laminin α1, α2, α4, and α5 chains, fibronectin, and tenascin-c in skeletal muscle of dystrophic 129ReJdy/dyMice. Exp Cell Res. 1999;246(1):165-82.
204. Talts JF, Sasaki T, Miosge N, Göhring W, Mann K, Mayne R, et al. Structural and functional analysis of the recombinant G domain of the laminin α4 chain and its proteolytic processing in tissues. Journal of Biological Chemistry. 2000;275(45):35192-9.
205. Yurchenco PD, McKee KK, Reinhard JR, Ruegg MA. Laminin-deficient muscular dystrophy: Molecular pathogenesis and structural repair strategies. Matrix biology : journal of the International Society for Matrix Biology. 2018;71-72:174-87.
206. Miner JH, Cunningham J, Sanes JR. Roles for laminin in embryogenesis: exencephaly, syndactyly, and placentopathy in mice lacking the laminin alpha5 chain. J Cell Biol. 1998;143(6):1713-23.
207. Sampaolo S, Napolitano F, Tirozzi A, Reccia MG, Lombardi L, Farina O, et al. Identification of the first dominant mutation of *LAMA*5 gene causing a complex multisystem syndrome due to dysfunction of the extracellular matrix. J Med Genet. 2017;54(10):710-20.
208. Hinkes BG, Mucha B, Vlangos CN, Gbadegesin R, Liu J, Hasselbacher K, et al. Nephrotic syndrome in the first year of life: two thirds of cases are caused by mutations in 4 genes (NPHS1, NPHS2, WT1, and *LAMB*2). Pediatrics. 2007;119(4):e907-19.
209. Chen YM, Kikkawa Y, Miner JH. A missense *LAMB*2 mutation causes congenital nephrotic syndrome by impairing laminin secretion. Journal of the American Society of Nephrology : JASN. 2011;22(5):849-58.
210. Togawa H, Nakanishi K, Mukaiyama H, Hama T, Shima Y, Nakano M, et al. First Japanese case of Pierson syndrome with mutations in *LAMB*2. Pediatrics international : official journal of the Japan Pediatric Society. 2013;55(2):229-31.
211. Zemrani B, Cachat F, Bonny O, Giannoni E, Durig J, Fellmann F, et al. A novel *LAMB*2 gene mutation associated with a severe phenotype in a neonate with Pierson syndrome. Eur J Med Res. 2016;21:19-.
212. Ferrigno O, Virolle T, Galliano MF, Chauvin N, Ortonne JP, Meneguzzi G, et al. Murine laminin alpha3A and alpha3B isoform chains are generated by usage of two promoters and alternative splicing. J Biol Chem. 1997;272(33):20502-7.
213. Matsui C, Wang CK, Nelson CF, Bauer EA, Hoeffler WK. The Assembly of Laminin-5 Subunits (∗). Journal of Biological Chemistry. 1995;270(40):23496-503.
214. Posteraro P, De Luca N, Meneguzzi G, El Hachem M, Angelo C, Gobello T, et al. Laminin-5 mutational analysis in an Italian cohort of patients with junctional epidermolysis bullosa. Journal of investigative dermatology. 2004;123(4):639-48.
215. Meng X, Klement JF, Leperi DA, Birk DE, Sasaki T, Timpl R, et al. Targeted inactivation of murine laminin γ2-chain gene recapitulates human junctional epidermolysis bullosa. Journal of investigative dermatology. 2003;121(4):720-31.
216. Pulkkinen L, Christiano AM, Airenne T, Haakana H, Tryggvason K, Uitto J. Mutations in the γ2 chain gene (*LAMC*2) of kalinin/laminin 5 in the junctional forms of epidermolysis bullosa. Nature genetics. 1994;6(3):293-8.
217. Kuster JE, Guarnieri MH, Ault JG, Flaherty L, Swiatek PJ. IAP insertion in the murine *LAMB*3 gene results in junctional epidermolysis bullosa. Mammalian genome. 1997;8(9):673-81.

218. Ryan MC, Lee K, Miyashita Y, Carter WG. Targeted disruption of the *LAMA*3 gene in mice reveals abnormalities in survival and late stage differentiation of epithelial cells. The Journal of cell biology. 1999;145(6):1309-24.
219. Pasmooij AM, Pas HH, Bolling MC, Jonkman MF. Revertant mosaicism in junctional epidermolysis bullosa due to multiple correcting second-site mutations in *LAMB*3. J Clin Invest. 2007;117(5):1240-8.
220. Sakai N, Waterman EA, Nguyen NT, Keene DR, Marinkovich MP. Observations of skin grafts derived from keratinocytes expressing selectively engineered mutant laminin-332 molecules. J Invest Dermatol. 2010;130(8):2147-50.
221. Jinek M, Chylinski K, Fonfara I, Hauer M, Doudna JA, Charpentier E. A programmable dual-RNA-guided DNA endonuclease in adaptive bacterial immunity. Science. 2012;337(6096):816-21.
222. Karvelis T, Gasiunas G, Miksys A, Barrangou R, Horvath P, Siksnys V. crRNA and tracrRNA guide Cas9-mediated DNA interference in Streptococcus thermophilus. RNA Biol. 2013;10(5):841-51.
223. Mali P, Esvelt KM, Church GM. Cas9 as a versatile tool for engineering biology. Nature Methods. 2013;10(10):957-63.
224. Mali P, Yang L, Esvelt KM, Aach J, Guell M, DiCarlo JE, et al. RNA-guided human genome engineering via Cas9. Science. 2013;339(6121):823-6.
225. Ran FA, Hsu PD, Lin CY, Gootenberg JS, Konermann S, Trevino AE, et al. Double nicking by RNA-guided CRISPR Cas9 for enhanced genome editing specificity. Cell. 2013;154(6):1380-9.
226. Sansbury BM, Hewes AM, Kmiec EB. Understanding the diversity of genetic outcomes from CRISPR-Cas generated homology-directed repair. Communications Biology. 2019;2(1):458.
227. Gutierrez-Guerrero A, Sanchez-Hernandez S, Galvani G, Pinedo-Gomez J, Martin-Guerra R, Sanchez-Gilabert A, et al. Comparison of Zinc Finger Nucleases Versus CRISPR-Specific Nucleases for Genome Editing of the Wiskott-Aldrich Syndrome Locus. Human gene therapy. 2018;29(3):366-80.
228. Waryah CB, Moses C, Arooj M, Blancafort P. Zinc Fingers, TALEs, and CRISPR Systems: A Comparison of Tools for Epigenome Editing. Methods Mol Biol. 2018;1767:19-63.
229. Kim S, Kim D, Cho SW, Kim J, Kim JS. Highly efficient RNA-guided genome editing in human cells via delivery of purified Cas9 ribonucleoproteins. Genome research. 2014;24(6):1012-9.
230. Li H, Beckman KA, Pessino V, Huang B, Weissman JS, Leonetti MD. Design and specificity of long ssDNA donors for CRISPR-based knock-in. bioRxiv. 2017:178905.
231. Lin S, Staahl BT, Alla RK, Doudna JA. Enhanced homology-directed human genome engineering by controlled timing of CRISPR/Cas9 delivery. eLife. 2014;3:e04766.
232. Tsai SQ, Nguyen NT, Malagon-Lopez J, Topkar VV, Aryee MJ, Joung JK. CIRCLE-seq: a highly sensitive in vitro screen for genome-wide CRISPR-Cas9 nuclease off-targets. Nat Methods. 2017;14(6):607-14.
233. Lino CA, Harper JC, Carney JP, Timlin JA. Delivering CRISPR: a review of the challenges and approaches. Drug Deliv. 2018;25(1):1234-57.
234. Giard DJ, Aaronson SA, Todaro GJ, Arnstein P, Kersey JH, Dosik H, et al. In Vitro Cultivation of Human Tumors: Establishment of Cell Lines Derived From a Series of Solid Tumors2. JNCI: Journal of the National Cancer Institute. 1973;51(5):1417-23.
235. Graham FL, Smiley J, Russell W, Nairn R. Characteristics of a human cell line transformed by DNA from human adenovirus type 5. Journal of general virology. 1977;36(1):59-72.

236. Qamar W, Khan MR, Arafah A. Optimization of conditions to extract high quality DNA for PCR analysis from whole blood using SDS-proteinase K method. Saudi J Biol Sci. 2017;24(7):1465-9.
237. Shaw L, Williams RL, Hamill KJ. CRISPR-Cas9-mediated labelling of the C-terminus of human laminin β1 leads to secretion inhibition. BMC Research Notes. 2020;13(1):90.
238. Martiel JL, Leal A, Kurzawa L, Balland M, Wang I, Vignaud T, et al. Measurement of cell traction forces with ImageJ. Methods in cell biology. 2015;125:269-87.
239. Rajput A, Dominguez San Martin I, Rose R, Beko A, LeVea C, Sharratt E, et al. Characterization of HCT116 Human Colon Cancer Cells in an Orthotopic Model. Journal of Surgical Research. 2008;147(2):276-81.
240. Lee AV, Oesterreich S, Davidson NE. MCF-7 Cells—Changing the Course of Breast Cancer Research and Care for 45 Years. JNCI: Journal of the National Cancer Institute. 2015;107(7).
241. Cailleau R, Young R, Olivé M, Reeves WJ, Jr. Breast tumor cell lines from pleural effusions. J Natl Cancer Inst. 1974;53(3):661-74.
242. Wolf G, Ziyadeh FN. Molecular mechanisms of diabetic renal hypertrophy. Kidney international. 1999;56(2):393-405.
243. Syed S, Karadaghy A, Zustiak S. Simple polyacrylamide-based multiwell stiffness assay for the study of stiffness-dependent cell responses. J Vis Exp. 2015(97):52643.
244. Schwarz US, Soiné JRD. Traction force microscopy on soft elastic substrates: A guide to recent computational advances. Biochimica et Biophysica Acta (BBA) - Molecular Cell Research. 2015;1853(11, Part B):3095-104.
245. Sunyer R, Jin AJ, Nossal R, Sackett DL. Fabrication of hydrogels with steep stiffness gradients for studying cell mechanical response. PloS one. 2012;7(10):e46107-e.
246. Guo L, Zhang F, Cai Y, Liu T. Expression profiling of integrins in lung cancer cells. Pathology, research and practice. 2009;205(12):847-53.
247. Busk M, Pytela R, Sheppard D. Characterization of the integrin alpha v beta 6 as a fibronectin-binding protein. J Biol Chem. 1992;267(9):5790-6.
248. López-Colomé AM, Lee-Rivera I, Benavides-Hidalgo R, López E. Paxillin: a crossroad in pathological cell migration. Journal of Hematology & Oncology. 2017;10(1):50.
249. Mierke CT. The role of vinculin in the regulation of the mechanical properties of cells. Cell biochemistry and biophysics. 2009;53(3):115-26.
250. Legerstee K, Geverts B, Slotman JA, Houtsmuller AB. Dynamics and distribution of paxillin, vinculin, zyxin and VASP depend on focal adhesion location and orientation. Scientific Reports. 2019;9(1):10460.
251. Lele TP, Pendse J, Kumar S, Salanga M, Karavitis J, Ingber DE. Mechanical forces alter zyxin unbinding kinetics within focal adhesions of living cells. Journal of cellular physiology. 2006;207(1):187-94.
252. Verderame M, Alcorta D, Egnor M, Smith K, Pollack R. Cytoskeletal F-actin patterns quantitated with fluorescein isothiocyanate-phalloidin in normal and transformed cells. Proceedings of the National Academy of Sciences of the United States of America. 1980;77(11):6624-8.
253. Kanai F, Marignani PA, Sarbassova D, Yagi R, Hall RA, Donowitz M, et al. TAZ: a novel transcriptional co-activator regulated by interactions with 14-3-3 and PDZ domain proteins. The EMBO journal. 2000;19(24):6778-91.
254. Sudol M. Yes-associated protein (YAP65) is a proline-rich phosphoprotein that binds to the SH3 domain of the Yes proto-oncogene product. Oncogene. 1994;9(8):2145-52.
255. Piccolo S, Dupont S, Cordenonsi M. The Biology of YAP/TAZ: Hippo Signaling and Beyond. Physiological Reviews. 2014;94(4):1287-312.
256. Nishiuchi R, Takagi J, Hayashi M, Ido H, Yagi Y, Sanzen N, et al. Ligand-binding specificities of laminin-binding integrins: A comprehensive survey of laminin–integrin

interactions using recombinant α3β1, α6β1, α7β1 and α6β4 integrins. Matrix biology. 2006;25(3):189-97.
257. Vachon PH, Xu H, Liu L, Loechel F, Hayashi Y, Arahata K, et al. Integrins (alpha7beta1) in muscle function and survival. Disrupted expression in merosin-deficient congenital muscular dystrophy. The Journal of clinical investigation. 1997;100(7):1870-81.
258. Cohn RD, Mayer U, Saher G, Herrmann R, Van Der Flier A, Sonnenberg A, et al. Secondary reduction of α7B integrin in laminin α2 deficient congenital muscular dystrophy supports an additional transmembrane link in skeletal muscle. Journal of the neurological sciences. 1999;163(2):140-52.
259. Hodges B, Hayashi Y, Nonaka I, Wang W, Arahata K, Kaufman S. Altered expression of the alpha7beta1 integrin in human and murine muscular dystrophies. Journal of cell science. 1997;110(22):2873-81.
260. Morello V, Cabodi S, Sigismund S, Camacho Leal MdP, Repetto D, Volante M, et al. B1 integrin controls EGFR signaling and tumorigenic properties of lung cancer cells. Oncogene. 2011;30:4087-96.
261. Shibue T, Weinberg RA. Integrin β₁-focal adhesion kinase signaling directs the proliferation of metastatic cancer cells disseminated in the lungs. Proceedings of the National Academy of Sciences. 2009;106(25):10290-5.
262. Harjunpää H, Llort Asens M, Guenther C, Fagerholm SC. Cell Adhesion Molecules and Their Roles and Regulation in the Immune and Tumor Microenvironment. Frontiers in Immunology. 2019;10.
263. Samanta D, Almo SC. Nectin family of cell-adhesion molecules: structural and molecular aspects of function and specificity. Cellular and molecular life sciences. 2015;72(4):645-58.
264. Pasapera AM, Schneider IC, Rericha E, Schlaepfer DD, Waterman CM. Myosin II activity regulates vinculin recruitment to focal adhesions through FAK-mediated paxillin phosphorylation. Journal of Cell Biology. 2010;188(6):877-90.
265. Engler AJ, Sen S, Sweeney HL, Discher DE. Matrix Elasticity Directs Stem Cell Lineage Specification. Cell. 2006;126(4):677-89.
266. Lautenschlaeger F. Cell compliance: cytoskeletal origin and importance for cellular function. 2011.
267. Yurchenco PD, Cheng YS, Colognato H. Laminin forms an independent network in basement membranes. Journal of Cell Biology. 1992;117(5):1119-33.
268. Hellewell AL, Rosini S, Adams JC. A Rapid, Scalable Method for the Isolation, Functional Study, and Analysis of Cell-derived Extracellular Matrix. J Vis Exp. 2017(119):55051.
269. Vehviläinen P, Hyytiäinen M, Keski-Oja J. Matrix association of latent TGF-beta binding protein-2 (LTBP-2) is dependent on fibrillin-1. Journal of cellular physiology. 2009;221(3):586-93.
270. Li N, Liu T, Li H, Zhang L, Chu L, Meng Q, et al. ILF2 promotes anchorage independence through direct regulation of PTEN. Oncol Lett. 2019;18(2):1689-96.
271. Jägers C, Roelink H. Association of Sonic Hedgehog with the extracellular matrix requires its zinc-coordination center. BMC Molecular and Cell Biology. 2021;22(1):22.
272. Zhou X, Qiu W, Sathirapongsasuti JF, Cho MH, Mancini JD, Lao T, et al. Gene expression analysis uncovers novel hedgehog interacting protein (HHIP) effects in human bronchial epithelial cells. Genomics. 2013;101(5):263-72.
273. Reuten R, Patel TR, McDougall M, Rama N, Nikodemus D, Gibert B, et al. Structural decoding of netrin-4 reveals a regulatory function towards mature basement membranes. Nature Communications. 2016;7(1):13515.
274. Doi M, Thyboll J, Kortesmaa J, Jansson K, Iivanainen A, Parvardeh M, et al. Recombinant Human Laminin-10 (α5β1γ1): PRODUCTION,

PURIFICATION, AND MIGRATION-PROMOTING ACTIVITY ON VASCULAR ENDOTHELIAL CELLS &#x2217. Journal of Biological Chemistry. 2002;277(15):12741-8.
275. Kortesmaa J, Yurchenco P, Tryggvason K. Recombinant Laminin-8 (α₄β₁γ₁): PRODUCTION, PURIFICATION, AND INTERACTIONS WITH INTEGRINS *. Journal of Biological Chemistry. 2000;275(20):14853-9.
276. Yurchenco PD, Quan Y, Colognato H, Mathus T, Harrison D, Yamada Y, et al. The α chain of laminin-1 is independently secreted and drives secretion of its β- and γ-chain partners. Proceedings of the National Academy of Sciences. 1997;94(19):10189-94.
277. Bodary SC, McLean JW. The integrin beta 1 subunit associates with the vitronectin receptor alpha v subunit to form a novel vitronectin receptor in a human embryonic kidney cell line. The Journal of biological chemistry. 1990;265(11):5938-41.
278. Yarwood SJ, Woodgett JR. Extracellular matrix composition determines the transcriptional response to epidermal growth factor receptor activation. Proceedings of the National Academy of Sciences. 2001;98(8):4472-7.
279. Conesa A, Madrigal P, Tarazona S, Gomez-Cabrero D, Cervera A, McPherson A, et al. A survey of best practices for RNA-seq data analysis. Genome Biol. 2016;17:13-.
280. Baillat G, Siret C, De*LAMA*rre E, Luis J. Early adhesion induces interaction of FAK and Fyn in lipid domains and activates raft-dependent Akt signaling in SW480 colon cancer cells. Biochimica et biophysica acta. 2008;1783(12):2323-31.
281. Mariotti A, Kedeshian PA, Dans M, Curatola AM, Gagnoux-Palacios L, Giancotti FG. EGF-R signaling through Fyn kinase disrupts the function of integrin α6β4 at hemidesmosomes : role in epithelial cell migration and carcinoma invasion. Journal of Cell Biology. 2001;155(3):447-58.
282. Neilson LM, Zhu J, Xie J, Malabarba MG, Sakamoto K, Wagner K-U, et al. Coactivation of Janus Tyrosine Kinase (Jak)1 Positively Modulates Prolactin-Jak2 Signaling in Breast Cancer: Recruitment of ERK and Signal Transducer and Activator of Transcription (Stat)3 and Enhancement of Akt and Stat5a/b Pathways. Molecular Endocrinology. 2007;21(9):2218-32.
283. Paul R, Luo M, Mo X, Lu J, Yeo SK, Guan J-L. FAK activates AKT-mTOR signaling to promote the growth and progression of MMTV-Wnt1-driven basal-like mammary tumors. Breast Cancer Research. 2020;22(1):59.
284. Heu R, Shahbazmohamadi S, Yorston J, Capeder P. Target Material Selection for Sputter Coating of SEM Samples. Microscopy Today. 2019;27(4):32-6.
285. Nguyen KX, Holtz ME, Richmond-Decker J, Muller DA. Spatial Resolution in Scanning Electron Microscopy and Scanning Transmission Electron Microscopy Without a Specimen Vacuum Chamber. Microscopy and Microanalysis. 2016;22(4):754-67.
286. BRUCH M, LANDWEHR R, ENGEL J. Dissection of laminin by cathepsin G into its long-arm and short-arm structures and localization of regions involved in calcium dependent stabilization and self-association. European journal of biochemistry. 1989;185(2):271-9.
287. Engel J, Odermatt E, Engel A, Madri JA, Furthmayr H, Rohde H, et al. Shapes, domain organizations and flexibility of laminin and fibronectin, two multifunctional proteins of the extracellular matrix. Journal of molecular biology. 1981;150(1):97-120.
288. Marinkovich M, Lunstrum G, Burgeson R. The anchoring filament protein kalinin is synthesized and secreted as a high molecular weight precursor. Journal of Biological Chemistry. 1992;267(25):17900-6.
289. Yurchenco PD, Quan Y, Colognato H, Mathus T, Harrison D, Yamada Y, et al. The α chain of laminin-1 is independently secreted and drives secretion of its β-and γ-chain partners. Proceedings of the National Academy of Sciences. 1997;94(19):10189-94.
290. Lattouf R, Younes R, Lutomski D, Naaman N, Godeau G, Senni K, et al. Picrosirius red staining: a useful tool to appraise collagen networks in normal and pathological tissues. The

journal of histochemistry and cytochemistry : official journal of the Histochemistry Society. 2014;62(10):751-8.
291. Lin R, Li X, Wu S, Qian S, Hou H, Dong M, et al. Suppression of latent transforming growth factor-β (TGF-β)-binding protein 1 (LTBP1) inhibits natural killer/ T cell lymphoma progression by inactivating the TGF-β/Smad and p38(MAPK) pathways. Exp Cell Res. 2021;407(1):112790.
292. Solovyan VT, Keski-Oja J. Apoptosis of human endothelial cells is accompanied by proteolytic processing of latent TGF-β binding proteins and activation of TGF-β. Cell Death & Differentiation. 2005;12(7):815-26.
293. Carracedo A, Pandolfi PP. The PTEN–PI3K pathway: of feedbacks and cross-talks. Oncogene. 2008;27(41):5527-41.
294. Wollman AJM, Nudd R, Hedlund EG, Leake MC. From Animaculum to single molecules: 300 years of the light microscope. Open Biology.5(4):150019.
295. Freeberg MAT, Kallenbach JG, Awad HA. Assessment of Cellular Responses of Tissue Constructs in vitro in Regenerative Engineering. In: Narayan R, editor. Encyclopedia of Biomedical Engineering. Oxford: Elsevier; 2019. p. 414-26.
296. Sherratt MJ, Meadows RS, Graham HK, Kielty CM, Holmes DF. ECM macromolecules: rotary shadowing and transmission electron microscopy. Methods in molecular biology (Clifton, NJ). 2009;522:175-81.
297. Schittny JC, Yurchenco PD. Terminal short arm domains of basement membrane laminin are critical for its self-assembly. The Journal of cell biology. 1990;110(3):825-32.
298. Yurchenco PD, Quan Y, Colognato H, Mathus T, Harrison D, Yamada Y, et al. The alpha chain of laminin-1 is independently secreted and drives secretion of its beta- and gamma-chain partners. Proceedings of the National Academy of Sciences of the United States of America. 1997;94(19):10189-94.
299. Hendricks GM. Metal Shadowing for Electron Microscopy. In: Kuo J, editor. Electron Microscopy: Methods and Protocols. Totowa, NJ: Humana Press; 2014. p. 73-93.
300. Engel J, Furthmayr H. Electron microscopy and other physical methods for the characterization of extracellular matrix components: laminin, fibronectin, collagen IV, collagen VI, and proteoglycans. Methods in enzymology. 1987;145:3-78.
301. Glaeser RM. Electron microscopy of biological specimens in liquid water. Biophysical journal. 2012;103(1):163-6.
302. Watson PE, Watson ID, Batt RD. Total body water volumes for adult males and females estimated from simple anthropometric measurements. The American Journal of Clinical Nutrition. 1980;33(1):27-39.
303. Ekblom P, Alitalo K, Vaheri A, Timpl R, Saxen L. Induction of a basement membrane glycoprotein in embryonic kidney: possible role of laminin in morphogenesis. Proceedings of the National Academy of Sciences. 1980;77(1):485-9.
304. Ikawa H, Trelstad RL, Hutson JM, Manganaro TF, Donahoe PK. Changing patterns of fibronectin, laminin, type IV collagen, and a basement membrane proteoglycan during rat Mullerian duct regression. Developmental biology. 1984;102(1):260-3.
305. Laurie GW, Bing JT, Kleinman HK, Hassell JR, Aumailley M, Martin GR, et al. Localization of binding sites for laminin, heparan sulfate proteoglycan and fibronectin on basement membrane (type IV) collagen. Journal of molecular biology. 1986;189(1):205-16.
306. Voss B, Rauterberg J. Localization of collagen types I, III, IV and V, fibronectin and laminin in human arteries by the indirect immunofluorescence method. Pathology - Research and Practice. 1986;181(5):568-75.
307. Bannerman PG, Mirsky R, Jessen KR, Timpl R, Duance VC. Light microscopic immunolocalization of laminin, type IV collagen, nidogen, heparan sulphate proteoglycan and fibronectin in the enteric nervous system of rat and guinea pig. Journal of neurocytology. 1986;15(6):733-43.

308. Fleischmajer R, Dessau W, Timpl R, Krieg T, Luderschmidt C, Wiestner M. Immunofluorescence analysis of collagen, fibronectin, and basement membrane protein in scleroderma skin. The Journal of investigative dermatology. 1980;75(3):270-4.
309. Sheppard CJR, Choudhury A. Image Formation in the Scanning Microscope. Optica Acta: International Journal of Optics. 1977;24(10):1051-73.
310. Ntziachristos V. Fluorescence molecular imaging. Annu Rev Biomed Eng. 2006;8:1-33.
311. Tran PT, Chang F. Transmitted Light Fluorescence Microscopy Revisited. The Biological Bulletin. 2001;201(2):235-6.
312. Fouquet C, Gilles J-F, Heck N, Dos Santos M, Schwartzmann R, Cannaya V, et al. Improving axial resolution in confocal microscopy with new high refractive index mounting media. PloS one. 2015;10(3):e0121096-e.
313. Peterson DA. Confocal Microscopy. In: Kompoliti K, Metman LV, editors. Encyclopedia of Movement Disorders. Oxford: Academic Press; 2010. p. 250-2.
314. Poole JJA, Mostaço-Guidolin LB. Optical Microscopy and the Extracellular Matrix Structure: A Review. Cells. 2021;10(7):1760.
315. Sonnenberg A, De Melker A, Martinez de Velasco A, Janssen H, Calafat J, Niessen C. Formation of hemidesmosomes in cells of a transformed murine mammary tumor cell line and mechanisms involved in adherence of these cells to laminin and kalinin. Journal of cell science. 1993;106(4):1083-102.
316. Baker SE, Hopkinson SB, Fitchmun M, Andreason GL, Frasier F, Plopper G, et al. Laminin-5 and hemidesmosomes: role of the alpha 3 chain subunit in hemidesmosome stability and assembly. Journal of cell science. 1996;109(10):2509-20.
317. Fontao L, Stutzmann J, Gendry P, Launay J. Regulation of the type II hemidesmosomal plaque assembly in intestinal epithelial cells. Experimental cell research. 1999;250(2):298-312.
318. Nagai T, Laser M, Baicu CF, Zile MR, Cooper IV G, Kuppuswamy D. Beta3-integrin–mediated focal adhesion complex formation: adult cardiocytes embedded in three-dimensional polymer matrices. The American journal of cardiology. 1999;83(12):38-43.
319. Colburn ZT, Jones JC. α(6)β(4) Integrin Regulates the Collective Migration of Epithelial Cells. American journal of respiratory cell and molecular biology. 2017;56(4):443-52.
320. Gonzalez AM, Gonzales M, Herron GS, Nagavarapu U, Hopkinson SB, Tsuruta D, et al. Complex interactions between the laminin α4 subunit and integrins regulate endothelial cell behavior in vitro and angiogenesis in vivo. Proceedings of the National Academy of Sciences. 2002;99(25):16075-80.
321. Sonnenberg A, Linders CJ, Modderman PW, Damsky CH, Aumailley M, Timpl R. Integrin recognition of different cell-binding fragments of laminin (P1, E3, E8) and evidence that alpha 6 beta 1 but not alpha 6 beta 4 functions as a major receptor for fragment E8. The Journal of cell biology. 1990;110(6):2145-55.
322. Buchwalow I, Samoilova V, Boecker W, Tiemann M. Non-specific binding of antibodies in immunohistochemistry: fallacies and facts. Scientific Reports. 2011;1(1):28.
323. Visscher K, Brakenhoff GJ, Visser TD. Fluorescence saturation in confocal microscopy. Journal of Microscopy. 1994;175(2):162-5.
324. Hopkinson SB, DeBiase PJ, Kligys K, Hamill K, Jones JC. Fluorescently tagged laminin subunits facilitate analyses of the properties, assembly and processing of laminins in live and fixed lung epithelial cells and keratinocytes. Matrix biology : journal of the International Society for Matrix Biology. 2008;27(7):640-7.
325. Hotta A, Kawakatsu T, Nakatani T, Sato T, Matsui C, Sukezane T, et al. Laminin-based cell adhesion anchors microtubule plus ends to the epithelial cell basal cortex through LL5α/β. The Journal of cell biology. 2010;189(5):901-17.

326. Bett AJ, Prevec L, Graham FL. Packaging capacity and stability of human adenovirus type 5 vectors. J Virol. 1993;67(10):5911-21.
327. Shroff H, Galbraith CG, Galbraith JA, Betzig E. Live-cell photoactivated localization microscopy of nanoscale adhesion dynamics. Nature methods. 2008;5(5):417-23.
328. Lee SH, Shin JY, Lee A, Bustamante C. Counting single photoactivatable fluorescent molecules by photoactivated localization microscopy (PALM). Proc Natl Acad Sci U S A. 2012;109(43):17436-41.
329. Pawley J. Handbook of biological confocal microscopy: Springer Science & Business Media; 2006.
330. Zhou X, Zhao R, Yanamandra AK, Hoth M, Qu B. Light-Sheet Scattering Microscopy to Visualize Long-Term Interactions Between Cells and Extracellular Matrix. Frontiers in Immunology. 2022;13.
331. Gurskaya NG, Verkhusha VV, Shcheglov AS, Staroverov DB, Chepurnykh TV, Fradkov AF, et al. Engineering of a monomeric green-to-red photoactivatable fluorescent protein induced by blue light. Nature biotechnology. 2006;24(4):461-5.
332. Shcherbakova DM, Sengupta P, Lippincott-Schwartz J, Verkhusha VV. Photocontrollable fluorescent proteins for superresolution imaging. Annual review of biophysics. 2014;43:303-29.
333. Chiu S-W, Leake MC. Functioning Nanomachines Seen in Real-Time in Living Bacteria Using Single-Molecule and Super-Resolution Fluorescence Imaging. International Journal of Molecular Sciences. 2011;12(4):2518-42.
334. Gagliano G, Nelson T, Saliba N, Vargas-Hernández S, Gustavsson A-K. Light Sheet Illumination for 3D Single-Molecule Super-Resolution Imaging of Neuronal Synapses. Frontiers in Synaptic Neuroscience. 2021;13.
335. Legant WR, Shao L, Grimm JB, Brown TA, Milkie DE, Avants BB, et al. High-density three-dimensional localization microscopy across large volumes. Nature methods. 2016;13(4):359-65.
336. Vangindertael J, Camacho R, Sempels W, Mizuno H, Dedecker P, Janssen KPF. An introduction to optical super-resolution microscopy for the adventurous biologist. Methods and Applications in Fluorescence. 2018;6(2):022003.
337. Hagedorn E, Sherwood D. Optically Highlighting Basement Membrane Components in C. elegans. 2011.
338. Sherwood D, Hagedorn E. Optically Highlighting Basement Membrane Components in C. elegans 2011 01/05/2019. Available from: https://protocolexchange.researchsquare.com/article/nprot-2058/v1.
339. Cáceres R, Bojanala N, Kelley LC, Dreier J, Manzi J, Di Federico F, et al. Forces drive basement membrane invasion in <em>Caenorhabditis elegans</em&gt. Proceedings of the National Academy of Sciences. 2018;115(45):11537.
340. Ihara S, Hagedorn EJ, Morrissey MA, Chi Q, Motegi F, Kramer JM, et al. Basement membrane sliding and targeted adhesion remodels tissue boundaries during uterine-vulval attachment in Caenorhabditis elegans. Nature cell biology. 2011;13(6):641-51.
341. Kao G, Huang C-c, Hedgecock EM, Hall DH, Wadsworth WG. The role of the laminin β subunit in laminin heterotrimer assembly and basement membrane function and development in C. elegans. Developmental biology. 2006;290(1):211-9.
342. Sroka I, Chen M, Cress A. Simplified Purification Procedure of Laminin-332 and Laminin-511 from Human Cell Lines. Biochemical and biophysical research communications. 2008;375:410-3.
343. Lee D, Hokinson D, Park S, Elvira R, Kusuma F, Lee J-M, et al. ER Stress Induces Cell Cycle Arrest at the G2/M Phase Through eIF2α Phosphorylation and GADD45α. International journal of molecular sciences. 2019;20(24):6309.

344. Carmignac V, Svensson M, Körner Z, Elowsson L, Matsumura C, Gawlik KI, et al. Autophagy is increased in laminin α2 chain-deficient muscle and its inhibition improves muscle morphology in a mouse model of MDC1A. Human molecular genetics. 2011;20(24):4891-902.
345. Helbling-Leclerc A, Zhang X, Topaloglu H, Cruaud C, Tesson F, Weissenbach J, et al. Mutations in the laminin α2–chain gene (*LAMA*2) cause merosin–deficient congenital muscular dystrophy. Nature Genetics. 1995;11:216.
346. Pierson M, Cordier J, Hervouuet F, Rauber G. [AN UNUSUAL CONGENITAL AND FAMILIAL CONGENITAL MALFORMATIVE COMBINATION INVOLVING THE EYE AND KIDNEY]. Journal de genetique humaine. 1963;12:184-213.
347. Jones LK, Lam R, McKee KK, Aleksandrova M, Dowling J, Alexander SI, et al. A mutation affecting laminin alpha 5 polymerisation gives rise to a syndromic developmental disorder. Development. 2020;147(21):dev189183.
348. Garbe JHO, Göhring W, Mann K, Timpl R, Sasaki T. Complete sequence, recombinant analysis and binding to laminins and sulphated ligands of the N-terminal domains of laminin alpha3B and alpha5 chains. Biochem J. 2002;362(Pt 1):213-21.
349. Philpot J, Sewry C, Pennock J, Dubowitz V. Clinical phenotype in congenital muscular dystrophy: correlation with expression of merosin in skeletal. Neuromuscular Disorders. 1995;5(4):301-5.
350. Alcazar J, Csapo R, Ara I, Alegre LM. On the Shape of the Force-Velocity Relationship in Skeletal Muscles: The Linear, the Hyperbolic, and the Double-Hyperbolic. Frontiers in Physiology. 2019;10.
351. Graham ZA, Gallagher PM, Cardozo CP. Focal adhesion kinase and its role in skeletal muscle. Journal of muscle research and cell motility. 2015;36(4-5):305-15.
352. Anastasi G, Cutroneo G, Santoro G, Arco A, Rizzo G, Bramanti P, et al. Costameric proteins in human skeletal muscle during muscular inactivity. Journal of Anatomy. 2008;213(3):284-95.
353. Bloch RJ, Gonzalez-Serratos H. Lateral force transmission across costameres in skeletal muscle. Exercise and sport sciences reviews. 2003;31(2):73-8.
354. Burkin DJ, Kaufman SJ. The α7β1 integrin in muscle development and disease. Cell and tissue research. 1999;296(1):183-90.
355. Arreguin AJ, Colognato H. Brain Dysfunction in *LAMA*2-Related Congenital Muscular Dystrophy: Lessons From Human Case Reports and Mouse Models. Frontiers in Molecular Neuroscience. 2020;13.
356. Tomaselli KJ, Neugebauer KM, Bixby JL, Lilien J, Reichard LF. N-cadherin and integrins: two receptor systems that mediate neuronal process outgrowth on astrocyte surfaces. Neuron. 1988;1(1):33-43.
357. Herrmann R, Straub V, Meyer K, Kahn T, Wagner M, Voit T. Congenital muscular dystrophy with laminin α2 chain deficiency: identification of a new intermediate phenotype and correlation of clinical findings to muscle immunohistochemistry. European journal of pediatrics. 1996;155(11):968-76.
358. Menezes MJ, McClenahan FK, Leiton CV, Aranmolate A, Shan X, Colognato H. The extracellular matrix protein laminin α2 regulates the maturation and function of the blood–brain barrier. Journal of Neuroscience. 2014;34(46):15260-80.
359. Villanova M, Malandrini A, Toti P, Salvestroni R, Six J, Martin J, et al. Localization of merosin in the normal human brain: implications for congenital muscular dystrophy with merosin deficiency. Journal of submicroscopic cytology and pathology. 1996;28(1):1-4.
360. Chun SJ, Rasband MN, Sidman RL, Habib AA, Vartanian T. Integrin-linked kinase is required for laminin-2–induced oligodendrocyte cell spreading and CNS myelination. The Journal of cell biology. 2003;163(2):397-408.

361. Lanfer B, Hermann A, Kirsch M, Freudenberg U, Reuner U, Werner C, et al. Directed growth of adult human white matter stem cell-derived neurons on aligned fibrillar collagen. Tissue engineering Part A. 2010;16(4):1103-13.
362. Accorsi A, Cramer ML, Girgenrath M. Fibrogenesis in *LAMA*2-Related Muscular Dystrophy Is a Central Tenet of Disease Etiology. Frontiers in Molecular Neuroscience. 2020;13.
363. Mehuron T, Kumar A, Duarte L, Yamauchi J, Accorsi A, Girgenrath M. Dysregulation of matricellular proteins is an early signature of pathology in laminin-deficient muscular dystrophy. Skeletal muscle. 2014;4(1):1-18.
364. Taniguchi M, Kurahashi H, Noguchi S, Sese J, Okinaga T, Tsukahara T, et al. Expression profiling of muscles from Fukuyama-type congenital muscular dystrophy and laminin-α2 deficient congenital muscular dystrophy; is congenital muscular dystrophy a primary fibrotic disease? Biochemical and biophysical research communications. 2006;342(2):489-502.
365. Thomas K, Engler AJ, Meyer GA. Extracellular matrix regulation in the muscle satellite cell niche. Connective tissue research. 2015;56(1):1-8.
366. Morales-Nebreda LI, Rogel MR, Eisenberg JL, Hamill KJ, Soberanes S, Nigdelioglu R, et al. Lung-Specific Loss of α3 Laminin Worsens Bleomycin-Induced Pulmonary Fibrosis. American journal of respiratory cell and molecular biology. 2015;52(4):503-12.
367. Zhu Z, Ding J, Ma Z, Iwashina T, Tredget EE. Alternatively activated macrophages derived from THP-1 cells promote the fibrogenic activities of human dermal fibroblasts. Wound repair and regeneration : official publication of the Wound Healing Society [and] the European Tissue Repair Society. 2017;25(3):377-88.
368. Jones K, Morgan G, Johnston H, Tobias V, Ouvrier R, Wilkinson I, et al. The expanding phenotype of laminin α2 chain (merosin) abnormalities: case series and review. Journal of Medical Genetics. 2001;38(10):649-57.
369. Uhlén M, Fagerberg L, Hallström BM, Lindskog C, Oksvold P, Mardinoglu A, et al. Tissue-based map of the human proteome. Science. 2015;347(6220):1260419.
370. Hiser W, Thirumala V, Wang J, Gillespie R, Bedri B, Zhou XJ. Pierson Syndrome in an Infant With Congenital Nephrotic Syndrome and Unique Brain Pathology. Kidney international reports. 2020;5(12):2371-4.
371. Miyagoe Y, Hanaoka K, Nonaka I, Hayasaka M, Nabeshima Y, Arahata K, et al. Laminin alpha2 chain-null mutant mice by targeted disruption of the *LAMA*2 gene: a new model of merosin (laminin 2)-deficient congenital muscular dystrophy. FEBS letters. 1997;415(1):33-9.
372. Packer D, Martin PT. Micro-laminin gene therapy can function as an inhibitor of muscle disease in the dy^W mouse model of MDC1A. Molecular Therapy - Methods & Clinical Development. 2021;21:274-87.
373. Yurchenco PD, McKee KK, Reinhard JR, Rüegg MA. Laminin-deficient muscular dystrophy: Molecular pathogenesis and structural repair strategies. Matrix Biology. 2018;71-72:174-87.
374. Reinhard JR, Lin S, McKee KK, Meinen S, Crosson SC, Sury M, et al. Linker proteins restore basement membrane and correct *LAMA*2-related muscular dystrophy in mice. Sci Transl Med. 2017;9(396):eaal4649.
375. Ringelmann B, Röder C, Hallmann R, Maley M, Davies M, Grounds M, et al. Expression of laminin alpha1, alpha2, alpha4, and alpha5 chains, fibronectin, and tenascin-C in skeletal muscle of dystrophic 129ReJ dy/dy mice. Exp Cell Res. 1999;246(1):165-82.
376. Meng X-m, Nikolic-Paterson DJ, Lan HY. TGF-β: the master regulator of fibrosis. Nature Reviews Nephrology. 2016;12(6):325-38.
377. Allen RE, Boxhorn LK. Inhibition of skeletal muscle satellite cell differentiation by transforming growth factor-beta. Journal of cellular physiology. 1987;133(3):567-72.

378. Meinen S, Lin S, Ruegg MA. Angiotensin II type 1 receptor antagonists alleviate muscle pathology in the mouse model for laminin-α2-deficient congenital muscular dystrophy (MDC1A). Skeletal Muscle. 2012;2(1):18.
379. Ron A, Azeloglu EU, Calizo RC, Hu M, Bhattacharya S, Chen Y, et al. Cell shape information is transduced through tension-independent mechanisms. Nature Communications. 2017;8(1):2145.
380. Darling NJ, Mobbs CL, González-Hau AL, Freer M, Przyborski S. Bioengineering Novel in vitro Co-culture Models That Represent the Human Intestinal Mucosa With Improved Caco-2 Structure and Barrier Function. Frontiers in Bioengineering and Biotechnology. 2020;8.
381. Yang S, Li S, Li XJ. Shortening the Half-Life of Cas9 Maintains Its Gene Editing Ability and Reduces Neuronal Toxicity. Cell reports. 2018;25(10):2653-9.e3.
382. Ran FA, Hsu PD, Wright J, Agarwala V, Scott DA, Zhang F. Genome engineering using the CRISPR-Cas9 system. Nature Protocols. 2013;8(11):2281-308.
383. Zanoni M, Piccinini F, Arienti C, Zamagni A, Santi S, Polico R, et al. 3D tumor spheroid models for in vitro therapeutic screening: a systematic approach to enhance the biological relevance of data obtained. Scientific Reports. 2016;6(1):19103.
384. Matejas V, Hinkes B, Alkandari F, Al-Gazali L, Annexstad E, Aytac MB, et al. Mutations in the Human Laminin β2 (*LAMB2*) Gene and the Associated Phenotypic Spectrum. Human mutation. 2010;31(9):992-1002.
385. Morais MRPT, Tian P, Lawless C, Murtuza-Baker S, Hopkinson L, Woods S, et al. Kidney organoids recapitulate human basement membrane assembly in health and disease. eLife. 2022;11:e73486.
386. Tian P, Lennon R. The myriad possibility of kidney organoids. Current opinion in nephrology and hypertension. 2019;28(3):211-8.
387. Tuffin J, Chesor M, Kuzmuk V, Johnson T, Satchell SC, Welsh GI, et al. GlomSpheres as a 3D co-culture spheroid model of the kidney glomerulus for rapid drug-screening. Communications Biology. 2021;4(1):1351.
388. Tholozan FMD, Gribbon C, Li Z, Goldberg MW, Prescott AR, McKie N, et al. FGF-2 release from the lens capsule by MMP-2 maintains lens epithelial cell viability. Molecular biology of the cell. 2007;18(11):4222-31.
389. Schwartz D, Veis A. Structure of bovine anterior lens capsule basement membrane collagen molecules from electron microscopy. Biopolymers. 1979;18(9):2363-7.
390. SCHWARTZ D, VEIS A. Characterization of Bovine Anterior-Lens-Capsule Basement-Membrane Collagen. European Journal of Biochemistry. 1980;103(1):29-37.
391. Yurchenco PD, Cheng Y-S, Colognato H. Laminin forms an independent network in basement membranes. The Journal of cell biology. 1992;117(5):1119-33.
392. Bickel M. The role of interleukin-8 in inflammation and mechanisms of regulation. Journal of periodontology. 1993;64(5 Suppl):456-60.
393. Lopez-Castejon G, Brough D. Understanding the mechanism of IL-1β secretion. Cytokine Growth Factor Rev. 2011;22(4):189-95.
394. McKee KK, Crosson SC, Meinen S, Reinhard JR, Rüegg MA, Yurchenco PD. Chimeric protein repair of laminin polymerization ameliorates muscular dystrophy phenotype. J Clin Invest. 2017;127(3):1075-89.
395. Troughton LD, Iorio V, Shaw L, Sugden CJ, Yamamoto K, Hamill KJ. Laminin N-terminus α31 regulates keratinocyte adhesion and migration through modifying the organisation and proteolytic processing of laminin 332. bioRxiv. 2020:617597.
396. Hamill KJ, Langbein L, Jones JCR, McLean WHI. Identification of a novel family of laminin N-terminal alternate splice isoforms: structural and functional characterization. The Journal of biological chemistry. 2009;284(51):35588-96.

397. Kikkawa Y, Sugawara Y, Harashima N, Fujii S, Ikari K, Kumai J, et al. Identification of laminin α5 short arm peptides active for endothelial cell attachment and tube formation. Journal of peptide science : an official publication of the European Peptide Society. 2017;23(7-8):666-73.
398. Kusuma N, Anderson RL, Pouliot N. Laminin α5-derived peptides modulate the properties of metastatic breast tumour cells. Clinical & experimental metastasis. 2011;28(8):909-21.
399. McKee KK, Hohenester E, Aleksandrova M, Yurchenco PD. Organization of the laminin polymer node. Matrix Biology. 2021;98:49-63.
400. Pulkkinen L, Meneguzzi G, McGrath JA, Xu Y, Blanchet-Bardon C, Ortonne JP, et al. Predominance of the recurrent mutation R635X in the *LAMB*3 gene in European patients with Herlitz junctional epidermolysis bullosa has implications for mutation detection strategy. The Journal of investigative dermatology. 1997;109(2):232-7.
401. Lincoln V, Cogan J, Hou Y, Hirsch M, Hao M, Alexeev V, et al. Gentamicin induces *LAMB*3 nonsense mutation readthrough and restores functional laminin 332 in junctional epidermolysis bullosa. Proceedings of the National Academy of Sciences. 2018;115(28):E6536-E45.
402. Benati D, Miselli F, Cocchiarella F, Patrizi C, Carretero M, Baldassarri S, et al. CRISPR/Cas9-Mediated In Situ Correction of *LAMB*3 Gene in Keratinocytes Derived from a Junctional Epidermolysis Bullosa Patient. Molecular Therapy. 2018;26(11):2592-603.
403. Guimbellot J, Sharma J, Rowe SM. Toward inclusive therapy with CFTR modulators: Progress and challenges. Pediatric Pulmonology. 2017;52(S48):S4-S14.